FACULDADE DE ENGENHARIA DA UNIVERSIDADE DO PORTO

Study of Mooring Systems for Offshore Wave Energy Converters

Guilherme Moura Paredes

Programa Doutoral em Engenharia Civil

Supervisor: Francisco de Almeida Taveira Pinto

Second Supervisor: Luís Manuel de Carvalho Gato

November 14, 2016

Study of Mooring Systems for Offshore Wave Energy Converters

Guilherme Moura Paredes

Programa Doutoral em Engenharia Civil

November 14, 2016

Resumo

Os conversores flutuantes de energia das ondas necessitam de ser fixados de modo a impedir que fiquem à deriva no mar ou que sofram danos. No alto mar, com águas de profundidade intermédia a elevada, a utilização de sistemas de amarração é uma opção atractiva por causa do seu custo reduzido. Devido às especificidades dos conversores flutuantes de energia das ondas (por exemplo a necessidade de oscilar em ressonâcia), a concepção de soluções de amarração adequadas requer o estudo de configurações de amarração diferentes das utilizadas em estruturas *offshore* mais comuns. De modo a fornecer alguma assistência nesta tarefa, são apresentados três resultados: um modelo numérico de cabos; uma técnica para seguir os movimentos de cabos de amarração em modelos reduzidos; e dados experimentais sobre testes em modelo reduzido de diferentes configurações de amarração. O modelo numérico de cabos utiliza o método de Galerkin com elementos espectrais/*hp* descontinuos, para resolver a equação diferencial parcial de cabos perfeitamente flexíveis. Apresenta convergência exponencial para a solução e mostra algumas características que indicam ter a capacidade de capturar ondas de choque. A técnica de seguimento de cabos regista vídeos subaquáticos de cabos de amarração em modelos reduzidos, que são processados utilizando um algorítmo especialmente desenvolvido para detectar e determinar a geometria dos cabos em função do tempo. Toda a extensão do cabo é detectada, e não apenas alguns pontos seleccionados ao longo do seu comprimento, não havendo necessidade de utilizar interpolação para reconstruir a geometria. As configurações de amarração estudadas em modelo reduzido são a catenária e duas configurações compactas, formadas por cabos tensos com flutuadores e pesos concentrados. O modelo físico é composto por uma bóia cilíndrica, que representa um conversor flutuante de energia das ondas genérico, que é fixado por cada uma das configurações estudadas. São apresentados dados acerca das tensões máximas e mínimas nos cabos, dos deslocamentos da bóia, funções de transferência de primeira e segunda ordem, entre outros parâmetros, para ensaios com ondas regulares e irregulares. As ferramentas e resultados indicados permitem tanto a investigadores como a projectistas obter um conhecimento mais profundo sobre o comportamento dinâmico de cabos de amarração, e ter mais informação na altura de decidir a solução mais apropriada para um sistema de amarração. O modelo numérico torna possível fazer a simulação de conversores amarrados em condições altamente dinâmicas, utilizado discretizações grosseiras. A técnica para seguir o movimento de cabos pode ser utilizada tanto para a validação e calibração de simulações numéricas, como para determinar as regiões mais activas de cabos de amarração, desenvolver formulações e estudos mais avançados sobre o seu amortecimento, etc. Os resultados experimentais salientam as vantagens e desvantagens das três configurações estudadas, tornando mais fácil a selecção do melhor conceito conforme o dispositivo e a situação em causa.

Abstract

Wave energy converters need to be secured to prevent them form drifting away in the sea or getting damaged. In offshore regions, with intermediate to deep waters, the use of mooring systems to keep the converters on station is an attractive solution because of its reduced cost. Due to the specificities of offshore wave energy converters (for example, the need to oscillate in resonance), the development of an appropriate mooring solution requires the study of mooring configurations different from those used in typical offshore structures. To provide some assistance in this task, three different outcomes are presented: a numerical model for mooring cables; a technique to track mooring cables in small scale models; and results of experimental tests of small scale models of different mooring configurations. The numerical model uses the spectral/*hp*-element discontinuous Galerkin method to solve the partial differential equation of perfectly flexible cables. It has exponential convergence to the solution and exhibits shock capturing features. The tracking technique records underwater videos of mooring cables in small scale models. These videos are processed using an especially developed algorithm that determines and outputs the geometry of the cable, represented by its medial axis, as a function of time. The cable is detected in its full length, and not only at selected points, so there is no need for interpolation to estimate its true shape. The mooring configurations studied in small scale physical models are the chain catenary, and two compact configuration using taut cables, floaters and clumpweights. The physical model is composed of a cylindrical buoy representing a generic wave energy converter that is kept on station by the different mooring configurations studied. Data is provided about the maximum and minimum tension in the cables, the displacements of the buoy, the response amplitude operators for the three configurations, among other parameters, when the model is subjected to regular and irregular waves. The tools and results mentioned allow researchers and developers to get a deeper insight into the dynamic behaviour of mooring cables, and to have more information in the selection of an appropriate mooring configuration. The numerical model makes it possible to carry out simulations of moored devices in highly dynamic conditions using coarse discretisations. The technique to track mooring cables can be used to validate numerical simulations, as well as to get a better understanding of the most active regions of mooring cables, accurate estimates of damping, etc. The results from the experiments pin-point the advantages and disadvantages of the three configurations studied, and make it easier to select the best one for a specific device and situation.

Acknowlegements

Although I am presented as the author of this thesis, it would not be possible to complete it without the assistance of several people, whose contribution I wish to acknowledge.

I would like to thank my supervisor, Prof. Francisco de Almeida Taveira Pinto, from FEUP, and my co-supervisor, Prof. Luís Manuel de Carvalho Gato, from IST, for proposing the research topic and for their support throughout my work.

I also want to express my most sincere gratitude to my family not only for its support and patience during my endeavour, but also for their additional insight and assistance in several tasks, and in particular my brother Miguel, for his companionship and encouragement.

A word of appreciation goes also to my Swedish friends, Johannes Palm, Claes Eskilsson and Lars "Lasse" Bergdahl. They have welcomed me during my mobility period in Sweden, at Chalmers University of Technology and, more than assisting me in my research, they made me feel at home. Their support and knowledge during and after my stay in Sweden were fundamental for the successful completion of my PhD work.

For his assistance in the tasks concerning image processing, I would also like to thank Prof. Miguel Fernando Paiva Velhote Correia, from FEUP.

I would also like to thank all my friends, who have been by my side during this time, keeping my spirit and motivation up. In particular, my friends at FEUP, for the laughs and good moments we shared, which contributed to an excellent work environment.

Finally, I acknowledge the support of Fundação para a Ciência e Tecnologia, for partially funding my research through PhD grant SFRH/BD/62040/2009 and research project PTDC/EME-MFE/103524/2008, financed by the POPH/FSE program.

Guilherme Moura Paredes

"By three methods we may learn wisdom: First, by reflection, which is noblest; Second, by imitation, which is easiest; and third by experience, which is the bitterest."

Attributed to Chinese philosopher Confucius

Contents

List of Figures

List of Tables

List of Symbols

Chapter 1

Introduction

Current mooring technology and design standards cannot entirely fulfil the needs of offshore wave energy converters. This is due to four properties of wave energy converters that set them aside from other floating structures: their purpose, deployment, investment/revenue relation and consequences in case of failure.

While the mooring system of an offshore platform has an extremely important role in preventing catastrophic failures, it amounts to only 2 % of the total investment [1]. With such a critical role in the safety of offshore platforms and reduced cost proportion, developers do not feel the need to optimise the design of mooring systems. In offshore wave energy converters, the consequences of failure of the mooring system are minor when compared with offshore platforms. As such, they do not require tight safety requirements. Nevertheless, the application of offshore standards has been recommended, and that results in mooring systems which might represent 18 % [1] to 30 % [2] of the total investment.

With a high percentage of the investment being associated with the mooring system, reducing its cost is fundamental for the financial success of any offshore wave energy enterprise. However, this is not the only requirement.

Independently of the type of device, offshore wave energy converters are to be installed in high energy areas in order to maximise their energy output. These are regions where the wave climate is powerful and, as consequence, where the converter and its mooring system will be under severe loading.

Some types of wave energy converters – the motion dependent converters – need to oscillate in the waves, often in resonance, in order to extract energy. These oscillations will subject the mooring system to high frequency, large amplitude motions, inducing high dynamic tensions in the mooring cables, especially when in resonance. This departs from the common desire to avoid resonant motions of floating structures, to a far more demanding regime than usual for mooring cables.

The complications caused by the loading regime of mooring cables of wave energy converters extend as far as the design tools of mooring systems. Numerical modelling of mooring cables is already challenging in traditional cases where resonance is to be minimised and, nevertheless,

there might be considerable dynamic tensions and motions of the cables. As will be detailed in the Literature Review, chapter 2, in these situations the numerical formulations might break down or it might be necessary to use fine discretisations. In scenarios where large amplitude oscillations and tensions are expected, these issues can become unmanageable.

The mooring system might also have a direct influence on the efficiency of motion dependent converters, since the cables change the dynamic properties of the converter by adding their own mass (and added mass), stiffness and damping. The stiffness and mass of the mooring system are not necessarily detrimental and might even improve the efficiency of the converter, as noted in [3]. As for the additional damping, while it contributes to the stability of general floating structures [4], in motion dependent wave energy converters it dissipates energy that could otherwise be harnessed.

The conclusions regarding the influence of the mooring system on a wave energy converter are not consensual and depend both on the approach used to study it and on the converter itself. In [5], the experimental results show that changing the pre-tension of a catenary mooring system can lead to variations of up to 16 % in power extraction. In [3] is it concluded that even the position of the fairlead on the wave energy converter can affect the performance. However, in [6] it is concluded that the catenary mooring system has little to no influence on the power extraction (less than 1 %). Similar results for a spherical point absorber are reached in [7] and in [8], where no significant influence of the mooring system is noted in numerical simulations.

In the same way as wind or solar power, some wave energy converters are envisioned to be deployed in parks that may contain tens to hundreds of machines. In order to maximise the energy yield, the converters can be closely spaced [9] and it is essential to prevent the devices from colliding with each other and their mooring cables to get entangled or otherwise interact.

It is paradoxical that at the same time that the devices might be required to oscillate in resonance to extract energy, they might also be expected to have small horizontal motions in order to avoid collisions. These are conflicting demands that require a new level of sophistication for the mooring systems and knowledge about their dynamics, more precisely, their motion. This is critical not only for the study of the interaction between mooring cables of nearby converters, but also to determine regions where mooring damping can be minimised or where the cables are subjected to significant wear. Such knowledge can be difficult to obtain using numerical models because of the complex interaction between mooring cables and water, which might, at least, require calibration using experimental measurements.

In spite of the difficulties and limitations of simulating mooring cables, surprisingly, there is little interest in techniques to study their behaviour in laboratory. With few exceptions, the bulk of the research regarding physical models of mooring cables is limited to measuring tension forces at one or more points along the cable, without considering their motion or geometry. While this might be acceptable for traditional floating structures, whose design is primarily based on the tension force, it does not seem to be acceptable for offshore wave energy converters.

Taking into account the characteristics mentioned above, a good mooring system for a floating wave energy converter must not only consider the possible effects on the device motions and power take-off, but it must also ensure survivability, be easy to monitor and maintain, and minimise

material and installation costs. It is also desirable that it takes as little space as possible on the seabed (seabed footprint) to allow the devices to be installed close to each other, a property that is not important, or even allowed, in other offshore structures.

Even though the specificities of wave energy converters described above have been recognised for some time, they have not yet been fully addressed by either the industry or the research community. More precisely, the design of mooring systems for offshore wave energy converters is still largely based on the procedures and guidelines of the offshore hydrocarbon industry. This can be seen, for example, in the design of the mooring system for the FLOW wave energy converter [10], which followed the safety requirements of offshore platforms and did not account for the impact on the performance of the converter. It is also seen in the mooring studied for the DEXA concept [5] which uses catenaries, the standard mooring solution. Even though it is a natural first choice for a mooring system, the catenary, as pointed out by [11] might not be the best solution for wave energy converters.

The comparison between the FLOW and the DEXA also shows that there is little consensus about appropriate mooring solutions: both concepts are hinged attenuators, but while the DEXA uses catenaries, the FLOW uses a compact mooring system of taut synthetic cables.

It is the aim of this work to try to fill in the gaps identified above by providing tools to assist developers in the design of mooring systems for floating wave energy converters. These tools come in three forms: a numerical model for mooring cables; a laboratory technique to track the motions of mooring cables in small scale models; and experimental results from physical model tests of different mooring configurations.

The numerical model for mooring cables, presented in chapter 3, is aimed to be especially adapted to the loading regime of motion dependent wave energy converters. This objective is attempted by the use of the spectral/*hp*-element discontinuous Galerkin method. The spectral/*hp*-element method can exhibit exponential convergence and so it can provide high accuracy solutions using coarse discretisations. Using higher order polynomials, it can easily represent geometries other than rectilinear, capturing well both the shape of the cable and the tension along the cable. Discontinuous Galerkin formulations do not enforce the continuity of the solution at the border of the elements. This allows shock waves (discontinuities) like snap loads to be captured. In the case of the Local Discontinuous Galerkin formulation, the mass matrix is block diagonal and can be more efficiently inverted than the fully coupled matrices of continuous formulations.

The tracking technique, presented in chapter 4, records underwater videos of mooring cables in wave tanks and processes those videos to determine the medial axis of the cables. Using video cameras it is possible to obtain information about the motions of the cables from a distance, without causing excessive interference in the experimental set-up. An advantage of the technique over others is that it captures the entire length of the cable and, therefore, it does not require interpolation. Moreover, it can be applied to a broad range of situations, since all the experimental steps are executed underwater, without the need for windows on the sides of wave tanks. A limitation in the presented work is that the technique is only developed as far as tracking single cables, without floaters and clumpweights.

The results from the experimental testing of different mooring configurations are presented in chapter 5. Their goal is to assist in clarifying the benefits and the downsides that different mooring configurations have when applied to offshore wave energy converters. The configurations selected for testing were developed based on the suggested work and research of different authors. They are analysed in terms of the space they take, how they respond to extreme loading regimes, how significant their influence is on the performance and motions of the wave energy converter, etc. The focus is put on motion dependent point absorbers that might be deployed in parks, as these are the devices that present the greater challenges for the mooring system, but the results can be used in a more general analysis.

Each of the chapters mentioned above is relatively self-contained and can be read independently, including the conclusions and suggested research. In any case, a general overview of the most important conclusions and possible developments are presented, respectively, in chapters 6 and 7.

Notation

Throughout this work an effort was made to keep the notation and symbols as simple and as consistent as possible, adhering to internationally recognised standards. Physical quantities and their symbols, as well as their units, are represented using the notation of the International System of Units (SI) and of the International Union of Pure and Applied Chemistry (IUPAC). Numbers are represented using the convention of the International Standards Organisation, where decimal separation is represented by a comma.

Regular lower-case letters, either Greek or Latin, represent scalar quantities while bold font lower-case letters are used for vectors; bold font upper-case Latin letters represent matrices.

Chapter 2

Literature Review

2.1 Modelling cable dynamics

The development of the theory and methods concerning the dynamics of cables in general, and mooring cables in particular, has been driven mostly by the needs of the offshore industry, in its different fields: hydrocarbons, shipping and cable layout. A large portion of the results are due to the work carried out by Irvine in the 1970's, compiled in [12], and Triantafyllou and its associates in the 1980's and early 1990's. Several important contributions have been made by other authors as well, but not in such a great extent.

As early as 1960, as part of the ongoing tests of nuclear blasts on ships, Walton and Polacheck [13] presented a finite difference scheme for the simulation of mooring cable dynamics. With only one reference to previous works regarding the numerical solution of the dynamics of mooring cables, this is probably one of the earliest attempts at systematising numerical methods for this problem.

The cable is assumed to be perfectly flexible (no torsional or bending stiffness), which will become the standard for mooring cables, and inextensible. Hydrodynamic effects are already accounted for in the form of added inertia and viscous quadratic drag for the transverse motions of the cable.

As in any finite difference scheme, the cable is divided into segments, but the mass and loads acting on the cable are concentrated, or lumped, at the nodes between each segment. Accelerations, velocities, displacements and forces are computed for the lumped masses. Although not designated as such, this is the foundation of the Lumped Mass Method. Non-linearities in the formulation, both in the loads and in the partial differential equation of cable dynamics, are linearised so that the system of equations relating all nodes can be solved in a matrix form. In order to correct the side-effects of the linearisation, at each time step the solution process is divided into two stages. The first stage computes approximate values for the desired variables; the second stage determines corrections to be added to the approximate values, obeying prescribed criteria. For stability, a leap-frog like method is used for time stepping.

Since elasticity is not accounted for, this formulation is only valid for situations where the excitation frequency of the cables is well below the frequency of longitudinal elastic waves.

Results are presented for some numerical simulations, but these are not compared with any experimental data for validation. However, it is already noted the influence that the hydrodynamic terms play in the stability of the equation of flexible cables. For a steady-state periodic excitation of the top end of the cable, a steady-state periodic response of the cable can only be obtained when hydrodynamic effects are accounted for. When hydrodynamic effects are neglected, the simulations never achieve a steady-state, presenting instead irregular oscillations. This instability of the equation of flexible cables will become important in future developments of numerical schemes.

The importance of the dynamic behaviour of mooring cables was highlighted by Larsen and Fylling in [14], where they compared the results of quasi-static simulations of mooring cables with those of dynamic simulations, under different loading regimes. The dynamic simulations used the linear finite element method for the cable and a simple linear spring model for the ground.

It was found that, for large water depths, the use of quasi-static analysis leads to under-estimation of the dynamic tension. Therefore, in the study of deep water mooring systems, quasi-static analysis should be replaced by dynamic analysis.

As for loading regimes, the results showed that the first order effects of wave loading on the dynamic tensions in mooring cables is relatively small, but depends on the type of cable used. Wire cables react to wave frequency excitations using their elastic stiffness, generating higher dynamic tensions than chain cables, which react mostly using their catenary stiffness. The most important cause of large dynamic tensions is the large and slow motion of the floating structure, which might be caused either by second order wave loads or by wind. The effect of currents on dynamic tensions is small, as they are relatively steady, causing mostly an increase of the mean tension component.

This early study highlights several key aspects that were the research focus of the following years.

Later, Triantafyllou *et al.* [15], presented a methodology for the preliminary design of mooring cables accounting for dynamic effects, featuring mostly the behaviour of cables whose end points are at different heights. The text covers a wide variety of subjects, including linear and non-linear analysis of cables, the mechanisms behind different loading and response regimes, the relative importance of linear and non-linear effects on cables with large and small sag-to-span ratio, the effect of elasticity and elastic waves on dynamic tension, etc.

On the subject of dynamic tensions, it is highlighted the significance of the hydrodynamic forces, namely viscous drag and added inertia. When the relative velocity between the cable and the water increases, so does the magnitude of the hydrodynamic forces and the resistance to transverse motions. Becoming unable to change its geometry to react to external loadings, the cable is forced to react by stretching, generating high dynamic tensions. As a solution to minimise dynamic tensions, the authors suggested the combination of cables with different elasticities, which would be mobilised under the different loading or excitation regimes.

Even though there is no formulation presented to model the interaction between the cable and the ground, it is discussed the importance of the ground in the tension in the cable. More precisely, it is recognised the relevance of the celerity of the cable touch-down position, and a limiting criterion is derived that determines when to account for this effect.

Finally, a procedure is presented for a linearised, frequency-domain study of mooring cables including drag effects, which showed a good agreement with non-linear time-domain simulations. This approach made it possible for a preliminary design to be done in the frequency domain, quickly testing different solutions and leaving lengthy time domain simulations for fine-tuning of details.

In the context of studying the dynamics of towed cables in sonar arrays, Ablow and Schechter [16] developed another implicit finite difference scheme to solve the equations of perfectly flexible cables, but now including elasticity.

Each cable segment has a local reference frame representing its orientation, and Euler angles are used to convert between local and global coordinates. There is a total of seven equations and seven unknowns for each segment that need to be assembled in the global cable matrix. Since the formulation is implicit, it is possible to use large time-steps in the simulations. Because of this, as the authors report, it was the first numerical formulation to solve the dynamics of cables in less time than the test case would take in reality.

When the tension is null, the system of equations becomes singular and the formulation breaks-down. In order to avoid the issue of zero tension at the free end of the cable, its last portion is modelled as rigid beam, with the same tension as the previous segment. As the model is not designed for highly dynamic situations, the problem of null tensions is not treated with much detail. The simulations presented are for cases with time varying inputs, although relatively smooth when compared with resonance phenomena. Singularity happens also when sections of the cable become vertical, because when the local tangent vector becomes aligned with the global vertical axis, the Euler angles become undefined.

The use of the Lumped Mass Method for the simulation of vessels moored with inextensible cables was presented by Ansari and Khan in [17]. The dynamics of both the mooring system and floating vessel are solved in the time-domain, but semi-independently: the dynamics of the vessel are affected by the mooring system, but dynamics of the mooring system are determined beforehand for a specified range of forced motions. First, for the selected mooring arrangement, simulations are carried out for the forced motions of the top end of the cables to determine the dynamic tension forces. This data is used to create curves of dynamic tension in the mooring cables as a function of their horizontal span. Afterwards, in the simulation of the moored vessel subjected to external loads, the mooring system is included by applying the dynamic tension forces at each position of the vessel read from the tension-horizontal span curves created earlier.

A case study is presented for a barge moored in shallow water. When compared to a quasi-static analysis, the dynamic analysis presents smaller maximum tensions in the most loaded cables, but higher average tensions in all the cables. As a consequence, the horizontal displacements are

smaller. This illustrates the impact that even a simplified dynamic analysis can have on improving a mooring design.

The advantages and disadvantages of the Lumped Mass Method and of the Finite Element Method when applied to solve the dynamics of cables for general oceanic applications are examined by Leonard and Nath in [18]. Although the authors acknowledge that higher order finite element methods are already being applied in cable dynamics, only the case of linear finite elements is evaluated, since it is the only one that can be directly compared with the lump mass method. The mathematical and numerical properties of each method are derived analytically so that they can be compared.

It is concluded that the finite element method, since it treats the cable as being continuous, might be better suited to model cables with coarse discretisations. However, because it solves a system of coupled differential equations, the solution for each time step can be computationally demanding. In the Lumped Mass Method, the discretisation of the cable as a set of point-wise masses results in a decoupled mass matrix, which can be efficiently inverted. But, at the same time, lumping the masses has an inherent error and requires finer discretisations than the finite element method, partially counteracting the advantage of having an uncoupled mass matrix. For both methods, it is stressed that the hydrodynamic forces, which are based on Morison's formula and experimental coefficients, are subjected to a large uncertainty and might dissipate any advantage of one method over another.

It is also mentioned that the selection of one method over another is strongly dependent on the familiarisation of those working with cable dynamics with each of the methods.

In [19], Nakamura *et al.* used a simplified numerical model to demonstrate the importance of the hydrodynamic damping and of the non-linear behaviour of catenary in slow drift motions of moored structures. Slow drift oscillations are more influenced by the damping and by dynamic effects of the mooring cables than wave frequency motions, which are practically unaffected.

The results of the simulations accounting for damping, added inertia and non-linear catenary effects agree well with experimental data, even though the model is a simplified one. On the contrary, the use of equivalent linear stiffness elements to model mooring cables leads to incorrect estimations of both the slow drift motions and the tensions in cables. This inaccuracy in the calculations depends on the excitation frequency and on whether the simulations use regular or irregular waves. For low frequencies, the tension in the cables is under-estimated and the motions are over-estimated. The opposite is true for higher frequencies. Additionally, when using linear stiffness elements, the peak frequency of the tension cycles in the wave frequency range is underestimated, which causes the fatigue damage to be also underestimated.

In order to prevent the singularity that occurs when the tension is zero, Burgess [20] presented a set of equations for cable dynamics which included the effects of bending and torsion stiffness. This ensures that even in the case of zero tension, there is a component of the constitutive relations that is always different from zero. Like in [16], a local coordinate frame is assigned to each segment of the cable and Euler angles are used to represent the local orientation.

The inclusion of the flexural terms increased considerably the complexity of the equations of motion when compared with the equation of perfectly flexible cables: this formulation required three vector equations (one for position, one for rotation and one for the constitutive relations) and six scalar equations (to convert from local to global coordinates).

Due to the use of Euler angles, the formulation breaks down when the tangent axis of the elements becomes vertical, just like in [16]. However, the numerical model of [20] is formulated in such a way as to allow Euler angles to be easily replaced in future developments by improved relations for the conversion of local to global coordinates, thereby avoiding this singularity.

In [21], Triantafyllou and Howell demonstrated analytically that the equation of perfectly flexible cables will always result in ill-posed problems when the tension is negative. Well-posedeness of problems of cable dynamics can only be guaranteed when additional stabilising terms are added to the equation. Ideally, these terms should have a physical meaning, like bending or torsion stiffness, but this is not required as long as they contribute to an accurate solution. The stabilising terms are not required to be intricate either: for example, well-posedness can be achieved using only simplified models of bending stiffness, even when the bending stiffness is small. In general, a solution will be possible if, in the equation of cable dynamics, there are terms with odd spatial derivatives with a higher order than those of the stiffness terms.

Papazoglou and Mavrakos [22] presented a clear discussion on the adequate scaling of mooring cables for physical modelling. Here, the authors described how the dynamics of submerged cables are fundamentally different from those of cables in air, a subject that had already been highlighted in [13]. On the one hand, the hydrodynamic terms oppose the transverse motion of the cables, forcing axial displacement and stretching that lead to large dynamic tensions, as explained in [15]. On the other hand, the resistance to transverse displacements causes the terminal velocity of free falling cables to be smaller in water than in air, enabling the cables to become completely slack and the tensions to go to zero. Both of these issues would be very unlikely to happen for cables in air, where the catenary stiffness would be dominant and prevent the cables from becoming slack. As the dynamic tension in the cables grows and exceeds the static tension, the elastic stiffness becomes dominant and elastic waves become an important phenomenon. In this regime, the motions of the cables are also large enough to allow them fall with their low terminal velocity and become slack. For taut or semi-taut cables, in spite of the hydrodynamic forces opposing their motions, small axial displacements of their top end might induce large transverse displacements across the cable.

With the exception of vortex induced vibrations, which increase the magnitude of the hydrodynamic forces, motions of the cable in directions normal to the plane of the excitation have little influence in the tension.

Time-domain numerical simulations are also presented and compared with experimental data. The numerical simulations used spectral numerical methods, combining the developments provided in other publications, even though they are not fully detailed. Although not used, references are also made to numerical methods using linear orthogonal polynomials and sinusoids, as well as Chebychev polynomials with the collocation method. Time integration is performed using New-

mark's method. The simulated and measured tensions are remarkably similar, except for high frequency oscillations that appear in the experimental measurements when the tension is close to zero. These oscillations are not present in the numerical simulations, which is speculated to be due to numerical damping.

As a solution to control the dynamic tensions, in [23] Mavrakos *et al.* studied the application of buoys in mooring cables. In order to avoid time-consuming non-linear simulations and examine several options, the dynamics of the cables and of the drag forces were linearised and analysed in the frequency domain. The study considered different buoy positions, number of buoys and buoyancy forces.

It was concluded that buoys can indeed reduce the dynamic tensions in mooring cables within a certain frequency range. However, it was also found that buoys might actually contribute to larger dynamic tensions than in a cable without any buoy and, therefore, their use should be thoroughly examined.

In the continuation of the previous study [23], Mavrakos *et al.* [24] performed large scale experiments of mooring configurations in a lake, in order to evaluate the benefits of using buoys for dynamic tension reduction.

The large scale experiments used a barge to apply motions to a mooring cable anchored to the bottom of the lake. Different cable and buoy configurations were studied, measuring both the tension and displacements at the buoys, at the anchor and at the barge. It is concluded that the use of buoys may indeed reduce the dynamic tension provided their application is carefully analysed, just like it was found in the earlier study presented in [23].

The large scale experiments were reproduced in time-domain and frequency-domain simulations. As expected, the results of time-domain simulations correlate better with the experimental measurements than the frequency-domain simulations, due to the inclusion of non-linear effects.

Although filtered, the experimental records of the tension present a significant level of high frequency oscillations, that the numerical simulations cannot reproduce, similar to what was reported in [22]. This effect is more evident for tensions measured at the top end of the cable than at lower positions. Another interesting result is the difficulty in modelling the ground, which has already been discussed. In one of the experimental set-ups, there is a substantial portion of the cable that is lying on the bottom of the lake and never fully lifts. Accurate simulations of this experimental case were obtained only when most of the cable lying on the ground was neglected in the numerical model, which demonstrated the importance of accurate models for interaction with the ground.

Large scale experiments were also performed by Johanning *et al.* [25] to determine the dynamics of a mooring cable in prototype scale. These experiments tested three different pre-tension states of a mooring cable: slack, fully lifted and taut.

The test set-up consisted of a single chain anchored to the seabead and excited at the top end by the motion of a vessel, akin to that of [23]. Although seemingly simple, the large dimensions of the test set-up proved to be a challenge and control over the different variables was hard to obtain.

The experimental data confirmed or supported results from previous studies in small scale, for example, [22], where the tension exhibited sharp peaks when the cable was pulled horizontally and smooth troughs when it was slackened. Numerical simulations of the large scale tests showed a reasonable agreement with the experimental results, except for the fact that the peak tensions were slightly underestimated. It is also pointed out that the simulations were affected by high frequency oscillations that the authors believe to be a numerical artefact of the Lumped Mass Method when the cable hits the ground. However, this might be a physical phenomenon, as described in [15] and in [22].

Another valuable contribution of this work is the description of the different problems encountered during the large scale experiments, which should be taken into account in any future work of the same type.

A detailed study of the damping induced by mooring cables and its different mechanisms was presented by Webster [4]. This analysis focused on methods to estimate damping, on the different damping mechanisms and their relative importance, on the evolution of the damping with pre-tension, as well as on other phenomena.

Mooring damping is determined using the work done by the horizontal component of the tension force during one complete oscillation cycle of the cable. Due to the damping, the tension force shows hysteresis during periodic excitations. The dissipated energy during one complete cycle is equal to the area enclosed by the curve of tension force vs. displacement, which is designated as the indicator diagram.

Using the data provided by indicator diagrams for different numerical simulations, it is shown that mooring cables have two different damping mechanisms: damping caused by the transverse motion of the cables in water and damping caused by elastic stretching of the cables. For slack cables under periodic excitation, the non-dimensional damping increases with non-dimensional pre-tension. This damping regime is dominated by the transverse motions of the cables and viscous drag, as noted in previous studies, and can be quite significant. However, after reaching a certain non-dimensional pre-tension, the non-dimensional damping starts to decrease. For high pre-tensions, the cable approaches the taut condition where transverse displacements are significantly restricted. In this situation, the reaction of the cable to external excitations is mostly by axial elastic stretching, which presents very little damping. And as the pre-tension increases, the higher the dominance of the elastic response over the geometrical one.

The damping regime is also dependent on the type of excitation, with horizontal excitations causing transverse motions and generating drag damping, while vertical excitations cause mostly axial stretching and, therefore, less damping. The later situation might be the most common for heaving wave energy converters.

Some parametric studies are also presented in order to evaluate the effects of scope, drag coefficient, excitation period, stiffness of the cable and current velocity. From all of these parameters, currents are the ones which have the least influence on the damping values. The damping is mostly affected by the parameters that determine whether the cables will react to excitations by changing their geometry or by axial stretching.

It is also suggested by Webster that it could be interesting to maximise the mooring induced damping in order to increase the stability of offshore platforms.

Following a methodology similar to that of Webster [4], Johanning *et al.* [26] presented experimental results of the determination of the damping of mooring cables. Part of the results are a preliminary analysis of the large scale experiments described in [25] and the rest refer to small scale experiments. In both cases, the experiments used a single mooring line.

The small scale experiments encompass a wide variation of the parameters of the mooring cable and of the excitation mechanism, including forced motion and decay tests.

It is concluded that decay tests are not suitable for the accurate determination of the damping of mooring cables, which should be estimated using forced motion tests. This is especially important for motion dependent wave energy converters, where the damping has a direct influence on the performance.

Unlike Webster [4], who observed that when the non-dimensional pre-tension is greater than a certain value, the non-dimensional mooring damping decreases, the experiments of [26] showed only an increase of the damping with the pre-tension. Moreover, it seems that for some conditions, the damping tends to increase even when the cable is working in the elastic regime. It is also shown that as the pre-tension of the mooring cable increases, the frequency of motion of the top end of the cable gains importance in the dynamic behaviour of the cable. Numerical simulations of the small scale experiments using commercial software agreed well with the experimental measurements, supporting the conclusions.

In the continuation of the work of Johanning *et al.* [25], Vickers and Johanning [27] performed large scale tests of three different mooring arrangements: a simple steel catenary cable; a steel catenary terminated at the upper end by a nylon rope; and a nylon rope using a floater and clumpweight to a create zig-zag pattern.

The configurations were installed in the sea and excited at the top end by a vessel. Although the analysis of the results is not very deep, it is observed that, given a sinusoidal motion amplitude, the catenary presents the highest damping in relation to the pre-tension of all the arrangements. On the other hand, the zig-zag configuration presents the smallest one. These are interesting results for developers of mooring configurations of wave energy converters seeking to minimise mooring damping.

With the exception of the simple catenary configuration, it was possible to reproduce the results obtained by Webster in [4], where the increase in the non-dimensional pre-tension first leads to an increase of the non-dimensional damping, and then to a decrease. It was not possible to obtain this result for the catenary because of the limitations in the pulling power of the vessel and in the holding power of the anchor for the high loads required for such an outcome.

In order to simplify the analysis of the results and obtain a way of comparing the data of the three configurations, a non-dimensionalisation parameter for the damping is presented using the pre-tension in the cables, instead of their submerged weight like Webster did [4]. Using the proposed non-dimensionalisation, the non-dimensional damping is a linear function of the motion

amplitude. However, as the authors point out, this linear tendency and the validity of this non-dimensional parameter need confirmation from controlled tests.

Aamo and Fossen [28] developed a finite element model specifically for mooring cables of vessels with limited motions. The objective of this numerical model was to minimise the computational effort and time in the determination of the solution.

It is assumed that mooring cables are pre-tensioned and therefore their tension never approaches zero. As such, there is no need to account for flexural terms, or any other stabilising parameter, to assure the well-posedeness of the problem and the dynamic equations are relatively simple. Inertia effects are neglected since, for limited motions, hydrodynamic loads are dominated by drag, which is included in a simplified way. As it is intended to model mooring cables, both ends of the cables are constrained: the bottom end is fixed to an anchor and the top end to the floating vessel. Under these assumptions it is demonstrated the existence and uniqueness of the solution for the class of problems that this model intends to solve.

The result is a an efficient code for mooring dynamics, that obtains higher efficiency than other formulations by neglecting terms and effects that would make it more general, but are not required for the desired type of problems.

Pascoal *et al.* [29] developed a simplified numerical model for the simulation of the effects of mooring cables on floating structures. This numerical model does not represent the cables themselves, for example, their geometry. Instead, as the authors explain, it represents forces *equivalent* to those applied by the mooring system on the floating structure.

The forces of the mooring system are approximated by a higher order Taylor series, which is simple to program, with coefficients that depend on the position, velocity and acceleration of the fairlead. In order to determine the coefficients for the Taylor series – the identification – it is necessary to run at least one time-domain simulation using a non-linear time-domain formulation. In this simulation, the mooring configuration that the equivalent model is to represent is subjected to forced motion respecting strict conditions: in the case presented, the forced motion is synthesised using Schroeder phases. The equivalent model is then fitted to the results of the simulations using a least squares fit. Once the coefficients are determined, different simulations can be run using the equivalent model without the need for re-identification.

Simulations are presented comparing the results of the equivalent force model to those of simulations using the Lumped Mass Method, showing a good agreement between the two methods.

The equivalent force model does not replace the need for accurate time-domain simulations in the verification of critical design stages. What it provides is a computationally efficient method to evaluate several mooring parameters in an early stage, without the need to resort in every occasion to time consuming numerical models.

To tackle some of the problems of earlier formulations, Montano *et al.* [30] presented a numerical model for the dynamics of perfectly flexible mooring cables using higher order mixed finite elements. The tension in the cable is a Lagrange multiplier and the constitutive axial stress-strain relation is solved together with the equation of motion of the cable. It is argued by the authors

that by enforcing the kinematic relation between displacement and strain in this manner, the formulation should be robust enough to prevent singularities even in the extreme case of inextensible materials.

Continuous polynomials are used to approximate the solution for the position, while fully discontinuous polynomials are used for the tension. Due to the use of higher order polynomials, this formulation presents exponential convergence to the solution. Additionally, by allowing the finite elements to have non-linear shapes, local compressions caused by the stacking of rigid linear elements are avoided, as the cable can acquire a naturally continuous curved geometry. Instabilities caused by the use of Euler angles in previous works are prevented by the use of quaternions.

As the downside of the higher order nature of the numerical model, it is demonstrated that, for common cables, the maximum allowed time step for explicit time-schemes can never be larger than 10^{-4} s, which is unbearably small for commercial applications. To minimise this problem, a backward-Euler scheme is used together with a damped Newton method. This allows the time step to be two orders of magnitude larger than for explicit schemes, partially compensating the extra computational effort. Another drawback of the formulation is that it appears that the tension is kept constant within each element, independently of the polynomial order used for the position. This might pose a problem for situations where large extensions might occur, urging the developmt of formulations where the tension is allowed to vary.

From what was described above, it is safe to state that the dynamic behaviour of mooring cables has been relatively well established, at least when they are applied to secure large floating structures. However, when applied to wave energy converters, especially to motion dependent devices oscillating in resonance, mooring cables might be subjected to high frequency large amplitude and transverse and longitudinal motions. This is the motion regime that generates high peak tensions in mooring cables, and it is a significantly different one from that expected in large floating structures. As such, it is necessary to develop new tools to study the dynamics of mooring cables, particularly numerical methods, that can handle the extreme loadings.

The next step in numerical modelling of mooring cables, and the one applied in this work (chapter 3), is an improvement to the method of Montano *et al.* presented above [30]: the use of a higher-order fully discontinuous Galerkin methods, where both the geometry and the tension are approximated with higher order polynomials. One of the possible discontinuous Galerkin methods is the Local Discontinuous Galerkin method, which, according to Arnold *et al.* [31], was first presented by Cockburn and Shu in [32].

The Local Discontinuous Galerkin (LDG) method and the Runge-Kutta Discontinuous Galerkin (RKDG) method are thoroughly discussed in [33] for different types of problems. Here, stability, convergence, numerical dissipation and other characteristics of the methods are demonstrated or derived even if, for some cases, they cannot be explicitly proven.

When higher order polynomials and higher order time integration schemes are used, the LDG and RKDG methods present exponential convergence (or even super-converge) to the solution and little numerical dissipation. These features have a special relevance in long time-domain

simulations, such as those used in the simulation of moored floating structures to determine the dynamic loads acting on the mooring system.

Due to the discontinuous nature of the formulations, the determination of the solution inside a certain element requires only the information from its bordering elements. As a result, the global mass matrix is block diagonal, leading to a faster inversion and allowing the paralelisation of the process.

In [33] it is also demonstrated the potential of the LDG and RKDG methods to capture shock waves and discontinuities with high accuracy. In the case studies presented, when higher-order discretisations are used, shocks are captured in only 2 or 3 elements. This is another important feature for the analysis of mooring systems of wave energy converters, which might have to endure snap loads [10, 34].

The application of higher-order finite elements is thoroughly presented in [35], including applications of discontinuous Galerkin methods. The special case of spectral elements is presented in more detail in [36]. These are mathematically dense works, but provide a solid foundation of both higher order and discontinuous methods.

Although higher order discretisations might have a considerable computational cost per mesh point when compared with constant or linear discretisations, for the same accuracy they allow the use of much coarser meshes, which results in an overall lower computational cost [33].

2.2 Mooring of wave energy converters

The dynamic interaction between waves and floating structures, either ships or offshore platforms, has been modelled using linear potential flow theory, which is presented clearly in [37] and [38]. The requirement of these structures to have small motions fits well in the small motion assumption of linear potential theory. Besides its simplicity and solid results, linear potential theory is also appreciated for the possibility of being used either in frequency or in time-domain simulations.

Being floating structures, it would be expected that floating wave energy converters could be modelled using linear potential theory as well. This can be true for some concepts, but others rely on large amplitude resonant motions to extract energy and fall out of the small motion assumption of linear potential theory. For these types of devices, more appropriate methods would be fully non-linear potential theory as in [39] or computational fluid dynamics (CFD) as in [40].

As mentioned in [41] CFD simulations are becoming more computationally affordable and start to compete with physical model testing. However, both CFD and the simpler fully non-linear potential theory are still too computationally demanding to be used for practical purposes. As a consequence, the simulation of floating wave energy converters still relies on linear potential theory. In order to incorporate non-linear effects, simulations are often executed in the time-domain, using convolution methods such as those of Cummins [42], van Oortmerssen [43] or others.

In the same way as with linear potential theory, it would also be reasonable that the design of floating wave energy converters be governed by the same rules and methods used for offshore

structures. However, as already recognised in 1995 by Bergdahl and Mårtensson [44], floating wave energy converters require specific design approaches.

In the study presented by Berdgahl and Mårtensson [44], several design guidelines for mooring systems are listed and analysed in terms of their suitability for wave energy converters. Two of these guidelines are selected for a deeper analysis: the DNV POSMOOR guidelines for offshore platforms and the DNV tentative rules for fish farms. The rationale behind the selection of these two guidelines is that the DNV POSMOOR are standard offshore guidelines, but are highly demanding in terms of safety, while the rules for fish farms have relaxed safety requirements that should resemble those needed for wave energy converters.

A case study is presented for the design of a mooring system for a wave energy converter using the two selected sets of DNV rules. As the water depth in the case study is relatively shallow, 35 m, a reasonably sized chain would not have enough catenary stiffness to resist the horizontal loads. As such, the horizontal loads must be resisted by cables with small enough stiffness to react by axial stretching, which requires either the use of wire rope or synthetic cables. Since wire cables would need to be around 1 km long to present enough yield, a nylon rope is chosen because, having a smaller stiffness, it requires a smaller length. A significant problem at the time of the study of [44] was that the DNV POSMOOR guidelines did not present enough information on the use of synthetic rope, while the tentative rules for fish farms were more clear.

Using this simple example, Berdgahl and Mårtensson [44] demonstrate that the use of common offshore guidelines may not warrant acceptable results for wave energy converters. Chain or steel catenaries, which were already commonly used, become unmanageably long or heavy in order to conform to offshore guidelines, while more adequate synthetic cables were not yet widely accepted.

In order to systematise the requirements for mooring systems of wave energy converters and guide the research efforts, Harris *et al.* [45] presented a deep review of the different types of wave energy converters and mooring technologies.

The authors first make a distinction between motion dependent devices, which need to oscillate with the waves to extract energy, and motion independent devices, that need not oscillate. This classification is essential because motion dependent devices require special approaches for the conception and analysis of the mooring system, while motion independent devices may use current practices, albeit with proper relaxation of safety demands.

Existing configurations and technologies are classified according to their suitability for the two types of devices into high, medium and low, taking into account parameters such as their cost, the space they take, their maintenance demands, etc. This classification is, at least partially, a reflection of the authors' opinions and might not be shared by other researchers. For example, the catenary is classified as being generally adequate due to its low cost and simplicity, although it might impose stiffness restrictions. Taut spread systems, on the other hand, are deemed to have limited use as they are not able to accommodate tidal variations (in [11], Fitzgerald and Bergdahl present an almost opposite opinion about the merits of these two mooring systems, as will be later detailed).

The use of active control systems for mooring cables is seen as too expensive to be used in wave energy converters. Other systems, such as the articulated leg column, although expensive, have the possibility of being interesting for specific wave energy technologies.

Emphasis is placed on the use of synthetic materials for the cables, due to their low weight and to the possibility of being used as an active component of the wave energy converter, for example, as springs. Chains might be appropriate in some circumstances because of their abrasion resistance and reliability. Wire cables are not considered adequate due to the possibility of being damaged by bending during transportation, installation and working life.

It is concluded that, in general, offshore guidelines can be applied to the design of mooring systems for wave energy converters, but there are fundamental differences that must be addressed. As the consequences of a failure of an unmanned wave energy converter are not as severe as for an offshore platform, the design should put more weight on the economic and financial issues of the device, as pointed in [44]. Appropriate safety factors and mooring technology will require data and experience from the installation of prototypes in the sea.

Similar conclusions are reached in [9] by Johanning *et al.*, where the issue of design guidelines and methodologies for floating marine energy converters is further discussed. In general, the existing guidelines for the design of mooring systems for offshore structures can be applied to marine energy converters, if they are properly adapted. More precisely, the design methodologies presented in the DNV POSMOOR rules and in the API RP-2SK are thought to be adequate, but the safety requirements must be eased. In fact, when applied to marine energy converters, the safety requirements in offshore guidelines will result in expensive solutions that might compromise the economic viability of the devices. As such, modifications to offshore guidelines must account for the working principles of the converters, for their economy and investment return rates, and for the less severe consequences of their failure.

At the request of Carbon Trust, DNV prepared a report about useful guidelines for the design and operation of wave energy converters [46]. For the design of mooring systems, this report refers to DNV's standard DNV-OS-E301 - Position Mooring [47] for offshore platforms, despite the earlier publications by Berdgahl and Mårtensson [44] and Harris *et al.* [45] indicating the need for adaptations.

A possible approach for the preliminary design of mooring systems for wave energy converters is suggested by Johanning *et al.* [48]. However, the method presented is simply a quasi-static design based on the inelastic catenary equations and is largely taken from the theory presented in [38] and [49]. A simple example is presented for the case of a cylindrical buoy moored by two diametrically opposed chain catenaries, which does not account for hydrodynamic effects of the mooring cables, as it is a preliminary design phase.

A more detailed description, and rather comprehensive approach, of the design of a mooring system for a wave energy converter is presented in [10] by Fonseca *et al.*, for the case of the FLOW hinged attenuator. The design procedure was based on the guidelines of the offshore industry, but included special requirements of wave energy converters.

As for any offshore structure, the focus of the design is on survivability, and no study is presented regarding the operational performance of the device. Full account is made of the different environmental loads, namely currents, wind and waves, for a return period of 100 years. Two extreme sea-states are selected for the design using the contour method. The dynamics of the wave energy converter were modelled using linear potential theory and quadratic transfer functions, while the dynamics of the mooring system were modelled using the method presented in [29]. Design loads and displacements, as well as safety factors were obtained from standard offshore guidelines.

The mooring configuration selected used taut hybrid cables mostly made of nylon rope, but terminated at the anchor by a chain segment and a buoy, to prevent the nylon cable from dragging along the seabed. This solution was the result of accounting for specific problems of wave energy converters if they are to be economically viable, such as reduced cost and total weight of the mooring system, large capacity to absorb peak loads and the need of easy deployment and maintenance.

Although compact, the study presents a clear methodology for the design of a mooring system for a wave energy converter, from statistical analysis of environmental loads to the final mooring solution.

The design of a mooring system for a wave energy converter is not limited to the minimisation of its cost: it must also account for the influence of the mooring system in the performance of the device and vice-versa, which is particularly important for motion dependent devices. As explained in [50], independently of the working principle of the device, extracting wave energy will generate extra drift forces due to the change in momentum of the wave field, which must be absorbed by the mooring system.

For the FLOW wave energy converter, the effects of wave energy extraction were studied by Fonseca *et al.* [51], using potential theory to simulate the dynamics of the device. It was demonstrated that extracting energy can cause a significant change in the behaviour of the device not only in the degrees of freedom used to extract energy (as would naturally be expected), but also in the coupled degrees of freedom. On the other hand, degrees of freedom that are not coupled to those used to extract energy are practically unaffected. The mean drift forces can increase by as much as 47 % and the peak drift can be twice as large when compared with the situation where no energy is extracted.

The significance of previous results is reinforced by the fact that the damping used to model the power take-off was not the theoretical optimum value and that no special control strategy was applied, meaning that the wave drift forces can be even higher for the same sea conditions.

Retzler [52] studied drift forces on the Pelamis in physical model tests, including the effects of wave energy extraction. As expected, it was observed that the drift forces increase significantly when there is energy extraction.

Interestingly, it was also found that extracting all the energy available per length of wave front, would cause drift forces which were only half as large as those caused by a perfectly reflected wave. An explanation for this is not reached, but it is speculated that the physics of the drift

forces caused by wave energy extraction might be different from those of reflected and transmitted waves. As such, different formulations should be developed to estimate drift forces due to energy extraction. An empirical formula for the estimation of the drift forces is provided, but it requires physical verification.

With the goal of examining the influence of the mooring system on wave energy converters, Fitzgerald and Bergdahl [11] studied five different mooring concepts, from simple catenaries to complex arrangements using clumpweights, buoys and different types of materials.

All the configurations were pre-designed to keep the floating wave energy converter safely on station under extreme waves and slowly varying forces, in a water depth of 50 m. A finite element code was used to simulate the dynamics of the most loaded cable in its displaced position when subjected to the mean environmental loads and to the expected motions of the top end caused by extreme waves.

For the conditions analysed, namely the shallow water depth, the catenary is demonstrated to be an inefficient solution. Although it can limit the horizontal displacement of the wave energy converter, achieving the necessary stiffness to resist the quasi-static displacements requires either extremely heavy or extremely long cables (lying mostly on the seabed). Neither of these solutions is appealing because of the cost and of the space taken on the seabead. Additionally, the catenary has a large resistive impedance (damping), dissipating energy that could otherwise be harnessed by the wave energy converter. These conclusions were already reached in [44] and are in disagreement with those of [9] and [45], as mentioned earlier. Because of the large hydrodynamic damping, the catenary is also prone to snap loads.

Lighter cables can be used if, in place of connecting the catenary straight to the wave energy converter, it is connected to a surface buoy which is connected to the wave energy converter by a taut synthetic cable. The horizontal cable decouples the wave frequency motions of the wave energy converter from the catenary, reducing both the peak loads in the mooring cables and the interference of the mooring systems in the energy conversion. This effect is enhanced if the synthetic cable has a reduced stiffness. The downside of this type of configuration is that it increases slightly the space taken by the mooring system and the horizontal displacements of the wave energy converter.

To reduce the horizontal span of the mooring configuration, a clumpweight can be used as a substitute for the catenary. The clumpweight is connected to the anchor by a small chain segment and connected to the surface buoy by a wire rope. Besides the smaller dimension, this arrangement generates smaller peak loads than the catenary. However, the horizontal displacement of the wave energy converter as well as the total weight of the mooring system are larger than if catenaries are used.

If vertically loaded anchors are used, the horizontal span of the mooring systems can be further reduced, since it is no longer necessary to ensure that the tension force is horizontal at the anchor.

One of the configurations using vertically loaded anchors was made of wire rope connecting the anchor to a floater, the floater to a clumpweight and, finally the clumpweight to the wave energy converter. This configuration is compact, has smaller peak loads than the catenary and has

a small impedance. However, its weight is similar to the catenary's and it allows larger horizontal motions of the wave energy converter. Another configuration analysed used only taut synthetic cables, connecting the wave energy converter directly to vertically loaded anchors. The peak loads in this configuration are similar to the previous configuration, but the maximum horizontal displacement of the wave energy converter and the seabed footprint are the smallest of all the studied configurations. Although seemingly restrictive to the wave frequency motion of the device, the use of synthetic cables with appropriate stiffness allows the device to react properly to wave excitations.

Still in the investigation of the influence of mooring systems on wave energy converters, Fitzgerald and Bergdahl [3] developed a hybrid time/frequency-domain method to model mooring systems. Their method can be compared to that of Pascoal *et al.* [29], in that it uses time-domain simulations to calibrate simpler mooring models for a particular case.

After defining the mooring configuration to be analysed, a series of environmental conditions in the operational range, including mean environmental forces, are defined. Using a time-domain model, the dynamic behaviour of the mooring cables is simulated for forced sinusoidal motions representing each environmental condition. A sinusoid is then fitted to the time history of the dynamic response of the mooring system. The parameters of the sinusoid are the hydrodynamic coefficients of the mooring system (stiffness, damping and inertia) for that environmental condition. In other words, the response of the mooring system is linearised for each of the specified environmental conditions. Using interpolation, it is possible to obtain linearisations for different environmental conditions, without the need to resort to more time-domain simulations.

The simulation of the coupled dynamics of the mooring system and of the wave energy converter are then solved in the frequency domain, by adding the hydrodynamic coefficients of the wave energy converter to those of the mooring system.

The method is demonstrated by being applied to different mooring systems securing a cylindrical wave energy converter, with important results. It is shown that the use of a single point mooring might be detrimental to the performance of motion dependent wave energy converters and that it couples the heave motion to the surge and pitch motions. A better option would be to attach the mooring cables around the perimeter of the wave energy converter. This arrangement not only keeps heave decoupled from both pitch and surge, but also keeps the performance of the moored wave energy converter almost equal to that of the unmoored device.

As in the previous study of Fitzgerald and Bergdahl [11], the simple catenary is shown to have a negative effect on the performance of the converter. Finally, a mixed configuration using simple catenaries together with catenaries connected to intermediate surface buoys might improve the performance of the device, by keeping it aligned with the desired wave direction and enhancing pitch motions.

In partial opposition of the results reached by Fitzgerald and Bergdahl [3, 11], presented above, are the results of Vicente *et al.* [7] concerning the numerical simulation of a heaving spherical point-absorber with a linear power take-off.

The performance of the wave energy converter under regular waves is analysed in two mooring scenarios: simple catenaries, and catenaries with intermediate submerged floaters. The simulations are carried out in the time-domain, using linear potential theory and Cummins formulation [42] for the wave energy converter, while the mooring system is modelled quasi-statically. No account is made of either dynamic effects such as drag, inertia and dynamic tension, or of second order loads. Under these assumptions, it is concluded that the mooring system has a small influence on the dynamics of the wave energy converter. However, it is also concluded that the use of intermediate floaters reduces the maximum horizontal displacement of the wave energy converter and increases the energy output.

A similar study is presented by the previous authors in [8], comparing the performance of a spherical point-absorber when it is moored by catenaries with when it is floating freely. Again, it is concluded that the mooring system has little influence on the performance of the wave energy converter. The most significant factors influencing the results of the simulations are the power take-off, and the dimensions and geometry of the case study.

Cerveira *et al.* [6] arrive at the same conclusions when studying the influence of mooring systems on a point absorber using the numerical method presented in [29]. The point absorber was a cylinder with a hemispherical cap on the bottom, and energy was extracted using the relative motions of heave and surge against an idealised fixed referential.

Three different conditions were compared: the point absorber extracting energy without mooring system; the point absorber extracting energy and moored with a slack mooring system; and the point absorber extracting energy and moored with a moderately slack mooring system. The characteristics of the power take-off are kept constant between the three test cases.

It is concluded that the mooring system has a reduced effect on the annual energy production for the region modelled in the study, with a variation of around 1 % of the total energy extracted between the unmoored and moored conditions. The mooring system has some influence in the pitch motions, but no power is extracted from this degree of freedom.

Part of the limited influence of the mooring system can probably be explained by the small values of the linearised added mass, stiffness and damping coefficients obtained for the mooring system, which were around two orders of magnitude smaller than the values for the floater and for the power take-off.

For the frequency domain analysis of the OEBuoy (similar to the backward bent duct buoy), Sheng *et al.* [53] used a simple linearisation to model a catenary mooring system. The method consisted of a straight forward approximation to the vertical and horizontal mooring forces using the first order coefficients of a Taylor series around the geometry of interest. No other details about the representation of the dynamics of the mooring system are provided. The dynamics of the buoy are simulated using linear potential theory. When compared with physical model experiments, this method produced good results for the resonance periods in the sway direction. However, in the surge direction, there was a significant difference between the measured and the predicted periods for one of the test cases. Part of this difference is justified by the authors by the small

dimensions of the physical model used in the experiments, that created difficulties in obtaining accurate measurements of its characteristics, a predicament of several physical models.

Dispite the considerable research efforts, researchers and developers seem to agree only in the need to adapt the existing mooring design guidelines to the safety requirements of wave energy converters. The extent of the impact of the mooring system on the efficiency of floating wave energy converters or the appropriateness of different mooring solutions, are still far from being consensual. There is, therefore, the need to study the behaviour of different mooring concepts idealised for wave energy converters, beyond simplfied numerical simulations or conjectures, retrieving physical data required to evalute their performance. This is the objective of the phyiscal model experiments presented in chapter 5.

The guidelines or recommended practices for the development and testing of wave energy converters are just as varied as the other fields of wave energy. Without referencing all of them, an important milestone was the publication of the Equimar guidelines [54], which synthesised suggested approaches and procedures in a single document, including those for physical model testing. In the case of physical modelling, its scope is broad enough to treat uncertainty analysis, definition of survival sea-states, design of experiment, data analysis, etc.

2.3 Tracking the motion of mooring cables

In spite of the problems enumerated earlier concerning the dynamic behaviour of cables in and out of water, the technology to track the motions of mooring cables, or cables in general, is scarce.

In [55], Howell and Triantafyllou track the motion of a cable in air using ball markers and video cameras. The ball markers were attached at selected positions along the cable, which was excited at its top end, and video cameras were used to record the movements of the markers during the experiments. Post processing was then applied to reconstruct the geometry of the cable through the motions of the markers in the videos. This technique could not be applied underwater, as bulky ball makers would change buoyancy and cross section of the cables, changing their dynamics.

Improving the technique of [55], Yang [56] developed an algorithm and an experimental procedure that was used to study the dynamics of mooring cables (therefore, submerged). Like in [55], Yang tracked selected points along the cable, but used white tape instead of using ball markers. The motion of the cables (or, more precisely, of the markers) was recorded using a video camera shooting through windows in the walls of the tank where the experiments were conducted. The geometry of the cable between the tape markers was reconstructed in post processing using interpolation.

If underwater video cameras were used, this technique could possibly be applied when the cables are not visible through side windows. However, this is not described nor exemplified. Imaging through side windows limits the application of the technique to two dimensional experiments that can be assembled in the field of view of those windows, as was the case in [56].

When studying the dynamics of a falling chain in air, [57] used a technique that was able to capture the entire length of the chain. Unfortunately, the method used is not fully described. It

can be speculated from the information given that it used a uniform background with a different colour from the chain so that, in post processing, it can be easily subtracted.

It is now clear that, as described in the first paragraph, the methods to track submerged cables can be further improved, which will be the main topic of chapter 4, by combining existing methods to detect the complete length of mooring cables.

Unlike the methods that track points, tracking the entire length presents several problems, as the geometry of a moving cable cannot be parametrised. As such, no model can be easily developed to simplify the detection of the changing geometry. A solution to this problem can be taken from [58], where Montague *et al.* used photographic cameras and image processing to measure the camber of steel slabs. A photograph was taken of the side of the slabs coming out of the production line. This photograph was first calibrated to correct the optical distortions inherent to all imaging systems. Then, the image of the slab was skeletonised in order to shrink the thickness of the slab to the geometry of its medial axis, which represents the camber. Like side images of slabs, a cable has a small thickness compared with its length, rendering this approach highly interesting.

With respect to the correction of image distortions, the theoretical models describing the most frequent distortions have been well established at least since the 1960's in the seminal works of Brown and its associates [59, 60]. These models are still used and the great majority of the developments have been focused on improving their algorithm and employment, in order to take advantage of the increasing processing power of computers, such as in [61].

The optical theory of underwater imaging is described in [62], along with its main difficulties. Acquisition of underwater images without degradation of their quality requires the use of significantly more complex technology than that used in air. Images obtained underwater without proper hardware are subjected to several types of distortions, blur, chromatic aberration, etc. that degrade their quality. The choice of the proper optical hardware must be a balance between its cost and the minimum quality that can be tolerated. In order to avoid the use of expensive hardware, it is common practice to use regular cameras for image acquisition and then use image processing to correct any problem. Research in this field is still very active, for example, [63] and [64], and has been driven by the development of underwater remotely operated vehicles. However, such developments diverge from the focus of the current work.

Chapter 3

Numerical Modelling of Mooring Cables

3.1 Introduction

This chapter describes a numerical model for mooring cable dynamics. The numerical model solves the partial differential equation of perfectly flexible cables, using the spectral/*hp*-element discontinuous Galerkin method, which is briefly introduced in section 3.2.

The equation of perfectly flexible cables is described in section 3.3, along with the most relevant external forces acting on a mooring cable: gravity, buoyancy, hydrodynamic forces and ground forces. Afterwards, in section 3.4, the discretised formulation for the equation of cable dynamics is derived.

In the linear finite element method, with basis functions of constant polynomial order $p = 1$, convergence to the solution can be achieved only by decreasing the characteristic size h of the elements. In the spectral/*hp*-element discontinuous Galerkin method, however, convergence can be achieved both by decreasing h and by increasing p [35]. Furthermore, for smooth solutions, increasing the polynomial order provides exponential convergence. This means that the solution can be obtained by solving a system of equations with fewer unknowns than a lower-order approximation [35]. In section 3.5 it will be shown that the numerical model developed presents such exponential convergence.

For a fixed error, spectral/*hp*-elements show little numerical diffusion when compared to low order schemes. This is important in long-time integration, such as the case of time-domain simulations of resonant floating wave energy converters.

A discontinuous Galerkin formulation does require not the solutions obtained from the numerical model to be continuous at the boundaries of adjacent elements [33]. As such, it can be argued that its use is better suited to capture shock waves than C^0 Galerkin formulations [33, 35]. This characteristic is especially interesting when modelling floating wave energy converters, as their resonant motions might induce snap loads on the mooring cables. The ability of the numerical

model to adequately determine the magnitude of snap loads will be demonstrated in sections 3.5, using simulations of a cable undergoing forced motions, and in 3.6, for the case of a moored buoy.

The properties of the model and the areas requiring further development are discussed in section 3.7, and the sum up with the most important conclusions is presented in section 3.8.

3.2 Spectral/hp-element Discontinuous Galerkin Method

This section follows partially the explanation given in [65]. Lets consider the advection equation in one dimension,

$$\frac{\partial u}{\partial t} - \nabla \cdot \mathbf{f}(u) = 0 \tag{3.1}$$

where u is the quantity being transported, t is time and $\mathbf{f}(u)$ is the flux of u through the boundary $\partial\Omega$ of the domain Ω. The equation is to be solved satisfying some initial and boundary conditions.

In the finite element method, the domain Ω is divided into N_{el} sub-domains Ω_e (the elements) with boundaries $\partial\Omega_e$ and characteristic size h, such that:

$$\bigcup_{e=1}^{N_{\text{el}}} \Omega_e = \Omega \tag{3.2}$$

$$\bigcap_{e=1}^{N_{\text{el}}} \Omega_e = \emptyset \tag{3.3}$$

and the exact solution u is approximated by a solution ${}^{\delta}u$. In the hp-element method, this approximate solution is a polynomial of order p or less:

$$u(x,t) \approx {}^{\delta}u(x,t) = \sum_{j=1}^{N_{\text{el}}\times(p+1)-k} {}^{\delta}u_j(t)\,\psi_j(x) \tag{3.4}$$

where ${}^{\delta}u_j$ are the polynomial coefficients, $\psi_j(x)$ are the polynomial basis functions and k is the number of linearly-dependent coefficients, equal to the number of internal element borders. The polynomials $\psi_j(x)$, which are selected beforehand, are a function only of position x, not of time. Commonly used polynomials for the basis functions are the Jacobi polynomials [35] and within these, the special cases of the Legendre, Lagrange and Chebychev polynomials.

In the discontinuous Galerkin formulation, the basis functions are defined locally on each element, independently of the adjacent ones, and the approximate solution is the sum of the solutions within each element:

$$u(x,t) \approx {}^{\delta}u(x,t) = \sum_{e=1}^{N_{el}} {}^{\delta}u^{e}(x,t) \tag{3.5a}$$

$${}^{\delta}u^{e}(x,t) = \sum_{j=1}^{p+1} {}^{\delta}u_{j}^{e}(t)\,\phi_{j}^{e} \tag{3.5b}$$

where ${}^{\delta}u^{e}$ is the local solution in element e, ${}^{\delta}u_{j}^{e}$ are the local polynomial coefficients and ϕ_{j}^{e} are the basis functions, which are the same for all the elements. For a discretisation using N_{el} elements with polynomial order p, there are a total of $N_{dof} = (p+1) \times N_{el}$ degrees of freedom corresponding to ${}^{\delta}u_{j}^{e}$ coefficients of all the elements. Substituting Equation 3.5b in Equation 3.1, and dropping the superscript δ for simplicity, the result is:

$$\frac{\partial u^{e}}{\partial t} - \nabla \cdot \mathbf{f}(u^{e}) = 0 \tag{3.6}$$

and the superscript e now represents the approximate solution obtained using a discontinuous Galerkin method. To obtain the weak Galerkin formulation, Equation 3.6 is first multiplied by the test functions (which are the same as the polynomial basis functions, $\phi_{i}(x)$) and then integrated with respect to space, x, for each element e:

$$\int_{\Omega_{e}} \phi_{i} \frac{\partial u^{e}}{\partial t}\,\mathrm{d}x + \int_{\Omega_{e}} \phi_{i} \nabla \cdot \mathbf{f}(u^{e})\,\mathrm{d}x = 0, \quad \forall i \in \{1,\ldots,p+1\} \tag{3.7}$$

Denoting inner product of two functions $f_{1} = f_{1}(x)$ and $f_{2} = f_{2}(x)$ in Ω_{e},

$$\int_{\Omega_{e}} f_{1} \cdot f_{2}\,\mathrm{d}x \tag{3.8}$$

by

$$(f_{1}, f_{2})_{\Omega_{e}} \tag{3.9}$$

Equation 3.6 becomes:

$$\left(\phi_{i}, \frac{\partial u^{e}}{\partial t}\right)_{\Omega_{e}} + (\phi_{i}, \nabla \cdot \mathbf{f}(u^{e}))_{\Omega_{e}} = 0, \quad \forall i \in \{1,\ldots,p+1\} \tag{3.10}$$

After integrating by parts the term with the spatial derivative $(\phi_{i}, \nabla \cdot \mathbf{f}(u^{e}))_{\Omega_{e}}$ in Equation 3.10, the following result is obtained:

$$\left(\phi_{i}, \frac{\partial u^{e}}{\partial t}\right)_{\Omega_{e}} - (\nabla \cdot \phi_{i}, \mathbf{f}(u^{e}))_{\Omega_{e}} + [\phi_{i}\mathbf{f}(u^{e})]\Big|_{\partial\Omega_{e}} = 0, \quad \forall i \in \{1,\ldots,p+1\} \tag{3.11}$$

The term in the square brackets $[\phi_i \mathbf{f}(u^e)]$ in Equation 3.11 is the flux at the borders $\partial\Omega_e$ of the elements. In a discontinuous Galerkin method, this term is replaced by a numerical flux $\left[\phi_i \widehat{\mathbf{f}(u^e)}\right]$ and Equation 3.12 becomes:

$$\left(\phi_i, \frac{\partial u^e}{\partial t}\right)_{\Omega_e} - (\nabla \cdot \phi_i, \mathbf{f}(u^e))_{\Omega_e} + \left[\phi_i \widehat{\mathbf{f}(u^e)}\right]\Big|_{\partial\Omega_e} = 0, \quad \forall i \in \{1, \ldots, p+1\} \tag{3.12}$$

In the numerical model developed, the numerical flux applied used a modified version of the Local Discontinuous Galerkin formulation [33], which will be described later in section 3.4. When the term with the spatial derivative in Equation 3.12, $(\nabla \cdot \phi_i, \mathbf{f}(u^e))_{\Omega_e}$, is again integrated by parts, the following result is obtained:

$$\left(\phi_i, \frac{\partial u^e}{\partial t}\right)_{\Omega_e} + (\phi_i, \nabla \cdot \mathbf{f}(u^e))_{\Omega_e} + \left[\phi_i \left(\widehat{\mathbf{f}(u^e)} - \mathbf{f}(u^e)\right)\right]\Big|_{\partial\Omega_e} = 0, \quad \forall i \in \{1, \ldots, p+1\} \tag{3.13}$$

Equation 3.13 represents the Green form of the Discontinuous Galerkin formulation [65], which is the one that will be used for the numerical model. Each term in Equation 3.13 represents an elemental matrix. For example, the first term,

$$\left(\phi_i, \frac{\partial u^e}{\partial t}\right)_{\Omega_e}, \quad \forall i \in \{1, \ldots, p+1\} \tag{3.14}$$

can be written as:

$$\left(\phi_i, \Phi \frac{\partial}{\partial t} \tilde{\mathbf{u}}^e\right)_{\Omega_e}, \quad \forall i \in \{1, \ldots, p+1\} \tag{3.15}$$

where

$$\Phi = [\phi_1 \quad \ldots \quad \phi_j \quad \ldots \quad \phi_{p+1}] \tag{3.16}$$

$$\tilde{\mathbf{u}}^e = \left[u_1^e \quad \ldots \quad u_j^e \quad \ldots \quad u_{p+1}^e\right]^T \tag{3.17}$$

and, by further rearranging the terms, expression 3.15, can be written as:

$$\mathbf{M}^e \cdot \frac{\partial \tilde{\mathbf{u}}^e}{\partial t} \tag{3.18}$$

where

$$M_{ij}^e = \int_{\Omega_e} \phi_i(x)\, \phi_j(x)\, \mathrm{d}x \tag{3.19}$$

is the entry i, j of the elemental matrix $\mathbf{M}^e$, also called elemental mass matrix (not to be confused with mass matrices representing the inertia of physical systems). The elemental matrices of the different elements are assembled in global matrices and the resulting system of ordinary differential equations is then solved for the vector $\mathbf{u}^e$ by matrix inversion.

As stated earlier, the discontinuous Galerkin formulation does not require the solution to be continuous at the border of adjacent elements, as is represented in Figure 3.1. In fact, in Equations 3.10 to 3.13, there is no explicit coupling to the surrounding elements.

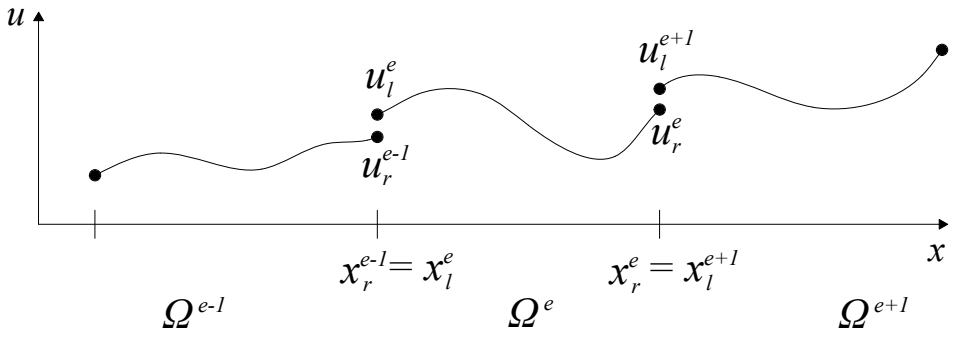

Figure 3.1: Illustration of the variables in the spectral/*hp*-element discontinuous Galerkin method. The indexes l and r indicate, respectively, the left and right borders of the elements.

The transfer of information between elements is achieved via the numerical flux $\mathbf{f}(\widehat{u^e})$. Using the notation in Figure 3.1, the numerical fluxes at the borders of an element have, generally, the form:

$$\mathbf{f}(\widehat{u^e})|_{x_l^e} = f_{\mathrm{l}}\left(u_{\mathrm{l}}^e, u_r^{e-1}\right) \tag{3.20a}$$

$$\mathbf{f}(\widehat{u^e})|_{x_r^e} = f_{\mathrm{r}}\left(u_{\mathrm{r}}^e, u_l^{e+1}\right) \tag{3.20b}$$

where f_{l} and f_{r} are general functions indicating that the fluxes at the boundaries of element Ω_e might depend on the values of u at, respectively, the right and left borders of the surrounding elements Ω_{e-1} and Ω_{e+1}.

The application of boundary conditions will be described in section 3.4, for the specific case of the numerical model developed, since they are applied through the numerical fluxes.

3.3 Cable Dynamics

Figure 3.2 represents a section of a cable that has a mass per unit length m_l and is under the action of distributed external forces $\mathbf{f}_{ext}$. A certain point on the cable has a constant lagragian coordinate s, that is independent of the cable extension ε and of its current geometry. This point is identified in a three-dimensional Cartesian reference frame $Oxyz$ by its coordinate vector $\mathbf{r}(s,t) = (r_x(s,t), r_y(s,t), r_z(s,t))$. Along its length, the cable has an internal tension $\boldsymbol{\tau}(s,t)$, with magnitude τ, that has the direction of the tangential vector $\mathbf{t}$ at every point, $\boldsymbol{\tau} = \tau\mathbf{t}$.

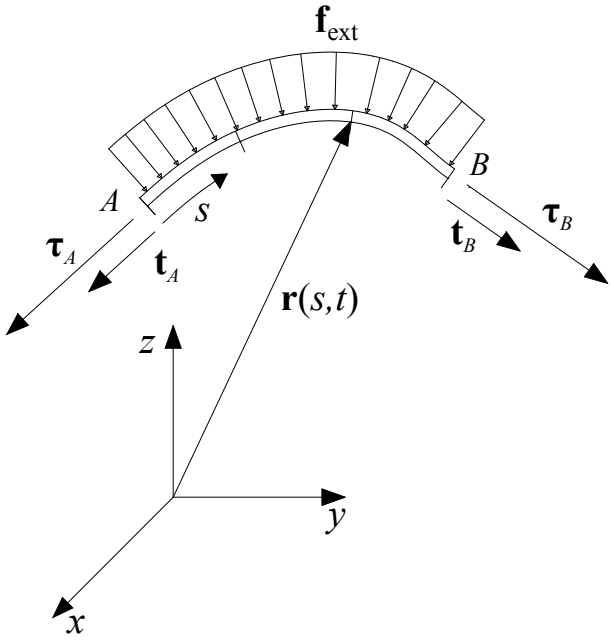

Figure 3.2: Representation of the variables used to describe the dynamics of a cable.

For a cable with neither bending nor torsion stiffness, the equation of motion is [66, 67]:

$$\frac{\partial^2 \mathbf{r}}{\partial t^2} = \frac{1}{m_l}\frac{\partial \boldsymbol{\tau}}{\partial s} + \frac{1+\varepsilon}{m_l}\mathbf{f}_{ext} \tag{3.21}$$

The extension ε is determined using the following relation:

$$\varepsilon = \left\| \frac{\partial \mathbf{r}}{\partial s} \right\| - 1 \tag{3.22}$$

Using Equation 3.22, the unit tangential vector $\mathbf{t}$ is given by

$$\mathbf{t} = \frac{\partial \mathbf{r}}{\partial s} \Big/ \left\| \frac{\partial \mathbf{r}}{\partial s} \right\| = \frac{1}{1+\varepsilon}\frac{\partial \mathbf{r}}{\partial s} \tag{3.23}$$

Equation 3.21 can also be written as:

$$\frac{\partial^2 \mathbf{r}}{\partial t^2} = \frac{1}{m_l}\frac{\partial}{\partial s}\left(\frac{\tau}{1+\varepsilon}\frac{\partial \mathbf{r}}{\partial s}\right) + \frac{1+\varepsilon}{m_l}\mathbf{f}_{ext} \tag{3.24}$$

The tension magnitude τ is determined using *Hooke's Law*,

$$\tau = EA_0\varepsilon \tag{3.25}$$

where E is the elasticity modulus and A_0 is a nominal cross section of the cable. For the case of a cable with constant cross section, A_0 is its real cross-section. However, when the cross-section varies, like in chains, A_0 must be an equivalent value that can model the cable as if it had – in what matters to elasticity calculations – a constant cross-section. In order to model hydrodynamic forces and ground interactions, different values of the nominal cross section, as well as of the diameter of the cable, will be required.

The vector $\mathbf{f}_{\text{ext}}$ of distributed external forces contains the contributions of weight, buoyancy, hydrodynamic forces and ground forces. The submerged weight per unit length γ_{l} (which is the net result of the buoyancy force and the weight) is given by:

$$\gamma_{\text{l}} = \left(\frac{\rho_{\text{c}} - \rho_{\text{w}}}{\rho_{\text{c}}}\right) m_{\text{l}}\mathbf{g} \tag{3.26}$$

where ρ_{c} and ρ_{w} are, respectively, the density of the cable and of the water, and $\mathbf{g}$ is the acceleration of gravity.

The hydrodynamic forces are accounted for using Morison's formulations for added mass force $\mathbf{f}_m$ (Equation 3.27), tangential drag $\mathbf{f}_{d\text{t}}$ (Equation 3.28) and normal drag $\mathbf{f}_{d\text{n}}$ (Equation 3.29):

$$\mathbf{f}_m = C_m A_1 \left(\mathbf{a}_{\text{rel}} - (\mathbf{a}_{\text{rel}} \cdot \mathbf{t})\,\mathbf{t}\right)(1+\varepsilon) \tag{3.27}$$

$$\mathbf{f}_{d\text{t}} = \frac{1}{2} C_{d\text{t}} \rho_{\text{w}} D_0 \left(\mathbf{v}_{\text{rel}} \cdot \mathbf{t}\right)^2 \mathbf{t}\,(1+\varepsilon) \tag{3.28}$$

$$\mathbf{f}_{d\text{n}} = \frac{1}{2} C_{d\text{n}} \rho_{\text{w}} D_0 \left\|\left(\mathbf{v}_{\text{rel}} - (\mathbf{v}_{\text{rel}} \cdot \mathbf{t})\,\mathbf{t}\right)\right\| \left(\mathbf{v}_{\text{rel}} - (\mathbf{v}_{\text{rel}} \cdot \mathbf{t})\,\mathbf{t}\right)(1+\varepsilon) \tag{3.29}$$

where C_m, $C_{d\text{t}}$ and $C_{d\text{n}}$ are, respectively, the coefficients of mass, tangential drag and normal drag, A_1 is a nominal cross section of the cable, D_0 is a nominal diameter of the cable and $\mathbf{v}_{\text{rel}}$ and $\mathbf{a}_{\text{rel}}$ are the relative velocity and acceleration between the cable and the water. The values of $\mathbf{v}_{\text{rel}}$ and $\mathbf{a}_{\text{rel}}$ are given by:

$$\mathbf{v}_{\text{rel}} = \mathbf{a}_{\text{w}} - \frac{\partial \mathbf{r}}{\partial t} \tag{3.30}$$

$$\mathbf{a}_{\text{rel}} = \mathbf{a}_{\text{w}} - \frac{\partial^2 \mathbf{r}}{\partial t^2} \tag{3.31}$$

where $\mathbf{v}_{\text{w}}$ and $\mathbf{a}_{\text{w}}$ are the water velocity and acceleration.

Similarly to the hydrodynamic forces, the ground forces are split between a component normal to the ground and a component tangential to the ground. In the normal direction, the soil acts as a bilinear spring-damper system. A stiffness force is applied to the cable when it is touching the soil, and a damping force is applied to the cable when it is penetrating the soil, but not when it is

being lifted [68, 69]:

$$\mathbf{f}_{\mathrm{sn}} = \begin{cases} \left(K_{\mathrm{s}} D_1 \Delta H - 2\zeta_{\mathrm{s}} \sqrt{K_{\mathrm{s}} D_1 m_{\mathrm{l}}} \min\left(0, v_{\mathrm{sn}}\right)\right) \mathbf{n}_{\mathrm{s}}, & \text{if} \quad \Delta H > 0 \\ 0, \quad \text{otherwise} \end{cases} \tag{3.32}$$

$$v_{\mathrm{sn}} = \frac{\partial \mathbf{r}}{\partial t} \cdot \mathbf{n}_{\mathrm{s}} \tag{3.33}$$

where $\mathbf{f}_{\mathrm{sn}}$ is the normal force, K_{s} is the bulk modulus of the soil, D_1 is a nominal diameter of the cable, ΔH is the normal penetration length in the soil, ζ_{s} is the soil's damping factor and v_{sn} is the projection of the velocity of the cable in the direction normal to the soil, given by the unit vector $\mathbf{n}_{\mathrm{s}}$.

In the tangential direction, the soil applies a variable Coulomb friction force: when the tangential velocity of the cable is between zero and a limiting velocity v_{lim}, the kinetic friction coefficient is linearly ramped from 0 to its maximum value μ_{s}; when the tangential velocity is above v_{lim}, the kinetic friction coefficient is constant:

$$\mathbf{f}_{\mathrm{st}} = -\left(\frac{\rho_{\mathrm{c}} - \rho_{\mathrm{w}}}{\rho_{\mathrm{c}}}\right) m_{\mathrm{l}} g\, \mu_{\mathrm{s}} \min\left(\frac{\|\mathbf{v}_{\mathrm{st}}\|}{v_{\mathrm{lim}}}, 1\right) \mathbf{t}_{\mathrm{s}} \tag{3.34}$$

$$\mathbf{v}_{\mathrm{st}} = \frac{\partial \mathbf{r}}{\partial t} - v_{\mathrm{sn}} \cdot \mathbf{n}_{\mathrm{s}} \tag{3.35}$$

$$\mathbf{t}_{\mathrm{s}} = \frac{\mathbf{v}_{\mathrm{st}}}{\|\mathbf{v}_{\mathrm{st}}\|} \tag{3.36}$$

where $\mathbf{f}_{\mathrm{st}}$ is the force applied by the soil on the cable in the tangential direction, g is the magnitude of the acceleration of gravity and $\mathbf{t}_{\mathrm{s}}$ is the unit vector in the direction of the tangential velocity of the cable.

3.4 Numerical Model

For the discretisation of the cable equation, the quantities length, time and mass per unit length are made non-dimensional by scaling them with a characteristic length l_{c}, time t_{c} and mass m_{lc},

$$m_{\mathrm{lc}} = m_{\mathrm{l}} \tag{3.37}$$

$$l_{\mathrm{c}} = l \tag{3.38}$$

$$t_{\mathrm{c}} = l\sqrt{\frac{m_{\mathrm{l}}}{\tau_0(1+\varepsilon)}} \tag{3.39}$$

where l is the unstretched length of the cable and τ_0 is the pre-tension [70]. Using the symbol "$\sim$" to denote the non-dimensionalised variables, Equation 3.24 becomes:

$$\frac{\partial^2 \widetilde{\mathbf{r}}}{\partial \widetilde{t}^2} = \frac{\partial}{\partial \widetilde{s}}\left(\frac{\widetilde{\tau}}{1+\varepsilon}\frac{\partial \widetilde{\mathbf{r}}}{\partial \widetilde{s}}\right) + (1+\varepsilon)\widetilde{\mathbf{f}}_{\mathrm{ext}} \tag{3.40}$$

Following the procedure of [30] to write the cable equation as a system of two first order partial differential equations in space, Equation 3.40 becomes:

$$\frac{\partial^2 \widetilde{\mathbf{r}}}{\partial \widetilde{t}^2} = \frac{\partial}{\partial \widetilde{s}}\left(\frac{\widetilde{\tau}}{1+\varepsilon}\widetilde{\mathbf{q}}\right) + (1+\varepsilon)\widetilde{\mathbf{f}}_{\text{ext}} \tag{3.41a}$$

$$\widetilde{\mathbf{q}} = \frac{\partial \widetilde{\mathbf{r}}}{\partial \widetilde{s}} \tag{3.41b}$$

or, using Equation 3.21,

$$\frac{\partial^2 \widetilde{\mathbf{r}}}{\partial \widetilde{t}^2} = \frac{\partial \widetilde{\boldsymbol{\tau}}}{\partial \widetilde{s}} + (1+\varepsilon)\widetilde{\mathbf{f}}_{\text{ext}} \tag{3.42a}$$

$$\widetilde{\mathbf{q}} = \frac{\partial \widetilde{\mathbf{r}}}{\partial \widetilde{s}} \tag{3.42b}$$

The exact solutions $\widetilde{\mathbf{r}}$ and $\widetilde{\mathbf{q}}$ are approximated by $\widetilde{\mathbf{r}}^e$ and $\widetilde{\mathbf{q}}^e$:

$$\widetilde{\mathbf{r}}(\widetilde{s}) \approx \widetilde{\mathbf{r}}^e(\widetilde{s}) = \sum \widetilde{\mathbf{r}}_j^e(\widetilde{t})\,\phi_j(\widetilde{s}) \tag{3.43}$$

$$\widetilde{\mathbf{q}}(\widetilde{s}) \approx \widetilde{\mathbf{q}}^e(\widetilde{s}) = \sum \widetilde{\mathbf{q}}_j^e(\widetilde{t})\,\phi_j(\widetilde{s}) \tag{3.44}$$

where $\widetilde{\mathbf{r}}_j^e = \left(\widetilde{r}_{jx}^e, \widetilde{r}_{jy}^e, \widetilde{r}_{jz}^e\right)$ and $\widetilde{\mathbf{q}}_j^e = \left(\widetilde{q}_{jx}^e, \widetilde{q}_{jy}^e, \widetilde{q}_{jz}^e\right)$. The final discretised equations are:

$$\left(\phi_i, \frac{\partial^2 \widetilde{\mathbf{r}}^e}{\partial \widetilde{t}^2}\right)_{\Omega_e} = \left(\phi_i, \frac{\partial}{\partial \widetilde{s}}(\widetilde{\boldsymbol{\tau}}^e)\right)_{\Omega_e} + \left[\phi_i\left(\widehat{\widetilde{\boldsymbol{\tau}}}^e - \widetilde{\boldsymbol{\tau}}^e\right)\right]\Big|_{\partial\Omega_e} + \left(\phi_i, (1+\varepsilon)\widetilde{\mathbf{f}}_{\text{ext}}\right)_{\Omega_e}, \quad \forall i \in \{1,\ldots,p+1\} \tag{3.45a}$$

$$(\phi_i, \widetilde{\mathbf{q}}^e)_{\Omega_e} = \left(\phi_i, \frac{\partial \widetilde{\mathbf{r}}^e}{\partial \widetilde{s}}\right)_{\Omega_e} + \left[\phi_i\left(\widehat{\widetilde{\mathbf{r}}}^e - \widetilde{\mathbf{r}}^e\right)\right]\Big|_{\partial\Omega_e}, \quad \forall i \in \{1,\ldots,p+1\} \tag{3.45b}$$

As is usual for dynamic problems, the second order time derivative $\partial^2 \widetilde{\mathbf{r}}^e / \partial \widetilde{t}^2$ is integrated by steps: instead of solving Equation 3.45a directly for the position $\widetilde{\mathbf{r}}^e$, the equation is first solved for the acceleration $\widetilde{\mathbf{a}}^e$, by setting

$$\widetilde{\mathbf{a}}^e = \frac{\partial^2 \widetilde{\mathbf{r}}^e}{\partial \widetilde{t}^2} \tag{3.46}$$

The acceleration is then integrated to velocity $\widetilde{\mathbf{v}}^e$ (which will be used in stabilising the numerical model) and then to position $\widetilde{\mathbf{r}}^e$. Several different methods can be used for this procedure. In the cases presented in sections 3.5 and 3.6, two different schemes were used: the Störmer-Verlet and the Leap-frog method.

The numerical fluxes were established using a modified version of the Local Discontinuous Galerkin formulation [33]. Lets define the operators $\{f\}$ and $[[f]]$ as:

$$\{f(x)\} = \frac{1}{2}\left(f_{\mathrm{l}}(x) + f_{\mathrm{r}}(x)\right) \tag{3.47}$$

$$[[f(x)]] = f_{\mathrm{l}}(x) - f_{\mathrm{r}}(x) \tag{3.48}$$

where, as in Figure 3.1, the indexes l and r are used to represent, respectively, the values of function f to the left and to the right of border point x. Using this notation, the numerical fluxes are expressed as:

$$\widehat{\widetilde{\mathbf{r}}}^e = \{\widetilde{\mathbf{r}}^e\} + \kappa\,[[\widetilde{\mathbf{r}}^e]] \tag{3.49}$$

$$\widehat{\widetilde{\boldsymbol{\tau}}}^e = \{\widetilde{\boldsymbol{\tau}}^e\} - \kappa\left[\left[\widetilde{\boldsymbol{\tau}}^e\right]\right] + \frac{\lambda_1}{\widetilde{h}}\,[[\widetilde{\mathbf{r}}^e]] + \lambda_2 \widetilde{h}\,[[\widetilde{\mathbf{v}}^e]] \tag{3.50}$$

where $\kappa \in [-1/2, 1/2]$ controls the up- and down-winding of the fluxes (for centred fluxes, $\kappa = 0$), λ_1 and λ_2 are constant, mesh independent parameters (the penalties) and $\widetilde{h}$ is the non-dimensional element size.

The terms containing λ_1 and λ_2 in Equation 3.50 are used to provide stability to the method, but the term containing λ_2 is not part of the Local Discontinuous Galerkin formulation. It was included here because it was found that it increased the robustness of the method, but it requires further investigation. The velocity values $\widetilde{\mathbf{v}}^e$ are obtained as an intermediate step when determining $\widetilde{\mathbf{r}}^e$, as explained above.

Evaluating the terms containing $\widetilde{\boldsymbol{\tau}}^e$ requires special attention. The computed variables in the numerical model are $\widetilde{\mathbf{r}}^e$ and $\widetilde{\mathbf{q}}^e$; $\widetilde{\boldsymbol{\tau}}^e$ has to be determined as an intermediate step, once the values of $\widetilde{\mathbf{q}}^e$ are known (see Equations 3.22, 3.25, 3.41a and 3.41b). Because of this, before computing the fluxes, the approximation $\widetilde{\mathbf{q}}^e = \sum \widetilde{\mathbf{q}}_j \phi_j$ has to be computed in order to determine ε and then $\widetilde{\tau}^e$. The value of $\widetilde{\tau}^e(s)$ is then multiplied by $\widetilde{\mathbf{q}}^e = \sum \widetilde{\mathbf{q}}_j(t)\,\phi_j(s)$ to obtain $\widetilde{\boldsymbol{\tau}}^e$. The fluxes have to be computed at the two boundaries of each element.

Boundary conditions are applied through the numerical fluxes. For a Dirichlet boundary condition $\widetilde{\mathbf{b}}_{\mathrm{D}}$ on a Dirichlet boundary $\partial_{\Omega_e \mathrm{D}}$ and a Neumann boundary condition $\widetilde{\mathbf{b}}_{\mathrm{N}}$ on a Neumann boundary $\partial_{\Omega_e \mathrm{N}}$, the fluxes at the boundaries become:

$$\left.\begin{aligned} \widehat{\widetilde{\mathbf{r}}}^e &= \widetilde{\mathbf{b}}_{\mathrm{D}} \\ \widehat{\widetilde{\boldsymbol{\tau}}}^e &= \widetilde{\boldsymbol{\tau}}^e + \frac{\lambda_1}{h}\left(\widetilde{\mathbf{r}}^e - \widetilde{\mathbf{b}}_{\mathrm{D}}\right) \end{aligned}\right\} \quad \text{on} \quad \partial_{\Omega_e \mathrm{D}} \tag{3.51}$$

$$\left.\begin{aligned} \widehat{\widetilde{\mathbf{r}}}^e &= \widetilde{\mathbf{r}}^e \\ \widehat{\widetilde{\boldsymbol{\tau}}}^e &= \widetilde{\mathbf{b}}_{\mathrm{N}} \end{aligned}\right\} \quad \text{on} \quad \partial_{\Omega_e \mathrm{N}} \tag{3.52}$$

3.5 Verification and Validation

3.5.1 Verification

Two test cases were selected to verify the properties of the numerical model. The first case is the shape acquired by an elastic cable when hung between its two ends; the second case is a wave propagating in a linear vibrating string. These two cases have analytical solutions that can be compared with the results given by the numerical model. For both cases, the numerical solution was obtained using different discretisations in the order p of Jacobi polynomials and in the element size h. A measurement of the quality of the results of the numerical model is given by the L_2 norm of the error $\mathscr{E}$:

$$\|\mathscr{E}\|_{L_2} = \sqrt{\int_\Omega (\mathbf{r} - \mathbf{r}^e)^2 \, \mathrm{d}\Omega} \tag{3.53}$$

In the first case, a cable with an unstretched length of 100,5 m was fixed by its ends to points 100 m apart at the same height. Its stiffness was $K = 200\,\mathrm{kN/m}$ and its mass per unit length was $m_\mathrm{l} = 1{,}738\,\mathrm{kg/m}$. The penalty terms were set to $\lambda_1 = 5000$ and $\lambda_2 = 0$ and centred fluxes were used ($\kappa = 0$). The solution to this case is provided by the equations of the elastic catenary [71]:

$$r_x = a_\tau \sinh^{-1}\left(\frac{s}{a_\tau}\right) + a_\tau \frac{m_\mathrm{l} g}{K} s \tag{3.54}$$

$$r_z = \sqrt{a_\tau^2 + s^2} + \frac{m_\mathrm{l} g}{2K} s^2 - a_\tau \tag{3.55}$$

$$a_\tau = \frac{\tau_\mathrm{H}}{m_\mathrm{l} g} \tag{3.56}$$

where τ_H is the horizontal component of the tension force and r_x and r_z are the horizontal and vertical component of the position vector $\mathbf{r}$. The origins of the coordinate systems for $\mathbf{r}$ and s are located at the lowest point of the cable. $\|\mathscr{E}\|_{L_2}$ is presented in Figure 3.3.

For a reduced number of elements (only two), when the polynomial order p is increased, the model shows the exponential convergence characteristic of p-type refinement, as demonstrated by the straight line in the semi-logarithmic plot, Figure 3.3a. On the other hand, for constant polynomial order, increasing the number of elements results in a much slower convergence to the exact solution. Even with six times the degrees of freedom used in p-type refinement, the error in h-type refinement is at least five orders of magnitude larger. This is the algebraic and sub-optimal convergence of h-type refinement, demonstrated by the hyperbolic lines on the semi-logarithmic plot and the straight lines on the logarithmic plot of Figure 3.3.

In the second case, the cable equation was linearised to have constant tension and extension, both in time and along the whole length of the cable. In this situation, the partial differential equation for the motion of the cable simplifies to the standard wave equation:

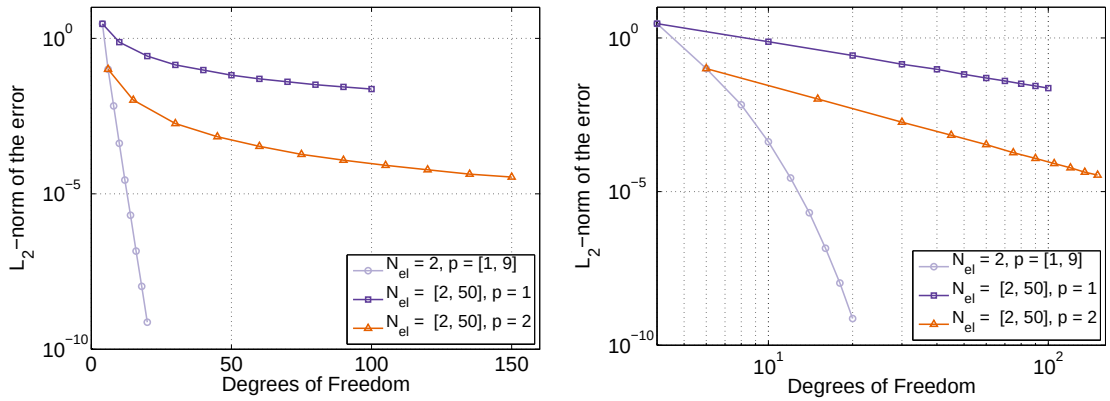

(a) Semi-logarithmic plot.

(b) Logarithm plot.

Figure 3.3: L_2 norm of the error, $\|\mathscr{E}\|_{L_2}$, in the simulation of the elastic catenary.

$$\frac{\mathrm{d}^2 r}{\mathrm{d}t^2} = \frac{\tau}{m_1(1+\varepsilon)}\frac{\partial^2 r}{\partial s^2} = c^2\frac{\partial^2 r}{\partial s^2} \tag{3.57}$$

For this test, a 0,5 m cable was stretched to 1 m and fixed at both ends. Its mass per unit length was 1 kg/m and its pre-tension was 1 N. The cable was initially deformed to have the shape of a half-sine and then released. The solution to this case is given by Equation 3.58 [72]:

$$r_y(s,t) = A\cos\left(c\frac{\pi}{L(1+\varepsilon)}t\right)\sin\left(\frac{\pi}{L(1+\varepsilon)}s\right) \tag{3.58}$$

where A is the amplitude of the sine, L is the stretched length of the cable and c is the transverse wave celerity (Equation 3.57). A full oscillation cycle (2 s) was simulated using the leap-frog scheme with a time step of 1×10^{-4} s, which was small enough to ensure that the error was dominated by the spatial discretisation. Like for the static case, the penalties were set to $\lambda_1 = 5000$ and $\lambda_2 = 0$ and centred fluxes were used ($\kappa = 0$). $\|\mathscr{E}\|_{L_2}$ is presented in Figure 3.4.

As was the case for the elastic catenary, p-type refinement yields exponential convergence for all the polynomial orders tested, as demonstrated by the straight lines in the semi-logarithmic plot. Moreover, increasing the polynomial order provides such a fast convergence that $\|\mathscr{E}\|_{L_2}$ reaches the magnitude of the computer round-off error at around 10^{-11} and saturates. On the other hand, increasing the number of elements for a polynomial order $p = 1$ (linear finite element method), increases the number of degrees of freedom, but $\|\mathscr{E}\|_{L_2}$ does not get anywhere near the computer round-off error.

As expected, for smooth solutions, when the polynomial order is increased, the model exhibits exponential convergence with a limited number of degrees of freedom, providing higher accuracy solutions with less computational work when compared with the traditional formulation.

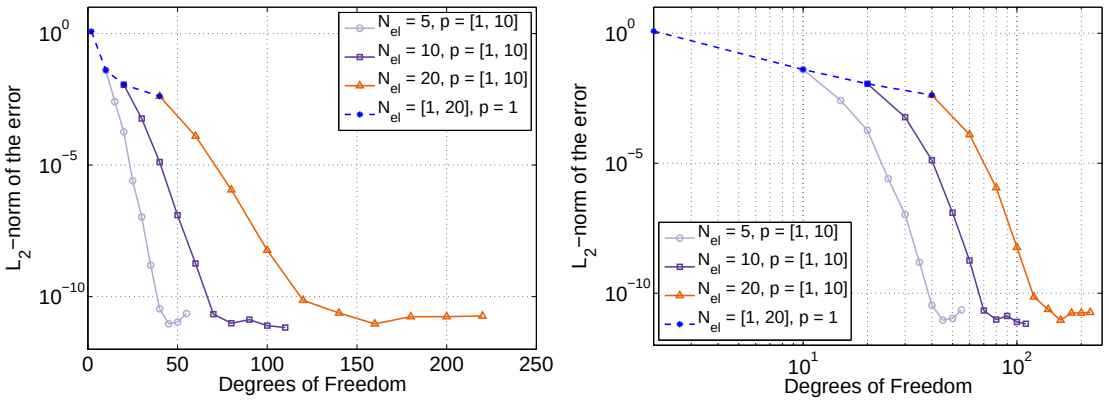

(a) Semi-logarithmic plot.

(b) Logarithm plot.

Figure 3.4: L_2 norm of the error, $\|\mathscr{E}\|_{L_2}$, in the simulation of the vibrating string.

3.5.2 Validation

The results of the numerical model were validated against the data presented in [73], about experiments on a submerged chain subjected to forced oscillations, Figure 3.5.

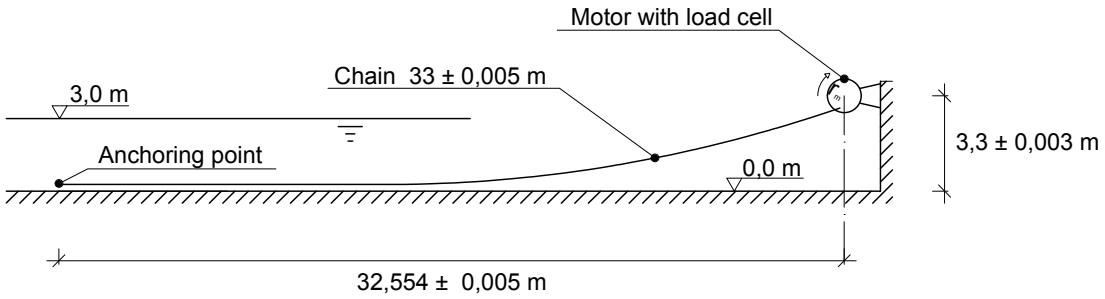

Figure 3.5: Experimental set-up simulated to validate the numerical model.

A motor, installed above the water level, was used to drive the upper end of the chain in a periodic circular motion with a radius of 0,20 m. At the connection to the motor, a load-cell was installed to record the tension. Table 3.1 presents the values of the most relevant parameters of the experimental set-up, as described in [73].

Two experimental cases were simulated using the numerical model: the chain being driven with a period $T = 3{,}50\,\mathrm{s}$ and with a period $T = 1{,}25\,\mathrm{s}$. The first case originated a slow motion of the chain, which caused the tension to vary smoothly throughout the cycle, whereas the second case originated quick motions that generated relative large and sharp peak loads.

The chain was modelled using 10 elements with Jacobi polynomials of order $p = 1$ to 7. The penalty terms were set to $\lambda_1 = 5000$ and $\lambda_2 = 1$ and the fluxes were upwinded ($\kappa = 1/2$). Fifteen consecutive cycles were simulated in order to achieve steady-state and investigate the numerical dispersion. For time stepping a leap-frog scheme was used with a time-step of $1 \times 10^{-4}\,\mathrm{s}$. The

Table 3.1: Parameters of the experimental set-up.

Parameter	Value
l (m)	33
ρ_c (kg/m^3)	7800
m_l (kg/m)	0,0818
EA (N)	10 000
$D_0 = D_1$ = Link thickness (m)	0,0022
C_m	3,8
C_{dt}	0,5
C_{dn}	2,5
K_s (GPa/m)	3
ζ_s	1
μ_s	0,3
v_{lim} (m/s)	0,01
ρ_w (kg/m^3)	1000

portions of the chain that were above the water level were subjected to their dry weight and no hydrodynamic forces.

The simulated tension forces at the top end of the chain are presented in Figures 3.6 and 3.7. For both excitation periods, the measured and the simulated tensions are remarkably similar. The shape of the tension cycle and the tension amplitude in the numerical simulations are close to those obtained in the experiments. The model is even able to capture small details, such as the indentation at the bottom and at the peak of the tension cycle for the excitation period of 1,25 s.

There is one notable difference between the simulated and the measured tension: the simulated tension has a higher ripple content than the measured one and this is most evident when the tension is close to zero. This phenomenon can have different origins, which are not fully understood. Part of it can be explained by the digitisation of the experimental data, but it might also be caused by the physics of the cable, by imperfections in the experimental set-up and or by numerical artefacts. Probably, it is a combination of all, as explained below. High frequency oscillations in the tension have been reported in experimental measurements [22, 24] and in numerical simulations [25], although their cause was not explained.

The experimental data was obtained from digitisation of tension plots printed on paper. These plots had ripple content, as do most experimental records (see, for example, Figure 5.17), which was impossible to resolve in the scale at which the plots were printed. As such, those ripples could not be digitised and the experimental tension looks smoother than it actually was.

If the ripples in the experimental data are due to the physics of the cable, then the numerical model is able to capture fine details of the behaviour of the cable. If they are a result of imperfections in the experimental set-up, such as vibrations of the load cell or of the motor driving the chain, noise in the data-logger, etc. then in the numerical results they are an artefact that must be eliminated.

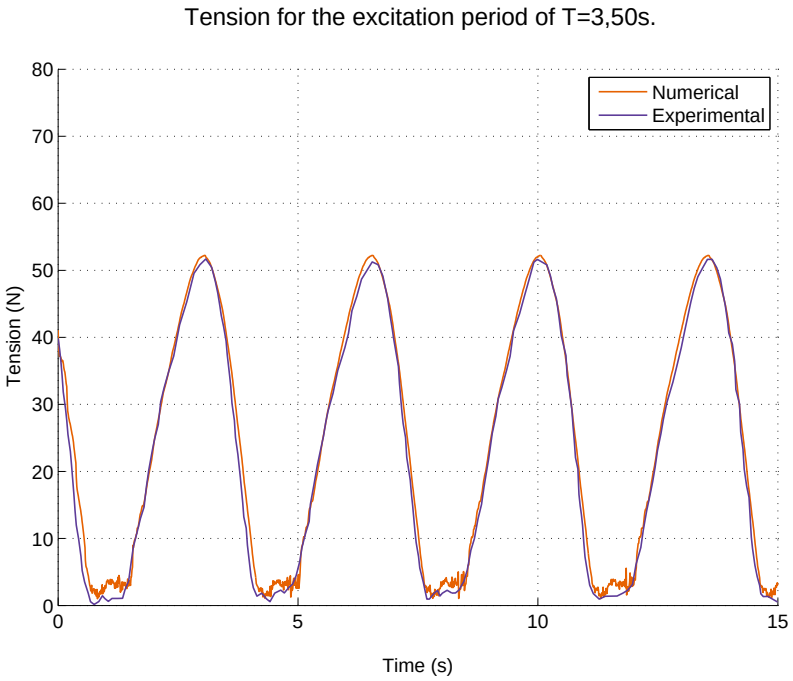

Figure 3.6: Measured and simulated tension for the rotation period $T = 3{,}50\,\mathrm{s}$.

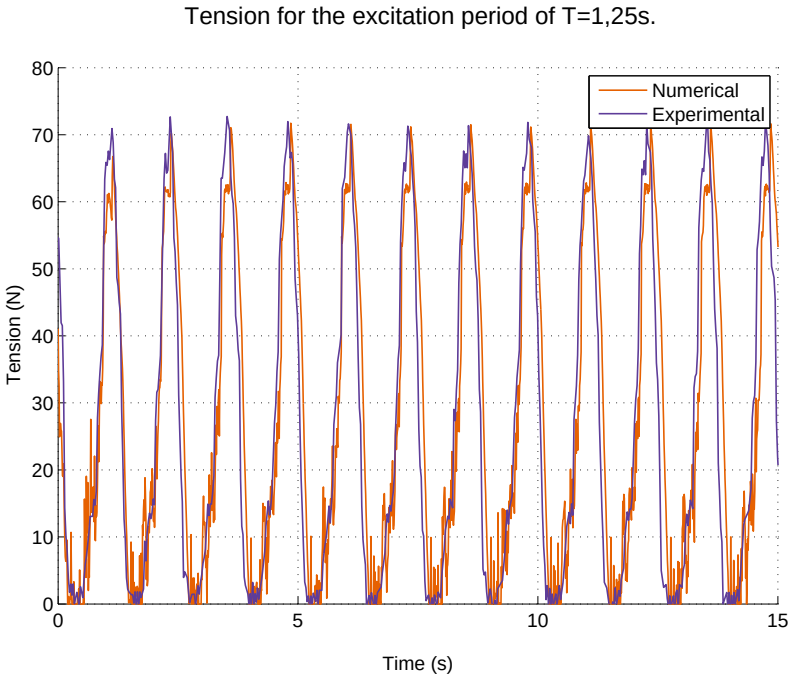

Figure 3.7: Measured and simulated tension for the rotation period $T = 1{,}25\,\mathrm{s}$.

The cable equation (Equation 3.24), which takes into account only axial stiffness, is a simplification of the dynamics of a real cable. This works well for cables under tension, but when the tension is small or zero, the equation becomes singular, and the solutions undetermined [20, 21]. In this situation, small variations in the input data, together with computer round-off errors, cause large variations in the solution and the resulting ripples. The penalty terms used in the numerical discretisation (λ_1 and λ_2) provide some robustness to the solution process by preventing the right-hand term to become zero and by damping part of the ripples. A real cable has both bending and torsional stiffness which, if included in the cable equation, would prevent it from becoming singular. However, modelling such a cable results in a much more complicated equation, which might not bring much added value when compared with its increased complexity.

It is known that modelling discontinuities using higher order functions may cause Gibbs-type oscillations, as in the classical case of approximating a square wave with a Fourier series. This might happen in the numerical model, since it uses high-order polynomials to approximate a solution that is allowed to be discontinuous at the element boundaries. Additional discontinuities are caused by shock loads: sharp and high amplitude tension peaks that occur when a slack cable is violently re-tensioned. This is seen to happen for $T = 1{,}25\,\mathrm{s}$, which presents a higher ripple content than the simulation with $T = 3{,}50\,\mathrm{s}$. To prevent this problem, numerical filters can be applied to the numerical model to remove the ripples, although they were not applied in these simulations. Even without any filtering, the ripple content is not too large and, for the excitation period $T = 3{,}50\,\mathrm{s}$, the ripples are not much larger than in the experimental records. Additionally, in both simulations, the ripples die out quickly when the tension increases.

In these simulations it was also noticed that the results are sensitive to the ground parameters. The ground model used was adopted from linear numerical models [68, 69] and might not be suitable for higher-order discretisations. This issue is further investigated and explained in [67] when describing this same numerical model for cable dynamics: according to [15], in a dynamic simulation where the cable interacts with the ground, shock waves might be generated at the points where the cable impacts the ground and propagate along the cable. This effect was noticed to happen in the numerical simulations. In lower order numerical models, with higher numerical dissipation, these ripples are naturally damped. However, in this numerical model, with little dissipation, they have little attenuation and require additional control measures, such as an improved ground model.

3.6 Moored Buoy Simulation

Since the aim of the numerical model developed is the simulation of moored floating wave energy converters, the model was used to reproduce the physical model experiments of a moored buoy presented in [74].

The experimental set-up, Figure 3.8, was composed of a cylindrical buoy in a wave tank, moored on the seaward side by a chain and, on leeward side, by a horizontal nylon string connected to a linear spring.

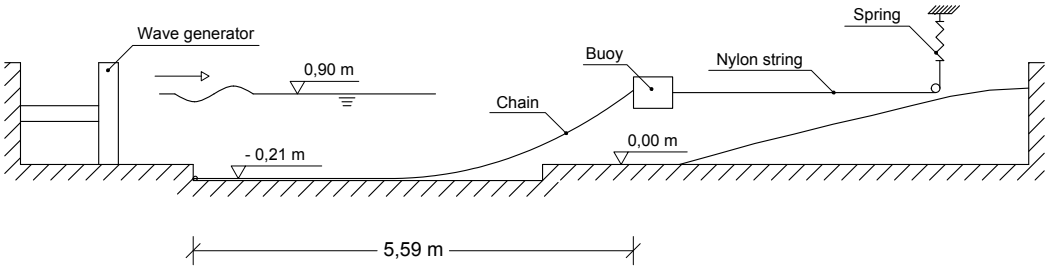

Figure 3.8: Experimental set-up reproduced in the simulation of the moored buoy.

Due to the design specifications imposed for the mass and for the inertia of the buoy, its construction was rather complicated and resulted in a somewhat fragile hull, Figure 3.9.

Figure 3.9: Hull of the buoy, made of a stainless steel frame wrapped in a polyethylene sheet.

The properties of the buoy were determined experimentally following the procedures described in [75] and are presented in Table 3.2.

Table 3.2: Properties of the model buoy. m_b - mass; D_b - diameter; H_b - height; y_{cg} - position of the centre of gravity above the bottom of the buoy; d_b - draft; I_{cf} - inertia around the horizontal axis through the centre of flotation.

m_b	D_b	H_b	y_{cg}	d_b	I_{cf}
35,28	0,500	0,400	0,108	0,180	0,85
±0,05kg	±0,002m	±0,002m	±0,004m	±0,008m	±0,03kg m^2

The chain and the nylon string were attached at diametrically opposed sides of the buoy, 0,200 m above the bottom of the buoy and 0,020 m above the water level. A load cell was in-

stalled in-line with the chain, at the connection of the chain to the buoy, to record the tension force, Figure 3.10.

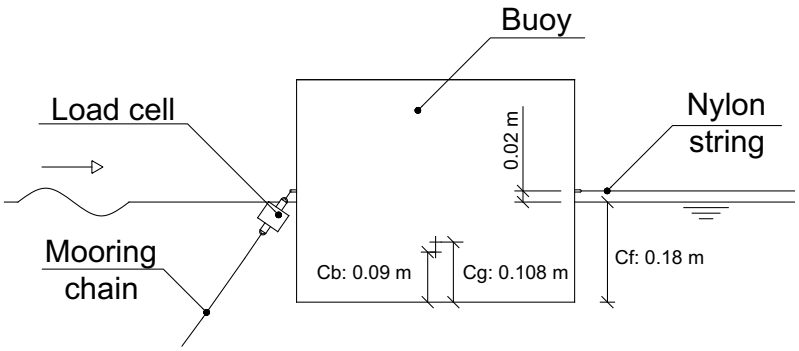

Figure 3.10: Placement of the load cell.

Long-crested regular waves with different heights, H, and periods, T, were generated in the direction parallel to the the plane of the mooring cables. In these test conditions it is reasonable to assume that the motion of the buoy was essentially two-dimensional and limited to surge, heave and pitch.

The properties of the chain are listed in Table 3.3. The values of the axial stiffness EA and of the hydrodynamic parameters were taken from [73] (such as in section 3.5.2) where a similar-sized chain was used in physical model experiments. When in rest position, the tension in the chain (the pre-tension) was 1,77 N.

Table 3.3: Properties of the chain.

Parameter	Value
EA (N)	$(1{,}0 \pm 0{,}7) \times 10^{4}$
$m_{\mathrm{l}}(\mathrm{kg/m})$	$(0{,}044 \pm 0{,}001) \times 10^{-4}$
$\gamma_{\mathrm{l}}(\mathrm{N/m})$	$(0{,}382 \pm 0{,}006) \times 10^{-3}$
Outer link length (m)	$(16{,}6 \pm 0{,}7) \times 10^{-3}$
Outer link width (m)	$(7{,}1 \pm 0{,}7) \times 10^{-3}$
Link thickness (m)	$(1{,}7 \pm 0{,}5) \times 10^{-3}$
$C_{d\mathrm{t}}$	0,5
$C_{d\mathrm{n}}$	2,5
C_m	3,8

The nylon string had a negligible mass and the stiffness of the linear spring was $5{,}36\,\mathrm{N/m}$. The mass of the spring was judged to have little influence on the shape or in the tension of the nylon string, since it was hung vertically above the water and the string was passed through a pulley before being attached to the spring, Figure 3.8. When in rest position, the elongation of the spring caused by the pre-tension of the nylon string was 0,243 m, yielding a pre-tension in the string of 1,3 N.

An infra-red motion tracking system was used to record the rigid body motion of the buoy in the six degrees of freedom and a resistive wave probe was used to measure the free surface elevation two meters to the port side of the rest position of the buoy.

Out of the experimental test series, three conditions were chosen to be simulated: $T = 1{,}30\,\mathrm{s}$, $H = 0{,}088\,\mathrm{m}$; $T = 1{,}40\,\mathrm{s}$, $H = 0{,}10\,\mathrm{m}$ and $T = 1{,}50\,\mathrm{s}$, $H = 0{,}123\,\mathrm{m}$. Longer and higher waves were not simulated as they had a pronounced second harmonic component; the shorter and smaller waves were not simulated as the uncertainty in the recorded displacements was large. Nevertheless, the three conditions selected will be enough to illustrate some more characteristics of the numerical model.

The buoy was modelled using linear potential theory, which, for a single excitation frequency, describes the motions as a linearly damped oscillator [37]:

$$(\mathbf{M}+\mathbf{A})\,\ddot{\boldsymbol{\xi}} + \mathbf{B}\,\dot{\boldsymbol{\xi}} + \mathbf{C}\,\boldsymbol{\xi} = \mathbf{f}_{\text{buoy}} \tag{3.59}$$

where $\mathbf{A}$ is the generalised mass matrix, $\mathbf{A}$ is the added mass matrix, $\mathbf{B}$ is the radiation damping matrix, $\mathbf{C}$ is the hydrostatic stiffness matrix, $\ddot{\boldsymbol{\xi}}$, $\dot{\boldsymbol{\xi}}$ and $\boldsymbol{\xi}$ are, respectively, the acceleration, velocity and position vectors in the six degrees of freedom and $\mathbf{f}_{\text{buoy}}$ is the vector of external forces acting on the buoy (wave forces, mooring forces, etc.). Wave induced forces and moments are also computed following linear potential theory:

$$\mathbf{f}_{\text{w}} = \mathbf{w}\,\eta\,\sin\left(\frac{2\pi}{T}t + \boldsymbol{\delta}\right) \tag{3.60}$$

where $\mathbf{f}_{\text{w}}$ is the vector of wave induced forces on the buoy, $\mathbf{w}$ is the vector of the wave force coefficients in the six degrees of freedom, η is the water surface elevation at the mean position of the buoy and $\boldsymbol{\delta}$ is the vector of the phase delay for each force and moment component.

Equation 3.59 was integrated in time using the Leap-frog scheme [76] with a time step $\Delta t = 1 \times 10^{-2}\,\mathrm{s}$. In reality, however, Equation 3.59 is only valid for floating structures subjected to linear external forces, which is not the case for a buoy moored with a catenary. For time integration with non-linear external forces, Equation 3.59 should be replaced by Cummins's formulation [42]. Since the mass of the buoy was much larger than the mass of the mooring system, it was assumed that the moored buoy had a weakly non-linear behaviour and, therefore, that it was valid to represent it using Equation 3.59.

The hydrodynamic parameters of the buoy (added mass, radiation damping and wave force coefficients) were determined using the formulation presented in [77] and are listed in Table 3.4. Keeping with the assumption of a weakly non-linear behaviour of the buoy, viscous drag terms were not included in the dynamics of the buoy.

The linear potential formulation used to determine the hydrodynamic coefficients assumes that the water depth is constant, which was not the case in the experiments, Figure 3.8. Since the buoy

Table 3.4: Hydrodynamic coefficients of the buoy.

T	Mode	A_{ij}	B_{ij}	w_i	δ_i (rad)
1,30 s	Surge	24,55 kg	31,73 kg/s	1057,8 N/m	1,475
	Heave	26,23 kg	37,94 kg/s	817,9 N/m	0,258
	Pitch	0,2599 kg m^2	0,033 36 kg m^2/s	34,30 N	−1,667
	Surge-Pitch	1,1739 kg m	1,0288 kg m/s	-	-
1,40 s	Surge	23,921 kg	20,82 kg/s	963,8 N/m	1,501
	Heave	27,05 kg	38,09 kg/s	921,8 N/m	0,206
	Pitch	0,2581 kg m^2	0,019 74 kg m^2/s	29,68 N	−1,641
	Surge-Pitch	1,1369 kg m	0,6410 kg m/s	-	-
1,50 s	Surge	23,17 kg	14,05 kg/s	880,2 N/m	1,519
	Heave	27,83 kg	37,47 kg/s	1016,4 N/m	0,168
	Pitch	0,2564 kg m^2	0,012 13 kg m^2/s	25,86 N	−1,623
	Surge-Pitch	1,1004 kg m	0,4129 kg m/s	-	-

is located at a point where the water depth is 0,900 m, this was the value used in the computation of the hydrodynamic coefficients.

The leeward nylon string mooring leg was modelled as a simple linear spring with a pre-strain of 0,243 m, that went slack when the strain was smaller than 0,000 m. The tension force of the nylon string leg was applied to the buoy at a point 0,200 m above its bottom and at a distance of 0,250 m from its central axis. For simplicity, it was assumed that this force was always horizontal, since the string had a negligible mass and, being taut, its angle to the horizontal at the connection to the buoy was around 2°.

The chain was discretised using 10 elements with 4$^{\text{th}}$ order Legendre polynomials ($N_{dof} = 50$). This discretisation was fine enough to provide grid independent simulations, as finer discretisations using 5$^{\text{th}}$ and 6$^{\text{th}}$ order polynomials did not show significant differences in the results. Crossed fluxes were used, meaning that the tension was up-winded and the position was down-winded, and the stabilisation parameters were $\lambda_1 = \lambda_2 = 1$.

As cables cannot be compressed, the simulated chain had a bilinear stress-strain relation, which allowed elongation, but did not allow compression. The values of the stiffness, mass and drag coefficients used to model the chain are presented in Table 3.3. In the computation of the hydrodynamic forces acting on the chain, the nominal diameters used were $D_0 = D_1 = 0{,}0027$ m, which is the diameter of a uniform cable made of the same material as the chain (steel, $\rho_{\text{st}} = 7800\,\text{kg/m}^3$), that would have the same mass per unit length.

The anchoring point was set to a depth of 1,11 m, at a horizontal distance of 5,59 m from the fairlead point when in rest position. The fairlead point was 0,2 m above the bottom of the buoy at a distance of 0,250 m from its central axis. As most of the chain was hanging over the central pit, the water depth used in the simulation of the dynamics of the chain was 1,11 m. This was also the depth used for the computation of the wave length and of the wave induced water velocity and

acceleration. The difference in the water depth used to model the chain and to model the buoy resulted in some additional discrepancies between the experimental and the simulated dynamics.

For the non-dimensionalisation, the characteristic length l_c was the length of the chain, 5,88 m and the characteristic time was 0,012 33 s. The simulations were time-stepped using an explicit Stormer-Verlet algorithm, with $\Delta t = 5 \times 10^{-5}$ s for the wave periods $T = 1{,}30$ s and $T = 1{,}40$ s, and $\Delta t = 2 \times 10^{-5}$ s for the period $T = 1{,}50$ s.

In order to control the numerical ripples seen in section 3.5.2, exponential filters were applied to the position and to the tension in the chain, with each polynomial coefficient being multiplied by a filter coefficient given by:

$$\sigma(j) = \exp\left(-\Gamma\left(\frac{j - N_c}{p + 1 - N_c}\right)^{\Lambda}\right), \quad \forall j \in \{1, \ldots, p+1\} \tag{3.61}$$

where $\sigma(j)$ is the filter coefficient applied to the polynomial coefficient j, Γ and Λ are parameters that control the sharpness of the filter and N_c is the cut-off term of the filter (the filter has no effect for $j < N_c$). This type of filter is described in [36]. In the simulations N_c was set to 0, Γ to 0,1 and Λ to 10.

Coupling the simulation of the chain to the simulation of the buoy was achieved through a special purpose function. At each time instant t^n, the position $\mathbf{p}^n$ of the attachment point of the chain to the buoy was computed and transferred to the numerical model for cable dynamics. The numerical model updated the previous position $\mathbf{p}^{n-1}$ of the upper end of the chain at time step t^{n-1} to the current position $\mathbf{p}^n$ and computed the evolution of the tension between the two positions. The tension at the current position and time $\boldsymbol{\tau}^n$ was then transferred to the linear potential theory solver simulating the buoy. This new tension force was used by the linear solver, along with the other loads, to determine the new position of the buoy and so on.

As the cable simulation requires a smaller time step than the simulation of the buoy, the numerical model of the cable used linear interpolation to estimate the position of the top end of the chain between the previous and the current position fed by the linear solver.

The characteristics used to model the ground are presented in Table 3.5. With the exception of the limiting velocity v_{lim}, they are the same as those used in subsection 3.5.2 since, in both situations, the tank floor was made of concrete.

Table 3.5: Characteristics of the ground used in the simulation of the moored buoy.

Parameter	Value
K_s (GPa/m)	3
ζ_s	1
μ_s	0,3
v_{lim} (m/s)	1×10^{-4}

The tension at the upper end of the chain and the motion of buoy referred to the centre of floatation are presented in Figures 3.11 to 3.13. Before analysing the results, it is important to point out that both the numerical simulations and the experiments suffered from problems and simplifications that affected the results. Some of these problems were detected only after the experiments and the simulations had been carried out.

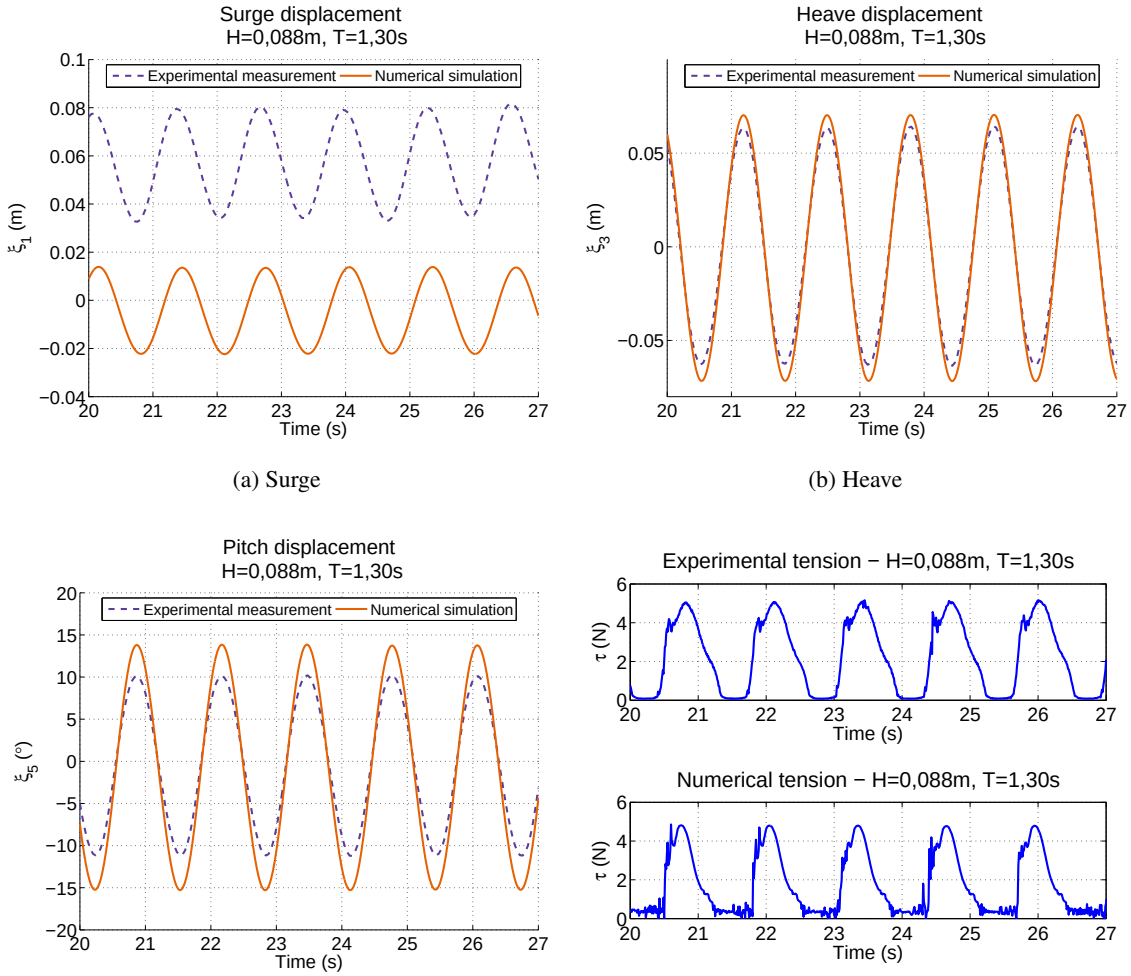

(a) Surge

(b) Heave

(c) Pitch

(d) Tension

Figure 3.11: Comparison of experimental data and simulated results for regular waves with height $H = 0{,}088\,\text{m}$ and period $T = 1{,}30\,\text{s}$.

In surge, it is clear the existence of an offset in the mean oscillating position between the numerical simulations and the experimental results. This offset is caused by second order drift forces which, in the experiments, displaced the buoy from its rest position. Linear potential theory takes into account only first order loads and no second order load. Therefore, the surge offset is not due to any failure in the numerical model for cable dynamics.

On a deeper analysis of the results, it is seen that, for the three periods tested, the maximum tension and the heave motions are well captured in the numerical simulations. The pitch and surge

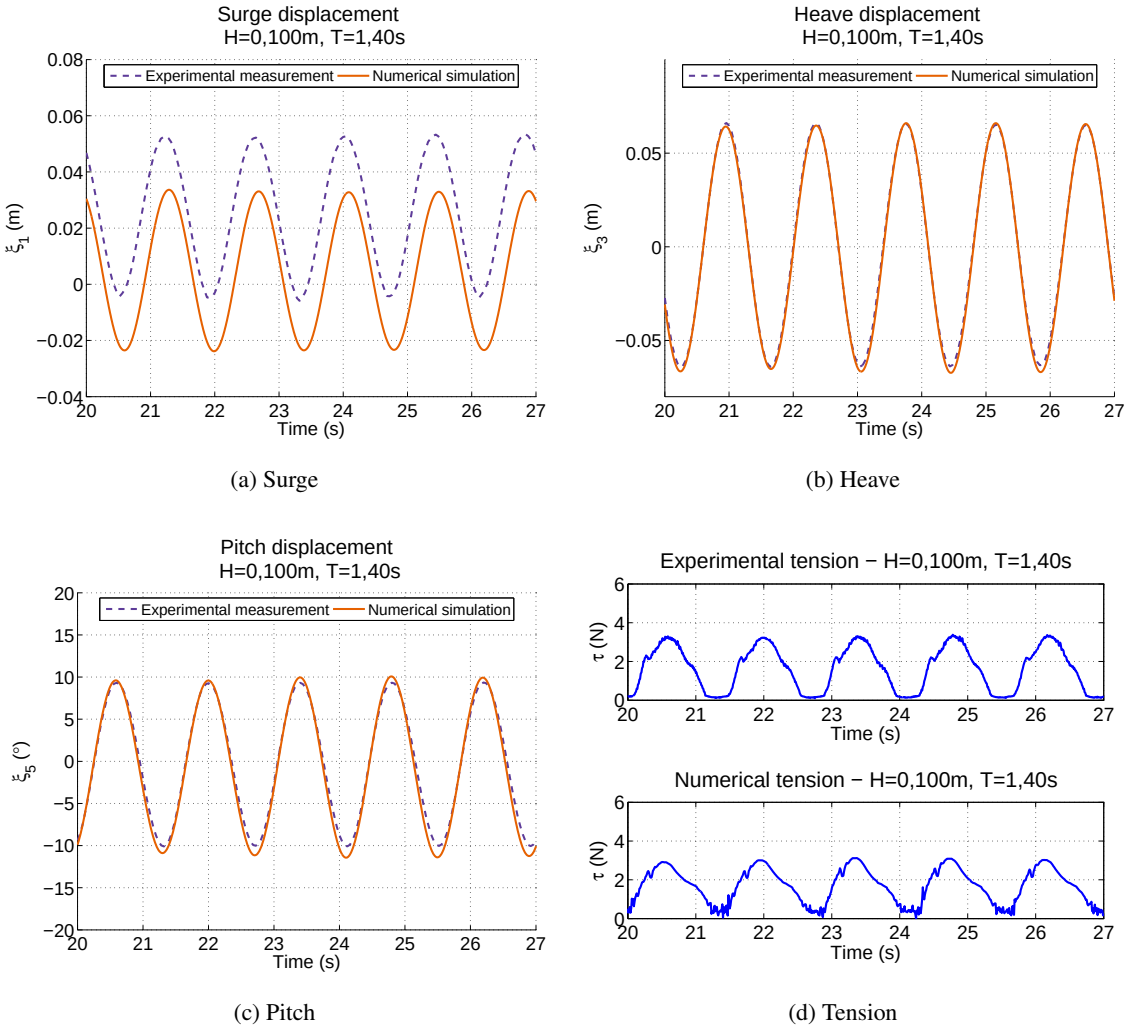

(a) Surge

(b) Heave

(c) Pitch

(d) Tension

Figure 3.12: Comparison of experimental data and simulated results for regular waves with height $H = 0{,}100\,\text{m}$ and period $T = 1{,}40\,\text{s}$.

motions (except for the surge offset) are well captured for $T = 1{,}40\,\text{s}$ and $T = 1{,}50\,\text{s}$. For $T = 1{,}30\,\text{s}$, the pitch and surge motions are only reasonably captured, with the pitch amplitude being larger than in the experiments, and the surge amplitude being smaller. The pitch resonance period was estimated to be $T = 1{,}19\,\text{s}$ in the experiments and $T = 1{,}20\,\text{s}$ in the numerical simulations. At $T = 1{,}30\,\text{s}$, the wave period is relatively close to the pitch resonance period, a situation where linear potential theory is known to overestimate the motion amplitude (especially when viscous damping is not modelled). As pitch and surge are coupled, this higher amplitude in pitch might induce a smaller than expected amplitude in surge.

When it comes to tension, the amplitude of the numerical ripples is not as significant as in the cases shown in subsection 3.5.2. Since the peak values of the tension are well captured, this might mean that the filter applied is performing well and improving the results and the quality of the numerical model. However, in contrast to the cases of subsection 3.5.2, the shape of the

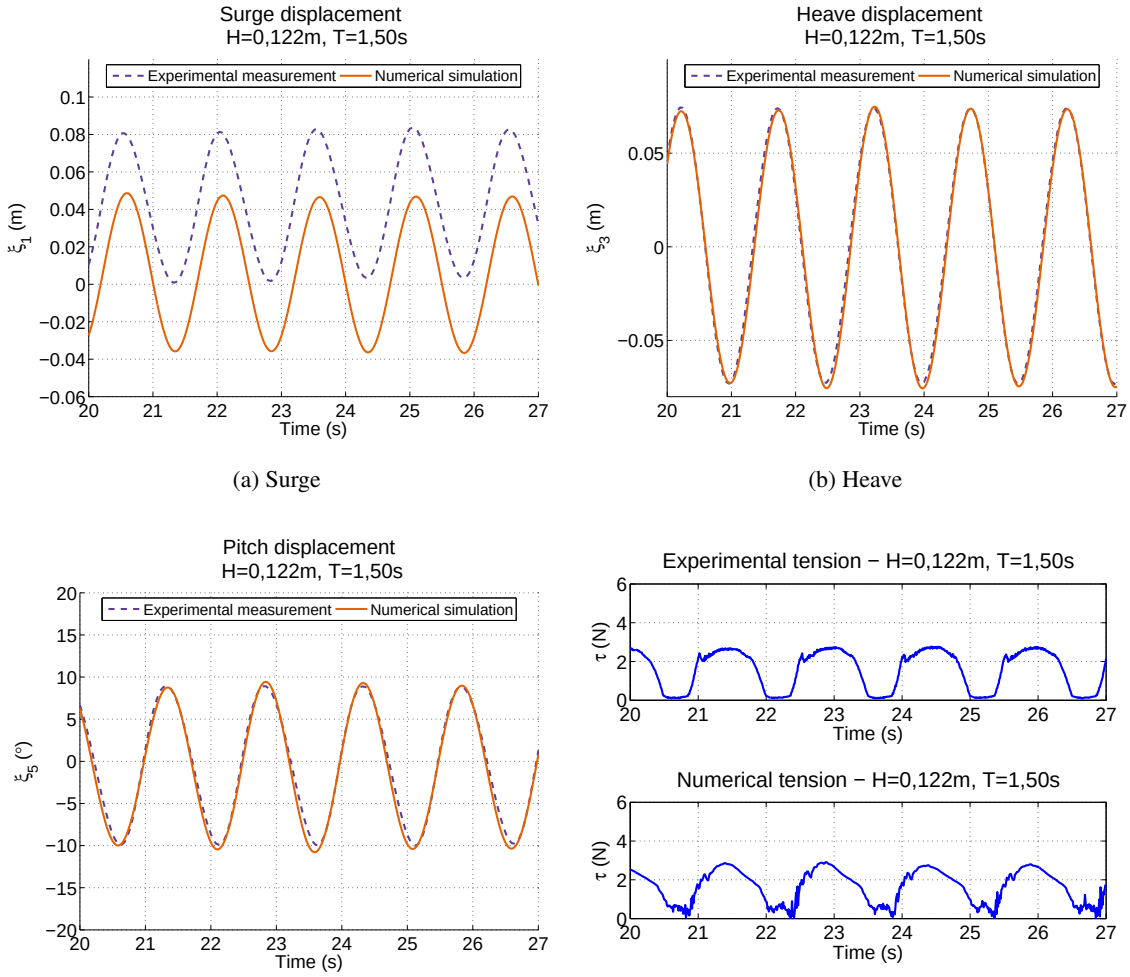

(a) Surge

(b) Heave

(c) Pitch

(d) Tension

Figure 3.13: Comparison of experimental data and simulated results for regular waves with height $H = 0{,}122\,\text{m}$ and period $T = 1{,}50\,\text{s}$.

tension cycle is not so well captured in these numerical simulations. The explanation for this is not fully understood, but it might be partially related to the load cell used in the experiments. Even though the load cell was submersible, it was not pressure compensated. This meant that the water pressure around the cell reduced the tension readings. At rest, this effect was estimated to reduce the measured tension by around 0,6 N to 0,8 N, but during the tests, the load cell moved with the buoy and the water pressure was not constant. As such, during the tests, the pressure effect was not constant, which might have changed the shape of the tension cycles. This does not necessarily mean that the experimental maximum tension in the experiments was higher than what was measured: the load cell could have been above the water level when the tension reached its maximum value. Additionally, it was later found out that the load cell might have also been somewhat damaged during the experiments.

Another effect that may explain the difference between the measured and the recorded data is, as mentioned earlier, the choice to integrate in time Equation 3.59 and 3.60 instead of Cummins's equation.

On a smaller scale, the fact that the numerical simulation could not account for the different water depths in the experiments might cause some variations in the results as well.

3.7 Discussion

The numerical model showed a remarkable performance in the simulations presented. With relatively few degrees of freedom, the maximum tension and the shape of tension cycle were well determined. Even in long simulations, the solution did not show appreciable signs of numerical dissipation or other integration errors that could build up with time. The only exception was the simulation of the moored buoy in section 3.6, where the results were not as good as for the other test cases. This particular test case was affected by the limitations of linear potential theory, used to model the dynamics of the buoy, and by limitations in the experimental data, due to problems with the sensors used in the physical model. Because of this, the results of this test case cannot be expected to be fully representative of the quality of the numerical model. However, the numerical model was still able to estimate correctly the peak tensions as measured in the physical model.

It was stated in [35] that the discontinuous Galerkin formulation can be expected to be better at capturing shock waves than lower-order continuous methods. The ability of the model to correctly estimate the peak tensions in the dynamic simulations (see sections 3.5.2 and 3.6), especially in the cases with short oscillating periods, suggests that it might really perform well in this sense.

An important issue is the existence of high frequency ripples in the tension. The cause of these ripples is not completely understood: they might be a physical phenomenon, or caused by limitations in the experimental set-up or in the numerical model. The presence of ripples in experimental measurements and numerical simulations of tension in cables has been known for some time, but never fully explained [15, 22, 24, 25, 67]. As the numerical model uses a discontinuous formulation, Gibbs oscillations might be generated at the boundary of adjacent elements. On the other hand, the data acquisition interval of the load cells in the experiments (1×10^{-2} s to 5×10^{-2} s) is much larger than the time-steps used in the simulations (1×10^{-4} s to 1×10^{-5} s). This might act as a filter, smoothing ripples in experimental measurements.

The equation of perfectly flexible cables is known to be ill-posed when the tension is low. Coincidently, the ripples are more prominent when the tension is low, which suggests a relation between the two. If this is true, the ripples are not caused by the specific discretisation presented here, but are due to the cable equation itself. In this case, the formulation will require stabilization and filtering to attenuate this issue. The penalty term λ_2 and the filter used in section 3.6 were applied exactly with this purpose. The penalty term λ_2, which can be compared to a damping coefficient, is not a standard term in the Local Discontinuous Galerkin formulation. Although beneficial in the simulations described, its effects on the numerical model and its optimization require a deeper study. As explained in [67] the ripples might also be caused (or magnified) by

the shock waves generated at the points where the cable impacts the ground, which was noted to happen in the simulations presented. This phenomenon and its attenuation also require further research. This ripple effect might be an evidence of the ability of the model to capture shock waves. Shock waves are discontinuities in the solution and, as already mentioned, modelling discontinuities with higher-order functions might cause Gibbs-type oscillations.

Finally, unlike lower order formulations, the time-step used in the test cases presented is rather small (about 1×10^{-4} s to 1×10^{-5} s). Using such a small time-step in the numerical model might counteract the gain in computational work from using fewer degrees of freedom when compared with other formulations. The requirement to use small time-steps is a consequence of using explicit time-stepping schemes and higher order polynomials [35]: the maximum time-step allowed decreases when either the polynomial order or the number of elements increase.

3.8 Conclusions

A numerical model for cable dynamics, which solves the partial differential equation of perfectly flexible cables using the spectral/*hp*-element discontinuous Galerkin method, was developed and presented.

It was demonstrated that the model has exponential convergence and that it can achieve high-quality solutions with few degrees of freedom, a classical feature of higher order formulations. The numerical model exhibited a remarkable performance in the reproduction of analytical and experimental cases, where it determined accurate solutions and showed some ability to capture shock loads. These features were targeted since the beginning of the development of the numerical model, and are some of the reasons why a higher-order discontinuous Galerkin formulation was used.

In the simulation of physical model tests of a moored buoy the results were not as good as expected. However, the simulation of the moored buoy did not depend solely on the numerical model for cable dynamics; it also depended on the simulation of the buoy itself, which was modelled with linear potential theory. This theory has strong limitations in its range of application, especially for periods near resonance. Furthermore, there were problems in the physical model experiments and the experimental data might have a large uncertainty. As such, these simulations, which were limited by the quality of the data they tried to reproduce, cannot be assumed to be representative of the numerical model developed.

Further developments are required in the stabilization parameters and in the ground interaction dynamics, in order to reduce numerical artefacts that stem from the low numerical dissipation of high-order methods and from the Discontinuous Galerkin formulation.

Since the numerical model requires small time-steps (due to the use of explicit time-stepping schemes together with higher order polynomials) part of the advantage of using few degrees of freedom might be lost. This limitation should be overcome by the use of implicit time-stepping schemes that allow the relaxation of the time-step requirements.

Chapter 4

Tracking Mooring Cables in Physical Models

4.1 Introduction

The tracking technique presented here measures the geometry of mooring cables in physical models, as when the moored object is excited by surface gravity waves, and has been described in an earlier publication [78]. It processes underwater videos of the mooring cables, moving with frequencies around those of the incident waves, and outputs the position of their medial axis. Being thin and long elements, it is assumed that cables can be represented by their medial axis without any impairment. When compared with other techniques, it has two major advantages: (i) by capturing the complete medial axis of cables, it has no need for interpolation and (ii) all the experimental steps are performed underwater, so it can be applied to a broad range of situations.

Since optics and image processing will play a major role in this task, a basic introduction to some of their concepts is presented in section 4.2.

The physical model set-up used to test and develop the technique is described in section 4.3. In the experimental phase of the technique standard photogrammetric methods, described in section 4.4, are applied in order to obtain data to correct short-comings in the videos and acquire essential parameters to convert the video data into physical values. Afterwards, a special-purpose processing algorithm, described in section 4.5 interprets the videos and outputs the geometry of the cable.

In section 4.6 it will be demonstrated that the technique is feasible and robust, performing well even when contrast conditions are far from optimal. A basic error analysis is provided in section 4.7 to show that, in spite of the prototype nature of this proof of concept, the error is acceptable. As this work describes a proof of concept, it has not been optimised yet. Some suggestions on further improvements are provided in sections 4.8 and 4.9.

The technique has only been tested using cables without floaters and sinkers. Furthermore, because there was only one camera available, three-dimensional motion could not be determined,

so the technique is only demonstrated for cables with two dimensional motion. However, the described procedures and algorithms can be easily expanded to determine three dimensional motions if more than one camera is used.

4.2 Optical Concepts

An image can be interpreted as a scalar function of two variables or coordinates, u and v, which are bounded by the dimensions of the image. Each point or pair of coordinates is assigned a value which represents the intensity of light, I, at that point. In analogue images, the function is continuous, but in a digital image the function is discrete. In the case of digital images, each point in the image is called a pixel.

For black and white images, the intensity may take the value 0 for background pixels (usually black) or 1 for foreground pixels (usually white). For 8 bit greyscale images, the intensity usually takes integer values from 0 (black) to 255 (white) with the values in-between representing different shades of grey. By specifying a colour map, the intensity values are converted into colours and the image can be visualised.

Since a digital image is a function, it can be subjected to mathematical operations, some of which will be described in the following text.

The optics of any imaging system are affected, more or less intensely, by some form of distortion, depending on its quality and purpose [59]. Two of these distortions (the most relevant for this work) are the radial and the tangential distortion. These two kinds of distortion will have a significant role in the experimental set-up, in the algorithm and in the error analysis.

Radial distortion may show up in two different ways: pincushion distortion, Figure 4.1 in the centre, where the magnification increases radially from the centre of the image, and barrel distortion, where the magnification decreases radially from the centre of the image, Figure 4.1 on the right.

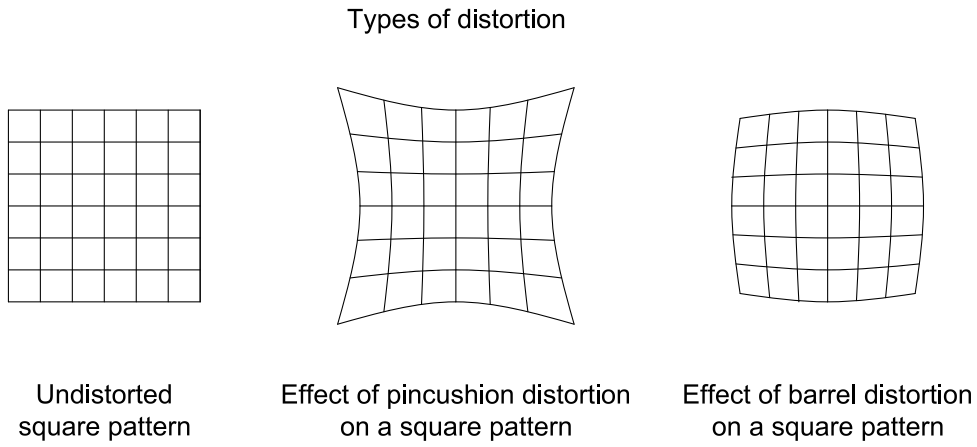

Figure 4.1: Representation of pincushion and barrel distortion on a square pattern.

Tangential distortion induces magnification that varies perpendicularly to the rays from the image centre. This type of distortion is generally caused by the imperfect alignment of the different optical components (decentering distortion) and comes associated with radial and other distortions in a complex phenomenon [60].

Radial and tangential distortions are usually modelled using the Conrady-Brown polynomial approximation [59, 60]. This model maps the position of the points in the distorted image to the position of the points in the distortion-free image. The coefficients of the polynomial are the *distortion parameters* of the camera and can be determined using different optimisation routines. Usually, these routines consist of acquiring a series of photographs of a regular pattern with a known geometry, and then estimating a fit of the polynomial that describes the distortion of the pattern in the photographs. The distortion parameters, together with the focal length, the position of the nodal points and the skewness of the image sensor are the *intrinsic parameters* of the camera. An image whose optical distortions have been corrected is said to be *linearised*. Some of the routines used to determine the intrinsic parameters are also able to determine the relative position between the camera and the target in six degrees of freedom (orientation and position). These are the *extrinsic parameters* of the camera.

If the images are captured underwater, the optical issues become more complex because the lens is immersed in a fluid (air) with a different refractive index than that of the medium surrounding the object being imaged (water). Unless specific and expensive equipment is used, several distortion artefacts will be added to the ones described above [62]. For example, the simple case of using a standard camera through a transparent flat plane (a glass wall of an aquarium or the glass of an under-water housing) will result in a reduced field of view of the camera, in the generation of pincushion distortion and in an image with multiple focus points [62, 64]. Part of these problems can be fixed using a hemispherical dome port between the lens and the water, instead of a flat one. This preserves the field of view of the camera and maintains a single focus point [62]. The downside of using a hemispherical dome port is that the image created will be a curved surface instead of a flat plane, as in most cameras. In order to have the entire image surface in focus, the depth of field (the thickness of the volume seen by the camera that is in focus) has to be large enough to encompass the depth of the surface. For a lens with a constant focal distance, this usually means that the aperture has to be reduced. A full mathematical description of this problem is given in [62].

Another problem arising when imaging underwater is that, in general, the linearisation procedures mentioned earlier are not valid. The Conrady-Brown model for correcting optical distortions was developed for cameras in air imaging subjects that are also in air, where the linearisation is valid for any camera-to-object distance and for different focus adjustments [63]. Special (and rather complex) procedures are required for underwater linearisation, an area which still requires some development. Under certain conditions, however, the in-air linearisation procedure can be applied underwater. For this to be valid, the linearisation must be performed underwater for the specific distance between the camera and the object of interest, and the optical characteristics of

the camera cannot be altered after linearisation. The restrictions mentioned above were adopted in the experimental set-up described later, so the in-air linearisation method could be used.

Since a photograph is a projection of a three dimensional object onto a plane, the result of the projection depends on the relative position between the camera and the object, Figure 4.2. The apparent change of shape of the object with change of the view point is known as *keystone effect* and is caused by the viewing axis not being perpendicular to the plane or planes captured in the image.

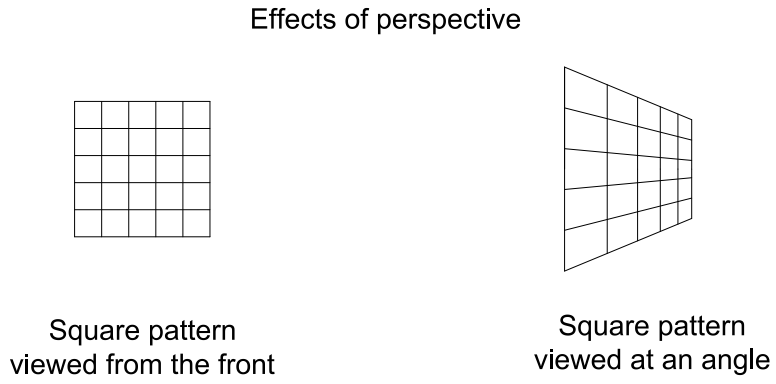

Figure 4.2: Keystone effect. When a face of an object is projected onto an oblique plane, the shapes in the resulting projection are not geometrically similar to the ones in the object.

The keystone effect can be partially corrected using an operation called homography. This operation takes the original image and re-projects it onto another plane [79, 80]. By re-projecting the photograph in a plane parallel to the one affected by the keystone effect, the effect is partially eliminated. Evidently, after applying an homography transformation, the keystone effect might appear in other objects in the image that are now viewed from an oblique angle and, hence, it might be impossible to correct this effect in the entire image at once. This operation is a simple matrix multiplication that requires only the intrinsic parameters of the camera, as well as the current and the desired orientation of the projection planes. When an image is corrected so that the real object and the object in the image have geometric similarity, the image is said to be *rectified*.

Accurate measurements using imaging techniques require geometric similarity between the object and its representation, implying that all of the distortions and optical effects be corrected. Once these effects are corrected, the use of an appropriate linear transformation *should* (ideally) convert the positions of the points of the image to coordinates in the desired reference frame. The image is then said to be *calibrated*. Calibration might be as simple as the multiplication of each of the coordinates of the points in the image by a constant.

Besides correcting optical artefacts, images can be subjected to another type of transformations: morphological operations. For this work, the most relevant are *dilation*, *thinning*, *edge-detection* and the *top-hat transform* .

Dilation enlarges objects or shapes by super-imposing on foreground pixels a specified shape, called *structuring element*, Figure 4.3. The structuring element has an origin which is matched to each foreground pixel when adding the two shapes together, Figure 4.3.

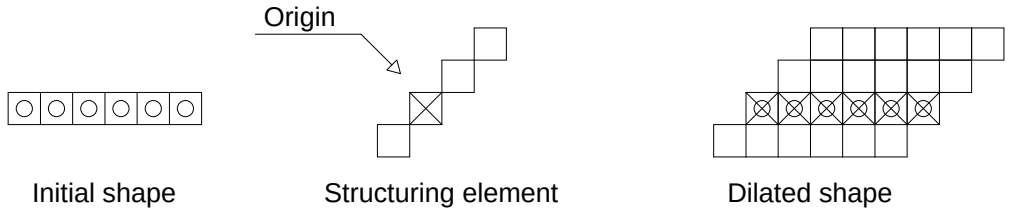

Figure 4.3: Dilation. The origin of the structuring element (marked with $\times$) is matched to each of the pixels in the initial shape (marked with $\circ$) and its pixels added together, resulting in the dilated shape.

Thinning is an operation that shrinks shapes by reducing their thickness by one or two pixels [81]. When executed several times, thinning will reduce objects to simple strokes, but it will never break the object or make it disappear, Figure 4.4.

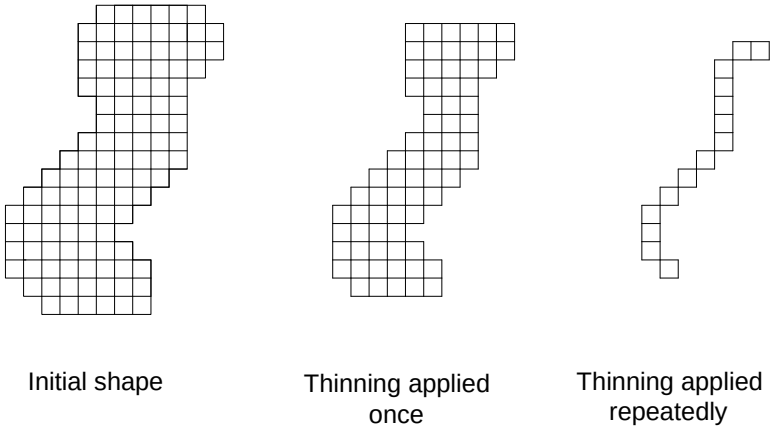

Figure 4.4: Thinning. Successively reducing the thickness of a shape will result in a one-pixel wide stroke that is approximately the medial axis of the shape.

For a simple shape, the remaining stroke after thinning has been applied several times is approximately the medial axis of the shape. Contrary to dilation, thinning does not require a structuring element.

Edge detection looks for regions in greyscale images with large gradients in the intensity values [81]. These regions usually correspond to edges of the objects in the image, but may also be generated by shadows, differences in illumination and other perturbations.

The *top-hat* transform detects the bright regions in an image that are narrower than a selected structuring element or, in simpler terms, regions where the structuring element cannot fit in, Figure 4.5. When an image, such as Figure 4.5a is represented as three-dimensional plot, Figure 4.5b, the brighter regions will appear as peaks and plateaus, while the darker regions will appear as valleys. Some of the bright regions, like the sharp peak on the right of Figure 4.5c, are narrower than the structuring element, which in this case is a simple 3 pixel wide cross. These regions

are detected and preserved by the *top-hat* transform, while the remaining ones are eliminated, Figure 4.5d.

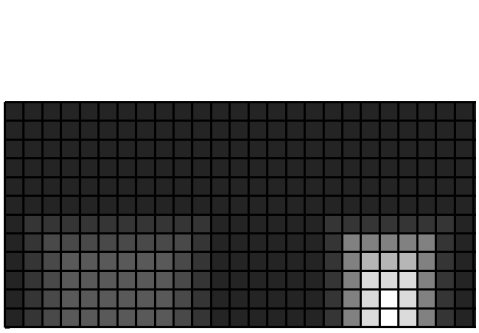

(a) Original image.

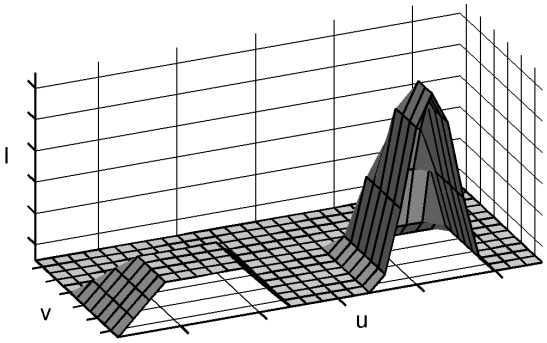

(b) Image represented as a 3D plot.

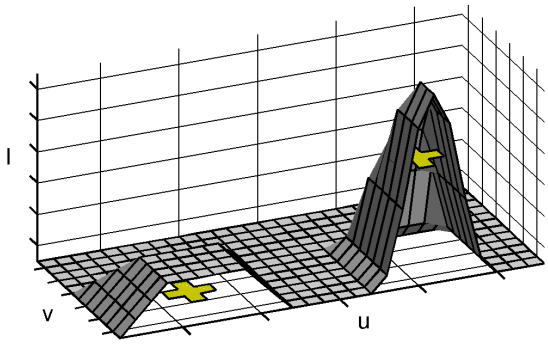

(c) Some bright regions are narrower than the structuring element (the cross).

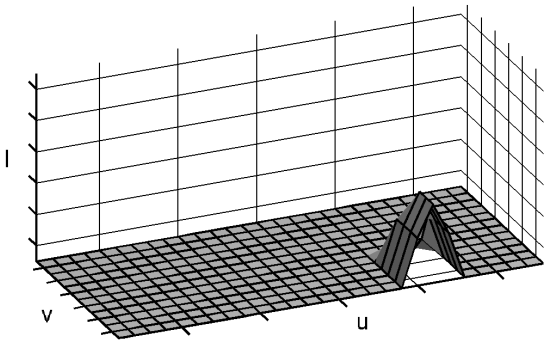

(d) Image after tophat transform.

Figure 4.5: The top-hat transform.

4.3 Experimental Set-up

A small scale model, composed of a cylindrical buoy moored by two chain catenaries, was set up in the wave tank of the Faculty of Engineering of the University of Porto to obtain videos of a mooring cable moving in water, Figures 4.6, 4.7 and 4.8. These videos were used to develop and test the tracking technique.

Due to time and budget constraints, the experimental set-up was built using the very same elements of the physical models studied in chapter 5, which explains the large span of the mooring cables.

The moored buoy was subjected to regular waves travelling parallel to the plane of the mooring cables, so their motion can be assumed two-dimensional. The waves generated had a height $H = 0{,}04\,\text{m}$ and periods ranging from $T = 0{,}80\,\text{s}$ to $T = 2{,}33\,\text{s}$.

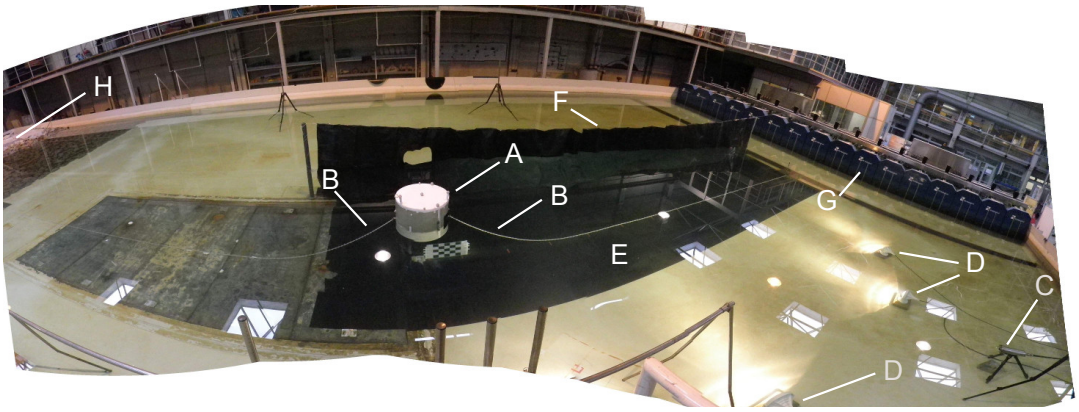

Figure 4.6: Panoramic view of the experimental set-up. The buoy (A) is in the centre with the mooring cables (B) extending to the left and to the right of it. On the right bottom corner is the housing (C) with the video camera (standing on a tripod). Floodlights (D) can be seen on the right part of the image. Beneath the buoy is a black film applied on the floor (E) and behind the buoy is a vertical black curtain (F). The wave generator (G) and the absorption beach (H) are in the top right and top left corners of the image.

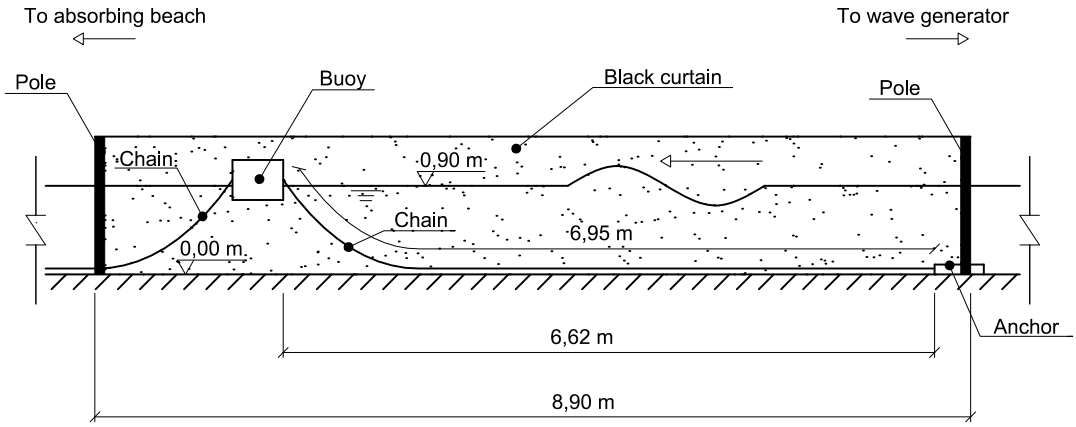

Figure 4.7: Side view of the experimental set-up.

A video camera placed by the side of the seaward mooring cable was used to record its motions during the tests. The camera, Figure 4.9a, had a resolution of 1280×1024 pixels and was fitted with a 2 megapixel wide-field lens (77,32°).

The videos were stored directly in a data acquisition computer using a cable connection which also allowed real-time monitoring and control of the camera parameters.

A water-tight housing had to be built to protect the video camera, since it was not waterproof, Figures 4.9c to 4.9e. This solution was favoured over using underwater video cameras because they were either too bulky and expensive or lacked essential features (such as real-time control). The housing was made of stainless steel with a quick release lid on the front and an umbilical connection on the back. Inside the housing, the camera was installed on a motorised platform to control the focus and the aperture, Figure 4.9b.

In order to minimize adverse optical effects, the housing had a spherical dome port, as it is common in underwater imaging [62], with a diameter of 0,0953 m. The use of a dome port requires the position of the nodal point of the lens and the centre of the dome port to be coincident [82].

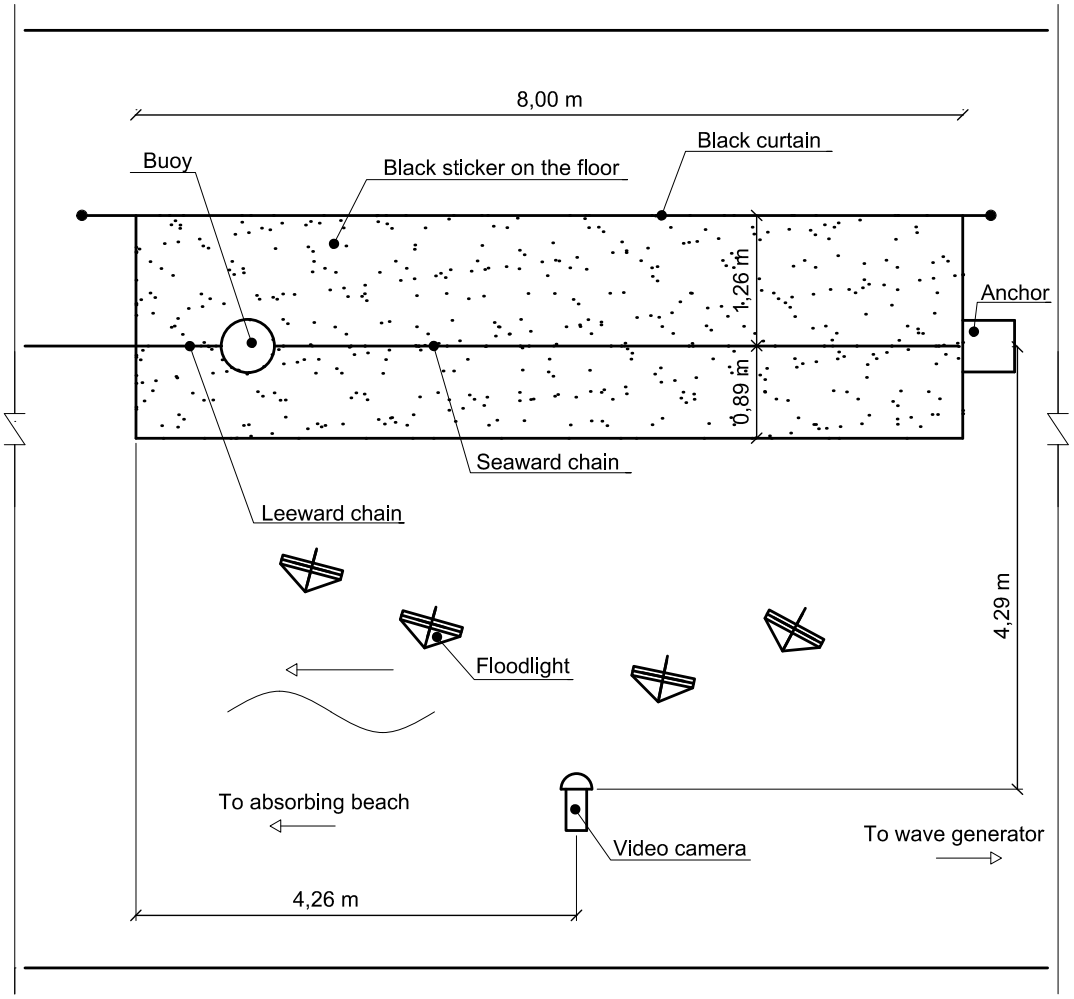

Figure 4.8: Top view of the experimental set-up.

Guiding pins on the lid of the housing ensured that the dome port would maintain its alignment with the camera even when the lid had to be removed. Despite the effort in designing the housing, neither the dome port could be provided in optical quality glass nor a perfect positioning of the camera could be guaranteed with the equipment available. As a consequence, there is a small distortion in the videos that could not be corrected using theoretical models.

To keep in focus all of the curved image generated by the dome port, the aperture of the camera was set to a low value, maximising the depth-of-field. Because of the reduced aperture, together with water quality issues, the recorded images had a somewhat low quality.

The simpler flat port was rejected because of the problems mentioned in section 4.2, which cannot be easily corrected. Additionally, earlier tests using a flat port demonstrated that it would be unsuitable because of the reduced field of view. This is illustrated in Figure 4.10, showing a photograph of a catenary with the same camera used in these experiments, but taken through a flat port. Although the cable spanned only 5,59 m, it was not possible to capture its whole length.

To capture the entire span of the seaward mooring chain, the camera had to be positioned 4,29 m away from the model, Figure 4.8. Since the floor and walls of the tank were light beige

(a) Video camera.

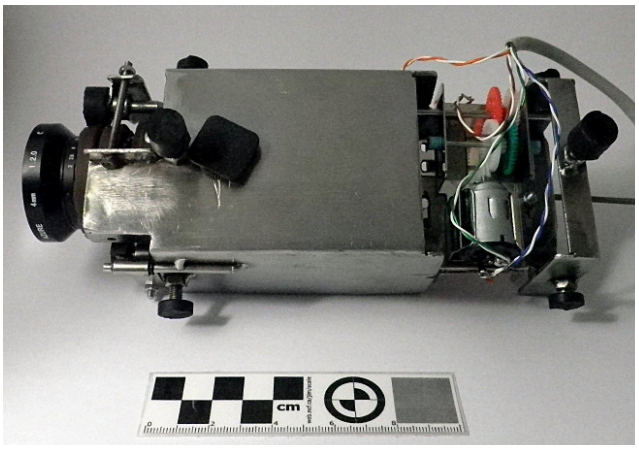

(b) Motorised control system.

(c) Underwater camera housing viewed from the side.

(d) Fully assembled imaging system viewed from the front.

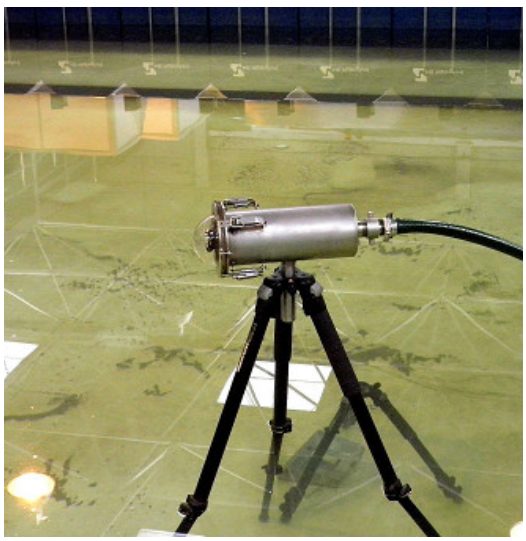

(e) Fully assembled imaging system viewed from the side

Figure 4.9: Components of the imaging system used to record the motions of the cables.

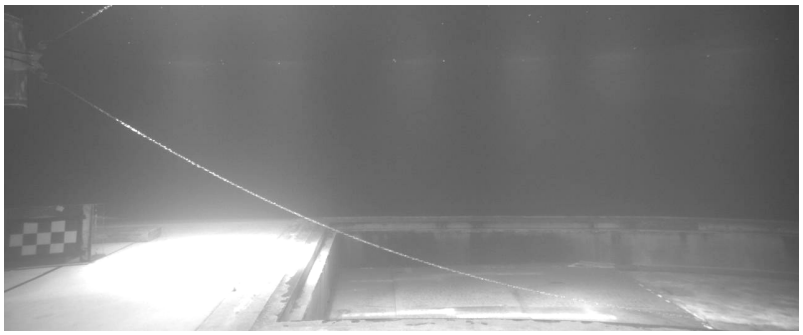

Figure 4.10: Photograph of a mooring cable taken through a flat port. The water depth is 0,900 m and the span of the cable is 5,59 m. The small field of view caused by the flat port of the housing made it impossible to capture the entire length of the cable. Pincushion distortion is also visible in the image, causing the edges of the pit to appear curved.

and the chain was silver grey, it was difficult to distinguish both from afar when under water. In addition, the tank water had a high content of suspended material (dust and minerals), which absorbed and scattered light. This problem could be so intense that, at times, it would completely hinder the acquisition of any video during the experiments. The large thickness of water between the camera and the cable, combined with the visibility problems, resulted in images with somewhat low contrast, Figure 4.11.

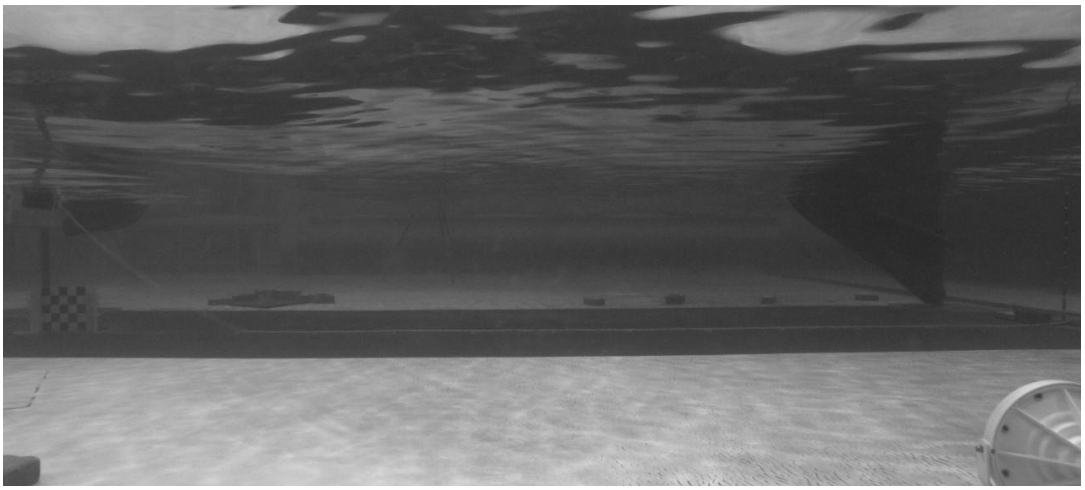

Figure 4.11: Underwater photograph of the cable with minimal contrast enhancement, showing a foggy haze caused by the suspended dirt in the water of the wave tank.

In order to improve contrast, the chain was brightened and the background was darkened. This solution was chosen for practical reasons: most wave tanks have dark walls (due either to construction or to dirt) and it is easier to make a small cable brighter so it stands out against a dark background, than to brighten the whole inside of a wave tank. A dark cable on a light background might even result in the cable fading in the image due to light scattering and to saturation of the image sensor in the video camera.

A coat of white paint was applied to the chain, which was also illuminated with four underwater floodlights placed along its length, distributing the light evenly, Figures 4.6 and 4.8. The use

of cheaper and simpler flood lights pointing downward to chain from above the water was tried in preliminary tests, but it caused severe saturation of the imaging sensor, Figure 4.12

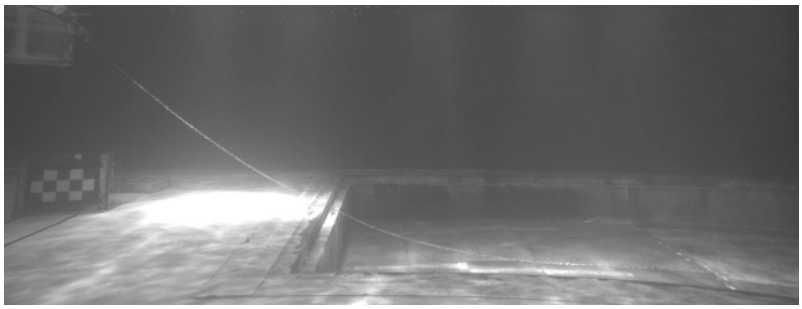

Figure 4.12: Saturation of the image caused by vertical light reflecting off the floor (on the left). The saturated region blocks the visibility of the portion of the chain near the corner of the pit.

Beneath the chain, the tank floor was covered with a black sticker film which had a matte surface, in order to minimise light reflections, Figures 4.6 to 4.8. Red markings were placed every 0,500 m on the black film in the direction of the cable starting at the anchoring point, to be used as references.

Behind the chain, a black curtain was hung between two poles, aligned with the wave direction, Figures 4.6 to 4.8. Imposing the use of a curtain would severely limit the range of application of the technique: for example, in multi-directional sea-states, a shadow region would be created. However, it will be shown in section 4.6 that the technique is fully functional when the vertical curtain is removed, which will be a requirement in most situations. In these experiments it was only used to improve the contrast conditions and the video quality for the development of the technique.

In spite of the seemingly elementary approach to improve contrast, it was the most effective one from all of the tested solutions. Besides what was described above, two other solutions were tried. In one of them, electroluminescent cables were threaded through the links of the chain, but they were too stiff and too large. In the other, ultra-violet light (UV) was used to illuminate the chain, which was painted with fluorescent and phosphorescent paint. The UV light should induce the fluorescence and phosphorescence of the paint in the chain and, being invisible to the camera, UV would not cause saturation. However, the power of the ultra-violet lights available was too weak to excite the paints and any light emitted by the chain was too faint to be useful.

Independently of the conditions in the used laboratory, it is always necessary to assure that the cables stand-out well enough to be detected by the processing software. This will usually result in the need to enhance contrast. Even though this might seem trivial, it is worth to emphasise it because, at least at the present moment, a feasible processing algorithm is very limited when compared to the human ability to interpret images.

It is important to remember that contrast in the experimental set-up is obtained by making the cable lighter than the surroundings, because the processing algorithm described later is designed to look for small bright regions in the images.

In some steps of the tracking technique described in the next section, namely for the linearisation and for the calibration, a flat target with a chess-like pattern will be required. The target that was used in this work is shown in Figure 4.13.

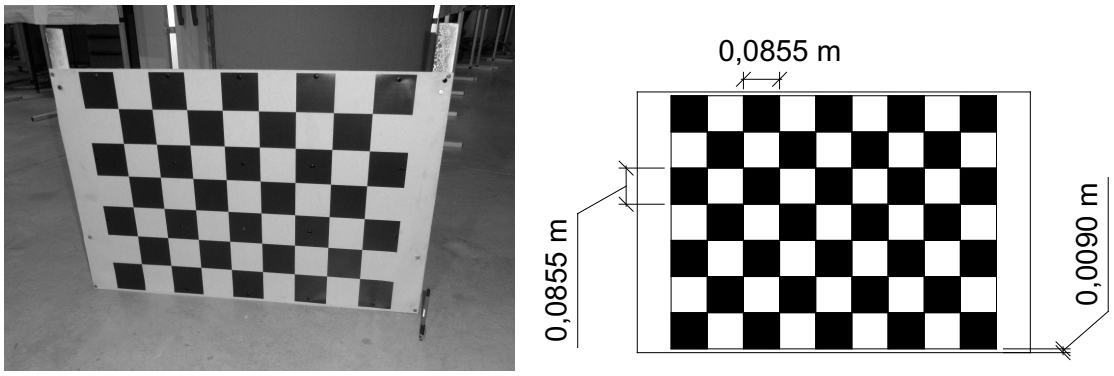

(a) (b)

Figure 4.13: Target used for the experimental steps of linearisation and calibration.

It was made of a square pattern printed on a white plastic film pinned to a chipboard panel. On its back it had metal supports to keep it vertical when placed on the floor.

For the procedures involving image processing and algorithm coding, the software suite *MATLAB* was used. Even though it is a proprietary software and relatively slow when compared to other programming languages, it provided a reasonable platform for prototyping. All efforts were made to use solely standard image processing functions, instead of any function exclusive to *MATLAB*, so that the algorithm developed could be programmed and tested in different environments. The special purpose "Camera Calibration Toolbox For MATLAB" [83] that will be used in some steps of the technique, as well as its source code, are freely available and can be fully inspected.

4.4 Tracking Technique - Experimental Procedure

Three different steps are required in the experimental phase: (i) linearisation, to obtain the intrinsic parameters of the camera required to correct the optical distortions; (ii) calibration, to obtain the relative position between the camera and the cable (the extrinsic parameters) and the correspondence between pixel and model coordinates, respectively; and (iii) video acquisition of the cables moving underwater.

Linearisation is a conditional step: it is only required if the camera is not designed to provide distortion-free images underwater or if the optical parameters of the camera are not known. The video camera used in the experiments distorts the images when it is used underwater so linearisation was a necessary step.

For the linearisation, the freely available Camera Calibration Toolbox for Matlab [83] was used. This toolbox is based on the Conrady-Brown distortion model [59, 60], see section 4.2, which, in general, is not valid when either the camera or the object being imaged are submerged. However, as noted by [64], the Conrady-Brown model may be applied underwater (and, in fact,

it frequently is) with some constraints: its application will be limited to a single camera-to-object distance. As an example, in the set-up used in these experiments, Figure 4.8, moving the camera sideways would not require a new linearisation, but moving the camera towards the cable would.

During linearisation, the target in Figure 4.13 is photographed in several positions in the plane of the seaward mooring cable along its span, Figure 4.14.

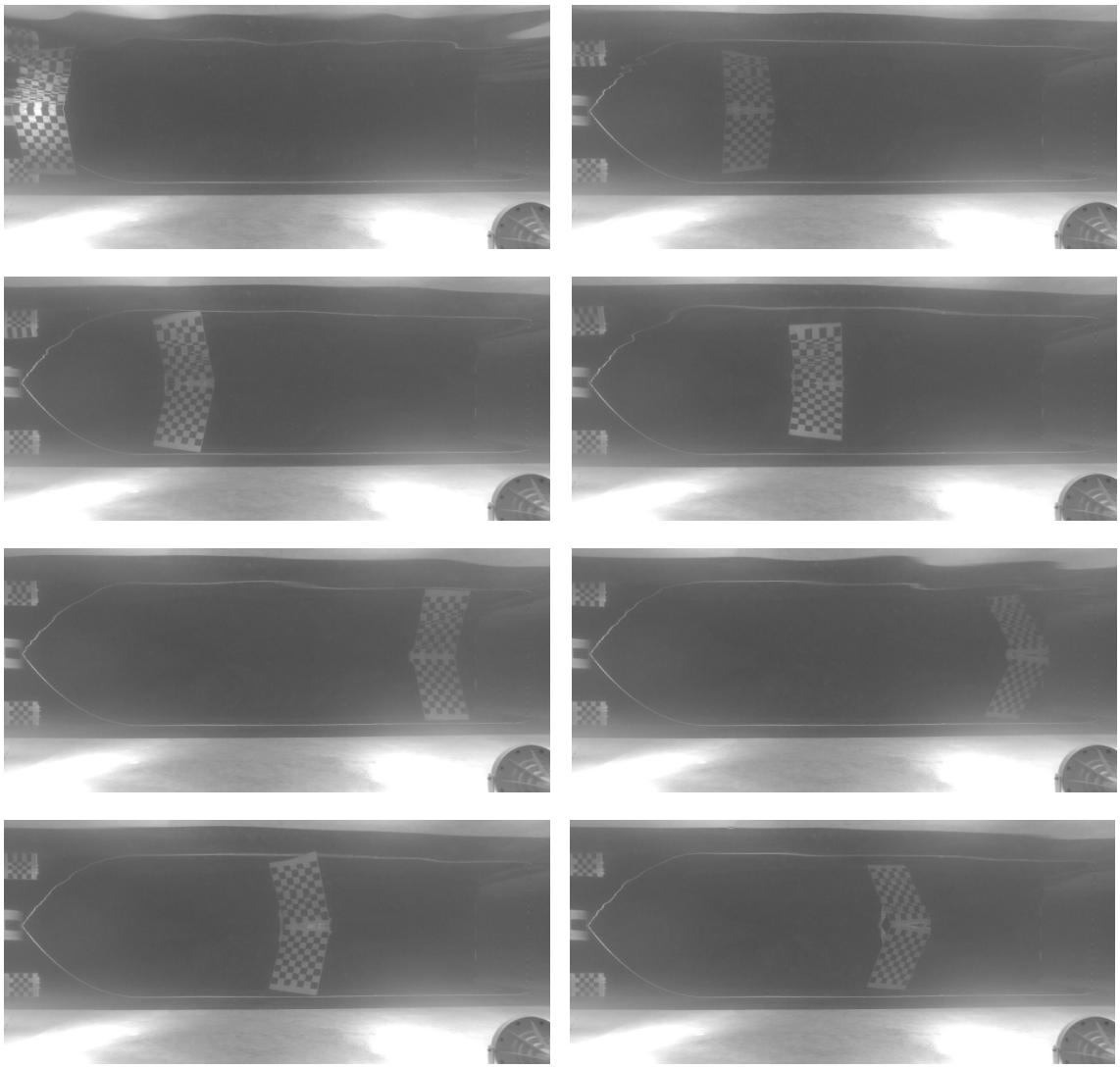

Figure 4.14: Examples of some photographs of the target during linearisation, in different orientations and positions along the plane of the cable.

Table 4.1 presents the intrinsic parameters of the imaging system used in the experiments, obtained after linearisation using the Conrady-Brown model. Following the recommendations of the toolbox user's manual, the coefficients were estimated only up to 4^{th} order; higher orders should not be used when the error in the coefficients is similar to the coefficients' magnitude. In the same way, the skewness of the camera sensor was not estimated as it was almost 90°, as is usual in modern, high quality cameras.

Table 4.1: Intrinsic parameters of the imaging system.

Parameter	x direction	y direction	Skew (°)
Focal length (pixel)	841 ± 24	838 ± 24	0
Image centre (pixel)	607 ± 21	554 ± 25	
Distortion coefficients			
1^{st} order	2^{nd} order	3^{rd} order	4^{th} order
$(-8{,}7 \pm 2{,}8) \times 10^{-2}$	$(9{,}5 \pm 4{,}1) \times 10^{-1}$	$(9{,}6 \pm 6{,}8) \times 10^{-3}$	$(2{,}5 \pm 6{,}6) \times 10^{-3}$

Although the fitted polynomial was limited to 4^{th} order, the error in the coefficients was still significant. This is probably due to the limitations of the video system caused by the quality of the dome port and by the inaccuracy in centring the dome and the lens of the camera.

4.4.1 Calibration

This step determines the transformation required to correct the keystone effect (see Figure 4.2) and to convert pixel coordinates to the desired model coordinates.

To acquire the calibration data, the target in Figure 4.13 is positioned in the plane of the cable in a known location, as shown in Figure 4.15. The target should not be tilted in any direction in relation to plane of the cable, so (in these experiments) it was held in place by the metal supports on its back. A single photograph is taken of the target in this position.

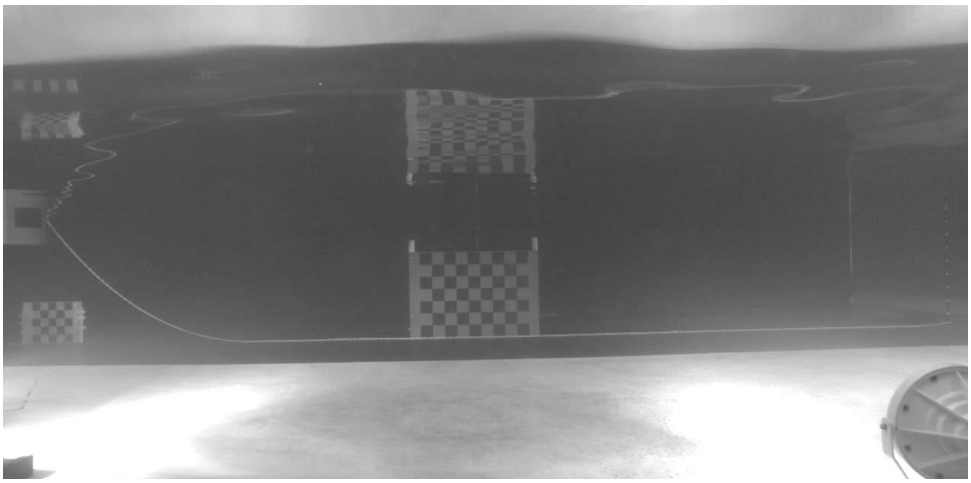

Figure 4.15: Position of the target during the calibration phase.

Knowing the intrinsic parameters of the imaging system, the distortions in the image are corrected. Then, the current orientation of the local reference frame of the target ($O\ x_t\ y_t\ z_t$) relative to the camera (the extrinsic parameters), are determined, Figure 4.16. Both of these steps are executed using the "Camera Calibration Toolbox for MATLAB".

Once the current extrinsic parameters are known, a new matrix of extrinsic parameters is built defining an orientation where the target is parallel to the imaging plane (in other words, where

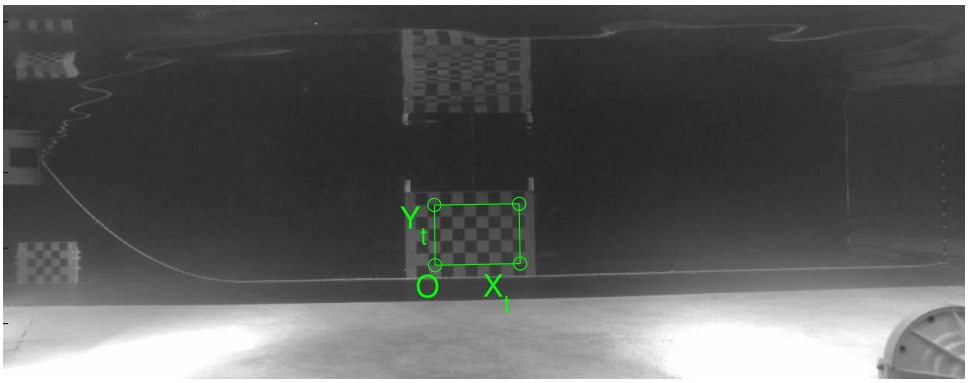

Figure 4.16: Local reference frame of the calibration target as established by the "Camera Calibration Toolbox for MATLAB". The z_t axis is not shown because it is almost perpendicular to the photograph.

the z_t axis is aligned with the camera viewing axis). This matrix is then used in the homography transformation to obtain the desired new orientation of the plane of the image. The local x_t and y_t axes do not need to be rotated, but they were anyway so that, for convenience, the images are properly oriented when displayed.

In the rectified image, four points are selected whose coordinates in the model are known, as illustrated in Figure 4.17.

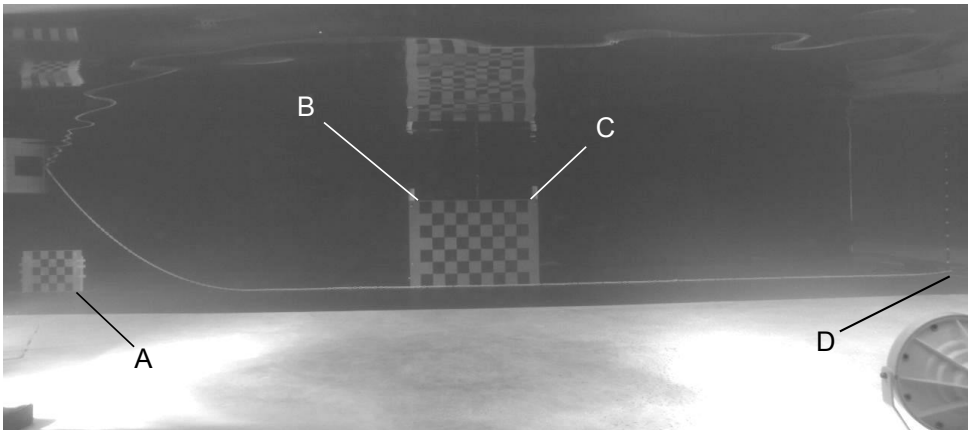

Figure 4.17: Points used for the calibration of the experimental set-up.

By defining a model coordinate frame (0 x_m y_m z_m) with the origin at the anchoring point, the x_m axis pointing to the left and the y_m axis pointing up, the coordinates of the points A, B, C and D in Figure 4.17 are established, Table 4.2. Inspecting Figure 4.17, the pixel coordinates of points A, B, C and D can also be determined. Then, a multivariate least-squares fit is used to compute the matrix that converts pixel to model coordinates. To minimize the conversion error, the points should be spread across the entire measurement region, but not aligned.

Image rectification and calibration could be merged into a single step, which would both simplify the procedure and make the Camera Calibration Toolbox for MATLAB necessary only for linearisation (if necessary at all). However, the technique is just a proof-of-concept and the extra

Table 4.2: Coordinates of the calibration points in the model reference frame.

Point	Coordinates
A	(6,500; 0,000) m
B	(4,000; 0,599) m
C	(3,231; 0,599) m
D	(0,000; 0,000) m

work demanded to merge rectification and calibration would not bring any new development or significant advantage at this stage.

The calibration is obviously dependent on the relative position and orientation between the camera and the cable.

4.4.2 Video Acquisition

Video acquisition (the recording of the motions of the cable) is the last experimental step. As the objective of the technique is to detect the geometry of cables as a function of time, the video specifications, namely the frame rate and the resolution, are of utmost importance.

The frame-rate is the acquisition frequency of the video camera. Just like for general data acquisition [84], it must be at least twice that of the highest frequency phenomena with a noticeable contribution to the shape of the cable.

The video resolution will determine the smallest dimension or detail that can be detected by the camera. Any physical characteristic or motion that, when viewed from the camera, is smaller than the width of a pixel, will be imaged together with its surroundings and will become undistinguishable. The size d of the details contained in each pixel is obtained by the simple equation:

$$d = \frac{L_t}{N_p} \tag{4.1}$$

where L_t is the total length covered in a certain direction and N_p is the number pixels in the length L_t. For instance, in the set-up used in this work, the horizontal field of view encompasses 8,90 m (including the regions to the left and to the right of the cable), Figure 4.7. Since the camera has a horizontal resolution of 1280 pixels, the resolution for this set-up is 0,007 m/pixel and no detail smaller than 0,007 m will be detected. To obtain finer resolutions, either the camera has to be placed closer to the cable or a camera with a higher resolution has to be used.

In practice, the minimum requirements for the frame rate and resolution only guarantee that the motions are detected, but not that their detailed evolution in time and space are appropriately captured. As such, the resolution and the frame rate should be well above the minimum values, in order to capture the behaviour with enough detail. Perturbations in the data acquisition, such as poor visibility or other interferences, will also demand the use higher data acquisition rates.

Additionally, the values of the frame rate and resolution are interdependent. They must be such that it is possible to record a change of shape or position with a specified magnitude in the time span between two frames. An example would be the need to capture the propagation of a transverse wave along the cable with variations in the displacement no larger than 0,001 m with a time-step no larger than 0,01 s.

For the experiments described in this chapter, the frame-rate was 15 frames per second (15 Hz). The frame-rate is considerably low when compared with usual acquisition frequencies in coastal engineering models (around 100 Hz). This low value was chosen because the file size of the videos grows rapidly with the frame-rate and, for this proof of concept, a large frame-rate was not required.

As stated in the Introduction, all the experimental steps (linearisation, calibration and video acquisition) are executed underwater, without any need for side windows in the tank or other access constraints.

4.5 Tracking Technique - Processing Algorithm

The algorithm will be explained using a worked example. For this, a small clip was extracted from a larger video. In this clip, the waves have a height $H = 0{,}04\,\text{m}$ and a period $T = 1{,}14\,\text{s}$.

The wave period is close to the resonance period of the moored buoy in heave ($T = 1{,}13\,\text{s}$) and pitch ($T = 1{,}16\,\text{s}$) in order to induce extreme velocities and displacements on the cable. To skip the ramping sequence of the wave generator (when the waves are small and vary in size), the clip begins with the cable in a non-stationary position, Figure 4.18, subjected to fully developed regular waves.

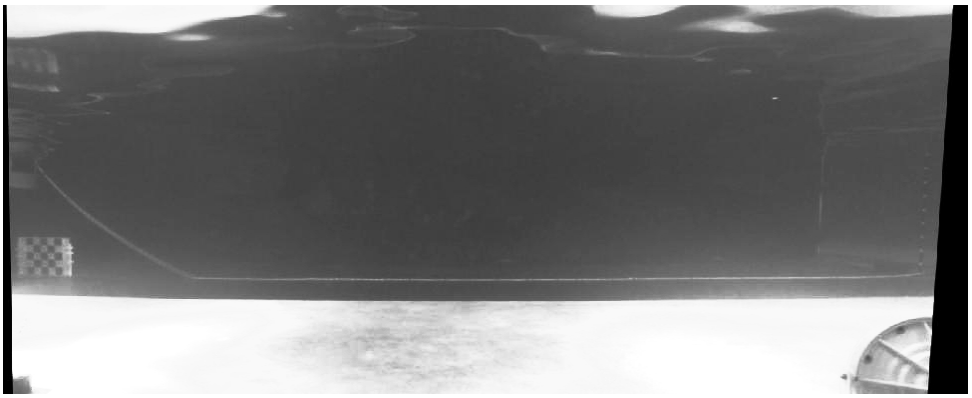

Figure 4.18: First frame of the processed clip, after correcting the distortion and the keystone effect. The cable is not in static equilibrium, because the clip was extracted from a longer video. The image histogram has been modified to enhance visibility when printed.

Before processing the video, the user estimates, by inspection, the maximum expected displacement (in pixels) of the cable between two successive frames. This information is important because it will be used by the algorithm to determine where in the image to search for the cable as it moves from frame to frame, as well as to remove unwanted features.

The first frame of the video is extracted and the distortion and perspective effects are corrected, Figure 4.18. Note the dull or foggy appearance of the image caused by the suspended dust in the water.

Even though a person can clearly identify the cable when looking at Figure 4.18, the algorithm is unable to do so without assistance. To this end, a search region is manually defined around the cable, Figure 4.19, which should be as tight as possible without intersecting the cable.

Figure 4.19: Initial search region (enclosed by the white contour) provided to the algorithm to assist in the detection the cable. The image histogram has been modified to enhance visibility when printed.

This region is stored as a mask, a logical matrix with the same dimensions as the image with entries that take the value 1 in positions corresponding to the search region and the value 0 everywhere else.

From now on, all processing will occur inside the search region, disregarding the rest of the image. The use of a search region not only speeds up the algorithm, because there is less data to process, but also and more importantly, limits the area where the algorithm can look for the cable, reducing the possibility of detecting unwanted features.

The search region is defined manually only for this first frame, just for the algorithm to have a starting point. Afterwards, the algorithm will use the medial axis of the cable in the current frame and the maximum expected displacement between two frames to automatically update the search region as the cable moves.

Selecting the search region can be compared to designating the set of markers that are to be tracked in conventional motion-capture technologies. If the experimental set-up is not altered, including the position of the camera, the search region has to be delimited only once and can then be used for the entire series of tests.

Once the search region is defined, the cable has to be separated from the background of the image. Since the cable is brighter than the background, the top-hat transform is applied to separate the image of the cable from the background, using a circular structuring element, Figure 4.20. The diameter of this structuring element (in pixels) should be equal to the average thickness of the cable in the image, which must be determined by visual inspection (for example, when defining the initial search region). It is important that the diameter of the structuring element is as close as possible to the thickness of the cable: if the diameter is too large, unwanted features might be detected and if the diameter is too small, the cable might not be completely detected.

In the images, the cable can be recognised by a being bright, long and thin shape. Therefore, an edge detector will efficiently trace its outline. For this, the *Canny* edge detector was used. This

Figure 4.20: The result of applying the top hat transform to the search region. Contrast has been enhanced over the entire image so that the result of the top-hat transform is clear, because this transform lowers the intensity of the processed regions.

edge detector can detect edges in several directions, even in images where the edge sharpness is poor [81], such as in photographs with motion blur.

The result of applying the Canny edge detector is shown in Figure 4.21, where all the data on and outside of the border of the search region was deleted.

Figure 4.21: The result of applying the Canny edged detector: the outline of the cable is efficiently traced.

The outline of the cable is clear and sharp, but the process is not yet complete: the cable is represented by its outline instead of its medial axis and there are small extraneous streaks around the cable, as in Figure 4.22.

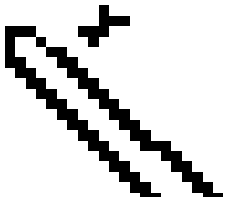

Figure 4.22: Example of an extraneous streak that will interfere in the detection of the cable. These streaks are caused by the application of the Canny edged detector. This image is taken from a later portion of the clip to illustrate this problem.

Analysing Figure 4.22, one can see that the small streaks are not longer than the width of search region. They cannot be longer because their size is limited by the search region. If the initial search region is tight enough around the cable, the maximum width of the search region in any subsequent frame is twice the maximum expected displacement (the cable can move to either side of its current position). With this in mind, all streaks shorter than twice the maximum expected displacement are deleted. Any extraneous streaks that might happen to be connected to the cable cannot be removed at this stage.

In order to fill in the outline of the cable and connect any loose segments, the image is dilated using a circular structuring element with a radius equal to half of the thickness of the cable, Figure 4.23. This is the smallest radius which ensures that the opposite edges are joined together. As such, this radius minimises the risk of distorting the geometry by merging together sections of the cable that are momentarily next to each other in the image, even though they belong to distant parts of the cable.

Figure 4.23: Outline of the cable filled in using dilation.

After filling in the outline, the cable is thinned until stability is achieved. This method was used in [58] to determine the camber of steel slabs. The result is the medial axis of the cable, with any existing extraneous branches still attached. These branches can now be removed. First, the branch points are detected and a small circular area around them is erased, breaking the branches apart. The area erased around the branch points is three pixels wide to ensure that any contact between the cable and the branches is removed and the branches are indeed separated. Then, just like for the extraneous streaks, any branches shorter than the maximum expected displacement are deleted. This operation could not be executed in the previous step (in the elimination of the other streaks), because the outline of the cable could have been broken in several places, making it impossible to differentiate the unwanted branches from the actual outline of the cable.

The erased regions around the branch points are redrawn by dilating the image using a circular structuring element with a diameter of three pixels (the same that was used to break the branches apart) and, afterwards, applying thinning once more, Figure 4.24.

Figure 4.24: Medial axis of the cable completely extracted from the image.

It is essential to use a circular structuring element, and not any other shape, in order to achieve a smooth geometry after thinning.

Now, the medial axis of the cable is adequately defined. Using the calibration matrix determined in the calibration step of the experimental phase, the pixel coordinates are converted to model coordinates and the actual profile of the cable is obtained, Figure 4.25.

In Figure 4.25 it can be seen that there is a sharp bend in the cable in the point where it touches the ground. This bend would likely not have been captured with techniques using discrete tracking points and hardly recovered using interpolation.

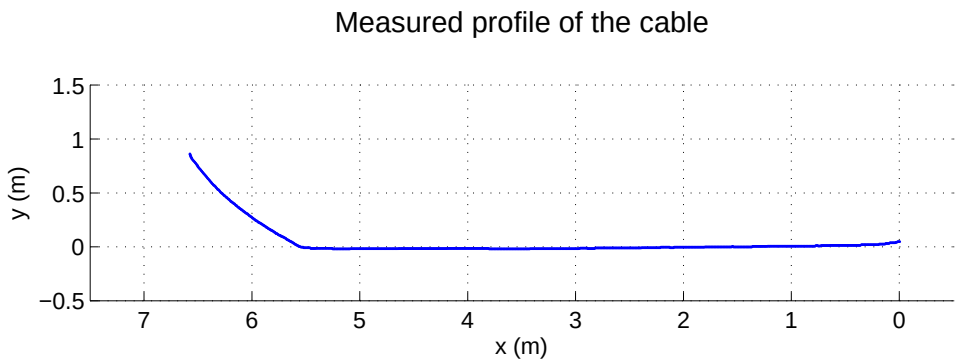

Figure 4.25: Cable profile calibrated to the model reference frame defined in section 4.4.1.

The medial axis of the cable is now used to define a new search region, to be applied in the next frame. If the cable has a certain maximum expected displacement between any two successive frames, then, from one frame to the next, it must be somewhere inside a region centred on the medial axis of the cable with a thickness equal to twice the maximum expected displacement. So, the medial axis of the cable, Figure 4.24 is dilated using a circular structuring element with a radius equal to the maximum expected displacement between two frames and the result is stored as a new mask, Figures 4.26.

Figure 4.26: New search region, automatically defined by the processing algorithm based on the medial axis of the cable.

The second frame is loaded and the entire process is repeated, but now the search region is updated automatically at the end of each cycle, based on the previous position of the medial axis of the cable. In this way, the search region is able to follow the cable. The same process is repeated recursively for the remaining frames of the video. A flowchart of the algorithm is shown in Figure 4.27 for a better understanding of the process.

During the experiments, some portions of the cable will inevitably come out of the water, especially near the top end, and the imaging system will not be able to see them. While these portions of the cable are out of the water, they cannot be tracked. However, as soon as they come back under water, they will be immediately detected: the search region is wide enough around the cable to encompass these portions that show up near the free surface.

After a first step where the user instructs the algorithm the position of the cable, the algorithm is able to follow it as it moves in the image and adjust accordingly. This is the key feature of this algorithm.

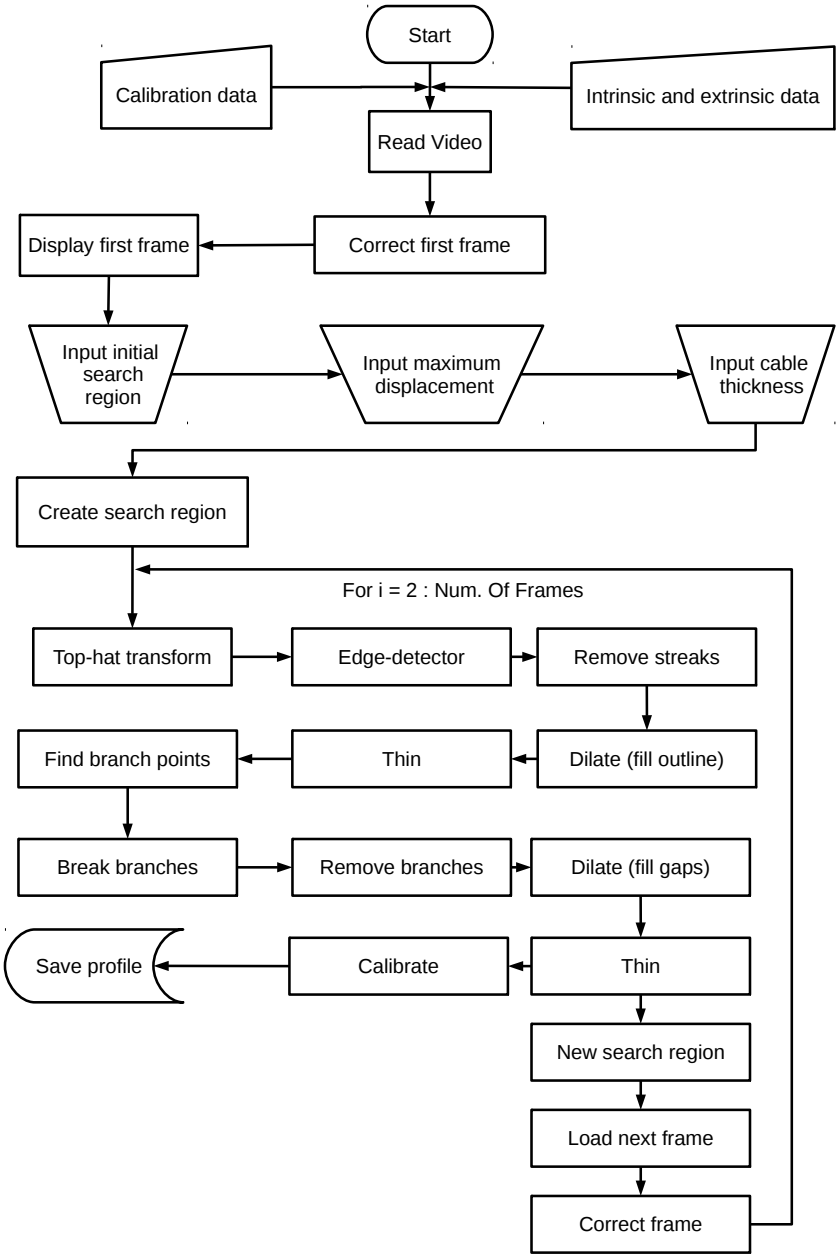

Figure 4.27: Flowchart of the algorithm used to process the videos.

4.6 Case Studies

To demonstrate the performance of the algorithm in non-optimal conditions, the vertical curtain was removed, Figure 4.28.

Notice the following three details: (i) the background is now much lighter than before, with varied shades in the area around the cable; (ii) there is one edge (the edge of the plastic film on the floor) that crosses the cable horizontally; and (iii) in the background, on the floor, there are some bricks on the right and a large black block on the left. In this set-up, two regular sea-states were tested: waves with a height $H = 0{,}04\,\text{m}$ and periods $T = 2{,}33\,\text{s}$ and $T = 1{,}14\,\text{s}$.

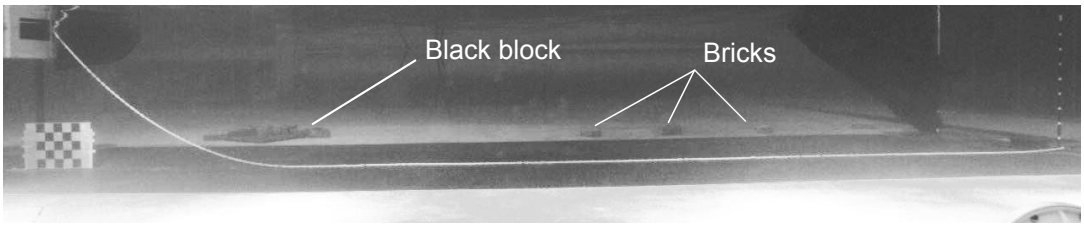

Figure 4.28: Experimental set-up after removing the curtain. The background has now several shades with varying intensity, random objects and distinct edges that might interfere with the algorithm. The image histogram has been modified to enhance visibility when printed.

In the waves with period $T = 2{,}33\,\text{s}$, the cable has moderate motions. Using the same settings as before (size of the structuring elements and expected displacement) to process a clip of this test, the cable is still correctly detected despite the poor visual conditions, Figure 4.29. This proves the suitability of the technique in low-quality contrast situations, but realistic experimental set-ups.

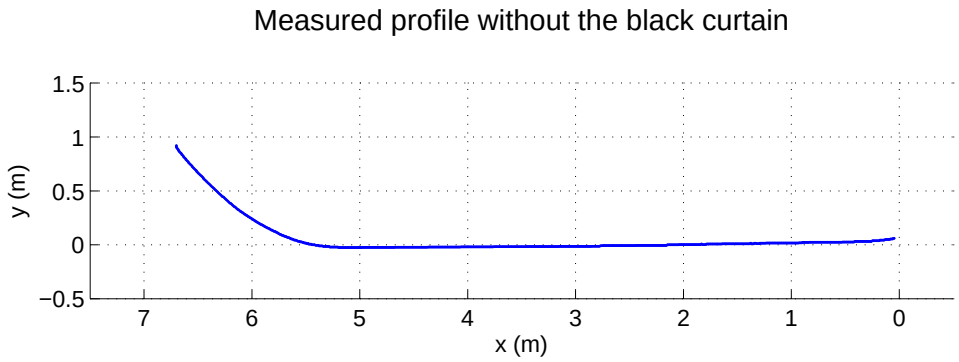

Figure 4.29: Detected profile of the cable in the experimental set-up without the vertical curtain, in waves with height $H = 0{,}04\,\text{m}$ and period $T = 2{,}33\,\text{s}$. Even though there are several perturbations in the background, the cable is fully detected.

In regular waves with period $T = 1{,}14\,\text{s}$, the buoy is close to resonance, as mentioned in section 4.5. The induced motions in the cable are so large that it crosses the corner of the black block, Figure 4.30, and the algorithm fails to detect the cable in this region, Figure 4.31.

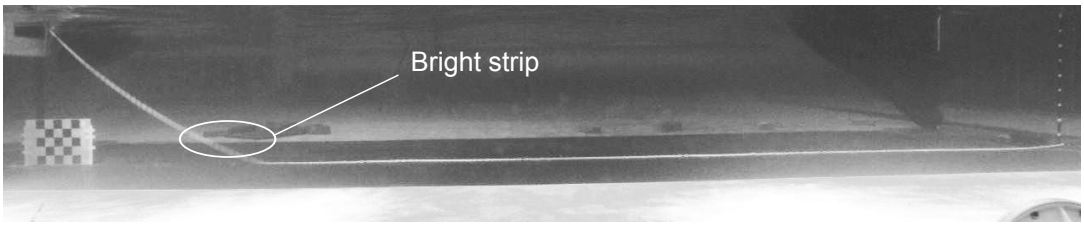

Figure 4.30: Interference of the non-uniform background. The area of the background between the plastic film on the floor and the black block is a bright strip that is merged with the cable when the top-hat transform is applied. The image histogram has been modified to enhance visibility when printed.

A narrow bright strip exists between the black film on the floor beneath the cable and the black block in the background. When the cable is close to this region, the narrow strip is picked up by

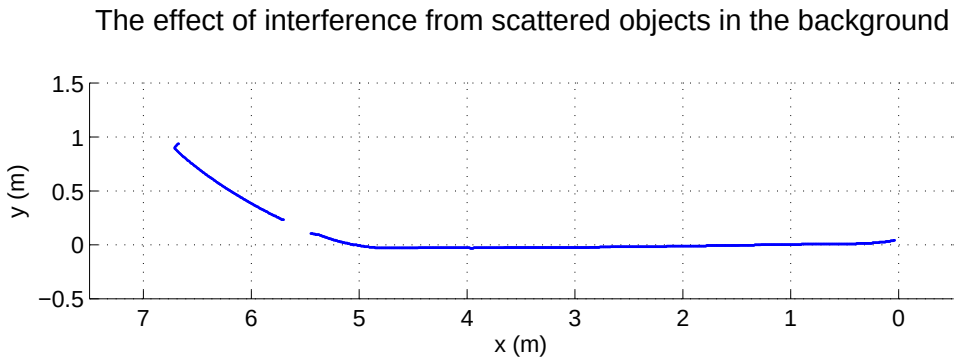

Figure 4.31: Gap in the detected profile of the cable caused by the interference of the background.

the top-hat transform, because the thickness of the strip is similar to the size of the structuring element used in the top-hat transform. The algorithm is now unable to distinguish the cable from the background and malfunctions. However, as the video progresses and the cable moves away from this strip, the algorithm resumes full detection without any intervention.

Comparing the results of the two test conditions presented, Figures 4.29 and 4.31, we can see that the only difference between the two is in the region of the narrow bright strip. This means that it is indeed the narrow bright strip that causes the failure and not the frequency nor the amplitude of the motions of the cable.

It is important to emphasise that the background objects in these experiments would not be present in an actual experiment; they were left as a test to the limits of the algorithm.

In conclusion, the algorithm is robust enough to perform well when the background is not ideal and the water is not absolutely clear (poor contrast), as long as there are no bright details with dimensions similar to the thickness of the cable in its vicinity (which does not seem to be a severe restriction).

4.7 Error Analysis

Although the technique presented is a proof-of-concept that has not been optimised, it is important to try to quantify its error and identify its sources. However, only simple error estimates can be provided. On the one hand, there is no analytical solution for the dynamics of a moving cable and numerical models have several simplifications and limitations; on the other hand, experimental data is lacking and that is the very problem that this technique seeks to solve. As a result, the error has to be estimated for a static situation. Since there was no practical way to measure the actual profile of the cable in the physical model, the data obtained using the tracking technique is compared with the solution of the inelastic catenary and with known coordinates of points in the physical model.

Figure 4.32 presents the profile measured with the technique and the profile of the inelastic catenary determined using the data from Figures 4.7 and 4.8. As it can be seen, the two profiles

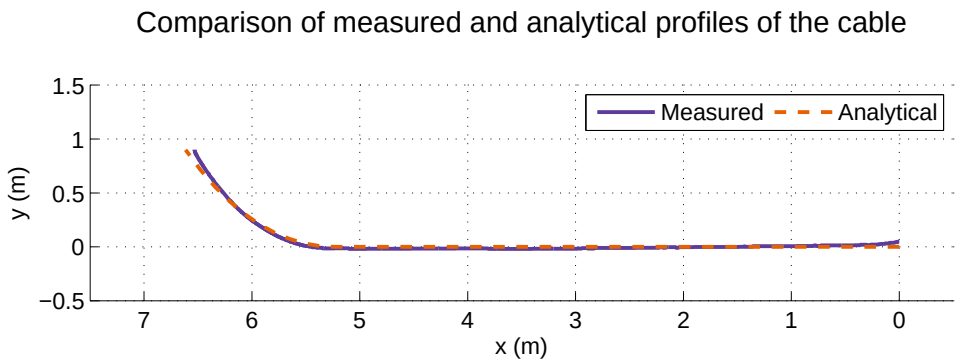

Figure 4.32: Comparison of the measured profile of the cable with the profile obtained from the equation of the inelastic catenary.

are almost identical. Because of the connection of the cable to the anchor in the experimental set-up, the anchoring point was around 0,05 m raised relative to the floor. This caused a small stretch of cable, between $x = 0{,}00$ m and $x = 0{,}25$ m to be suspended, while in the theoretical profile it is assumed that the cable is resting on the floor.

Also noticeable in Figure 4.32, as well as in Figures 4.25, 4.29 and 4.31, is a region, between $x = 2{,}0$ m and $x = 5{,}5$ m, where the cable has slightly negative vertical coordinates, indicating that it would be below the floor of the wave tank. This impossible situation is caused by the portion of the cable that is resting on the floor in the physical model wobbling around a mean position, instead of laying in a perfectly straight line while on the ground. The sections of the cable that are closer to the camera are represented in lower regions of the image which, when converted to physical model coordinates, correspond to negative vertical coordinates. However, this perturbation is not too significant.

In the whole span of the cable, the upper end point was the only one whose coordinates could be measured directly (the other point was the anchoring point, which, by definition, has coordinates $(0,0)$ m, see Figure 4.17). As such, this is the only point that can be used for an actual quantitative estimation of the error. The error is defined as the difference between the known and the measured coordinates in each direction.

The vertical coordinate of the upper endpoint was measured using a 1 m ruler to determine the water depth at the point where the cable comes out of the water and was $0{,}9000 \pm 0{,}0005$m. The abscissa (the horizontal distance between the buoy and the anchor) had to be measured at the water surface using a measuring tape and was estimated to be 6,615 m. Because the buoy was displaced while making the measurements (both by touching its hull with the measuring tape and by the waves generated by the operator making the measurements) and because of parallax errors, the abscissa can only be interpreted as a rough estimate of the actual coordinate. The coordinates determined for the upper endpoint using the tracking technique are $(6{,}5331; 0{,}9004)$ m resulting in a difference of 4×10^{-4} m (0,04 %) for the height and a difference of 0,08 m (1,2 %) for the abscissa. The difference in height is smaller than the uncertainty of ruler used to measure the actual height. As such, it is only possible to state that the measurement is within 5×10^{-4} m of the

real value, limited by the uncertainty of the direct measurement. For the abscissa, the difference is simply a rough estimate, with a large uncertainty. Note that the error is non-linearly distributed across the image and that these error estimates refer only to the upper endpoint.

The possible causes for the error are the following: the misalignment between the target and the plane of the cable, causing an incorrect re-projection of the image; the misalignment of the camera in relation to the optics of the watertight housing, distorting the image; the quality of the dome port, which also distorted the image; the linearisation being executed in a medium for which it was not envisaged; the selection, both in number and position, of the points used for calibration; the assumption that the profile of the inelastic catenary can describe the cable in the physical model; the uncertainty in the measurements of the dimensions of the cable in the physical model; and finally, the procedure used to determine the calibration matrix for the whole image, which assumed the conversion factors are constant across the image.

4.8 Discussion

After processing the videos, the geometry of the cable in each frame was obtained. This result is relevant on its own: it can be used to validate and calibrate numerical models; to determine the sections of the cable subject to wear near the touch-down point; to estimate the envelope of the displacement of the cables; for qualitative analyses of the most active regions of the cable; for correlations between the geometry of the cable and tension force, wave height, wave phase, water velocity, etc.

If the water velocity and acceleration are measured in synchrony with the video acquisition (for example, using particle image velocimetry) it becomes possible to estimate the hydrodynamic forces acting on the cable. This will be important for wave energy converters, where damping losses are to be minimised.

The self adjusting search region efficiently tracks the cable as it moves. It reduces the processing time, prevents the detection of unwanted features and is even able to detect the portions of the cable that come back under water. However, there is a drawback: because the search region is wider than the cable, it might expand from the point where the cable goes out of the water to include the reflections on the free surface. This will occur when the water is still, but tends to disappear once the surface is moving and the reflections break apart. A possible way to deal with reflections could be to disregard any point whose coordinates are above the still water level.

One of the biggest problems in the development and application of the technique was the poor visibility underwater, caused by suspended dust. Even though good contrast is required in any situation, the suspended dust forced the use of “heavy actions” in order to achieve it. This issue cannot be viewed as a limitation or failure of the technique. It is not reasonable to expect that a technique developed to be used in a laboratory, where test conditions should be rigorously controlled, works flawlessly in an inadequate environment. The positive side of this obstacle is that the technique developed proved to be robust and to work under unfavourable conditions.

The actions taken to improve the contrast may seem to be detrimental to the application of the technique, but it is not necessarily so. The paint coat applied to the chain was so thin that the submerged weight per unit length of the chain only changed from 1,24 N/m to 1,25 N/m, which can be neglected in most situations. The black sticker film on the floor is easy to obtain and apply and has no interference on the outcome of the experiment, unless bottom surface roughness is important. In this case, black paint may be used when preparing the surface. Depending on the visibility, there might be no need to enhance the contrast at all.

The black curtain was only used in the experiments to enhance visibility for the initial development of the technique, but it was shown that the algorithm is robust enough to work well even when the curtain is removed.

Even though the cases presented were essentially two-dimensional, this is not an inherent limitation of the technique. Measuring three dimensional motion requires at least two video cameras, but only one was available at this instance. The algorithm and the experimental procedure can easily be expanded to detect three dimensional motions using stereoscopy theory [79]. The camera calibration toolbox used in this work is also able to linearise and calibrate pairs of cameras for stereo-vision [83].

The algorithm is not limited to track a single cable. It was the large span of the cables that limited the number of cables that could be captured on video. It is entirely possible to define more than one search region and track multiple cables simultaneously. The algorithm imposes no limitation on this matter.

The error of the measurements is acceptable, around 0,0005 m (0,04 %) in the vertical direction and around 0,08 m (1,2 %) in the horizontal direction. It must be remembered that the objective of this work is to demonstrate the feasibility of the technique; an accurate error analysis requires improved optical equipment (including an additional camera to estimate three-dimensional motions) and optimisation of the photogrammetric procedures, objectives that were not pursued in this work.

Nevertheless, there is one important source of error that it is necessary to analyse: the use of a single matrix to convert pixel to model coordinates, as mentioned in section 4.7. This matrix was determined using a least squares fit, which minimises the total quadratic error of the fit across the image. It is assumed that, after linearisation and rectification, there are no distortions in the image. This was not the case here and, as a result, the conversion factors are not constant across the image. For example, using solely points B and C (Figure 4.17) on the target to determine the horizontal conversion factor, the result would be 0,0053 m/pixel. However, using points A and D, the factor would be 0,0056 m/pixel. The difference between the conversion factors might seem small, but with 1168 pixels between points A and D, the results after conversion will have a significant difference. Fixing this problem requires non-linear, local fitting procedures, that need to be developed for underwater applications.

The extracted profile of the cable will present a step-like appearance (see Figure 4.22). This is the result of digitizing an image into pixels and depends on the resolution of the camera. Smoothing operations, like LOWESS, could be applied to achieve a smoother result, but this comes at a

cost: the harder the smoothing, the more details are lost. Moreover, smoothing will affect mainly the regions where there are rapid changes in the profile of the cable, like in the touch-down point, Figure 4.25. As the algorithm is intended to capture fine details that are not detected using other techniques, smoothing would defeat the purpose of tracking the entire length of the cable and so it was not considered. Nonetheless, sub-pixel smoothing and interpolation, that preserves the details of the cable, may be important.

4.9 Conclusions

A technique to track mooring cables in physical models was presented. The technique combines existing photogrammetric methods and a video processing algorithm to determine the geometry of the mooring cables as a function of time.

Because the technique detects the whole length of the cables, all the singularities in the geometry of the cables were captured. This geometry of the cables may be used directly for qualitative analysis or be post-processed to obtain hydrodynamic data and other relevant information. This is important in situations where the motions of the cables must be well determined or when the cables undergo large deformations.

Since all the experimental steps were performed underwater, and there was no need for visual access through side windows in the wave tank, it was shown that the technique can be used even in complex physical models.

It was also demonstrated that the tracking technique is robust enough to perform well even when laboratory conditions are far from ideal. The requirements imposed on the experimental set-up *solely due to the usage of the technique* were modest and no more than what is usually done for any experiment; only few and simple adjustments were required for the technique to be applied.

Chapter 5

Physical Modelling of Mooring Configurations

5.1 Introduction

This chapter reports the most meaningful results of this work for the *short term* development of mooring systems for floating wave energy converters: the performance of different types of mooring configurations in physical model tests.

Three different types of mooring configurations were tested, based on the results presented in [3] and [11], Figure 5.1: (i) a compact (low-footprint) configuration consisting of a synthetic cable that is taut using a floater; (ii) a compact configuration composed of a synthetic cable, a floater and a clumpweight in a zig-zag geometry; and (iii) a chain catenary. For simplicity, the configurations will be denoted by CON1, CON2 and CAT, respectively.

The use of a floater in CON1 reduces the vertical loads on the wave energy converter and decouples the vertical motion of the converter from the horizontal motions of the mooring system [3]. Further adding clumpweights to CON1 to obtain a zig-zag geometry, CON2, creates a compliant configuration with a small seabed footprint and smaller dynamic tensions than the catenary [11]. The catenary, in turn, is the standard mooring solution, so it is a natural reference frame to compare the results of the compact configurations and it has been used in studies concerning wave energy converters [5, 7, 85]

The tests focused on how the different types of mooring systems behave relative to each other solely due to their geometry and load distribution. There was no study detailing the influence of a particular component of the mooring system. More specifically, the axial stiffness of the cables was chosen to be high enough for the axial stretching to be negligible.

The physical models, described in detail in section 5.3, had three mooring legs 120° apart around a cylindrical buoy, which represented a generic wave energy converter. This type of mooring arrangement was chosen because it is advantageous for arrays, allowing a high concentration of devices for a given area and the possibility of anchors to be shared by several devices. A similar

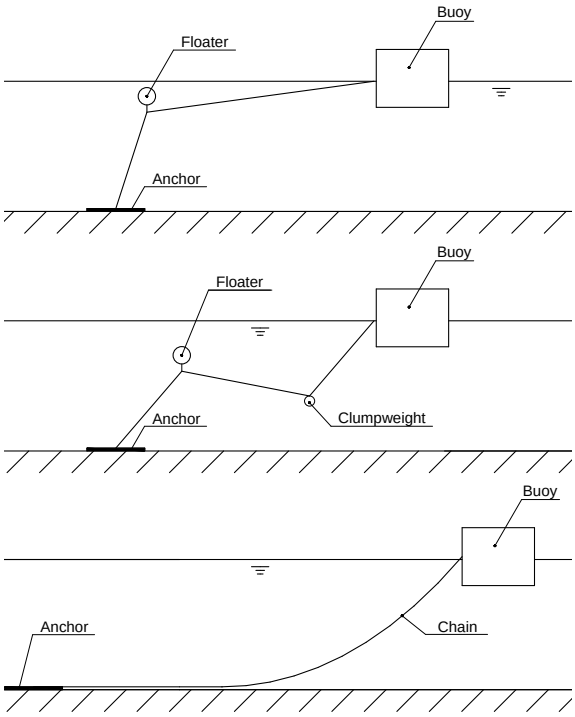

Figure 5.1: Schematics of the tested configurations: CON1 on the top, CON2 in the centre and CAT on bottom.

arrangement is studied in [85], using catenaries and in [86], for a configuration using a floater similar to the one presented in this work.

To design the mooring system, a procedure was developed, section 5.2, based on the guidelines for floating offshore oil and gas platforms, but with modifications adapted to the non-standard compact configurations.

Each configuration is evaluated based on its hydrodynamic coefficients, section 5.6.2, on the response amplitude operators, section 5.6.3 and on its behaviour in irregular waves, section 5.6.4. Rigorous experimental and analysis methods, described in sections 5.4 and 5.5 were used to obtain the maximum reliability for the results.

Some important simplifications were made in these experiments: there is no simulation of power take-off, no simulation of tide level variation and no simulation of arrays. In small scale models it is cumbersome or impossible to adequately model the power take-off [87, 88]: using Froude similarity, for a geometric scale λ_l, forces scale as λ_l^3 and power as $\lambda_l^{3,5}$. Besides this, introducing a power take-off would restrict the conclusions of the experimental work to devices with that specific power take-off principle, but the aim of these experiments is to study only the effect of the mooring configurations alone. The results can then be applied in the study of a particular case, knowing that the power take-off system increases the loads in the mooring cables and the surge displacements [50]. The variation of the mean sea level caused by tides was not modelled due to time restrictions; tests in arrays were not conducted due to limitations in space

and resources. Both of these parameters are expected to influence the behaviour of the device and of the mooring system.

The results presented here are part of a larger set of tests, including variations of each configuration for sensitivity analysis, which will the subject of a subsequent publication.

5.2 Mooring Design

5.2.1 Design Procedure

The design of the mooring system was adapted from the guidelines DNV-OS-E301 [47] and API RP-2SK [89] for the design of mooring systems for floating oil and gas platforms using catenaries. These guidelines establish limits on the maxima tension in the mooring cables and displacement of the platforms. To maintain geometric similarity with a prototype wave energy converter, the major restriction on the design is the limitation of the maximum displacement.

To start with, an analogy is made with the design of offshore platforms. In [49] it is suggested that, in the pre-design stage of a floating platform, the maximum horizontal displacement is not allowed to exceed 15 % of the water depth, in order to avoid damage to risers. Floating wave energy converters have no risers, but a similar limitation can be imposed, for example, to avoid damage to electrical connections. For the physical model tested in the experiments, the maximum allowed horizontal displacement, x_{max}, was set to 20 % of the water depth.

Out in the sea, a floating structure is subjected to wind, currents and waves. However, since the wave tank of the Faculty of Engineering of the University of Porto is only able to simulate waves, no account was made of current or wind loads. Only waves, which excite first order (wave frequency) and second order (permanent and slowly varying) forces, were accounted for in the design.

Following the guidelines [47] and [89], it was assumed that the mooring system had a negligible effect on the first order displacements of the buoy (those caused by the first order wave loads). The role of the mooring system is only to resist the permanent and slowly varying horizontal loads, limiting the horizontal displacements that they induce, x_s. Limiting the displacements due to first order wave loads, x_w, is achieved by the careful choice of the dynamic properties of the floating structure alone: inertia, hydrodynamic stiffness and damping. In the end, the sum of the first and second order displacements must be smaller than the maximum allowed displacement x_{max}:

$$x_{max} \geq x_s + x_w \tag{5.1}$$

Due to several constraints, the dimensions and dynamic properties of the buoy were selected before the design of the mooring system, as explained in section 5.3. Since x_{max} is imposed and x_w depends solely on the properties of the buoy, which are already defined, the problem of designing

the mooring system is that of determining the maximum allowed x_s:

$$x_s \leq x_{max} - x_w \tag{5.2}$$

and then of calculating the necessary stiffness of the mooring system to prevent x_s from being exceeded.

The first order wave displacements were estimated in regular waves with the expected maximum wave height of the design sea-states, for a range of different periods, simulated using linear potential theory (the formulation presented in [77]). The design value of x_w was set to the maximum horizontal displacement obtained in the simulations.

As there were no second order codes available to estimate the slowly varying loads, F_{xs}, these were not determined explicitly. Instead, they were accounted for in the determination of the horizontal mean drift loads, F_{xp}, using the approximation presented in [38], for a surface piercing cylinder with radius r in regular waves with height H:

$$F_{xp} = \frac{2}{3}\rho_w g \left(\frac{H}{2}\right)^2 r \tag{5.3}$$

where ρ_w is the water density and g is the magnitude of the acceleration of gravity. To account for the slowly varying loads in irregular waves, the wave height used in Equation 5.3 was an increased value of the largest significant wave height of the design sea-states, which will be termed H_s^*. The result was an approximate value of the magnitude of the permanent and slowly varying wave forces. The design calculations are summarised in annex A.

In the case of the catenary, it must be ensured that, in the most severe event, there are no vertical forces at the anchor, meaning that the chain can never be fully lifted. The selection of a chain that would fit this and the previous requirements was aided by the charts and data provided in [49] for the pre-design of catenary mooring systems.

The compact configurations are non-standard and so there are no guidelines or empirical data to further assist in their design. To solve this problem, some restrictions were imposed on the design of the configurations, defining their requirements and ensuring a fair comparison between them:

a) all configurations should have, as much as possible, the same horizontal reaction force for the maximum allowed second order displacement x_s;

b) in the compact configurations, the buoyancy force of each and every floater should be the same and, if applicable, equal to the magnitude of the submerged weight of each and every clumpweight;

c) the buoyancy of the floaters should be the same for both compact configurations;

d) for the compact configurations, the horizontal distance from the anchor to the buoy should be the same;

e) the compact configurations should use, as much as possible, the same materials, lengths of cable and position of floaters;

f) in the compact configurations, the design should guarantee, as much as possible, that the floaters never come out of the water and, if applicable, that the clumpweights never touch the floor;

g) to take advantage of the reduced dimensions of the compact configurations, the distance from the anchor to the buoy should be twice the water depth;

h) the catenary is allowed to have a larger anchor-to-buoy distance and length of cable than the compact configurations due to its working principle.

Restriction a) is a consequence of the design procedure described above, that should be applied to all configurations; restrictions b), c), d) and e) are applied for symmetry reasons and to reduce the factors that might induce unexplained variability in the results; restriction f) is imposed to avoid sudden losses of restoring force and tension in the cables, resulting in large displacements of the buoy with probable snap loads in the cables; restriction g) is an *ad hoc* imposition and restriction h) comes from the nature of a catenary mooring system and cannot be avoided. Considering these rules, it was then possible to design adequate compact configurations and to have a fair comparison between the three different configurations.

Instead of the simplified method presented above, a more sophisticated approach could have been used, carrying out time-domain dynamic simulations of the floating wave energy converter coupled to the mooring system. This would be justified for the design of an actual full-scale mooring system or for an optimization problem, but not for the purpose of these experiments. The objective here is a comparative assessment of the behaviour of different mooring configurations in general. The only requirements are that the configurations have designs that can be compared in a fair way, while avoiding major flaws that might mask the quality of the results. A simple design procedure is acceptable, as long as it is scientifically reasonable and applied for all the test cases. The additional work of preparing a complex numerical model and the time required for each simulation would be unreasonably high in view of the expected outcome.

5.2.2 Design Data

The extreme sea-states selected for the design of the mooring system were based on the conditions of the Portuguese Pilot Zone (a region off the West coast of Portugal near Figueira da Foz) taken from [10] and are presented in Table 5.1.

A JONSWAP spectrum with a shape parameter $\gamma_J = 3{,}3$ was used to represent the irregular sea-states, as will be detailed in section 5.2.2. The peak periods (T_P) of the survival sea-states were estimated from the zero-crossing periods (T_z) using the relation $T_P = 1{,}287T_{02} = 1{,}287T_z$, where T_{02} is a spectral moment parameter used as an approximation to T_z for narrow-banded spectra, [90]. Two operational sea-states were also selected using the data from [91], by choosing the ones

Table 5.1: Considered irregular sea-states in prototype scale.

	Prototype		
Type	H_s (m)	T_z (s)	T_P (s)
Operational	3,0	-	9,0
Operational	3,0	-	13,0
Survival	8,6	9,0	11,6
Survival	9,5	11,0	14,2

with the most available energy (combined power and probability of occurrence) offshore Figueira da Foz, Table 5.1. A detailed description of this is given in Annex B. As in [10], a water depth of 90 m was assumed to be characteristic of the location.

5.3 Experimental Set-up

Due to the wave tank dimensions and to the limitations of the wave generator for long and high waves, the model was built using a geometrical scale $\lambda_l = 1/100$, resulting in a water depth of 0,900 m. As is customary for wave dynamics [92], the characteristics of the sea-states were scaled using Froude similarity, Table 5.2.

Table 5.2: Irregular sea-states in model scale. OP - operational; SURV - survival.

	Model	
Type	H_s (m)	T_P (s)
OP1	0,030	0,90
OP2	0,030	1,30
SURV1	0,086	1,16
SURV2	0,095	1,42

The geometrical scale used to build the buoy was $\lambda_l = 1/50$, twice the scale of the remaining components of the model, $\lambda_l = 1/100$. Using the scale $\lambda_l = 1/100$, a typical floating point absorber with a diameter of 20 m would have a model diameter of only 0,200 m. Its motions and the tension forces in the cables would be too small to be measured with an acceptable accuracy. With a larger scale applied to the buoy, its diameter was 0,500 m and its motions and tension forces became larger. This decision was based on the results of previous experiments simulating a floating point absorber, where the motions and forces were so small that the measurements had low precision [74]. The scale distortion was deemed acceptable because the experiments did not intend to reproduce any existing concept.

The buoy was composed of a cylindrical hull of fibre-reinforced plastic and an inner ballast made of rubber, Figure 5.2. Around the bottom of the hull there was a slight bulge, Figure 5.3, and so its shape deviates slightly from that of a perfect cylinder. However, this imperfection is not too large.

In [54] it is advised to test extreme sea-states near the resonance periods of floating wave energy converters. To comply with this recommendation, the ballast was designed so that the

(a) (b)

Figure 5.2: Photographs of the hull (on the left) and of the rubber ballast (on the right).

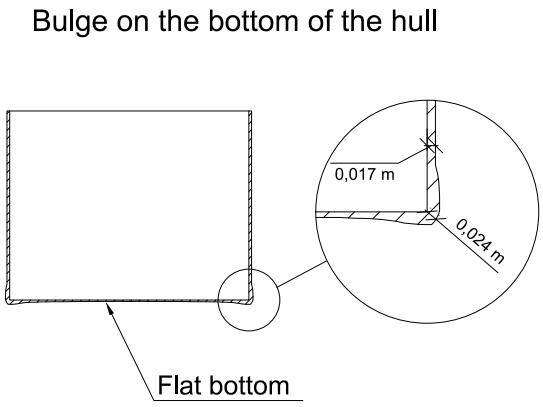

Figure 5.3: Cross section of the hull of the buoy showing the bulge. The deformation caused by the bulge on the bottom is not significant when compared with the regular thickness of the hull.

natural periods of the free buoy in heave and pitch were close to the peak period of the sea-state SURV1. Contrary to what would probably be expected, the resonance periods of the buoy were not intended to be close to the peak periods of the operational sea-states. This reflects the fact that, unless good control strategies are developed, a device will not always be able to operate in the most favourable sea-states for power extraction. In the particular case of the region modelled in this study, there would be at least two important operating conditions (OP1 and OP2) and the device cannot have optimal performance at both of them. This can also be interpreted as the device being optimised to have an overall good performance over a range of different sea-states with high energy content, instead of being tuned for a particular sea-state.

The properties of the buoy, *excluding any extra fixture or adapter*, are shown in Table 5.3, where the position of the centre of gravity y_{cg} is given relative to the flat bottom. The position of the centre of gravity and the inertia around horizontal axis through the centre of gravity I_{cg} were

determined experimentally using the procedures described in [75], to ensure maximum accuracy of the measurements. A detailed description of these procedures is given in Annex C.

Table 5.3: Properties of the buoy. - mass; D_b - diameter; H_b - height.

m_b	D_b	H_b	I_{cg}	y_{cg}
35,50	0,515	0,400	0,87	0,0758
$\pm$0,05 kg	$\pm$0,002 m	$\pm$0,002 m	$\pm$0,02 kg m^2	$\pm$0,004 m

Millimetre paper rulers were glued to the hull in four different positions to allow the free-board, f, and the draft, d_b, to be measured, Table 5.4.

Table 5.4: Draft of the buoy for each configuration.

	Free	CON1	CON2	CAT
d_b ($\pm$0,003 m)	0,176	0,177	0,189	0,180

The design of the mooring configurations was carried out after determining the dimensions of the buoy, Figure 5.4. The layout of the mooring legs is shown in Figure 5.5. In order to resist the permanent and slowly varying forces and to keep the horizontal displacement of the buoy within 20 % of the water depth, the required horizontal stiffness of the mooring system was estimated to be 41,0 N/m. Detailed information on the design of the configurations is presented in Annex A.

The pre-tension in the mooring system for each configuration is presented in Table 5.5 and the total mass of each configuration as built is presented in Table 5.6

Table 5.5: Pre-tension in the cables.

	CON1	CON2	CAT
Cable 1	(2,8 $\pm$ 0,2) N	(10,6 $\pm$ 0,2) N	(3,0 $\pm$ 0,2) N
Cable 2	(3,1 $\pm$ 0,2) N	(11,0 $\pm$ 0,2) N	(3,1 $\pm$ 0,2) N

Table 5.6: Mass of the mooring configurations. CAT* accounts only for the portions of the chains suspended when in rest position.

	CON1	CON2	CAT	CAT*
Mass (kg)	0,790 $\pm$ 0,002	3,936 $\pm$ 0,002	3,045 $\pm$ 0,001	0,875 $\pm$ 0,001

Originally, the mooring configurations were designed for two-dimensional experiments with only two mooring legs, opposite to each other. It was only after the mooring system was designed that it was decided to test the triangular arrangement for the mooring legs shown in Figure 5.5. The dimensions of the mooring legs were not adjusted for this, which led to the mooring configurations having a somewhat lower horizontal stiffness than what was established in the design phase. In either case, it was not possible to have the stiffness of the three configurations exactly matching each other due to the guidelines established in the previous sections and due to limitations in the material available to build the models.

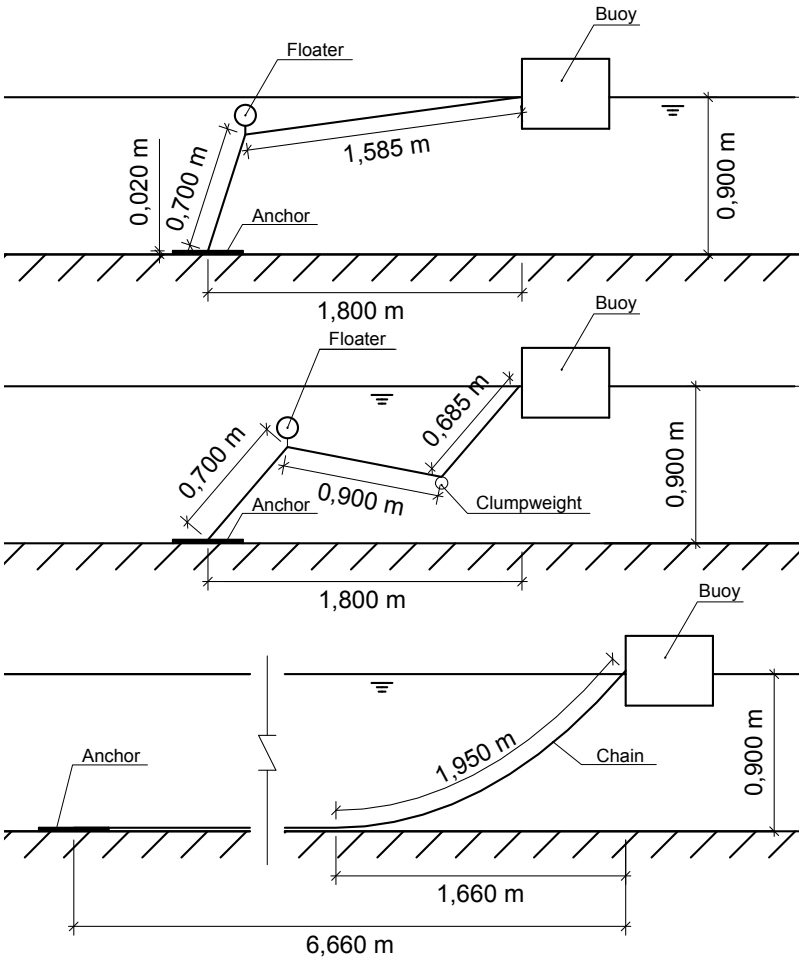

Figure 5.4: Dimensions of the mooring configurations.

In order to obtain the required secant stiffness of $4{,}10\,\mathrm{N/m}$ for the compact configurations, the magnitude of buoyancy of the floaters and of the submerged weight of the clumpweights should be $10{,}0\,\mathrm{N}$. Hollow acrylic spheres were used to build floaters and lead fishing weights were used for the clumpweights. Small weights were added to the acrylic spheres and to the clumpweights in order to calibrate, respectively, their buoyancy and their submerged weight to the desired values. Figure 5.6 shows the elements of one of the mooring legs of CON2, which contains all of the components used in the compact configurations. Tables 5.7 and 5.8 summarise the properties of the floaters and of the clumpweights after building and calibration.

Table 5.7: Properties of the floaters. Indexes 1, 2 and 3 refer to the cable where the floater was installed.

	Mass (kg)	Buoyancy (N)	Diameter (m)
F1	$0{,}252 \pm 0{,}001$	$9{,}97 \pm 0{,}06$	$0{,}135 \pm 0{,}003$
F2	$0{,}276 \pm 0{,}001$	$10{,}05 \pm 0{,}06$	$0{,}135 \pm 0{,}003$
F3	$0{,}232 \pm 0{,}001$	$9{,}96 \pm 0{,}06$	$0{,}135 \pm 0{,}003$

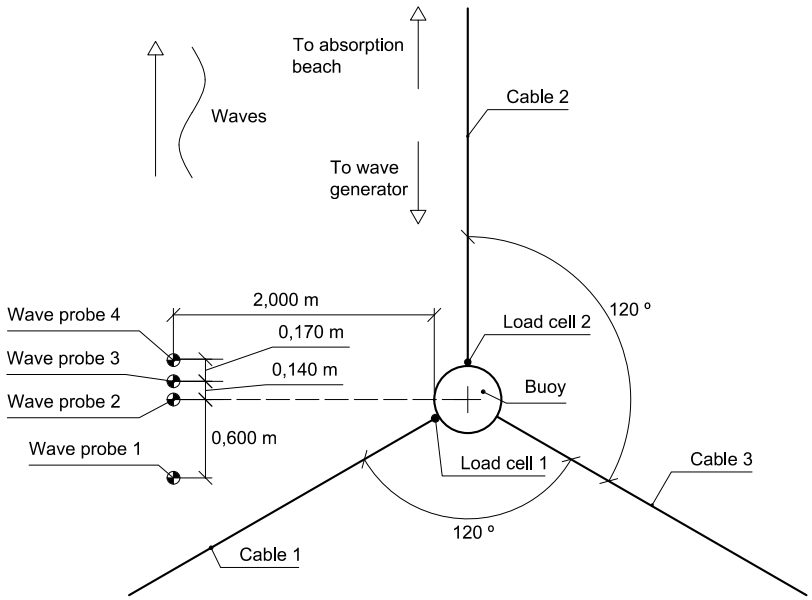

Figure 5.5: Top view of the experimental set-up.

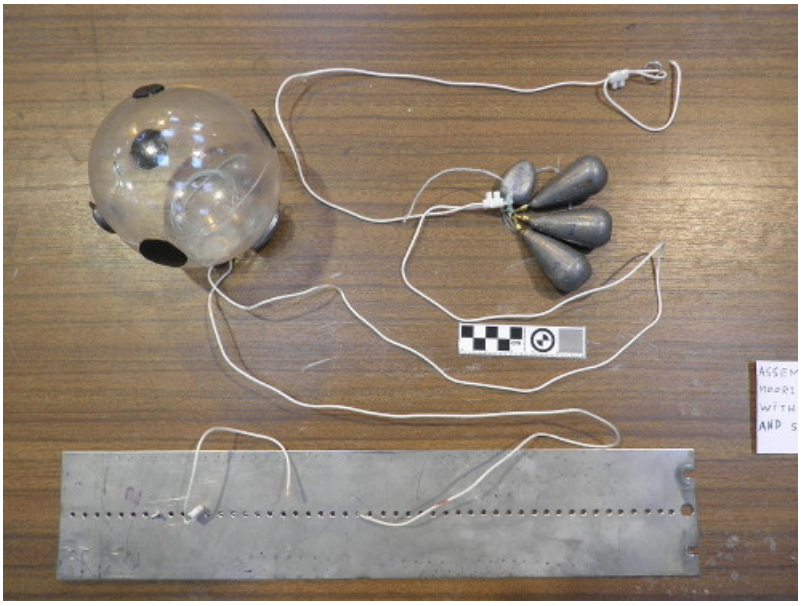

Figure 5.6: Fully assembled components of a mooring leg of CON2. All the mooring components used in the compact configurations are shown: the mooring cable with the acrylic floater and calibration weights (on the top left), the fishing weights used for the clumpweights (on the top right), and the anchor plate (on the bottom).

In the case of CAT, the required horizontal span of the cable according to the procedure described in [49] was 5,737 m. However, in the physical model, CAT had span of 6,66 m, which is 0,923 m longer than required. This extra length of chain was added for practical reasons: to anchor the chain close to the walls of the wave tank. This increased span of the chain is judged to have little interference in the experiments. In the worst case design scenario, the lift-off point

Table 5.8: Properties of the clumpweights. Indexes 1, 2 and 3 refer to the cable where the clumpweight was installed.

	Mass (kg)	Submerged weight (N)
W1	$1{,}115 \pm 0{,}001$	$9{,}968 \pm 0{,}001$
W2	$1{,}125 \pm 0{,}001$	$10{,}051 \pm 0{,}001$
W3	$1{,}113 \pm 0{,}001$	$9{,}959 \pm 0{,}001$

of the chain should be at a distance of 5,737 m from the buoy, so the extra length of cable would be resting on the floor. As both the theoretical and the actual spans of CAT are significantly larger than the span of compact configurations (1,80 m), the extra length will not affect the ranking of the configurations in this particular point.

The cable in the compact mooring configurations was made of polyester with a braided sheath and a parallel strand core, Figure 5.7, and its properties are presented in Table 5.9. This type of cable was chosen because it had negligible extension and bending stiffness in the range of tension forces anticipated, and so elasticity would not be a significant variable in the outcome of the tests.

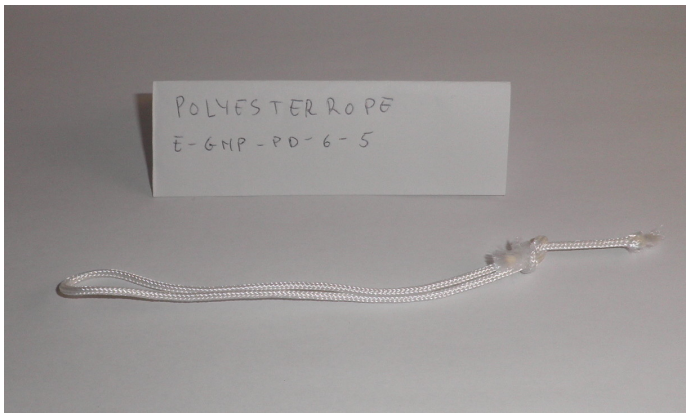

Figure 5.7: Sample of the synthetic cable used for the compact configurations.

Table 5.9: Properties of the synthetic cables.

EA (N)	m_l (kg/m)	γ_l (N/m)
$(1{,}6 \pm 0{,}3) \times 10^5$	$(3{,}2 \pm 0{,}2) \times 10^{-3}$	$(8{,}0 \pm 0{,}2) \times 10^{-3}$

The chain used to model CAT was made of zinc plated steel, Figure 5.8 and its properties are presented in Table 5.10. It was selected, among the commercially available sizes, to be the one with the lightest weight per unit length that could both prevent excessive displacements and have a span that could fit in the wave tank. The acquisition of the appropriate chain to build the model cannot be separated from the design stage, since the design depends on knowing the characteristics of the available chains.

There is a large uncertainty in the values of the axial stiffness because the laboratory tasked with conducting the tensile tests on the samples did not have the appropriate equipment to test

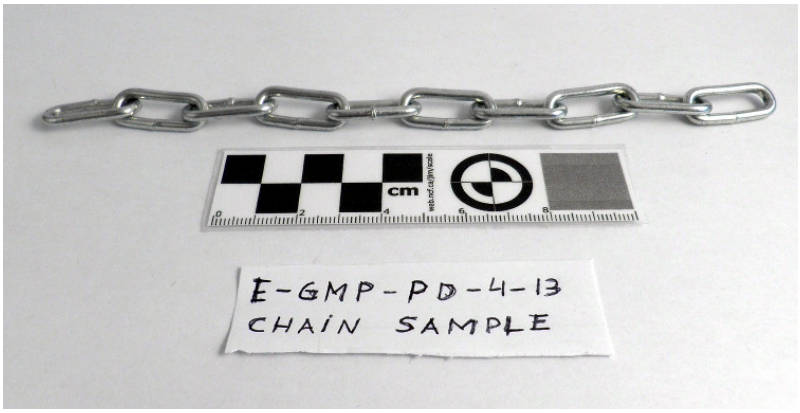

Figure 5.8: Sample of the chain used in the CAT mooring.

Table 5.10: Properties of the chain.

Parameter	Value
EA	$(1{,}6 \pm 0{,}7) \times 10^6$ N
m_l	$(0{,}1447 \pm 0{,}0001)$ kg/m
γ_l	$(1{,}243 \pm 0{,}006)$ N/m
Link inner length	$(2{,}064 \pm 0{,}007) \times 10^{-2}$ m
Link inner width	$(5{,}72 \pm 0{,}07) \times 10^{-3}$ m
Link thickness	$(2{,}99 \pm 0{,}05) \times 10^{-3}$ m

cables and the procedure used was not rigorous. More details on this are provided in Annex D, section D.9.3.

Steel blocks were used as gravity anchors for the mooring systems, Figure 5.9. Each block was 0,50 m wide by 0,50 m deep by 0,02 m high and weighed around 333 N underwater. At the anchor, the cables were fixed to a removable stainless steel plate to allow the quick exchange of the mooring system and anchoring point without the need to move the anchors, Figures 5.6 and 5.9.

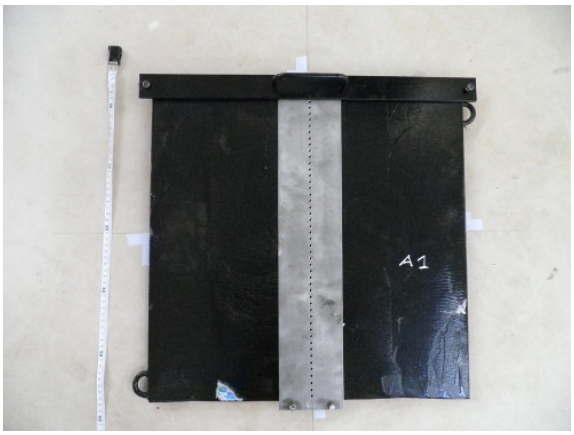

Figure 5.9: Top view of the anchor with its removable anchor plate (the silver grey plate in the centre).

The cables were connected to the buoy using adapters bolted on the sides of the hull, Figures 5.10, which had a mass of $(0{,}0572 \pm 0{,}0018)$kg. The attachment point of the cables was located 0,220 m from the top of the buoy and 0,015 m from the surface of the hull.

Figure 5.10: Adapters used for attaching the cables and load cells to the buoy. On the left side of the adapter a pulley is installed that was meant to guide the cable to the load cell, which would be fixed to the right side of the adapter. However, this arrangement was abandoned.

Load cells, Figure 5.11, were installed at the top-end of the left seaward cable and of the leeward cable as shown in Figure 5.5. The right seaward cable was not instrumented because it was assumed, due to symmetry, that the tension would be the same as in the left seaward cable. The length of the cables where the load cells were installed was adequately shortened to account for the length of the load cells and their accessories.

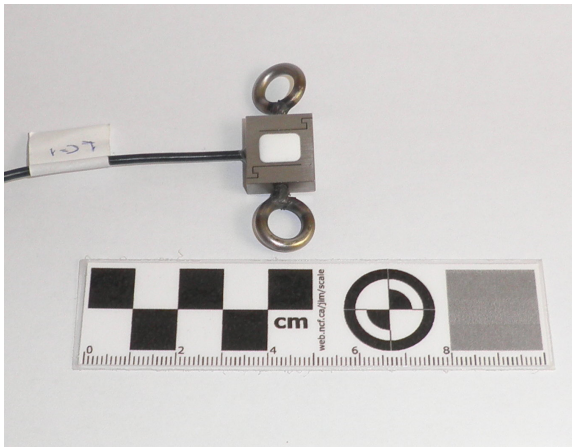

Figure 5.11: Load cell (the small steel square) used to measure the tension force in the mooring cables, with the holding rings (used to connect the load cell to the cable and to the adapter) screwed in.

Initially, it was planned for the load cells to be screwed to one end of the adapters, remaining fixed relative to the buoy, and for the mooring cables to go through the pulley shown in Figure 5.10, before being attached to the load cells. This would both keep the load cells out of the water (to avoid submergence effects) and the direction of the tension force aligned with the sensing axes of the cells. These issues caused problems in the measurements of the tension forces in the

work reported in [74]. However, preliminary tests determined that the friction in the pulleys was unacceptably high, so it was decided to flip the adapters upside down, Figure 5.12, and install the load cells *inline*, Figure 5.13. The impact of having the load-cells inline is judged to be minimal, since their length, including accessories, was 0,046 m, their mass was only $(0{,}0141 \pm 0{,}0001)$ kg and the signal cables were quite thin and flexible. Due to their S-type construction, the effects of submergence of the loads cells on the tension force readings was verified to be minimal.

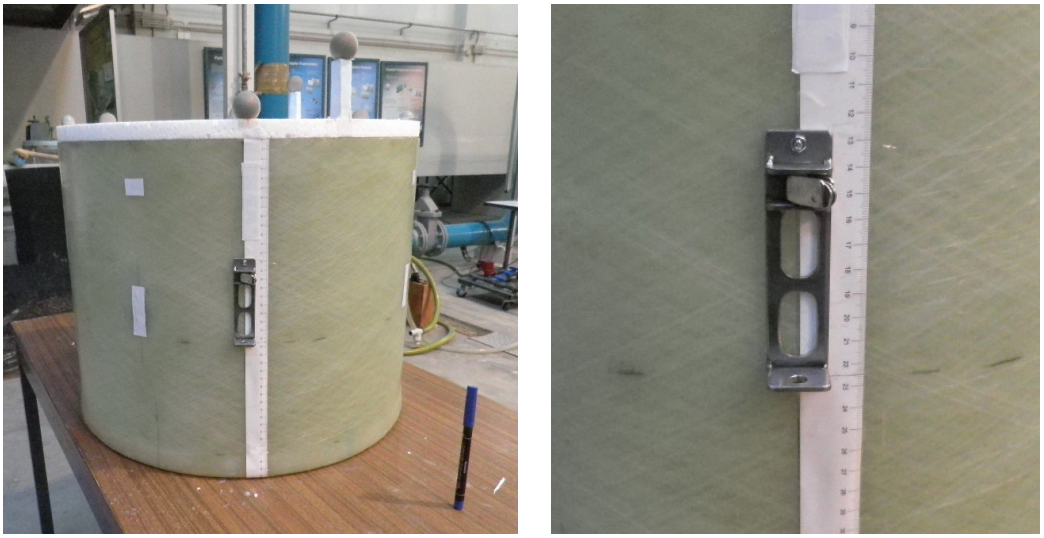

(a) (b)

Figure 5.12: Installation of the adapter on the buoy. (a) general view of the adapter; (b) detailed view of the adapter, showing its orientation and position.

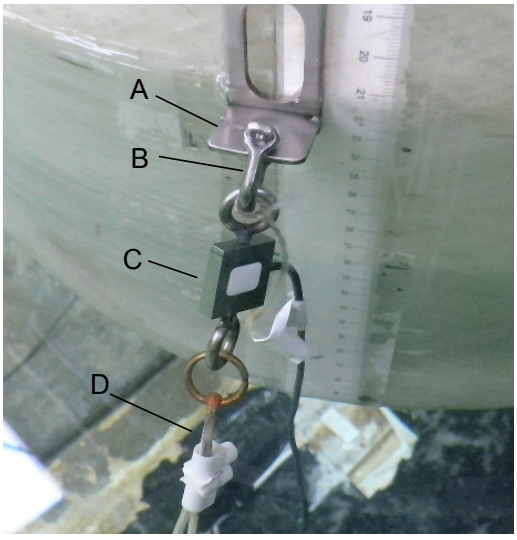

Figure 5.13: Inline assembly of the load cell. A - load cell adapter; B - shackle securing the load cell to the adapter; C - load cell; D - mooring cable.

To measure the wave height, resistive wave probes were installed as shown in Figure 5.5. The spacing of the probes was selected using the method of Mansard and Funke for analysis of wave reflections, as described in the data analysis software manual [93].

The motion of the buoy was measured with an infra-red motion capture system. This system uses infra-red cameras to emmit infra-red light and record the reflections from extremely lightweight infra-red markers. Two of these cameras were positioned above the wave tank (one seaward of the buoy and one leeward) and infra-red markers were placed on the buoy's lid, Figure 5.14.

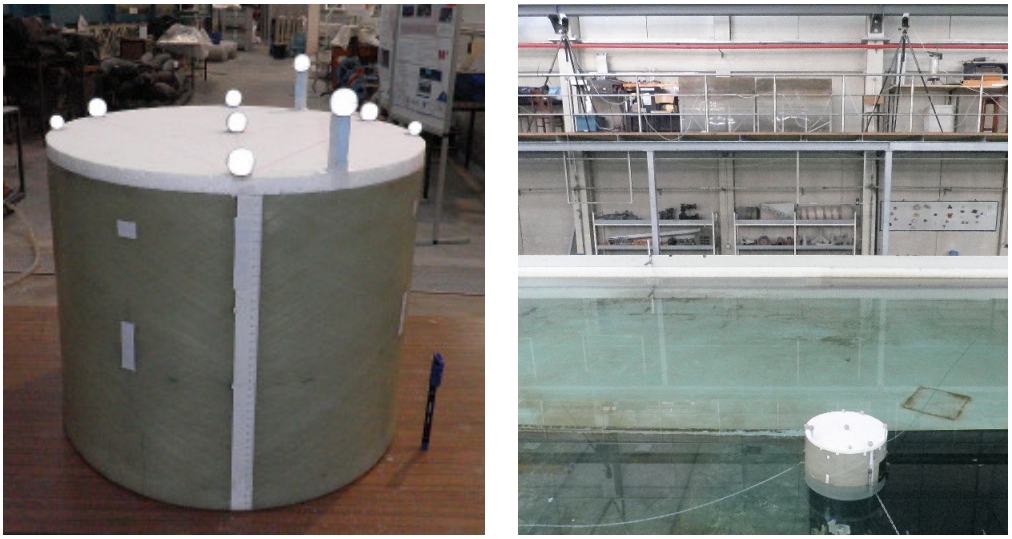

(a) (b)

Figure 5.14: Infrared system used to track the motions of the buoy: (a) markers; (b) infra-red cameras standing on tripods on the upper catwalk.

A panorama view of the fully assembled experimental set-up for CON1 is shown in Figure 5.15. Close up views of CON2 and CAT, also when assembled in the wave tank, are shown in Figure 5.16.

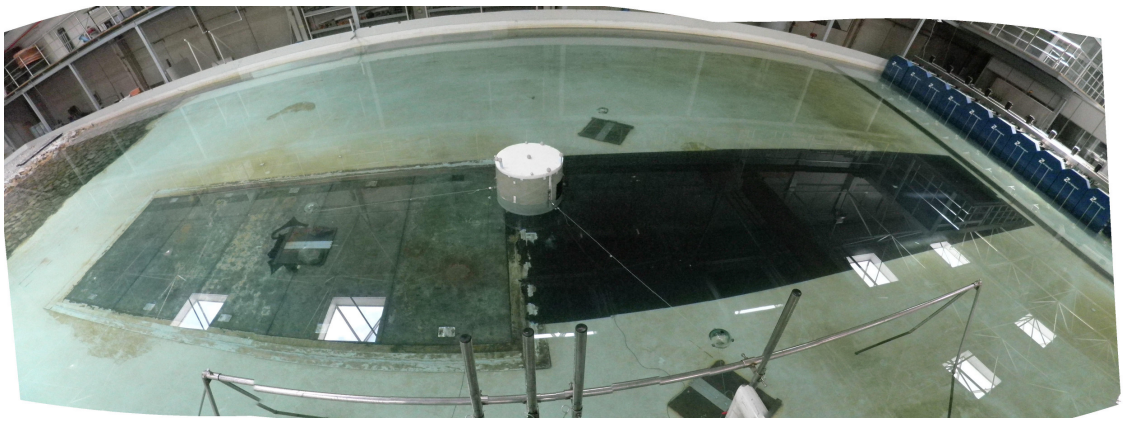

Figure 5.15: Panorama view of the experimental set-up for CON1. The model is in the centre. On the left of the photograph is the absorption beach and on the right is the wave generator. On the bottom of the photograph are the bars that hold the wave probes.

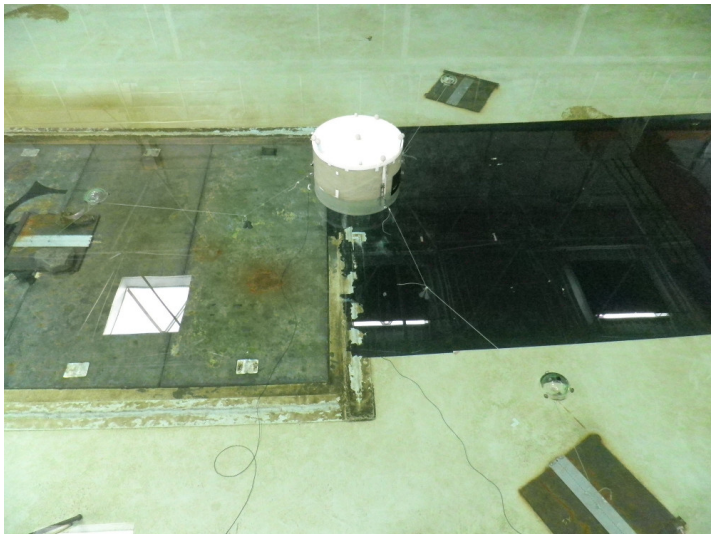

(a) CON2.

(b) CAT.

Figure 5.16: Photographs of the tested configurations assembled in the wave tank.

All the sensors (load cells, wave probes and motion capture) were synchronised and their data recorded in the same computer and software; however, while the motion data was recorded directly in engineering units, the data from the load cells and from the wave probes had to be recorded in analogue mode (more precisely, as voltage). Post processing was required to convert the analogue data to the proper units. A detailed uncertainty analysis for the data conversion is presented in Annex D.

Extreme care was taken in the measurement of the properties and in the calibration of the components of the model and of the measuring equipment. This included not only the careful measurement of the properties and quantities themselves, but also the design and preparation of the measuring procedures in order to have the greatest accuracy and most reliable uncertainty quantification. The details concerning these matters are described in Annex D and were based on the methods proposed in [54, 75, 94].

5.4 Experimental Methods

Four types of tests were conducted: i) quasi-static displacement tests, to determine the load-excursion behaviour of the mooring systems in surge; ii) decay tests, to determine the natural periods of the buoy-mooring system and *estimates* of the hydrodynamic parameters; iii) regular wave tests, to determine the response amplitude operators and non-linear effects; and iv) irregular wave tests, to determine the behaviour of each mooring configuration under realistic loading conditions. The generated waves were long-crested, propagating in a direction parallel to the plane of the leeward mooring cable, Figure 5.5. In this situation, the sway, roll and yaw degrees of freedom do not have significant excitation forces and the motion of the buoy is effectively reduced to the surge, the heave and the pitch degrees of freedom.

The quasi-static displacement tests were performed using a string to slowly pull the buoy horizontally in direction of the x axis, Figure 5.5 (the direction of the leeward mooring cable), and then slowly releasing the buoy back to rest position. This was done for the leeward and for the seaward direction of the model. Particular care was taken during the tests to prevent the pulling force on the string to rotate the buoy around the pitch axis.

In the decay tests, the buoy was displaced from its equilibrium position in a single degree of freedom and then released. This was done for the surge, heave and pitch degrees of freedom, each one at a time. Each test was conducted at least fifteen times in order to reduce the uncertainty in the measurements.

In the regular wave tests, waves were generated with twenty different periods ranging from $T = 0{,}80\,\mathrm{s}$ to $T = 2{,}33\,\mathrm{s}$ (in model scale). Around the expected resonance peaks of the system, the wave periods were closely spaced in order to obtain a good resolution. This was done for two target wave heights: $H = 0{,}04\,\mathrm{m}$ and $H = 0{,}08\,\mathrm{m}$ (in model scale), in order to study non-linear effects on the behaviour of the buoy-mooring arrangement. The tests lasted 270 s in order to record

at least 100 waves for the longest periods and to allow for the initial transients to die out. Each test started with the buoy in rest position, with minimal or no movement at all.

Prior to setting up the model, the regular sea-states were calibrated in order to have the average wave height as close as possible to the target wave height. This was done by adjusting the gain of the wave generator, a magnifying factor of the target wave height. However, the need to improve the resolution of the response amplitude operators around the resonance peaks, required some regular sea-states to be defined during the experiments and run without having been previously calibrated. As a consequence, the average wave height of some of these regular sea-states is somewhat different from the desired value. To partially compensate the lack of calibration, the gain of these uncalibrated sea-states was estimated based on the gain of the calibrated sea-states with the closest periods.

The irregular wave tests used the sea-states mentioned in Table 5.2. Their duration was set to the equivalent of at least three hours in prototype scale (10 800 s) as recommended in [47] and [54], which, scaled to model values using Froude similarity (for $\lambda_l = 1/100$, the time scale is $\lambda_t = 1/10$), resulted in a duration of 1080 s. In order to obtain sufficiently resolved spectra in post-processing, see section 5.5, the duration of the tests was increased to 1575 s [84]. A JONSWAP spectrum was used for the generation of the sea-states with a shape parameter $\gamma_J = 3.3$, because it leads to waves with greater steepness, as recommended in [54]. Since a pseudo-random method was used to generate the irregular sea-states, the length of the sea-state repetition cycle (do not confuse with the test duration) of the wave generator was set to be 1843 s [93]. This was the smallest possible cycle length that the wave generator could create which would not be smaller than the test duration [95].

Still in accordance with the recommendations proposed in [54], the execution of both regular and irregular sea-states was conducted in a random order to reduce the bias effects on the experiments and selected regular sea-states were repeated to assess the repeatability of the experiments.

All the tests requiring waves were run with active absorption to ensure the maximum quality of the generated wave conditions.

To achieve a good time resolution and allow the removal of electro-magnetic interference, the acquisition frequency of all sensors was 100 Hz. According to [93], the maximum excitation frequency on a sea-state is expected to be around $8/T_P$. This excitation frequency was maximum when T_P was minimum (10 Hz for $T_P = 0{,}80$ s). The 4^{th} super-harmonic of the maximum excitation frequency will be 36 Hz, which is well below the Nyquist frequency (50 Hz) and, so, it will be adequately captured.

As was the case for the construction of the model, proper care was taken to ensure that the laboratory equipment was correctly used, in order to maximise the quality of the results and allow an accurate estimate of their uncertainty. The procedures used for operation of the laboratory equipment are described in Annex C.

5.5 Data Processing

Time domain analysis of the data was performed using zero down-crossing analysis for the surface elevation and for the displacements of the buoy, and mean down-crossing for the tension, as indicated in [47]. The crossing time instant was determined by linear interpolation between the discrete time instants just before and after the crossing level; the crest and trough values and time instants were interpolated using a parabolic fit to the discrete data points around the recorded maximum and minimum values [75].

Electro-magnetic noise in the records was removed prior to the analysis using a zero-phase moving average filter, with a seven point kernel for the surface elevation records, a five point kernel for the position records and nine to twelve point kernels for the tension records. These parameters were verified not to induce an unacceptable loss of amplitude of the signals, Figure 5.17. Individual cycles in the records with less than 10 data points (spanning less than 0,1 s) were assumed to be spurious oscillations instead of real ones, and were added to the previous wave or cycle longer than 10 points or 0,1 s.

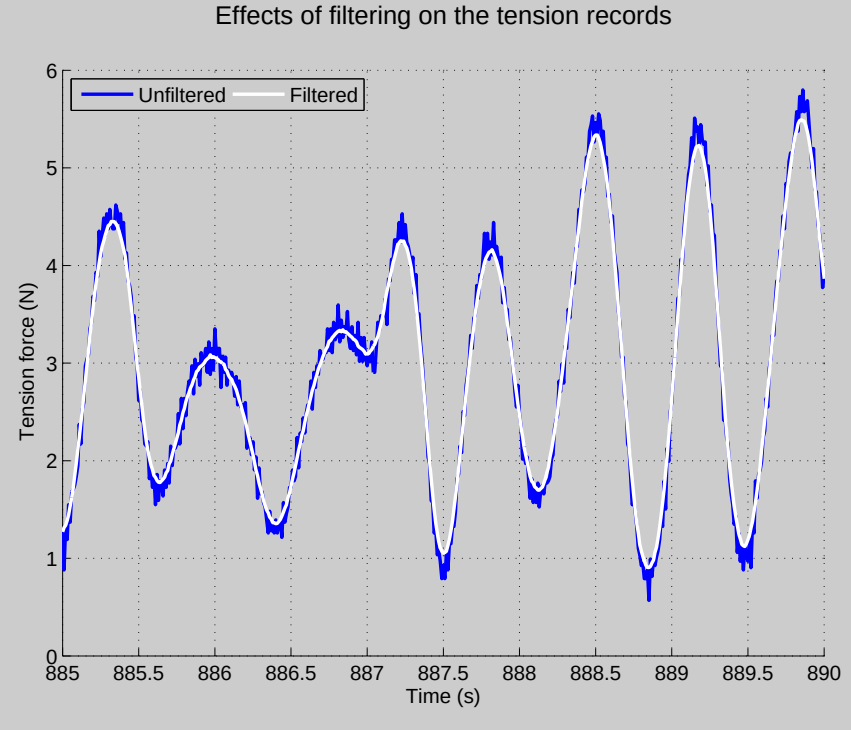

Figure 5.17: Effects of filtering.

For the quasi-static displacement tests, the $x-y$ position of the attachment points of cables 1 and 2 was plotted against the tension force readings. The position-tension data was smoothed using *locally weighted scatterplot smoothing* (LOWESS) and then projected to obtain the restoring force in the surge direction, Figure 5.18. It was assumed that cable 3 had the same behaviour as cable 2. The formulation for this procedure is presented in Annex A. Since it was impossible to

measure the inclination angle of the load cells during the tests, this angle was estimated using the static equilibrium equations of the mooring configurations for each position of the buoy, Annex A.

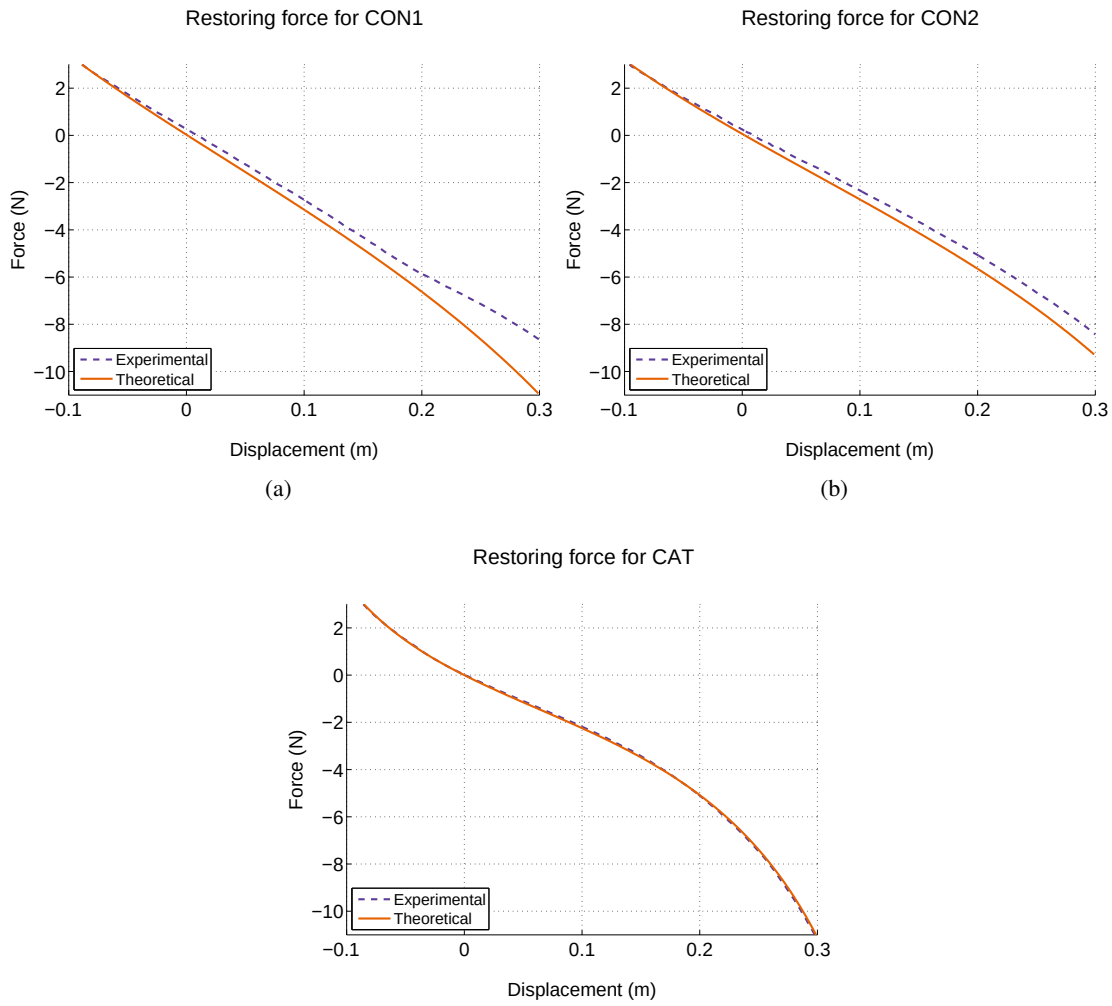

Figure 5.18: Restoring force as a function of the surge displacement: (a) CON1; (b) CON2; (c) CAT.

The experimental values of the restoring force in CON1 and CON2 are lower than what would be expected (4,10 N when displaced 0,10 m, see Annex A) because of in building imperfections in the model and because of the assumptions made in the determination of the restoring force.

The damped natural periods of the modes of motion were estimated from the data obtained in the decay tests. For each test, the time elapsed between the first and the last crest and between the first and the last trough was measured and divided by the number of cycles encompassed by those time spans. The average of all the periods for each degree of freedom was taken as the best estimate for the natural period.

It was assumed that during the decay tests, the degrees of freedom were uncoupled from each other and that the motion was linearly damped, with constant hydrodynamic coefficients and stiff-

ness. Under these assumptions, the displacement of the buoy ξ as a function of time t in each degree of freedom can be described by [75]:

$$\xi(t) = \xi_0 e^{(-\zeta \cdot \omega_n \cdot t)} \cos\left(\sqrt{1-\zeta^2} \cdot \omega_n + \delta\right) \tag{5.4}$$

where ξ_0 is the initial displacement when the buoy was released, ζ is the damping factor, ω_n is the natural (undamped) angular frequency of the buoy-mooring system and δ is a phase angle. The term $\zeta \cdot \omega_n$ in the exponential argument was determined by taking the slope of a straight line fitted to the natural logarithm of the peaks of $|\xi(t)|$, Figure 5.19.

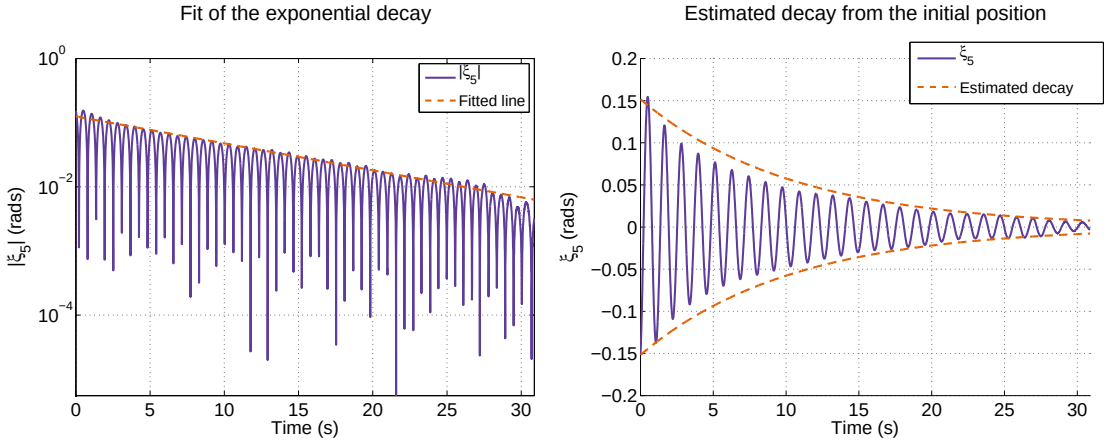

Figure 5.19: Determination of the damping. (a) Example of least squares fitting a straight line to the extremes of the natural logarithm of the decaying motion of one test; (b) decay curve determined using the mean exponential argument of all the tests and the initial position ξ_0 of the displayed sample record.

Knowing the value of $\zeta \cdot \omega_n$, the undamped natural frequency and the damping factor can be estimated using the relation [75]:

$$\omega_d = \omega_n \sqrt{1-\zeta^2} \tag{5.5}$$

where ω_d is the damped angular frequency of the buoy, determined directly from the damped natural periods.

Having determined the stiffness and the undamped oscillating frequency of the buoy-mooring system, the total mass of the system (real plus added mass), m^t, is determined using the following equation [75]:

$$m^t = K^t \omega_n^2 \tag{5.6}$$

where K^t is the stiffness of the buoy-mooring system. The added mass, m^a, is obtained from the real mass, m_t (Equation 5.6), by subtracting the real mass, measured with a scale. The total

damping coefficient, b^{t}, is determined by:

$$b^{t} = 2m^{t}\zeta\omega_{n} \tag{5.7}$$

The total stiffness of the buoy-mooring system, K^{t}, as well as the individual contributions from the buoy, K_{b}, and from the mooring system, K_{m}, are frequency independent and can be determined easily, either experimentally or analytically, as shown in subsection 5.6.1.

Both the total damping, b^{t}, and the total mass, m^{t}, of the model vary with frequency and contain contributions from the buoy and from the mooring system. In order to determine the contributions of each component of the model, first the total mass and the damping coefficient of the buoy alone, m_{b}^{t} and b_{b}^{t} respectively, need to be determined for the same oscillating frequency as the coupled buoy-mooring system. Then, the contribution of the buoy is subtracted from the total value (m^{t} and b^{t}) to obtain the contribution of the mooring system, m_{m}^{t} and b_{m}^{t}, respectively. With the available equipment it was possible to execute decay tests only at the natural frequencies of each configuration, including the buoy floating freely. This meant that the added mass and damping of the free buoy could only be determined for its natural frequencies, which were not the same as when the buoy was moored. Furthermore, because there is no restoring force in surge for an un-moored floating structure, the hydrodynamic coefficients for surge could not be determined at all for the free buoy.

The computation of the response amplitude operators was carried out using a modification of the method described in [85]. The regular wave records were filtered using a windowed-sinc filter with a Blackman window [96]. This eliminated all components with periods above 3,25 s, effectively removing any slowly varying oscillations and drift trends, Figure 5.20. Afterwards, a Fast Fourier Transform (FFT) of the filtered record was taken and the amplitude and frequency of the first order component extracted. These were then used as a first guess in an iterative least-squares fitting algorithm looking for the phase, frequency and amplitude that best fit the signal around that first guess. The quality of the fit was assessed using the coefficient of determination.

The variance spectrum of the surface elevation was determined using Welch's method with a Hann window and 50 % overlap between sub-series [97]. The initial portion of the record with the transients was removed and the data was filtered with a windowed-sinc filter to eliminate all frequency components above 10 Hz. The record was then split into 31 sub-series around 97 s long to obtain a resolution of 0,01 Hz (the exact value of the resolution varies from record to record depending on the length of the transient portion) and estimates with a standard deviation of 18,4 % of the mean, as recommended in [54]. In the computation of the spectral parameters, the spectra were interpolated using zero-padding to a 65536 point FFT. The peak frequency was determined using the centroid method proposed in [98].

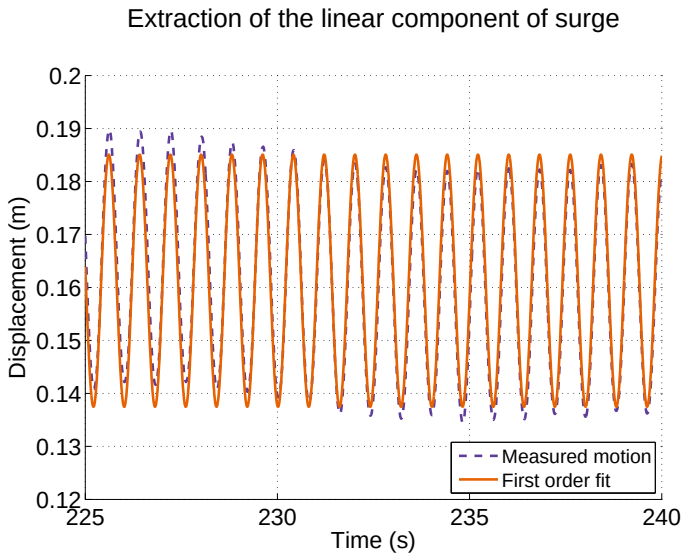

Figure 5.20: Comparison between the measured and the linear displacement component (in this case, surge). The linear component is estimated by extracting the first order component of the measured motion spectrum.

5.6 Results and Discussion

5.6.1 Quasi-static Displacement Tests

The experimentally determined plots of secant stiffness of the mooring system K_{m} as a function of surge displacement are presented in Figure 5.21. Just like for the restoring force, the experimental values are lower than expected, which is both attributed to imperfections in the model and to the assumptions made to determine the stiffness.

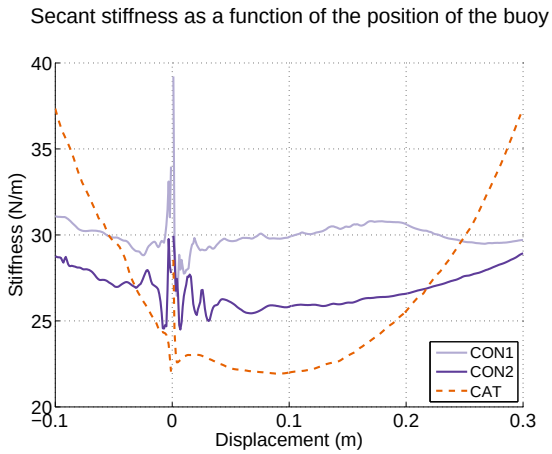

Figure 5.21: Secant stiffness of the configurations. The oscillations near zero displacement are due to the division of the force value by very small displacements.

It was not possible to experimentally determine the stiffness for heave and pitch. Instead, they were computed using the equations of static equilibrium for each configuration (see Annex A) for

small displacements around the rest position ($\pm 0,01$ m for heave and $\pm 1^\circ$ for pitch). The uncertainty of the estimates of the stiffness for heave and pitch should be higher than for surge, since the calculations were based on approximate assumptions for the geometry of the configurations.

5.6.2 Decay Tests

The damped natural periods of the buoy are presented in Table 5.11. As expected, the three configurations affect the dynamics of the buoy differently, which is clear from the different values of the natural oscillating periods.

Table 5.11: Damped natural periods of the buoy.

Mode of Motion	Free	CON1	CON2	CAT
Surge (s)	-	$8,561 \pm 0,006$	$9,22 \pm 0,08$	$9,14 \pm 0,01$
Heave (s)	$1,112 \pm 0,006$	$1,118 \pm 0,008$	$1,132 \pm 0,006$	$1,130 \pm 0,009$
Pitch (s)	$1,170 \pm 0,005$	$1,145 \pm 0,005$	$1,168 \pm 0,005$	$1,163 \pm 0,006$

For surge, CON1 presents the shortest oscillating period, while CON2 and CAT present similar oscillating periods which are slightly longer than in CON1. When compared with the free buoy, CON1 has the least influence in the oscillating period in heave (which was already expected due to its geometry) and CON2 has the least influence in pitch. CAT has some influence on both pitch and heave.

To understand how the different configurations influence the dynamics of the buoy, some hydrodynamic parameters were estimated, Tables 5.12 to 5.14. These parameters were computed as explained in section 5.5. There is data for only one frequency per configuration and degree of freedom because, as mentioned in section 5.5, the decay tests could only be executed for the natural damped frequency of each configuration.

The added mass, $m_{\mathrm{b}}^{\mathrm{a}}$, and radiation damping coefficient, b_{b}^{r}, of the buoy determined using linear potential theory [77] are also provided for comparison.

Since the added mass and damping depend on the oscillating frequency, which is different for all configurations, a comparison of the results of the four cases might not be completely valid. The comparison should be most accurate between CON2 and CAT, as they have similar oscillating periods.

Because there is no restoring force in surge when the buoy is free, there is no oscillatory motion in this situation and no parameter is estimated. The analysis in surge is justified only for the moored situations. For heave and pitch it was possible to determine hydrodynamic parameters for the free buoy, so it was possible to determine the total mass for the mooring system, $m_{\mathrm{m}}^{\mathrm{t}}$, accounting for its real plus its added mass.

In surge, although the linear added mass of the buoy for CON1 is similar to that of CAT, and CON1 has the smallest draft, its total mass is larger than CAT. This is probably caused by the floaters with their large volume. The same holds for the damping coefficients.

Table 5.12: Hydrodynamic parameters for surge.

Parameter	Free	CON1	CON2	CAT
ω_d (rad/s)	-	0,7339	0,6818	0,6877
ω_n (rad/s)	-	0,7341	0,6820	0,6879
ζ	-	0,0224	0,0235	0,0242
K^t (N/m)	-	28,65	28,28	23,63
K_m (N/m)	-	28,65	28,28	23,63
m^t (kg)	-	53,16	60,80	49,94
m_b^a (kg)	-	18,28	20,14	18,73
b^t (kg/s)	-	1,7491	1,9500	1,6658
b_b^r (kg/s)	-	0,0196	0,0182	0,0167

Table 5.13: Hydrodynamic parameters for heave.

Parameter	Free	CON1	CON2	CAT
ω_d (rad/s)	5,650	5,620	5,551	5,560
ω_n (rad/s)	5,667	5,644	5,568	5,583
ζ	0,0759	0,0924	0,0782	0,0897
K^t (N/m)	2039,5	2047,8	2059,6	2054,9
K_m (N/m)	-	8,3	20,0	15,4
m^t (kg)	63,51	64,28	66,44	65,93
m_m^t (kg)	-	1,48	3,49	3,00
m_{be}^a (kg)	27,67	28,44	30,60	30,09
m_b^a (kg)	26,92	26,96	27,11	27,06
b^t (kg/s)	54,67	67,04	57,90	66,00
b_b^r (kg/s)	37,92	37,94	35,91	36,04

CON2 and CAT have similar oscillating periods, but the total mass of CON2 is around 10 kg higher than the one of CAT, while the difference in the real masses is only 3,06 kg, Table 5.6 (relative to the hanging mass of CAT). This can support the conclusion that the floaters introduce a significant added mass and damping (the clumpweights too, but to a lesser extent), but it might also be caused by the higher draft of CON2 relative to CAT.

Since CON1 has a larger total mass than CAT, its shorter surge oscillating period is probably due to the higher stiffness.

In heave, CON1 has the oscillating period closest to the free buoy because it also has the stiffness and total mass that are closest to the values of the free buoy.

For the free buoy, the total added mass of the configuration, m^a, is the same as the experimentally determined added mass of the buoy alone, m_{be}^a, which is remarkably similar to value estimated using linear potential theory, m_b^a. It is then reasonable to assume that the estimates of

Table 5.14: Hydrodynamic parameters for pitch.

Parameter	Free	CON1	CON2	CAT
ω_d (rad/s)	5,370	5,487	5,379	5,403
ω_n (rad/s)	5,371	5,488	5,380	5,404
ζ	0,0140	0,0137	0,0164	0,0249
K^t (N·m)	37,76	39,41	42,43	39,44
K_m (N/m)	-	1,44	1,84	0,84
m^t (kg·m^2)	1,31	1,31	1,47	1,35
m_b^a (kg·m^2)	0,283	0,285	0,311	0,291
b^t (kg·m^2/s)	0,1970	0,1962	0,258	0,363
b_b^r (kg·m^2/s)	0,0493	0,0605	0,1019	0,0655

the added mass of the buoy using linear potential theory are equally accurate for the other configurations. In this situation, two of the four components of the total mass are known: the real and the added masses of the buoy. The difference between the sum of these values and the total mass of the model is the total mass of the mooring system m_m^t.

Using this reasoning, the mooring system of CON1 brings to the model a total mass of 1,48 kg; CON2, with its clumpweights and floaters, brings a total mass of 3,49 kg; and the chains in CAT bring a total mass of 3,00 kg, which is close to the value of CON2, despite the large difference in the real masses of mooring components, Table 5.6. It seems that the chains have a large hydrodynamic influence in heave.

When it comes to the damping coefficient, CON2 has a somewhat close value to the one of the free buoy, while CON1 and CAT have higher damping coefficients. Since CON2 and CAT have similar oscillating periods, but CON2 has a higher draft than CAT, it seems that the chains cause more damping than the floaters and the clumpweights together. However, CON1, whose major sources of damping are the floaters, has a higher damping coefficient than CAT, when it was perhaps expected to have a smaller one. Part of this can be due to the difference in oscillating frequencies, but it might also be that the floaters do generate high damping. The key difference between CON1 and CON2 might be how the geometry of the mooring legs influences the motion of the floaters. In CON1, the floaters are connected directly to the buoy, so any motion of the buoy is transmitted straight to the floaters. On the contrary, in CON2, the displacement of the buoy is distributed between the floaters and the clumpweights. In this configuration, the bulky floaters have smaller motions than in CON1, therefore generation less damping, while the clumpweights because of their a small size, do not cause an excessive increase in the damping.

In spite of having a larger damping than the free buoy, the oscillating period of CON1 is not much longer than the free buoy because the damping factor is still small and its influence on the oscillating frequency is of quadratic order, Equations 5.4 and 5.5.

In pitch, it is CON2 that has the natural period closest to the one of the free buoy. As a coincidence, the mooring system increases the stiffness and the total inertia proportionally, preventing a large shift in the natural period.

In CON1, the only significant effect of the mooring system is increasing the stiffness and, therefore, the natural oscillating frequency; there is almost no variation in the total mass or in the damping coefficient when compared to the free buoy.

CAT increases both the stiffness and the total inertia, but the resulting values do not balance as well as in the case of CON2, leading to a slightly higher natural frequency than for the free buoy. In this case, the increased stiffness is mostly due to the larger draft of the buoy caused by the weight of the chains, and not by the moment of the tension forces, like in CON1 and CON2, as seen by the value of the mooring system stiffness.

Both CON2 and CAT lead to increased damping when compared with the free buoy, with CAT having the highest damping coefficient in pitch. A possible explanation for this is that in the compact configurations, the buoy can rotate with little motions of the floaters and of the clumpweights: in CON1, the cable connected to the buoy can pivot about the connection to the floater, while in CON2 there will be some motion of the clumpweights, but also a significant rotation of the cable connecting them to the buoy. On the other hand, in CAT, the entire chain has to be dragged through the water when the buoy rotates.

5.6.3 Regular Waves

The response amplitude operators (RAO) obtained with the regular wave tests are presented in Figures 5.22 to 5.24. The displacement amplitudes in surge, ξ_1, and in heave, ξ_3, were non-dimensionalised using the wave amplitude, a, and in pitch, ξ_5, using the wave slope, k.

Two striking results are evident when analysing the plots: first, for each wave height and degree of freedom, the variation of the RAO between the three configurations is unexpectedly small; second, the wave height has a greater impact in the response than the mooring configuration.

The peak in the surge response for periods between 1,10 s and 1,20 s is not due to any resonant motion in surge, but due to the resonant motions of heave and pitch. In all configurations, the surge resonance period is longer than 8 s, which is much longer than the longest wave period tested, $T = 2{,}33$ s, so there is little to no surge resonant motion. For both wave heights, CON2 has the highest response amplitude for the long periods (longer than 1,10 s-1,15 s), while CON1 has the highest response for shorter periods. Looking at the damping values determined for surge in the decay tests, Table 5.12, it would be expected that CON2, with the largest damping, had the smallest response. However, the estimated damping is strictly valid only for the surge resonance period. For increasingly larger periods beyond 1,30 s-1,40 s, the difference between the response of CON2 and the responses of CON1 and of CAT becomes smaller. The excitation period is approaching the surge resonance period and the hydrodynamic coefficients of the configurations are probably approaching the values presented in Table 5.12, where the damping of CON2 is the largest.

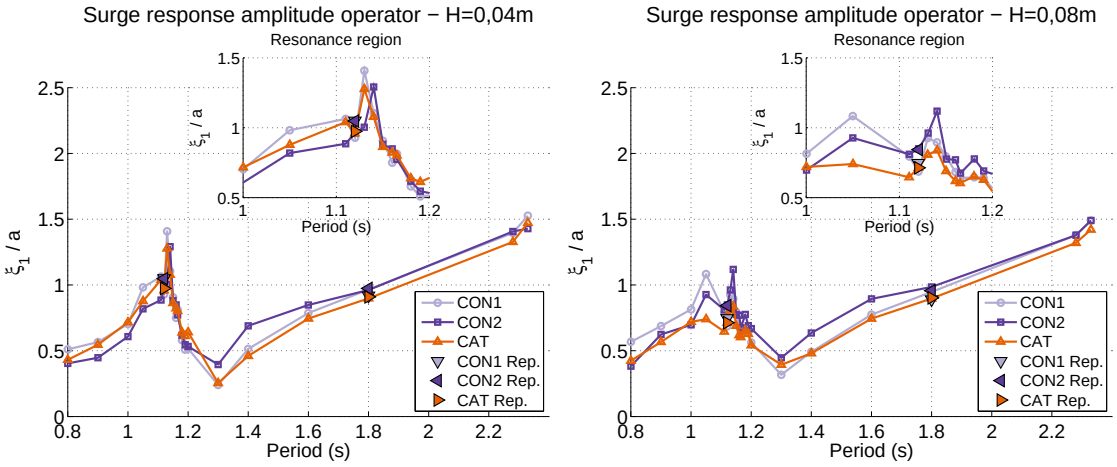

(a) (b)

Figure 5.22: Response amplitude operator for surge. (a) response for a regular wave height $H = 0{,}04\,\text{m}$; (b) response for a regular wave height $H = 0{,}08\,\text{m}$. ξ_1 - surge displacement amplitude; "Rep." denotes the repeated tests.

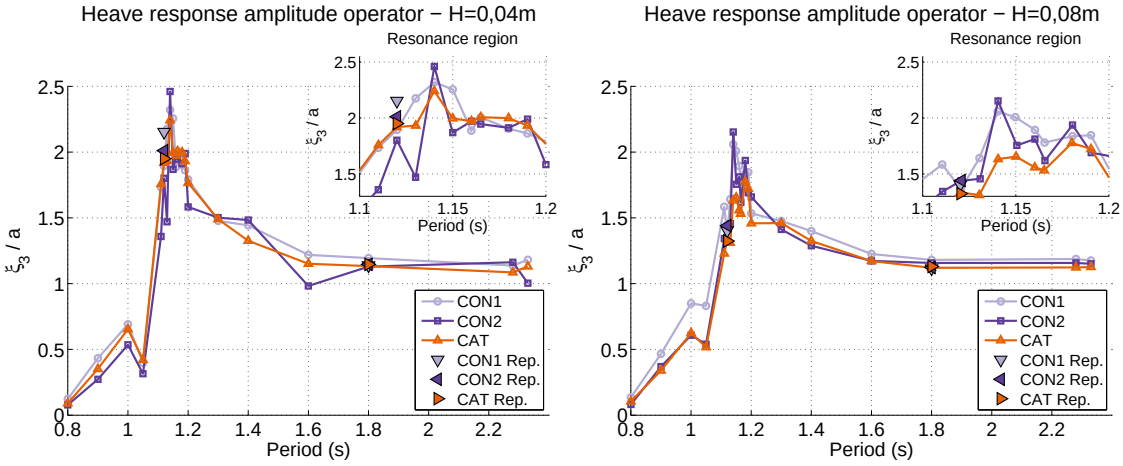

(a) (b)

Figure 5.23: Response amplitude operator for heave. (a) response for a regular wave height $H = 0{,}04\,\text{m}$; (b) response for a regular wave height $H = 0{,}08\,\text{m}$. ξ_3 - heave displacement amplitude; "Rep." denotes the repeated tests.

The behaviour shown in Figures 5.22a and 5.22b hints that, for devices using the surge motion to extract energy, CON1 might be better in smaller periods while CON2 might be better for longer ones.

In heave, CON1 has the highest response for both wave heights tested, so it will likely have the best performance for energy extraction in this degree of freedom. The only exception occurs at the heave resonance peak, where CON2 has a larger response. This is in line with the estimated damping for heave presented in Table 5.13, where CON1, at the resonance frequency of heave, has the highest damping.

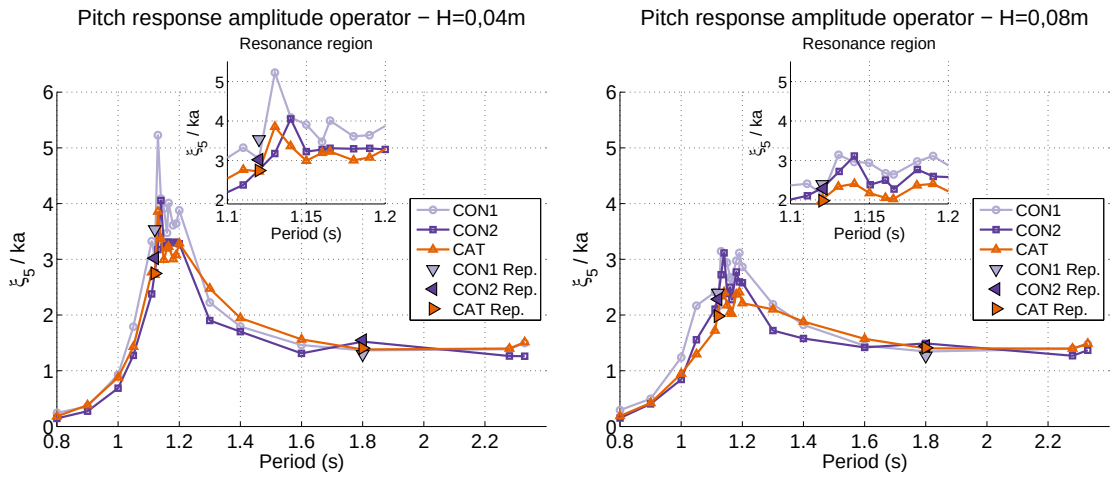

Figure 5.24: Response amplitude operator for pitch. (a) response for a regular wave height $H = 0{,}04\,\text{m}$; (b) response for a regular wave height $H = 0{,}08\,\text{m}$. ξ_5 - pitch displacement amplitude "Rep." denotes the repeated tests.

For the period of 1,05 s, there is a sharp break in the response in heave, that is common to all configurations in both wave heights. This phenomena is not due to any problem in data analysis, but to real phenomena for this period which affected only the heave motion. For a relatively steady wave height and period, after the initial transients of the waves and of the motion of the buoy, the heave amplitude just slowly decreased, in an exponential way, Figure 5.25. This decaying motion lasted for about 520 s before it stabilised (the standard duration for regular wave tests was 270 s). An explanation for this phenomena could not be reached, but a possibility is the build up of wave reflections inside the tank.

In pitch, CON1 has the highest response for periods up to 1,20 s to 1,30 s; for longer periods, CON2 and CAT perform slightly better than CON1. This is similar to what happens in surge and it is probably not a coincidence, but caused by the coupling between the two degrees of freedom. Heave, on the contrary, is uncoupled from the other degrees of freedom [38].

There is probably a significant *outlier* component in the peak value of the pitch RAO of CON1 for the wave height $H = 0,04$ m at the period $T = 1{,}13$ s, since it presents a sharp increase in the response, in contrast with the smooth appearance of the RAO for other periods and for the other configurations.

The response amplitude operators decrease when the wave height increases. In a purely first order process, the RAOs should be constant when the wave height changes, so this variation is likely due to second order and other non-linear effects. Among these, the most relevant would be the second order drift forces (which depend on the square of the wave height), the viscous damping, and also the non-linearity of the mooring system, whose stiffness varies with the mean position of the buoy. All configurations seem to be equally affected by this decrease in response amplitude, which might mean that its causes are more likely associated with the buoy than with the mooring system.

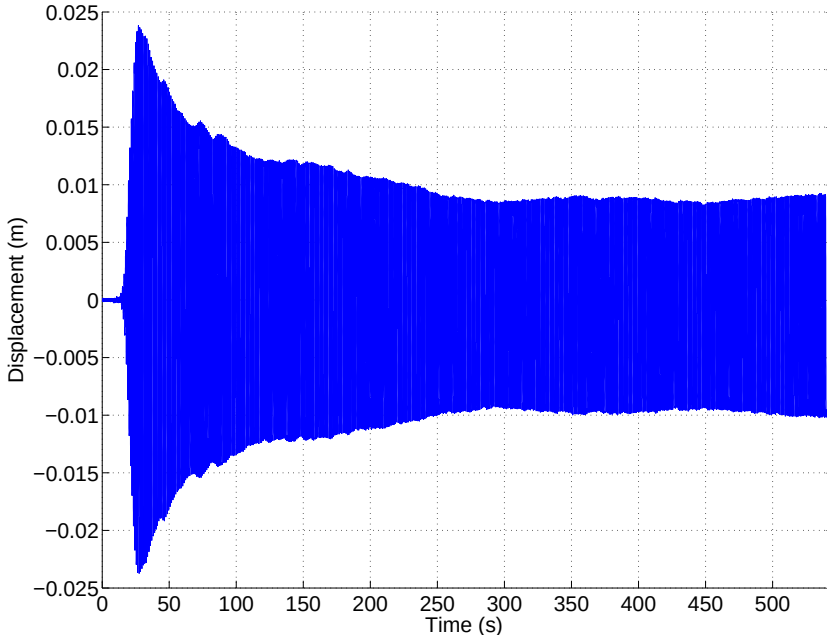

Figure 5.25: Decaying amplitude of the heave motion in regular waves with period $T = 1{,}05\,\mathrm{s}$.

The other important type of motion is the the second order surge drift, $\bar{\xi}_1$, plotted for the same two wave heights in Figure 5.26, in a non-dimensional format.

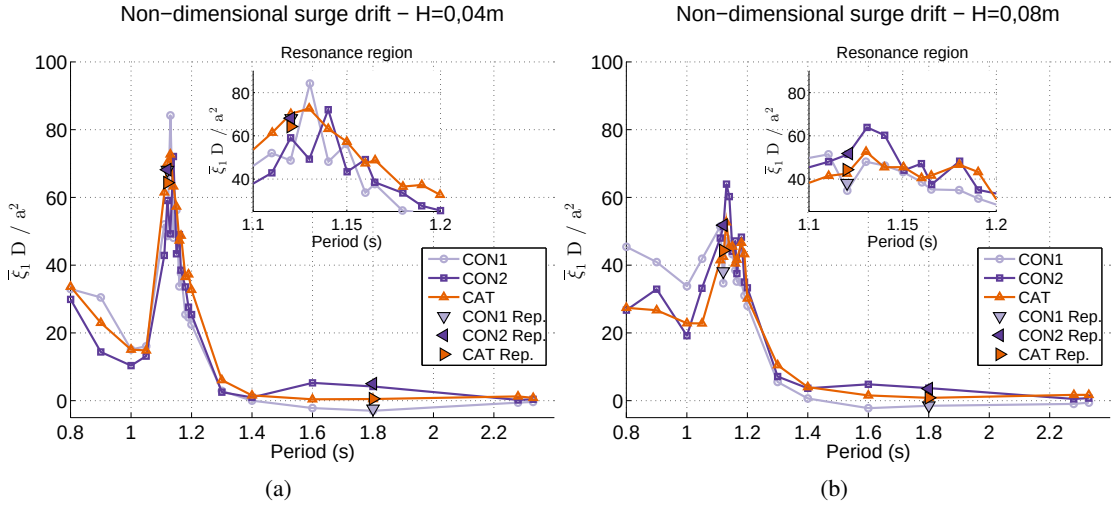

(a) (b)

Figure 5.26: Non-dimensionl mean surge drift.

The plots exhibit the typical variation of the surge drift as a function of the wave period: large values for small periods and small values for large periods. In the range of periods around the heave and pitch resonance, the drift values are high because of the large first order motions of the buoy at these periods. Interestingly, the non-dimensional surge drift in the range of periods around heave-pitch resonance is smaller for the wave height $H = 0{,}08\,\mathrm{m}$ than for $H = 0{,}04\,\mathrm{m}$, even though

the drift forces are four times as large in the former when compared with the later. This is probably caused by the stiffening of the mooring system with the increasing displacement.

Although CON1 has the largest stiffness and should be better at resisting drift forces, it seems that it allows the largest drift displacements in the smaller periods, exactly when the drift forces have a greater importance. This was not expected.

In the range of periods of the survival sea-states, $T_P = 1{,}16\,s$ to $T_P = 1{,}42\,s$, CON2 and CAT have similar drifts, with CAT having slightly larger drifts than CON2. In the survivability tests with irregular sea-states, this same result will be seen to happen as well.

Except at the heave-pitch resonance range, the plots are fairly similar between configurations and between wave heights. The variation of the drift with the wave height and the rough shape of the plots in general are largely due to the unsteadiness of the motion during the tests and to the data analysis procedure. During the tests, the mean oscillating position of the buoy in surge varied slowly, instead of being constant, as it should be in regular waves (although different than the rest position). This could have been caused by the long period transient motion of buoy in surge, that took a long time to die out. Only the small segments of the records where the mean position was relatively stable could be used to estimate the drift, but they were not fully representative of the entire records. Consequently, there is a large variability in the drift values. This variability was amplified by the non-dimensionalisation using the square of the wave height. The waves did not have the exact height $H = 0{,}04\,m$ for all periods, having instead slight variations. For the smaller waves, small variations in the wave height result in large variations of the non-dimensionalisation constant.

Finally, there is the tension in the most loaded cable (cable 1) which is analysed from three points of view: the average maximum tension, $\bar{\tau}_{max}$, the mean tension, $\bar{\tau}$, and the average dynamic tension, $\bar{\tau}_{dyn}$. The average maximum tension is the mean value of the peak tension recorded in each oscillation in regular waves, while the average dynamic tension is defined as the mean of the difference between the maximum and the minimum tension in each cycle.

The non-dimensional maximum tension is plotted in Figure 5.27. The results are not surprising. CON2, with the highest pre-tension, has the highest maximum tension, while CON1 and CAT, with similar pre-tensions have similar maximum tensions.

In the region of heave-pitch resonance, the peak of the maximum tension is due to the quick and large motions of the buoy when in resonance, which is supported by the large values of the dynamic tension in this range, Figure 5.28.

When the wave height increases, the non-dimensional maximum tension decreases. This happens because the mean tension component of the maximum tension is almost constant, Figure 5.29, so when the wave height increases, its non-dimensional value decreases. This effect is more notorious for CON2, where the non-dimensional mean tension is reduced by almost 50 % when the wave height doubles in size, because it has the highest pre-tension (which dominates the mean tension) of the three configurations.

Outside the resonance peak, for decreasing periods, the maximum tension seems to rise probably because of the increasing magnitude of the second order drift forces, which also increases

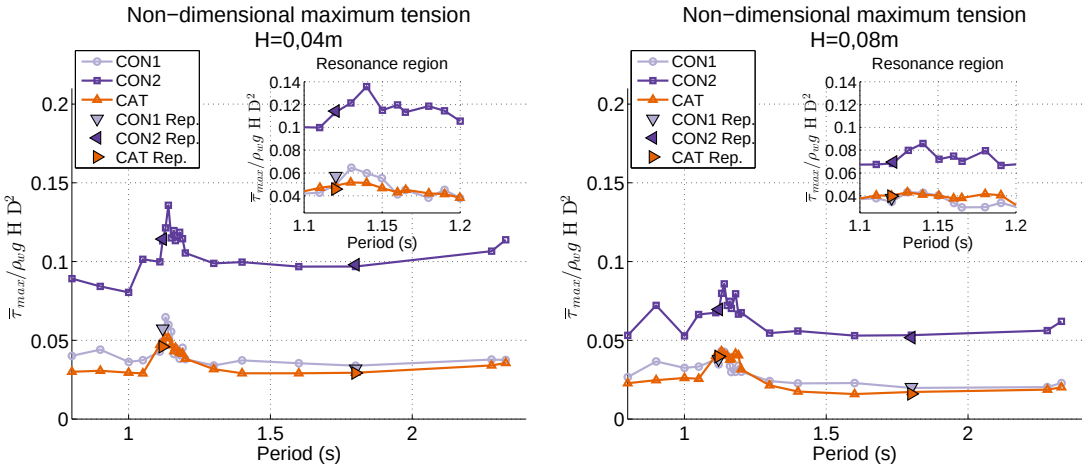

(a) (b)

Figure 5.27: Non-dimensional maximum tension.

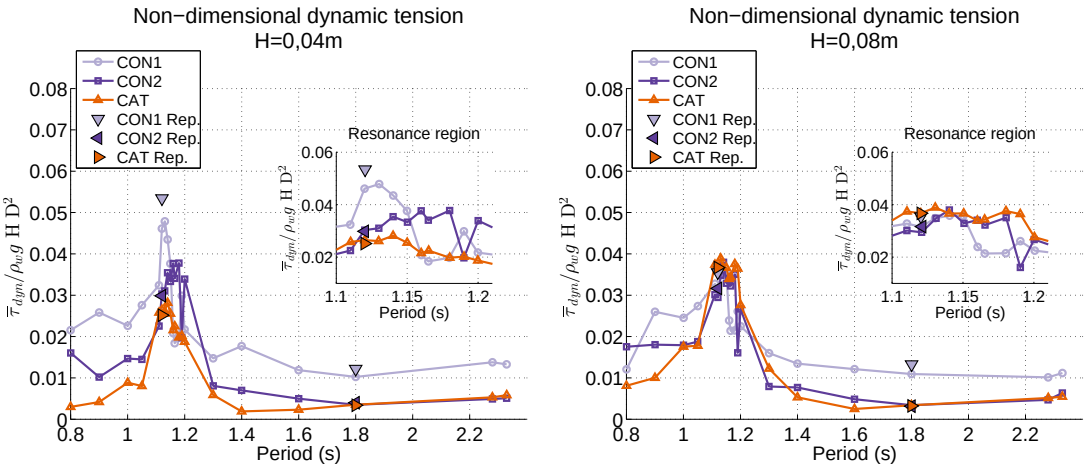

(a) (b)

Figure 5.28: Non-dimensional dynamic tension.

their contribution to the mean tension. For increasing periods, the maximum tension seems to rise probably because of the interaction with the resonant motion of surge.

This analysis has a catch: the fact that CON2 has the highest maximum tension in regular waves, does not mean that it will have the highest maximum tension in irregular waves. While in CON2 the dynamic tension is just a fraction of the mean tension, in CON1 and in CAT both tensions have the same magnitude. This means that both CON1 and CAT are susceptible to having null tension in the cables (which did happen for some of the periods tested), a tell-tale sign of imminent snap loads and high peak tensions. In fact, this is what will be seen in the results of the irregular wave tests, where CON2 will present the best results for the tension while CON1 and CAT will show poor performances.

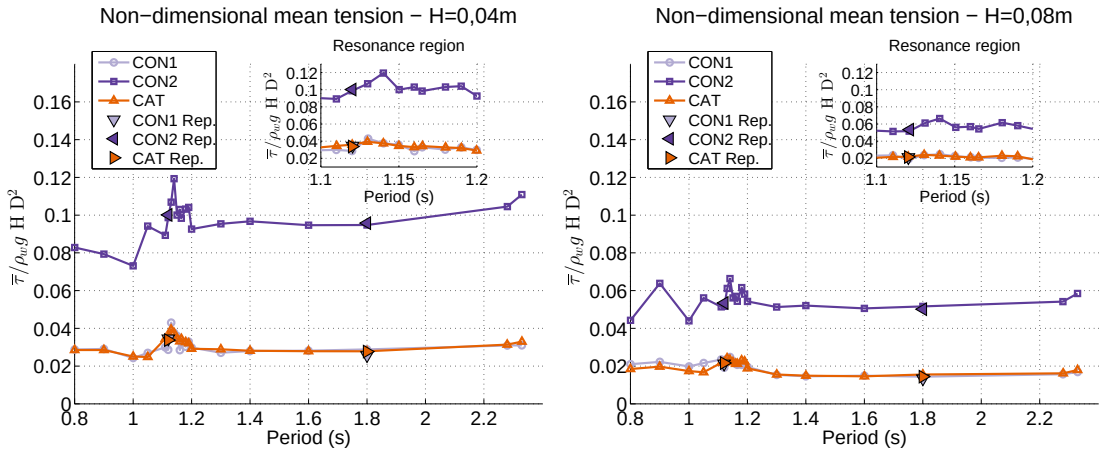

Figure 5.29: Non-dimensional mean tension.

The similarity between the dynamic tension plots for 0,04 m and 0,08 m waves indicates that, in the range of periods tested, it should vary linearly with the wave height, just like the first order wave loads and motions that induce the dynamic tension.

In general, CON1 has the highest dynamic tension for both wave heights, with the exception of the resonance periods for $H = 0{,}08$ m. CON2 has practically no variation in the dynamic tension when the wave height changes, while CAT has a 25 % increase for $H = 0{,}08$ m when compared with $H = 0{,}04$ m.

Just like for the drift, the tension plots do not have a smooth appearance, which is both due to the unsteadiness of the tension, and to the tension cycles in some of the periods tested having several peaks. Most of these peaks were above the mean tension value and so they were detected in the zero-crossing analysis. Averaging all the values of all of the peaks in each record resulted in average peak values lower than what they would be if only the single largest peak in each cycle was detected. An example of this is shown in Figure 5.30.

Another consequence of the multi-peak shape of the tension cycle is the fatigue damage to the cables. Although this effect was not a research priority in these experiments, some important conclusions can be made. The existence of several peaks per cycle will increase the fatigue damage to the cables, especially when the tension is high.

CON2 presents the most complex cycles, which can have more than three peaks each. The mooring legs in this configuration (with a floater and a clumpweight) together with the buoy, act as three degree-of-freedom oscillator, that has three natural oscillating frequencies, and might have other complex non-linear interactions.

CON1, with a floater, acts as a two degree of freedom oscillator and has two natural oscillating frequencies. The tension cycles are not as complex as for CON2, but it still has multi-peak cycles.

CAT acts simply as a spring and has only one natural oscillating frequency. Nevertheless, it also shows several peaks per cycle in some periods, probably because of the non-linearity of mooring systems. No configuration is immune to this effect.

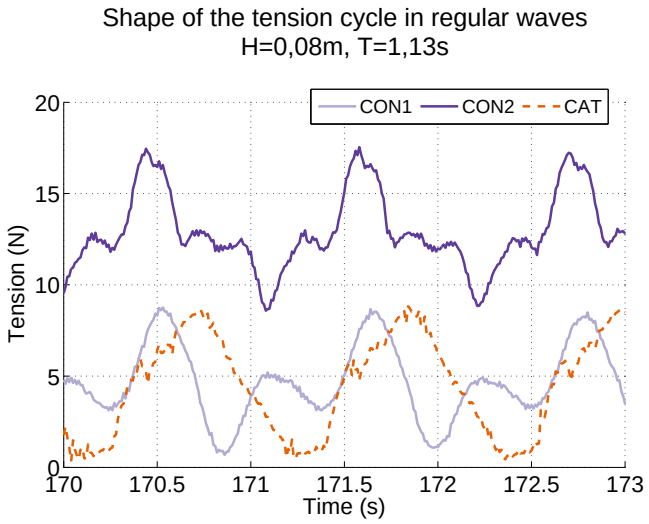

Figure 5.30: Shape of the tension cycles of the three configurations in regular waves with $H = 0{,}08\,\text{m}$ and $T = 1{,}13\,\text{s}$, showing multiple peaks per cycle.

Since CON2 has the highest pre-tension and the most complex cycles, it can be argued that it will be subjected to the most severe fatigue damage. However, for synthetic cables the fatigue dynamics are not as well understood as for steel elements and so no definite conclusions can be made.

5.6.4 Irregular Waves

Before going through the results, it is important to discuss two points in the test conditions. The first one is the assurance that, given the irregular and random nature of the sea-states, the different configurations were indeed subjected to equivalent conditions. This can be judged by the measured significant wave height and peak period in each test, Table 5.15. The measured values are close to the target ones, but they are not exactly the same. Since the experiments do not attempt to reproduce a specific situation, this is not so important, as long as the differences are small.

Table 5.15: Desired and measured sea-state parameters for the irregular wave tests.

Parameter	Target sea-state	CON1	CON2	CAT
H_s (m)	0,030	0,031	0,031	0,029
T_P (s)	0,90	0,90	0,90	0,90
H_s (m)	0,030	0,034	0,033	0,033
T_P (s)	1,30	1,28	1,28	1,30
H_s (m)	0,086	0,083	0,084	0,082
T_P (s)	1,16	1,16	1,16	1,16
H_s (m)	0,095	0,094	0,096	0,093
T_P (s)	1,42	1,39	1,39	1,39

What matters is that the generated test conditions for each target sea-state are the same for the three configurations. As the maximum difference between test conditions is 6,9 % for the significant wave height (sea-state OP1) and 1,5 % for the period (sea-state OP2), it can be assumed that the test conditions are much the same for all the configurations. Furthermore, each target sea-state had only one realisation of the random wave phases, which meant that even the generated time series were the same for the three configurations.

The realisation of the wave phases brings up the second point: the variability of the results due to the randomness of the waves. In order to establish with some confidence the results of the irregular wave tests, each target sea-state would have to be run with, at least, ten different wave phase realisations. Due to lack of time, it was only possible to have one realisation, which is not enough to cover the possible variability of the results. When the results of the three configurations do not show significant differences, the conclusions might be hindered by this bias.

Now, for the evaluation of the performance of the different configurations, the major factor to consider is the power extraction. Since there was no power take-off installed, this is estimated using the mean squared velocity of the buoy in each degree of freedom, Table 5.16. For a linearly damped power take-off, the mean squared velocity can be assumed to be proportional to the average power that would be extracted by the device. This assumption can be up for debate, but it will at least provide an estimate.

Table 5.16: Displacement in operational sea-states. ξ_1 - surge; ξ_3 - heave; ξ_5 - pitch; p.p - peak-to-peak amplitude. Overbar denotes mean value.

	OP1			OP2		
Parameter	CON1	CON2	CAT	CON1	CON2	CAT
$\overline{\xi}_1$ ($\cdot 10^{-3}$ m)	6,1	5,3	5,6	4,8	4,3	4,6
$\overline{\xi}_{1p.p}$ ($\cdot 10^{-3}$ m)	19,8	18,1	16,1	19,6	20,0	17,5
$\overline{\dot{\xi}^2}_1$ (m^2/s^2)	0,064	0,059	0,060	0,088	0,085	0,073
max ξ_1 ($\cdot 10^{-3}$ m)	46,2	43,8	43,3	47,4	43,6	40,0
$\overline{\xi}_{3p.p}$ ($\cdot 10^{-3}$ m)	9,1	8,5	8,5	25,3	25,1	24,5
$\overline{\dot{\xi}^2}_3$ (m^2/s^2)	0,048	0,039	0,040	0,271	0,263	0,250
max ξ_3 ($\cdot 10^{-3}$ m)	13,5	13,5	13,0	35,6	34,3	33,0
$\overline{\xi}_{5p.p}(^\circ)$	3,8	3,4	3,2	9,1	8,5	7,8
$\overline{\dot{\xi}^2}_5$(rad^2/s^2)	2,348	1,827	1,649	11,043	9,4708	7,775
max $\xi_5(^\circ)$	5,4	4,9	4,5	10,7	10,2	9,1

CON1 allows the highest power extraction in both sea-states in all degrees of freedom. This is in accordance with the general analysis of the response amplitude operators, sub-section 5.6.3, where CON1 had an overall better performance than CON2 and than CAT. CON2 appears as the second best configuration, since its performance is lower than CAT only for surge and heave and only in sea-state OP1; CAT is, then, the configuration with the worst overall performance in terms of power extraction.

Judging from the surge response amplitude operator, Figure 5.22a, it would be expected that CON2 had a better performance than CON1 for the sea-state OP2 ($T_P = 1{,}30\,s$), which does not happen. However, the differences between the response amplitude operators of CON1 and CON2 and between the mean squared velocities of the three configurations for $T_P = 1{,}30\,s$ in surge are small and might be due to experimental variability and randomness.

For pitch, in OP2 ($T_P = 1{,}30\,s$), CAT should have a slightly better performance than CON1, Figure 5.24a, or, at least, similar, Figure 5.24b. Instead, CAT has the worst performance and CON1 has the best one, with a difference of almost 42 % in power extracted. The fact that CAT has a higher estimated total damping, Table 5.14, can be a possible explanation for the lower performance in irregular seas, when compared with regular waves. Once again, randomness might have had an impact on the results.

The remaining motion parameters ($\overline{\xi}$, $\overline{\xi}_{p.p}$ and $\max\xi$) follow the same trend as the mean squared velocity (which is consistent), but with even smaller differences between configurations.

In operational sea-states, peak tensions are, usually, not an important factor, since they tend to be much smaller than in survival conditions. However, they are presented in Table 5.17 because of an interesting situation: CON1 is already showing both large dynamic tensions (equal to or greater than the mean tension) and, up to the uncertainty in readings, null tensions. In contrast, CON2 and CAT have low dynamic tensions and are able to keep both cables under tension. The potential for this situation was already highlighted in sub-section 5.6.3.

Table 5.17: Tension in operational sea-states. τ - tension; p.p - peak-to-peak amplitude. Overbar denotes mean value. Indexes 1 and 2 refer to the cable where the tension was measured.

	OP1			OP2		
Parameter	CON1	CON2	CAT	CON1	CON2	CAT
H_s (m)	0,031	0,031	0,029	0,034	0,033	0,033
T_P (s)	0,90	0,90	0,90	1,28	1,28	1,30
$\overline{\tau}_1$ ($\pm$0,2N)	2,9	10,8	3,1	2,9	10,7	3,1
$\max\tau_1$ ($\pm$0,2N)	5,8	11,9	3,6	5,1	12,1	3,9
$\min\tau_1$ ($\pm$0,2N)	0,2	9,6	2,7	0,7	9,2	2,4
τ_{dyn1} ($\pm$0,3N)	2,9	1,1	0,5	2,2	1,5	0,8
$\overline{\tau}_2$ ($\pm$0,2N)	3,0	11,1	3,0	3,0	11,1	3,0
$\max\tau_2$ ($\pm$0,2N)	6,6	12,3	3,6	5,9	12,6	3,8
$\min\tau_2$ ($\pm$0,2N)	0,1	9,9	2,5	0,3	9,3	2,0
τ_{dyn2} ($\pm$0,3N)	3,6	1,2	0,6	2,9	1,6	0,8

For the survival sea-states, the focus is on the extreme motions and tensions, Tables 5.18 and 5.19.

To ensure the integrity of power lines (or similar components connected to the wave energy converter) and to avoid possible crashes between devices, the most relevant criterion is the maximum surge displacement.

Table 5.18: Displacements in survival sea-states. ξ_1 - surge; ξ_3 - heave; ξ_5 - pitch; p.p - peak-to-peak amplitude. Overbar denotes mean value.

	SURV1			SURV2		
Parameter	CON1	CON2	CAT	CON1	CON2	CAT
$\overline{\xi}_1$ ($\cdot 10^{-3}$ m)	62,5	63,2	63,6	31,9	39,0	39,6
$\overline{\xi}_{1p.p}$ ($\cdot 10^{-3}$ m)	131,2	135,2	119,5	81,7	92,8	90,0
$\max \xi_1$ ($\cdot 10^{-3}$ m)	311,6	318,6	278,7	186,8	222,7	210,8
$\max \xi_{1p.p}$ ($\cdot 10^{-3}$ m)	428,5	442,0	348,9	247,5	286,8	255,3
$\overline{\xi}_{3p.p}$ ($\cdot 10^{-3}$ m)	71,6	69,6	66,6	74,8	70,7	71,6
$\max \xi_3$ ($\cdot 10^{-3}$ m)	87,2	83,4	77,6	108,9	98,5	100,9
$\max \xi_{3p.p}$ ($\cdot 10^{-3}$ m)	171,7	164,3	154,8	198,4	183,1	183,0
$\overline{\xi}_{5p.p}(^\circ)$	21,8	19,1	18,0	17,6	14,8	15,5
$\max \xi_5(^\circ)$	25,7	22,2	20,7	21,3	17,4	18,8
$\max \xi_{5p.p}(^\circ)$	44,6	38,7	37,1	40,2	34,0	35,1

In section 5.2, in the design of the mooring system, the maximum surge displacement allowed for the buoy was set to be 0,200 m, which is far exceed by all configurations. The reason for this, already mentioned in section 5.2, is the fact that the mooring legs were initially designed to be opposite to each other, but were later installed in a triangular arrangement, reducing the overall stiffness in surge.

The largest surge displacement occurs, in both sea-states, in CON2; CAT has the best results in the sea-state SURV1, while in sea-state SURV2 it is CON1. The inferior performance of CON2 might be due to it having more components subjected to drift forces (floaters and clumpweights) than CON1 or CAT. As before the differences between the values of the three configurations are too small to exclude randomness of the sea-states as the cause for these results.

The extreme surge displacement might be interpreted under a different light. Figure 5.31 shows all the peak values of the surge displacement in the survival sea-states, ranked by their magnitude. For CON1, in the sea-state SURV1, the last two values are repeated. This almost certainly means that this configuration reached a state where the mooring leg is fully taut. Although this does not imply the failure of the mooring system, when the cable is fully taut the tensions can increase sharply, so this condition should be avoided. This situation, which did not happen for any other configuration, could mean that CON1 has a limited displacement only because it reached a deformation limit.

Figure 5.31 reveals another interesting effect. While for sea-state SURV2 ($T_P = 1{,}42$ s) the peak values rise steadily with the rank for all configurations, in sea-state SURV1 ($T_P = 1{,}16$ s) there is a sudden increase in the peak magnitudes when the rank reaches 100 to 125. Also, there are fewer, but significantly larger peaks for sea-state SURV1 when compared with sea-state SURV2. The examination of the response amplitude operator of surge for waves with height $H = 0{,}08$ m, Figure 5.22b, shows that the surge response for the period $T = 1{,}16$ s should be slightly higher

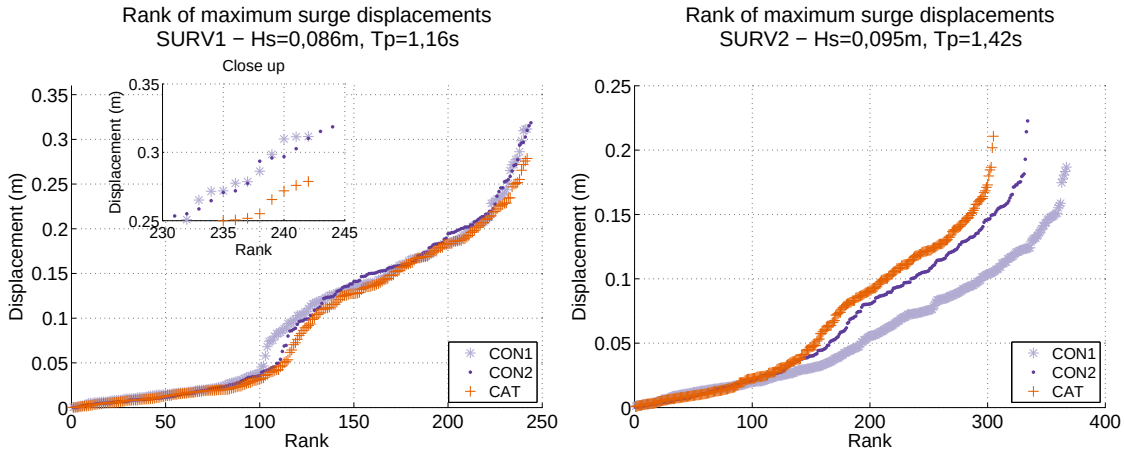

Figure 5.31: Rank of maximum surge displacements of the three configurations in the survival sea-states.

than for $T = 1{,}42\,\mathrm{s}$ waves. However, the difference in the response amplitude should not be very large and, with a larger significant wave height, SURV2 could have approximately the same surge response as sea-state SURV1.

The fact that sea-state SURV1 has the fewer peaks, although it is the one with the shorter peak period, suggests that this effect might be caused by second order forces. This is supported by the value of the mean surge position, Table 5.18, which is larger in SURV1 than in SURV2.

When the peak surge values are plotted against the period of the respective surge cycle, Figures 5.32a and 5.32b, the dynamic nature of the effect becomes clear.

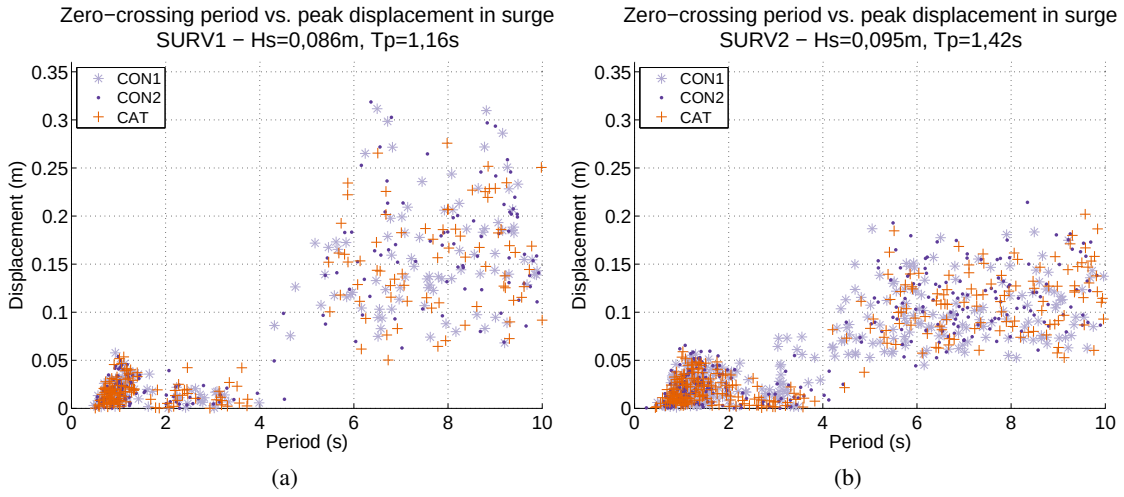

Figure 5.32: Distribution of surge displacements with the corresponding zero-crossing periods of the three configurations in the survival sea-states.

For both sea-states, the concentration of points in the left bottom part of the plots corresponds to wave frequency cycles, since waves are the main excitation mechanism. In sea-state SURV2,

the remaining points are more or less evenly distributed in the plot. However, for the sea-state SURV1, there is a second cluster of points, although not very pronounced, in the 8 s-10 s interval. This period interval encompasses the surge resonance periods of the mooring configurations. This suggests that the jump in the magnitude of the peaks in sea-state SURV1 is caused by excitation in the surge resonance period, which is likely to come from second order forces. It is interesting to note that this second order excitation affects the three configurations similarly.

Extreme displacements and extreme displacement amplitudes (not necessarily the same) might cause damage to several components of a wave energy converter, especially to electrical cables and to the power take-off system. Most designs try to avoid this by incorporating safety mechanisms in the device itself, because it might be challenging to conceive a mooring system that can both allow large displacements in operational conditions and prevent large displacements in survival conditions. Nevertheless it is important to see how the different configurations behave in this aspect.

CON2, which has the largest surge displacements, has also the largest surge amplitudes for both sea-states. In heave and pitch, CON1 has both the largest displacement and the largest displacement amplitude. This should not be a surprise, since CON1 is the best for extracting energy because it allows greater motions of the buoy.

CAT has the smallest displacement and displacement amplitudes for sea-state SURV1 in all degrees of freedom. This is in agreement with the response amplitude operators for $T = 1{,}16$ s, Figures 5.23b and 5.24b, where CAT presents the smallest value. In sea-state SURV2, CAT has the second smallest displacements and displacement amplitudes, but they are very close to the actual smallest values. In extreme displacements, CAT seems to be the configuration with the best performance.

For the purpose of safe station-keeping, the critical factor is the extreme tension in the cables: maximum, minimum and dynamic, Table 5.19. In irregular waves, as defined in [47], the dynamic tension is the difference between the absolute maximum tension and the mean tension.

The time series of the tension in cable 1 for the three configurations in the survival sea-states are plotted in Figure 5.33. Some aspects the behaviour of the configuration can be quickly grasped just by looking at the this figure: CON1 has a low mean tension, with moderate and closely spaced peak tensions; CON2 has a high mean tension, but small and relatively spaced peak tensions; the catenary has low mean tension, with sharp and high peak tensions.

The extreme tensions occur, for all the configurations and for both cables, in sea-state SURV1. This is the sea-state that generates the most intense response in surge, the mode of motion that is most influenced by the mooring system.

CON2 has the highest maximum tension values. Even though the tension behaviour is far from linear, this should be anticipated, as CON2 has also the highest pre-tension.

Within the uncertainty of the measurements, CON2 and CAT have the same maximum tension, around 17 N, which is the absolute maximum tension recorded. This is somewhat surprising, since the pre-tension in CAT is significantly lower than in CON2. The consequence of this is that

Table 5.19: Tension in survival sea-states.p.p - peak-to-peak amplitude. Overbar denotes mean value. Indexes 1 and 2 refer to the cable where the tension was measured.

	SURV1			SURV2		
	$T_P = 1{,}16\,s$			$T_P = 1{,}42\,s$		
Parameter	CON1	CON2	CAT	CON1	CON2	CAT
$\overline{\tau}_1$ ($\pm$0,2N)	3,6	11,2	3,8	3,2	11,0	3,4
max τ_1 ($\pm$0,2N)	11,0	17,3	17,5	9,6	14,8	11,2
min τ_1 ($\pm$0,2N)	0,0	6,5	0,2	0,0	7,8	0,3
τ_{dyn1} ($\pm$0,3N)	7,4	6,2	13,7	6,4	3,9	7,8
$\overline{\tau}_2$ ($\pm$0,2N)	2,3	10,5	2,4	2,6	10,7	2,6
max τ_2 ($\pm$0,2N)	8,9	15,1	8,6	8,0	13,6	6,6
min τ_2 ($\pm$0,2N)	0,0	5,7	0,5	0,0	7,1	0,7
τ_{dyn2} ($\pm$0,3N)	6,5	4,6	6,2	5,4	2,8	4,0

although CAT has a lower pre-tension, it would have to be designed to withstand the same forces as CON2.

In CON1 and in CAT the minimum tension in both cables and in both sea-states is practically 0,0 N. CON2, on the other hand, never presented tensions below 9,2 N. Keeping the cables under tension is important to avoid snap loads and local compression in the cables and CON2 is the only one that meets this requirement.

The dynamic tensions in CON1 and in CAT are larger than in CON2. In fact, in CON1 and in CAT the dynamic tension is almost as large as the maximum tension, while in CON2 the dynamic tension is around half of the maximum tension. This is the direct result of CON1 and CAT allowing the tension to go to 0 N, which results in snap loads. This can be seen more clearly in Figure 5.34, where peak and dynamic tensions are plotted, for each configuration, by the rank of their peak tensions: the higher tensions are always associated with high dynamic tensions.

CON2 is probably the best configuration when it comes to tension in the cables because it has the smallest dynamic loading and its mooring components have to resist peak loads that are not much higher than the mean load.

Overall, CON1 stands out as a good choice to maximize power production, but it has a poor performance in tension in the cables. CON2, being a hybrid between a compact configuration such as CON1 and a heavy configuration such as CAT, gathers the strong points from both. It seems to be a good compromise solution, with smaller values of extracted power than CON1 (yet higher than CAT), but with an excellent performance of the dynamic behaviour of the mooring cables. CAT has the best performance in minimizing the extreme displacements and displacement amplitudes, which is important mostly for surge, where active mechanisms to protect wave energy converters might not be feasible. However, it has the worst performance in power extraction and generates very high dynamic tensions. Additionally, it takes a lot of space in the seabed.

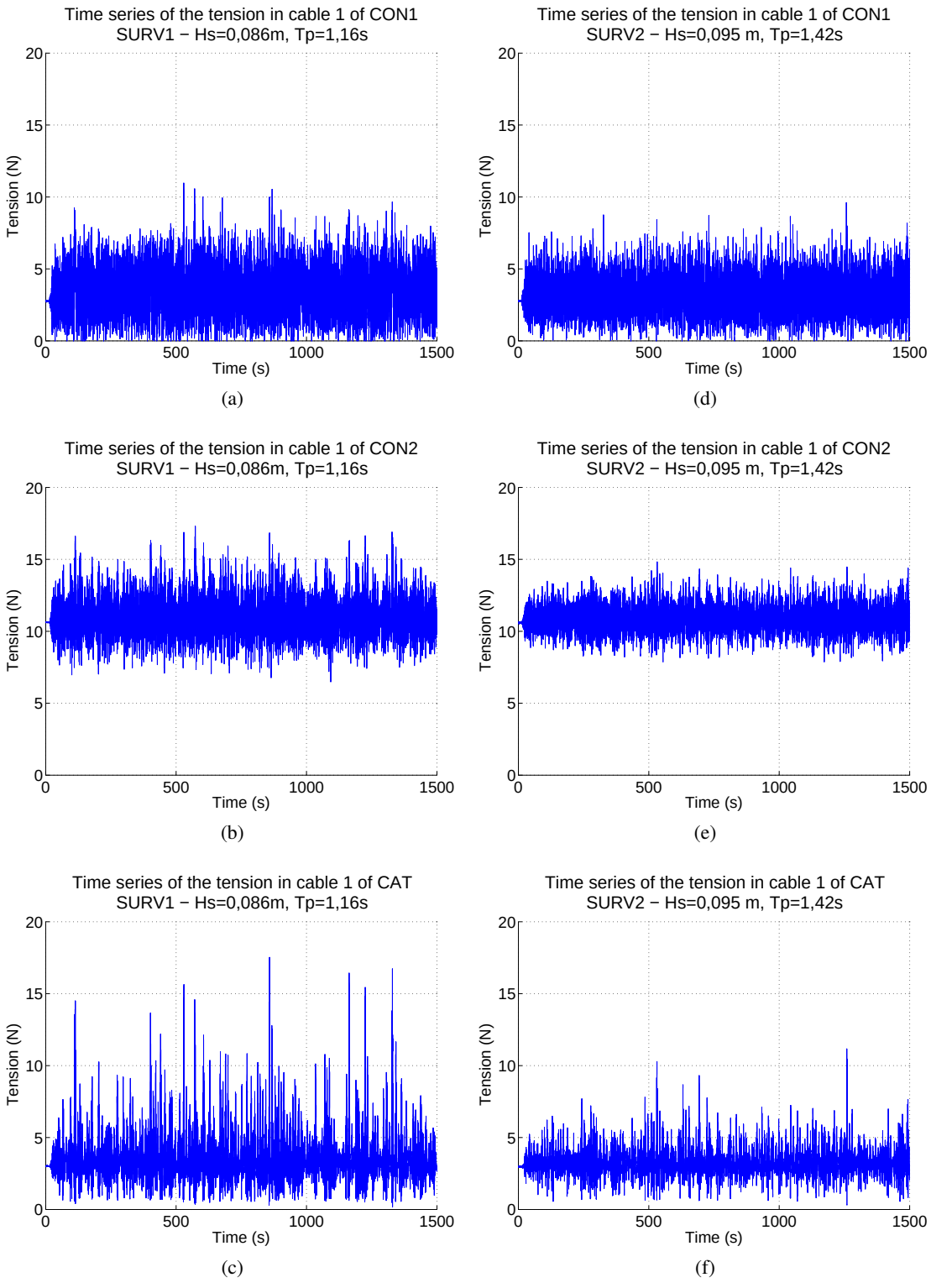

Figure 5.33: Time series of the tension in cable 1 in the survival sea-states. (a) - (c) SURV1; (d) - (f) SURV2.

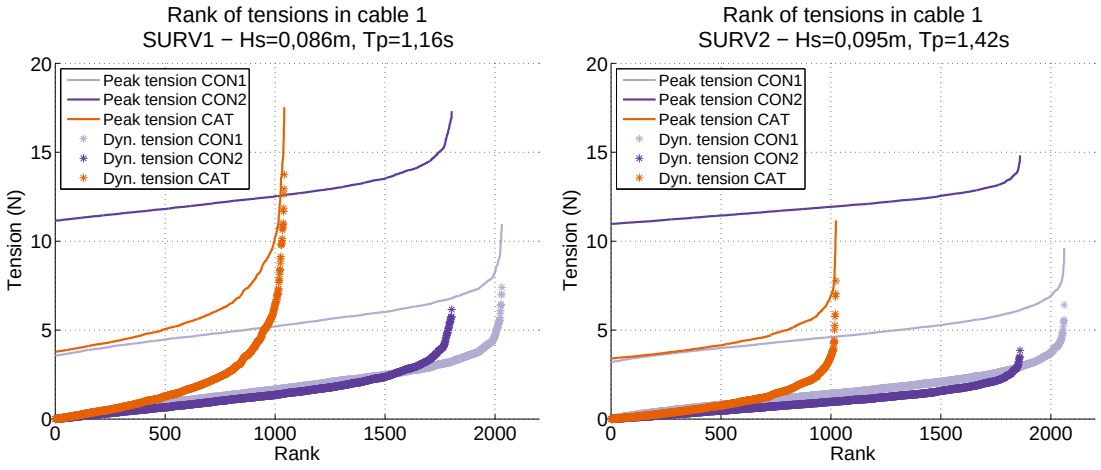

Figure 5.34: Rank of peak tensions and associated dynamic tensions for the three configurations in survival sea-states. (a) SURV1; (b) SURV2

5.7 Additional Remarks

The choice of the best configuration depends also on other factors, such as weather variability, restrictions related to the impact of certain types of anchors or mooring configurations on the seabed, etc. In sheltered regions or in regions where the difference between operational and survival conditions is not very large, mooring systems like CON1 might perform better than in the tests presented here, when it comes to keeping the cables under tension. The type of soil might hinder the use of drag embedment anchors or anchors resisting vertical loads, which would not allow some of the configurations to be used at all.

The position of the attachment point of the mooring cables (fairlead) has an influence in the dynamic behaviour of wave energy converters. Attaching all the mooring cables to a single point on the device would decouple the pitch motion from the motions of the mooring cables, which could improve power extraction in pitch or, at least, make it less dependent on the mooring system. The irregular tests presented here were performed using long crested waves acting on a single device without power take-off. When the devices are set-up in dense arrays and subjected to short-crested waves, both the displacements of the devices and the tensions in the cables will be magnified [86]. The use of a power take-off in operational conditions will also increase the tensions in the cables and the surge drift, when compared to the results presented [50].

Despite the differences between configurations, some of the results, such as the response amplitude operators, show only small variations between configurations. On the one hand, this might mean that the configurations have little effect on the dynamics of the buoy. On the other hand, this might mean that the results are dominated by the large size and mass of the buoy compared to the size of the other components of the model, due to the use of a distorted scale.

As mentioned in section 5.1, tests were performed to assess sensitivity of the results of the compact configurations to variations of their properties. These results could not be presented here, but they will be the subject of a future publication.

Finally, each sea-state in the irregular wave tests had only one random phase realisation, which was used for the three configurations (but different realisations between sea-states). Being a random event, several realisations should have been done for each sea-state ([47] requires at least 10) in order to remove the variability of the results. This was not done due to the limited time available for testing. As a consequence, and because the results do not have a very large variation between the three configurations, there will be some uncertainty in the conclusions.

5.8 Conclusions

Three mooring configurations for wave energy converters were tested in physical models and the results presented. The configurations were: (i) a compact mooring arrangement composed of a synthetic cable with an intermediate floater (CON1); (ii) a compact mooring configuration composed of a synthetic cable with a floater and a clumpweight, creating a zig-zag pattern (CON2); and (iii) a catenary (CAT).

The parameters analysed included those commonly used in the design of mooring systems, such as maximum surge displacement or maximum loads in the cables, but also parameters relevant to wave energy converters, such as the mean squared velocity in each mode of motion (to estimate power extraction) or peak-to-peak amplitudes (to estimate extreme loads in the power take-off).

CON1 provided the best results for power extraction and had the least interference in the heave motion (where its natural period is almost the same as for the buoy floating freely). This happens because the vertical motion of the wave energy converter is decoupled from the motions of the mooring cables. However, this configuration was not so good at maintaining the tension in cables and had high dynamic tensions in extreme conditions.

CON2 did not have as good a performance in power extraction as CON1, but it proved to be superior in handling the tension in the cables. It was able to keep the cable under tension at all times, while simultaneously minimising the dynamic tension. It had also the smallest impact in the natural pitch period. In general, it seems to be a good compromise between CON1 and CAT, combining the strong points of both with its own strong points, in a globally optimised solution.

CAT had a good performance in extreme sea-states, where it limited the maximum displacements and the maximum displacement amplitudes. The downside of this is that it also had the worst performance in power extraction. Like CON1, it was not able to keep the cable under tension at all times and, additionally, it had the largest dynamic tension, leading to the highest maximum tension. It had also, by far, the largest footprint of the three configurations, which results in added costs and environmental impact. Still, even though it has not been especially designed for wave energy converters, CAT might have an acceptable performance, depending on the working principle of the device and on the sea-states in which it should operate.

In spite of the ranking of each configuration for each parameter, the differences between the configurations are not large in any situation.

Chapter 6

Conclusions

Three major outcomes were obtained with this thesis: (i) a numerical model for the simulation of mooring cables; (ii) a technique to track the motions of mooring cables in small scale models; and (iii) the physical model study of mooring configurations for offshore wave energy converters. These results try to answer the needs, outlined in the Introduction, of new tools for the study and development of mooring systems for wave energy converters and of an improved understanding of their dynamic behaviour.

The numerical model developed used the spectral/*hp*-element discontinuous Galerkin method to solve the partial differential equation of perfectly flexible cables. It was able to reproduce both analytical and experimental results with remarkable quality. The model did not perform so well in the simulation of a physical model of a moored buoy. However, this cannot be fully attributed to the numerical model. On the contrary, it is probably the result of having used linear potential theory to simulate the dynamics of the buoy (which does not account for important second order effects) and of the considerable uncertainty in some of the data measured in the physical model experiments.

Due to its higher order discontinuous formulation, the numerical model demonstrated exponential convergence to the solution and evidenced the ability to capture shocks, in the form of peak tensions. These goals were targeted from the beginning. Additionally, the use of a discontinuous formulation resulted in the mass matrix of the numerical model being block diagonal, which can be inverted more efficiently than the sparse matrices of continuous formulations. All of these characteristics result in the numerical model being capable of providing high accuracy solutions using coarse discretisations. Theoretically, it is also possible to obtain faster computational times using this numerical model than lower order or continuous ones. However, this very much depends on the time-marching scheme used and on the programming language in which the numerical model is coded. Higher order methods require smaller time-steps than lower order ones, which might counteract the gain of using coarser discretisations.

The experimental technique to track mooring cables was able to capture the full length of a mooring cable in a wave tank when the buoy it secured was excited by waves. As it captured the full length of the cable, it also captured singularities that would remain undetected by techniques

tracking a discrete set of points along the cable. An example of such singularity was the break in the slope of the cable at the point where it touches the floor of the wave tank, while it was moving back and forth.

The algorithm developed to process the videos proved to be robust enough to work even when visibility conditions were far from ideal. However, in spite of its robustness, some care was still required in the preparation of the experimental set-up. More specifically, when viewed from the camera, the experimental set-up cannot have any detail in the vicinity of the cable with a dimension similar to the thickness of the cable. It was also necessary to ensure enough contrast between the cable and the background of the image.

The range of application of the technique is wide, from concept design to fundamental research on mooring cable dynamics. By outputting the geometry of cables as a function of time, this technique provides data that was previously hard to obtain. This information can be used to validate and calibrate numerical models, to determine the regions where the cable is mostly likely to be damaged by dragging or rubbing against the seabed, etc.

By post-processing the videos it is possible to determine the velocity and the acceleration of desired points along the cable. When this is combined with measurements of water velocity in the vicinity of the cable, it becomes possible to study the hydrodynamic drag and inertia effects of mooring cables.

Using the common measurements of water surface elevation and tension in the cable, the data provided by the technique allows deeper studies of phenomena such as snap loads, shock waves caused by the cable hitting the seabed, correlation of the tension in the cable with its geometry and velocity, with the wave phase, etc.

Although applied only in a two dimensional experiment, there is no inherent limitation preventing the use of the technique in three-dimensional cases.

The physical model experiments of mooring systems analysed three different configurations: CON1, using taut synthetic cables with a floater near the surface; CON2, using taut synthetic cables with a floater and a clumpweight creating a zig-zag shape; and CAT, a chain catenary.

The general conclusion of the experiments is that no single mooring configuration can be selected as the absolute best to secure a floating wave energy converter. All the configurations have advantages that cannot be matched by the others, and their relevance depends on many parameters, of which the type of wave energy converter is just one.

CON1, using taut cables and floaters, allowed motion dependent devices to have the best performance in power extraction because it allowed larger motions, but this might not be so important for motion independent devices. Being compact it used little material, had a reduced weight and allowed a dense arrangement of devices in arrays, all of which are important in reducing the cost of deployment. This configuration was also the one causing the smaller difference between the dynamic behaviour of the free buoy and of the moored buoy, so it is the one which allows developers to design a wave energy converter with the least concern about the impact of the mooring system. However, it was not so good at coping with high dynamic tensions and extreme displacements.

CON2, using taut cables, floaters and clumpweights did not perform as well as CON1 in terms of energy extraction, but the difference was small. However, it was the best configuration at keeping the dynamic tensions low, and it was the only one that was able to prevent the mooring cables from getting slack. Like CON1, it has several advantages because it is compact, but more material is required for clumpweights, which also make it heavier and, therefore, more expensive than CON1.

In comparison with CON1 and CON2, CAT had the worst performance when it came to allowing energy to be extracted by motion dependent devices, but it was the best at preventing extreme displacements. Like CON1 it was susceptible to high dynamic tensions and, some times, allowed the cables to become slack. An apparent disadvantage when compared to CON1 and CON2 is that it occupied a considerable space on the seabed and does not allow devices to be deployed in dense arrays. However, since it uses cheaper anchoring technology than CON1 and CON2, and it is an already established technology, it can well be a good choice for motion independent devices.

Chapter 7

Suggested Future Developments

7.1 Numerical Model for Mooring Cables

One of the most important subjects to be analysed in the numerical model is the existence of high frequency ripples. These are especially apparent when the tension is low and when the cable impacts the ground. It is not known whether these are physical phenomena captured by the numerical model or numerical artefacts that should be dealt with. For this it will likely be necessary the development of improved models describing the interaction between the cable and the ground, to eliminate this as a possible cause.

It is also suggested that the results of the numerical model be compared with more experimental data. This data should come from simple experiments, with high accuracy measurements and broad parametric variations. There should be a reduced number of variables influencing the behaviour of the cables in the experiments, and complex physical models, such as the case of the moored buoy used in this work, should be avoided. Possible set-ups include the use of a motor to drive one end of the cable in a periodic motion. Only after the conduction of these tests, and the nuances of the numerical model are thoroughly investigated and well understood, should its results be compared with complex physical models: first with a cable subjected only to waves, then subjected to both waves and forced motions of the top end, and finally subjected to waves while mooring a simple buoy.

Also required is the formal demonstration of the properties of the numerical model, namely its convergence and shock capturing ability, as well as a more thorough study of the non-standard stabilisation parameter λ_2.

For improved performance it is suggested the application of implicit time-stepping schemes and coding the model in languages such as Fortran or C++, although this is more a technical issue.

7.2 Tracking Technique for Mooring Cables in Physical Models

Reducing the error associated with the technique is the foremost important development to achieve engineering and scientific quality. This will require the use of equipment with enhanced optical quality than the one used in this work. After this, the next step, if needed, is the development or the application of improved procedures to linearise the camera and calibrate the experimental set-up. The complexity of the work required for this task depends on the optics used and on their quality.

Also necessary, even with high-quality optical equipment, is development calibration procedures, that can determine how the error, the distortion and the calibration factors are distributed across the image, and estimate local corrections and conversion factors.

The algorithm should be expanded so that it becomes able to track single and multiple segment cables, with floaters and clumpweights, in three dimensions. This requires more the application of already existing knowledge than carrying out research, but it is vital for the technique to be truly powerful.

The possibility of tracking the trajectory of specified points on the cable after acquiring the videos, as well as of determining the velocity and acceleration of all the sections of the cable, should also be included in the algorithm, instead of being a post-processing step. Once this achieved, the technique can be used to its full potential by combining it with measurements water velocity around the cable.

Sub-pixel interpolation, although not critical, will also be an interesting development.

Some simplification of the methods should also be considered, aimed at reducing the work required by the operator using the technique. This should include the automatic detection of the cable in the videos and the elimination of the need to linearise the camera for each experiment.

7.3 Experimental Work

There are two important improvements that are strongly suggested. One is the determination of the hydrodynamic properties of the buoy and of the mooring cables, separately, for different oscillating frequencies, with and without waves. This will allow a better use of the experimental results, since it will be possible to estimate with much greater accuracy the impact of the mooring configurations. The other is the test of the configurations with different phase realisations for the same sea-state conditions.

It is also important that the mooring configurations be tested with different directions of the incoming waves and with different positions of the attachments of the cables to the hull. Variations on the pre-tension have been tested, but not yet fully analysed. Other parametric variations can be imagined to be tested with the same physical model. And, of course, it can even be suggested the definition of new configurations for analysis.

Considering a wider variation of the experimental set-up, it is necessary to test the configurations in properly scaled models, instead of distorted ones. This task can be considerably difficult

because it requires dynamic scaling of the stiffness of the cables, of the floater and of the clump-weights.

The configurations should ultimately be tested in arrays, which will require large wave tanks, in order to examine the interaction between devices. A power take-off can be included in future experiments. This should be done with some care, since it causes changes in the dynamics of the buoy and reduces the scope of the conclusions to specific types of power take-off system.

Appendix A

Mooring Design

A.1 Design Loads and Displacements

Water depth: 0,900 m
x_{max} (20% of the water depth) = 0,180 m $\approx$ 0,200 m
Maximum significant wave height of the design sea-states, $H_{s-\max} = 0{,}0950\,\text{m}$
Maximum expected wave height $H_{max} = 2H_{s-\max} = 0{,}190\,\text{m} \approx 0{,}200\,\text{m}$

The first order (wave frequency) displacements of the free buoy, x_w, in regular waves were estimated using linear potential theory and are presented in Table A.1.

Table A.1: First order horizonal displacements of the free buoy estimated using linear potential theory.

T(s)	x_w(m)
0,9	0,058
1,1	0,080
1,3	0,050
1,8	0,099

$x_\text{w} = 0{,}099\,\text{m} \approx 0{,}100\,\text{m}$
$x_\text{s} = x_{max} - x_\text{w} = 0{,}100\,\text{m}$

$$F_{xs} = \frac{2}{3}\rho_\text{w} g \left(\frac{H_\text{s}^*}{2}\right)^2 r \tag{A.1}$$

where H_s^* is an increased value of the maximum significant wave height, to account for the effect of the slowly varying forces. The parameters used in equation A.1 and the magnitude of the second order drift forces are presented in Table A.2.

Table A.2: Parameters for the estimation of the second order wave forces.

Parameter	Value
ρ_{w} (kg/m^3)	1000
g (m/s^2)	9,81
H_{s}^* (m)	0,100
r (m)	0,257 25
F_{xs} (N)	4,0875

The mooring systems must be able to provide a horizontal restoring force of at least 4,1 N when the buoy is displaced horizontally from rest position by 0,100 m, which is equivalent to a horizontal secant stiffness of 41 N/m.

A.2 Equations of Static Equilibrium of the Mooring Configurations

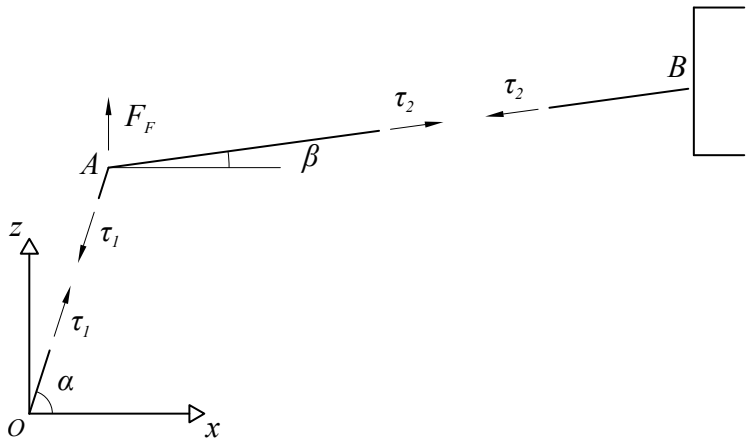

Figure A.1: Free body diagram for CON1. F_{F} - buoyancy force of the floaters.

$$\overline{OA}^2 = x_A^2 + z_A^2 \tag{A.2}$$

$$\overline{AB}^2 = (x_B - x_A)^2 + (z_B - z_A)^2 \tag{A.3}$$

$$\tau_1 \sin(\alpha) = F_{\mathrm{F}} + \tau_2 \sin(\beta) \tag{A.4}$$

$$\tau_1 \cos(\alpha) = \tau_2 \cos(\beta) \tag{A.5}$$

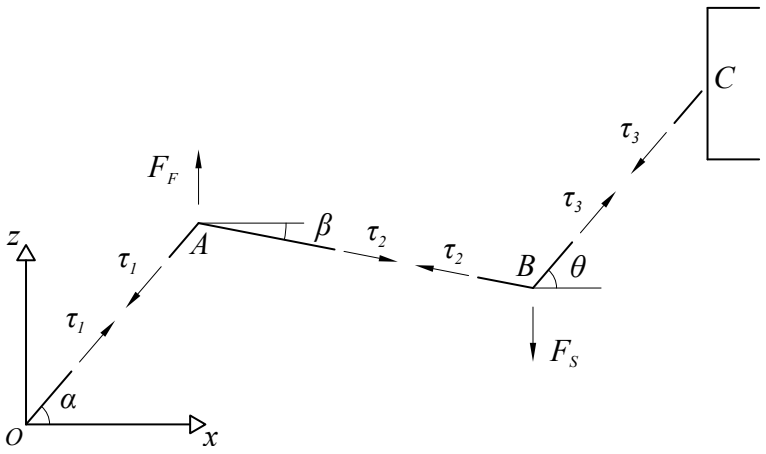

Figure A.2: Free body diagram for CON2. F_{F} - buoyancy force of the floaters; F_{S} - submerged weight of the clumpweights.

$$\overline{OA}^2 = x_A^2 + z_A^2 \tag{A.6}$$

$$\overline{AB}^2 = (x_B - x_A)^2 + (z_B - z_A)^2 \tag{A.7}$$

$$\overline{BC}^2 = (x_C - x_B)^2 + (z_C - z_B)^2 \tag{A.8}$$

$$\tau_1 \sin(\alpha) = F_F + T_2 \sin(\beta) \tag{A.9}$$

$$\tau_1 \cos(\alpha) = \tau_2 \cos(\beta) \tag{A.10}$$

$$\tau_2 \cos(\beta) = \tau_3 \cos(\theta) \tag{A.11}$$

$$F_F = \tau_1 \sin(\alpha) + \tau_2 \sin(\beta) \tag{A.12}$$

$$F_{\mathrm{S}} = \tau_2 \sin(\beta) + \tau_3 \sin(\theta) \tag{A.13}$$

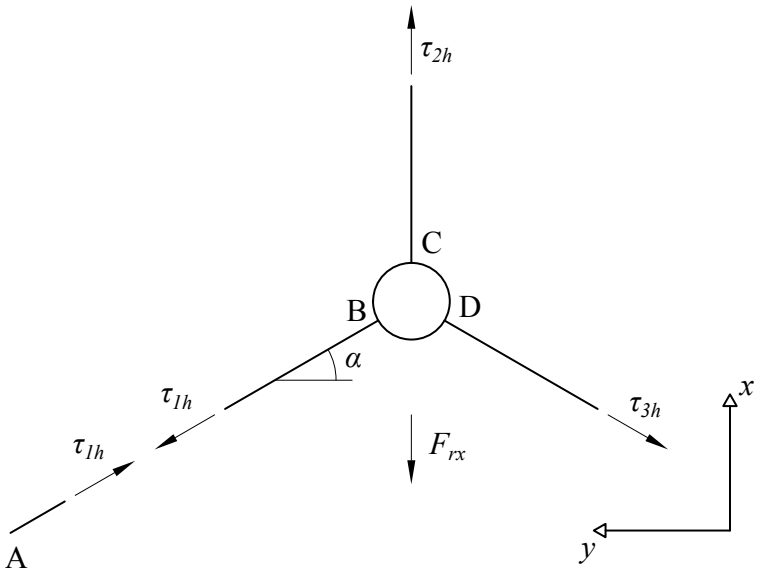

Figure A.3: Horizontal components of the restoring force. F_{rx} - horizontal restoring force in the x direction; τ_{ih} - horizontal component of the tension force in cable i.

$$\tan(\alpha) = (x_B - x_A) / (y_B - y_A) \tag{A.14}$$

$$\tau_{1hx} = \tau_{1hx} \sin(\alpha) \tag{A.15}$$

$$F_{rx} = \tau_{2hx} - (\tau_{1hx} + \tau_{3hx}) \tag{A.16}$$

Appendix B

Sea-state Definition

The operational sea-states were estimated from the data published in [91], while the survival sea-states were taken directly from [10].

The information provided in [91] is subdivided into regions along the Portuguese coast and into incoming wave directions and periods. For the region used as a reference in the physical model experiments (the Portuguese Pilot Zone, near Figueira da Foz), the most relevant data is that of waves comming from the West and North-West quadrants, Tables B.1 and B.2, which account for 90,10 % of all records for this region.

Table B.1: Distribution of wave heights and periods for the Northwest quadrant offshore Figueira da Foz.

	T_P(s)			
H_s(m)	3-7	7-11	11-15	>15
<1	0,5 %	5,6 %	2,4 %	0 %
1-3	1,0 %	25,9 %	38,3 %	2,6 %
3-5	0,0 %	2,0 %	14,1 %	4,8 %
>5	0,0 %	0,0 %	1,1 %	1,6 %
Total		71,3 %		

Table B.2: Distribution of wave heights and periods for the West quadrant offshore Figueira da Foz.

	T_P(s)			
H_s(m)	3-7	7-11	11-15	>15
<1	1,5 %	6,1 %	3,9 %	0,4 %
1-3	1,6 %	24,6 %	37,4 %	4,4 %
3-5	0,0 %	4,1 %	10,6 %	2,5 %
>5	0,0 %	0,0 %	1,2 %	1,8 %
Total		18,8 %		

The total probability of occurrence of each sea-state was obtained by multiplying, for each quadrant, the probability of occurrence of each sea-state in that quadrant by the probability of waves coming from that quadrant. The results from the West and from the North-West quadrants were then added together, Table B.3.

Table B.3: Wave height and period distribution for the combined West and Northwest quadrants offshore Figueira da Foz.

	T_P(s)			
H_s(m)	3-7	7-11	11-15	>15
<1	0,6 %	5,1 %	2,4 %	1,9 %
1-3	1,0 %	23,1 %	34,3 %	4,3 %
3-5	0,0 %	2,2 %	12,0 %	1,6 %
>5	0,0 %	0,0 %	1,0 %	1,5 %

The estimates of available energy were determined by multiplying the probability of occurrence of each sea-state by the respective average power density, $\overline{P}$, (using the average significant wave height and peak period of the range), Table B.4, through the equation:

$$\overline{P} = \frac{{H_{m0}}^2 T_e \rho_w g^2}{64\pi} \tag{B.1}$$

where H_{m0} is the estimate of the significant wave height from the wave spectrum, ρ_w is the water density, g is the magnitude of the acceleration of gravity and $T_e = 1{,}2/1{,}4 T_P$ is the energy period.

Table B.4: Estimated yearly available energy distribution offshore Figueira da Foz (W·year/m).

	T_P(s)			
H_s(m)	5	9	13	>15
0,5	3	49	33	30
2	85	3496	7509	1072
4	0	1330	10536	1626
5	0	0	1380	2333

Two sea-states were selected for the periods with the most available energy ($T_P = 9\,s$ and $T_P = 13\,s$) by taking, for each period, the mean of the two wave heights with the most available energy ($H_s = 2\,m$ and $H_s = 4\,m$), Table B.5.

Table B.5: Selected irregular sea-states.

H_s (m)	T_P (s)
3,0	9,0
3,0	13,0

Appendix C

Usage of Equipment

This annex describes the procedures for calibration and operation of the equipment used in the experimental work.

C.1 Wave Tank

The wave tank of the Faculty of Engineering of the University of Porto is equipped with a multi-paddle piston wave maker, with active absorption. All tests, including the calibration of the wave tank, were run using active absorption.

The calibration of the tank was executed in order to assure that, at the position where the model was to be installed, the wave heights and periods of the sea-states had, as much as possible, the desired values.

To calibrate the tank, all the planned sea-states were run without the model in the wave tank, while wave probes recorded the surface elevation at the position where the model was to be installed. After a sea-state was run, the average wave height (for the regular tests) or the significant wave height (for the irregular tests) was determined. If the measured value of the wave height was off from the desired value, a gain would be applied to the initial value of the target wave height until the desired wave weight was reached.

After each experiment was executed in the wave tank, including the decay tests, the water in the wave tank was allowed to settle for **at least** 20 min for any waves to die out before the next test was started.

C.2 Load Cells and Wave Probes

The data from the load cells and from the wave probes were recorded as voltage in the same computer used to track the motion of the buoy. To achieve this, the analogue voltage signal form the probes and from the load cells was passed through an analogue-to-digital (A\D) converter type PCI-DAS1602/16 manufactured by Measurement Computing. As per recommendation of the

manufacturer [99], the data acquisition computer, the board and all other sensors and electronic equipment were allowed to warm up for at least 15 min before the collection of any data.

During the calibration of the probes and load cells and during the experiments, all electronic sensors, even those that were not needed for the current test, were turned on and their data recorded. This assured that any electric and electronic interference between the different equipments was kept constant throughout all the experimental phases. Although seemingly detrimental, this procedure allowed part of the interference caused by the various equipments to be eliminated using the calibration data, since the conditions of the experiments were the same as during calibration.

C.2.1 Load Cells

The load cells were tested and calibrated before the beginning of the experiments.

To check if the cells were properly water-proofed by the manufacturer, they were submerged for 72 h. Two readings were taken of the signal of each load cell before and after being submerged: one without any load applied to the load cells and the other with a small load. Since the signal values were the same before and after being submerged, Table C.1, it was concluded that the load cells were in full working order.

Table C.1: Readings of the signal of the load cells before and after submergence. LC - Load cell.

Condition	LC1 (before)	LC1 (after)	LC2 (before)	LC2 (after)
No load applied	11,90 mA	11,70 mA	12,01 mA	12,01 mA
Load applied	13,21 mA	13,36 mA	13,34 mA	13,32 mA

For the calibration, each load cell was tightly screwed vertically to a rigid frame and loads with accurately known values were applied to the bottom end of the cells Figure C.1. The list and order of the loads applied are presented in Table C.2.

The voltage corresponding to each load was recorded in the data acquisition computer for a total of 30 s at 100 Hz, totalling 3000 data points. The loads were applied in a random order, listed also in Table C.2, in order to eliminate any bias effect due to changes in temperature, deformation of the load cell, etc,

During the experimental phase, when the test schedule was half completed, the load cells were again calibrated to check if their properties had changed. The difference between the two calibrations was minimal.

C.2.2 Wave Probes

After filling up the wave tank, no test with waves was run in the following 24 h to allow the ionic content of the water to stabilise and reduce the drift of the measurements of the wave probes.

The wave probes were calibrated in the morning of each day any experiments were run. This was required because the sensitivity of the wave probes depends on the properties of the water

Figure C.1: Set-up for calibration of the load cells. The load cell is the small square rectangle on the top of the image, from which a load is hanging on a hook.

Table C.2: Loads applied in the calibration of the load cells.

Order of application	Load ($\pm$0,001 N)
1	1,050
2	97,766
3	2,021
4	19,610
5	68,523
6	5,003
7	0,559
8	9,830
9	48,981
10	0,265
11	0,167
12	87,996
13	39,083
14	0,000
15	0,069
16	58,742

which varied from day to day (for example, the mineral content) and some times even during the same day.

Only three points were used for calibrating the wave probes: 0,000 m, 0,040 m and $-$0,040 m relative to a standard position. These three points were judged to be enough as they correspond to a height difference of 0,080 m, which includes the range of all regular waves and all but the largest third of the irregular waves in the survival sea-states. As the wave probes are highly linear, the use of more points was not required.

The prongs of the wave probes were all parallel to the wave front and care was taken to ensure that the wave probes were aligned with each other and with the wave direction.

After assembly in the wave tank, the mast securing each probe was aligned vertically using a spirit level to minimise any reading errors due to tilts.

As recommended by the manufacturer [93], the distance between the wave probes was measured at the water surface.

C.3 Motion Capture

The motion capture system was assembled, calibrated and operated according the the specifications of the manufacturer [100]. It was only calibrated sporadically when the need arose, which would happen when either the cameras or the infra-red markers on the buoy were accidentally disturbed. After each test the data recorded by the motion capture system was checked in order to ensured that the measurement residue was below 0,002 m. Unfortunately, this value cannot be translated directly into an uncertainty in the position of the buoy, because the manufacturer of the motion tracking system did not provide the necessary information for these calculations.

C.4 Centre of Gravity

The centre of gravity was determined indirectly, by balancing the buoy on a horizontal rotation axis, C_r, and applying an external load, F, to the hull, as illustrated in Figure C.2. Without any load applied, the buoy would (theoretically) remain in a vertical position. By applying the external load to the top of the hull, in a direction 90° to the horizontal rotation axis, a moment is created which causes the buoy to rotate by an angle α.

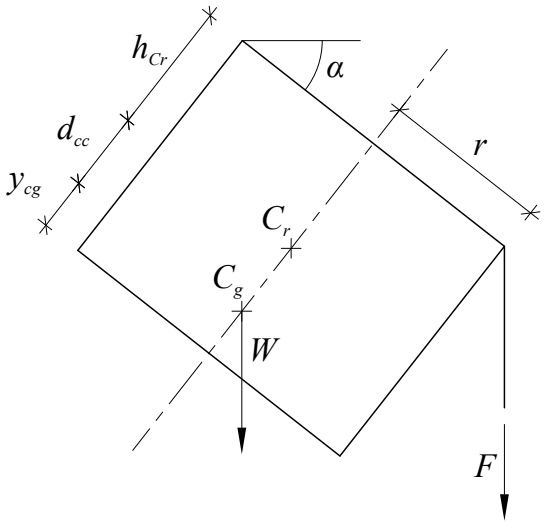

Figure C.2: Schematics of the procedure for the determination of the centre of gravity. C_g - centre of gravity; C_r - centre of rotation.

The moment of the external load is counter-balanced by the moment due to the weight W of the buoy. Knowing α it is possible to determine the vertical distance d_{cc} between the rotation axis and the centre of gravity, C_g, by the following equation:

$$d_{cc} = \frac{F}{W}\left(h_{Cr} + \frac{r}{\tan(\alpha)}\right) \tag{C.1}$$

For the experimental determination of the centre of gravity, the rotation axis was created by two steel wedges screwed to the hull of the buoy at diametrically opposed positions, Figure C.3. The buoy with the wedges was placed on flat horizontal supports, that allowed the buoy to rotate around the tip of the wedges, Figure C.4.

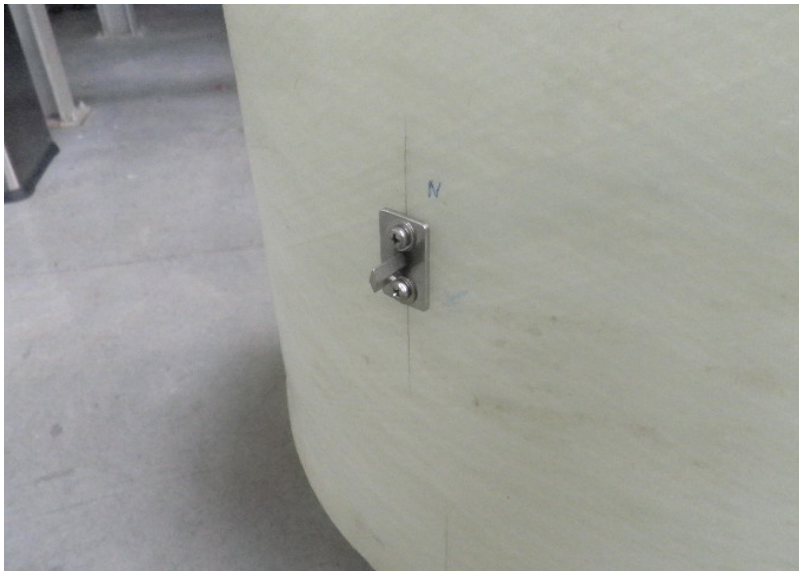

Figure C.3: Steel wedge screwed to the hull of the buoy used in the determination of the centre of gravity.

The rotation angle α caused by the application of the external load was measured with a digital inclinometer placed on the lid of the buoy, as close as possible to its longitudinal axis, Figure C.5. Measurements were made with different loads, applied in random order, first on the front of the buoy and then on the back. The wedges were installed in two different directions 90° to one another (N-S and E-W, Figure C.6), providing a total of four sets of readings.

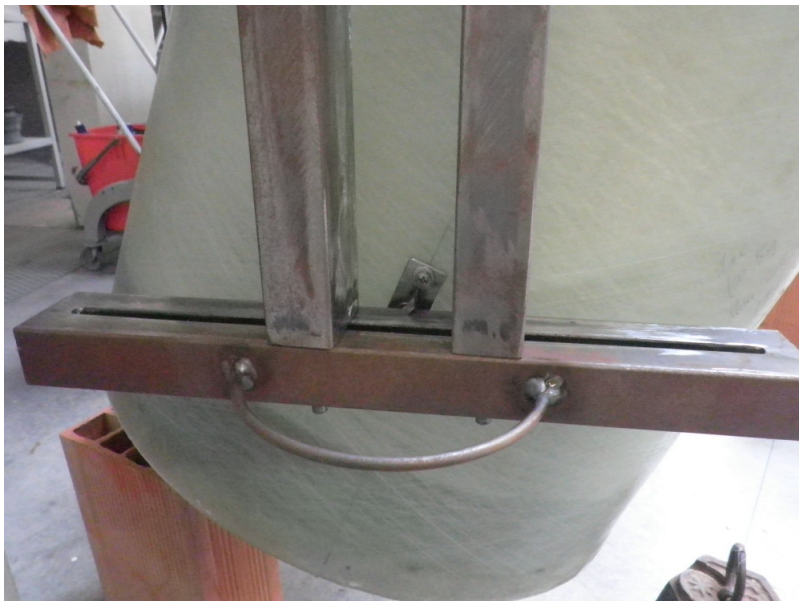

Figure C.4: Buoy with the wedges resting on steel supports.

Figure C.5: Determination of the centre of gravity. An external load (the hexagonal steel mass) is hanging from to the top of the hull by a string and the rotation angle α is measured by the inclinometer on the styrofoam lid. The buoy is resting on the steel frames by its side.

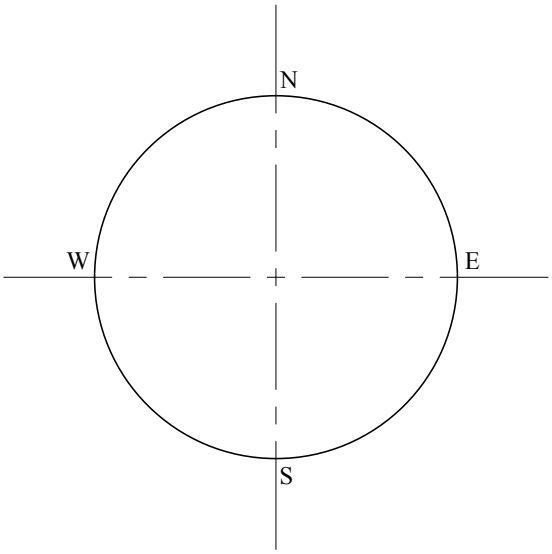

Figure C.6: Nomenclature of the directions of the horizontal axes on the buoy.

C.5 Moment of Inertia

The inertia of the buoy around the horizontal axis through the centre of gravity was determined indirectly, by hanging the buoy by cables attached to the hull and swinging it like a pendulum, Figure C.7.

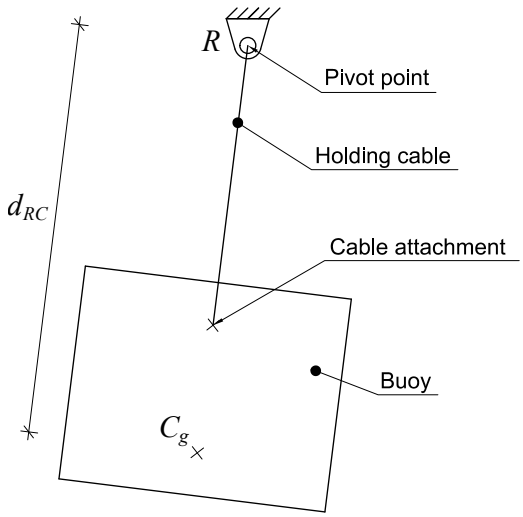

Figure C.7: Schematics of the set-up used to determine the inertia of buoy. d_{RC} - distance from the pivot point R to the centre of gravity C_g.

Knowing the period of the oscillation, the inertia can be determined using the following equation:

$$I_{cg} = \left(\frac{T}{2\pi}\right) W d_{RC} - m_{\mathrm{b}} d_{RC}^2 \tag{C.2}$$

where I_{cg} is the mass moment of inertia through the centre of gravity, T is the oscillation period, W is the weight of the buoy, m_{b} is the mass and d_{RC} is the distance between the centre of gravity and the pivot point of the cables, R.

The cables holding the buoy were attached at diametrically opposed sides, at the same height in order to prevent torsional motions while swinging. To measure the period, a *smartphone* was placed on the lid of the buoy with an application recording the acceleration as a function of time.

C.6 Calibration of the Floaters

The buoyancy of the floaters was calibrated by placing the floaters in a water filled basin and attaching a clumpweight to each one. The clumpweights had been previously calibrated, so their submerged weight was accurately known and was at most 0,05 N off from the desired 10,00 N value. Afterwards, small weights (stainless steel washers and small pieces of lead) were added

to each floater until they would barely be able to float. At this point, the buoyancy of the floaters would be almost exactly the same as the submerged weight of the clumpweights, but with unknown uncertainty.

By trial and error, small pieces of rubber were placed on top of each floater (only one at each try) until it was found the smallest piece that would cause each floater to sink. The uncertainty in the buoyancy of the floaters was assumed to be the submerged weight of the largest piece of rubber used, which was 0,06 N.

Appendix D

Uncertainty Analysis

D.1 General Method

The estimation of the standard uncertainty u_X of a property X follows the division of uncertainty sources into systematic and random. The systematic uncertainty is denoted by b_X, while the random uncertainty, when applicable, is the standard deviation s_X of the values of X [94]. The standard uncertainty is obtained as follows:

$$u_X = \sqrt{{s_X}^2 + b_X^2} \tag{D.1}$$

The expanded uncertainty of $U_{Xk\%}$, with a confidence of $k\%$ is obtained from u_X by:

$$U_{Xk\%} = t_{k\%} u_X \tag{D.2}$$

where $t_{k\%}$ is the coefficient from the Student t-distribution for the $k\%$ probability, with the adequate degrees of freedom. The expanded uncertainty for all values presented in this work is the $U_{X95\%}$. When the number of measurements is equal to, or greater then 10, sometimes the coefficient $t_{k\%}$ was simplified to the value 2 [94].

When the mean value $\overline{X}$ of a sample of X is used to estimate the mean of the parent population, μ_X, the standard deviation of the mean, $s_{\overline{X}}$, is obtained from the standard deviation of the sample of X, s_X, from:

$$s_{\overline{X}} = \frac{s_X}{\sqrt{N}} \tag{D.3}$$

where N is the number of samples used to estimate $\overline{X}$.

In situations where several measurements are required to estimate the value of a variable, the best estimate is taken to be the mean of the measurements, $\overline{X}$. When the measurement is obtained as a single reading from a measuring equipment which, independently of how many repetitions are

made, will always be the same, the best estimate is the value X itself. In this case, the uncertainty of the measuring equipment is assumed to be the $U_{X95\%}$. An example of this could be the weight measured by a scale.

When the final result must be obtained from equations combining different variables, the uncertainty in the final result is propagated from the input variables using the Taylor Series Method. For a property f that is a function of several variables

$$f = f(X_1, X_2, ..., X_i, ..., X_n) \tag{D.4}$$

the uncertainty is estimated in the following way:

$$u_f = \sqrt{\sum \left(\frac{\partial f}{\partial X_i}\right)^2 \left(b_X^i + s_X^i\right)^2} \tag{D.5}$$

where s_X^i and b_X^i are, respectively, the random and the systematic uncertainty in quantity X due to variable i.

D.2 Calibrated Masses

The properties of the masses used to apply the loads in the determination of the centre of gravity and in the calibration of the load cells are listed in Table D.1.

Table D.1: Properties of the masses used in the determination of the centre of gravity and in the calibration of the load cells.

Name	Mass ($\times 10^{-3}$ kg)	$U_{m95\%}$($\times 10^{-3}$ kg)	Weight ($\times 10^{-3}$ N)	$U_{w95\%}$($\times 10^{-3}$ N)
1	1,008	0,001	9,888 48	0,009 81
2	2,030	0,001	19,914 30	0,009 81
5	5,011	0,001	49,157 91	0,009 81
10	10,006	0,001	98,158 86	0,009 81
20	20,038	0,001	196,572 78	0,009 81
50	49,447	0,001	485,075 07	0,009 81
100	99,716	0,001	978,213 96	0,009 81
200	198,55	0,01	1947,7755	0,0981
500	502,78	0,01	4932,2718	0,0981
1000	995,36	0,01	9764,4816	0,0981
2000	1992,07	0,01	19 542,2067	0,0981
2000'	1985,3	0,01	19 475,7930	0,0981
5000	4985,86	0,01	48 911,2866	0,0981
Hook	7,1	0,1	69,651	0,981

D.3 Height of the Buoy

The average height of the buoy was determined from four measurements around its perimeter, Table D.2. The uncertainty calculations are presented in Table D.3.

Table D.2: Measurements of the height of the buoy.

Measurement	Value (m)
1	0,4000
2	0,4000
3	0,4015
4	0,4005

Table D.3: Estimation of the uncertainty in the height of the buoy.

Parameter	Value
$\overline{H}_\mathrm{b}$ (m)	0,4005
b_{H_b} (m)	0,0005
s_{H_b} (m)	0,000 707 106 781
$s_{\overline{H}_\mathrm{b}}$ (m)	0,000 408 248 29
u_{H_b} (m)	0,000 645 497 224
$t_{95\%}$	3,182
$U_{H_\mathrm{b}95\%}$ (m)	0,002 053 972 168

D.4 Diameter of the Buoy

The average diameter of the buoy was determined from two measurements at its top, in two orthogonal directions, Table D.4. The uncertainty calculations are presented in Table D.5.

Table D.4: Measurements of the diameter of the buoy.

Measurement	Value (m)
1	0,5145
2	0,5145

Table D.5: Estimation of the uncertainty in the diameter of the buoy.

Parameter	Value
$\overline{D}_{\mathrm{b}}$ (m)	0,5145
$b_{D_{\mathrm{b}}}$ (m)	0,0005
$s_{D_{\mathrm{b}}}$ (m)	0,0000
$s_{\overline{D}_{\mathrm{b}}}$ (m)	0,0000
$u_{D_{\mathrm{b}}}$ (m)	0,0005
$t_{95\%}$	4,3030
$U_{D_{\mathrm{b}}95\%}$ (m)	0,0022

D.5 Determination of the Centre of Gravity

The position of the centre of gravity was estimated using the method described in section C.4, equation C.1:

$$d_{cc} = \frac{F}{W}\left(h_{Cr} + \frac{r}{\tan(\alpha)}\right) \tag{D.6}$$

where the variables d_{cc}, F, W, h_{Cr}, r and α are defined in Figure C.2. The uncertainty in the position of the centre of gravity was estimated using the relations derived below, from equation D.6:

$$u_{d_{cc}i} = \sqrt{\sum\left(\frac{\partial d_{cc}}{\partial X_j}\right)^2 \left(b_{X_j}\right)^2} \tag{D.7}$$

where $u_{d_{cc}i}$ is the uncertainty in the measurement i of distance d_{cc} and X_j are the variables in equation D.6. There is no random uncertainty in the calculation of $u_{d_{cc}i}$ because, for each measurement with a certain applied load, the values of the variables were always the same, no matter how many times the measurement is repeated. The uncertainties $u_{d_{cc}i}$ are condensed into the systematic uncertainty of the estimation of d_{cc} using in the following way:

$$b_{d_{cc}} = \sqrt{\sum\left(u_{d_{cc}i}\right)^2}/N \tag{D.8}$$

where N is the number of measurements. The uncertainty in the position of the centre of gravity relative to the bottom of the buoy, including random uncertainty, is then calculated as demonstrated below:

$$u_{d_{cc}} = \sqrt{\sum \left(b_{d_{cc}}^2 + s_{\bar{d}_{cc}}^2 \right)} \tag{D.9}$$

$$y_{cg} = H_{\mathrm{b}} - (d_{cc} + h_{Cr}) \tag{D.10}$$

$$u_{y_{cg}} = \sqrt{u_{H_{\mathrm{b}}}^2 + u_{d_{cc}}^2 + u_{h_{Cr}}^2} \tag{D.11}$$

The value of the variables used in the determination of the position of the centre of gravity and of its uncertainty are listed in Table D.6. The results obtained for the distance d_{cc} in each measurement are listed in Table D.7. The results of the intermediate calculations of the uncertainty are presented in Tables D.8 and D.9 and the final results of the uncertainty are presented in Table D.10.

Table D.6: Value of the parameters required for the estimation of the uncertainty in the position of the centre of gravity.

Parameter	Value	u_X
Mass, m_{b} (kg)	35,50	0,05
W (N)	348,255	0,4905
r (m)	0,257 25	0,002
α (rad)	-	0,001 745 329 3
F (N)	-	0,000 990 761 4
h_{Cr} (m)	N/A	$5{,}15 \times 10^{-4}$
H_{b} (m)	0,400	$6{,}22 \times 10^{-4}$

Table D.7: Measurements of the distance d_{cc}.

Axis	h_{Cr} (m)	Loads applied	Total mass (kg)	F (N)	$\alpha(^\circ)$	d_{cc}
N-S Forward	0,2015	2000	1992,07	19,542 206 7	8,0	0,114 020 972 6
N-S Forward	0,2015	5000	4985,86	48,911 286 6	21,6	0,119 553 806 7
N-S Forward	0,2015	1000	995,36	9,764 481 6	4,2	0,103 870 118 2
N-S Forward	0,2015	2000+2000'	3977,37	39,017 999 7	16,8	0,118 038 606 3
N-S Forward	0,2015	5000+1000	5981,22	58,675 768 2	26,8	0,119 753 870 7
N-S Forward	0,2015	2000+1000	2987,43	29,306 688 3	11,9	0,119 685 596 2
N-S Backward	0,2015	2000	1992,07	19,542 206 7	6,6	0,136 069 423 5
N-S Backward	0,2015	5000	4985,86	48,911 286 6	20,2	0,126 498 294 1
N-S Backward	0,2015	1000	995,36	9,764 481 6	2,8	0,153 127 263 0
N-S Backward	0,2015	2000+2000'	3977,37	39,017 999 7	15,3	0,127 930 999 7
N-S Backward	0,2015	5000+1000	5981,22	58,675 768 2	25,4	0,125 229 433 6
N-S Backward	0,2015	2000+1000	2987,43	29,306 688 3	10,8	0,130 441 437 4
E-W Forward	0,2020	2000	1992,07	19,542 206 7	7,3	0,124 007 783 2
E-W Forward	0,2020	5000	4985,86	48,911 286 6	20,9	0,122 950 065 7
E-W Forward	0,2020	1000	995,36	9,764 481 6	3,3	0,130 750 391 8
E-W Forward	0,2020	2000+2000'	3977,37	39,017 999 7	16,0	0,123 117 792 7
E-W Forward	0,2020	5000+1000	5981,22	58,675 768 2	26,1	0,122 465 493 5
E-W Forward	0,2020	2000+1000	2987,43	29,306 688 3	11,5	0,123 382 891 0
E-W Backward	0,2020	2000	1992,07	19,542 206 7	7,5	0,120 969 586 8
E-W Backward	0,2020	5000	4985,86	48,911 286 6	21,5	0,120 056 302 6
E-W Backward	0,2020	1000	995,36	9,764 481 6	3,8	0,114 251 477 1
E-W Backward	0,2020	2000+2000'	3977,37	39,017 999 7	16,6	0,119 285 020 0
E-W Backward	0,2020	5000+1000	5981,22	58,675 768 2	26,6	0,120 545 403 3
E-W Backward	0,2020	2000+1000	2987,43	29,306 688 3	12,1	0,117 958 382 4

Table D.8: Partial derivatives of equation D.6 with respect to its variables, for each measurement presented in Table D.7.

Measurement	$\partial d_{cc}/\partial F \times 10^{-3}$ (m/N)	$\partial d_{cc}/\partial h_{Cr} \times 10^{-2}$	$\partial d_{cc}/\partial r \times 10^{-1}$	$\partial d_{cc}/\partial \alpha \times 10^{-1}$ (m/°)	$\partial d_{cc}/\partial W \times 10^{-4}$ (m/N)
1	5,834 600 684	5,611 464 789	3,992 764 666	7,452 826 611	−3,274 065 629
2	2,444 298 954	14,044 676 056	3,547 280 249	2,666 106 791	−3,432 938 699
3	10,637 545 589	2,803 830 986	3,818 091 302	13,447 201 869	−2,982 587 994
4	3,025 234 691	11,203 859 155	3,710 897 185	3,450 100 755	−3,389 430 339
5	2,040 942 528	16,848 507 042	3,335 437 473	2,132 060 882	−3,438 683 455
6	4,083 900 403	8,415 295 775	3,993 344 030	5,091 313 223	−3,436 722 981
7	6,962 848 443	5,611 464 789	4,849 847 306	10,927 247 343	−3,907 177 886
8	2,586 280 242	14,044 676 056	3,817 231 171	3,030 250 166	−3,632 346 819
9	15,682 067 852	2,803 830 986	5,732 849 118	30,226 103 943	−4,396 986 777
10	3,278 768 791	11,203 859 155	4,095 441 147	4,139 357 633	−3,673 486 373
11	2,134 261 509	16,848 507 042	3,548 287 342	2,355 773 690	−3,595 912 006
12	4,450 910 184	8,415 295 775	4,411 452 534	6,165 555 414	−3,745 572 567
13	6,345 638 702	5,611 464 789	4,380 433 545	8,940 924 333	−3,560 832 814
14	2,513 736 078	14,044 676 056	3,677 937 096	2,839 019 433	−3,530 460 890
15	13,390 407 921	2,803 830 986	4,862 727 415	21,767 315 825	−3,754 444 064
16	3,155 410 161	11,203 859 155	3,907 250 024	3,793 559 271	−3,535 277 102
17	2,087 156 202	16,848 507 042	3,439 208 184	2,239 399 337	−3,516 546 596
18	4,210 059 141	8,415 295 775	4,136 250 020	5,446 457 883	−3,542 889 290
19	6,190 170 265	5,611 464 789	4,262 330 675	8,472 982 084	−3,473 592 248
20	2,454 572 572	14,044 676 056	3,565 448 732	2,689 776 809	−3,447 367 663
21	11,700 721 227	2,803 830 986	4,221 370 189	16,421 852 721	−3,280 684 473
22	3,057 179 273	11,203 859 155	3,758 259 829	3,531 326 793	−3,425 220 599
23	2,054 432 469	16,848 507 042	3,364 569 110	2,161 862 105	−3,461 411 992
24	4,024 964 581	8,415 295 775	3,925 384 769	4,926 804 051	−3,387 126 743

Table D.9: Systematic uncertainty due to the different variables of equation D.6 for each measurement presented in Table D.7.

Measurement	$b^{F}_{d_{cc}} \times 10^{-7}$ (m)	$b^{hcr}_{d_{cc}} \times 10^{-5}$ (m)	$b^{r}_{d_{cc}} \times 10^{-4}$ (m)	$b^{\alpha}_{d_{cc}} \times 10^{-4}$ (m)	$b^{W}_{d_{cc}} \times 10^{-4}$ (m)
1	5,780 697 343	3,928 025 352	7,985 529 331	13,007 636 294	−1,605 929 191
2	2,421 717 138	9,831 273 239	7,094 560 498	4,653 234 172	−1,683 856 432
3	10,539 269 926	1,962 681 690	7,636 182 603	23,469 794 779	−1,462 959 411
4	2,997 285 862	7,842 701 408	7,421 794 370	6,021 561 770	−1,662 515 581
5	2,022 087 147	11,793 954 930	6,670 874 945	3,721 148 225	−1,686 674 235
6	4,046 171 022	5,890 707 042	7,986 688 061	8,886 017 900	−1,685 712 622
7	6,898 521 711	3,928 025 352	9,699 694 611	19,071 644 432	−1,916 470 753
8	2,562 386 722	9,831 273 239	7,634 462 342	5,288 784 255	−1,781 666 115
9	15,537 188 041	1,962 681 690	11,465 698 236	52,754 503 385	−2,156 722 014
10	3,248 477 670	7,842 701 408	8,190 882 293	7,224 541 962	−1,801 845 066
11	2,114 543 994	11,793 954 930	7,096 574 684	4,111 600 732	−1,763 794 839
12	4,409 790 159	5,890 707 042	8,822 905 068	10,760 924 218	−1,837 203 344
13	6,287 014 103	3,928 025 352	8,760 867 090	15,604 856 779	−1,746 588 495
14	2,490 512 762	9,831 273 239	7,355 874 192	4,955 023 664	−1,731 691 067
15	13,266 699 759	1,962 681 690	9,725 454 829	37,991 133 048	−1,841 554 813
16	3,126 258 698	7,842 701 408	7,814 500 049	6,621 009 964	−1,734 053 419
17	2,067 873 872	11,793 954 930	6,878 416 368	3,908 489 169	−1,724 866 106
18	4,171 164 234	5,890 707 042	8,272 500 039	9,505 862 264	−1,737 787 197
19	6,132 981 971	3,928 025 352	8,524 661 349	14,788 143 483	−1,703 796 997
20	2,431 895 843	9,831 273 239	7,130 897 463	4,694 546 145	−1,690 933 839
21	11,592 623 347	1,962 681 690	8,442 740 378	28,661 539 926	−1,609 175 734
22	3,028 935 322	7,842 701 408	7,516 519 659	6,163 327 951	−1,680 070 704
23	2,035 452 460	11,793 954 930	6,729 138 220	3,773 161 170	−1,697 822 582
24	3,987 779 682	5,890 707 042	7,850 769 538	8,598 895 228	−1,661 385 668

Table D.10: Estimation of the uncertainty in the position of the centre of gravity of the buoy.

Parameter	Value
$\overline{d}_{cc}$ (m)	0,123 081 684
$s_{d_{cc}}$ (m)	0,009 031 084
$s_{\overline{d}_{cc}}$ (m)	0,001 843 462
$b_{d_{cc}}$ (m)	0,000 390 934
$u_{d_{cc}}$ (m)	0,001 884 458
y_{cg} (m)	0,075 793 316
$u_{y_{cg}}$ (m)	0,002 050 193
$t_{95\%y_{cg}}$ (m)	2
$U_{95\%y_{cg}}$ (m)	0,004 100 386

D.6 Determination of the Moment of Inertia

The moment of inertia about the horizontal axis through the centre of gravity was estimated using the method described in section C.5 and equation C.2:

$$I_{cg} = \left(\frac{T}{2\pi}\right) W d_{RC} - m_{\mathrm{b}} d_{RC}^2 \tag{D.12}$$

(D.13)

where the variables I_{cg}, T, W, d_{RC} and m_{b} have been defined in section C.5 and in Figure C.7. The distance was determined using the relation

$$d_{RC} = d_{cg} + d_c - d_1 - 2e \tag{D.14}$$

and the variables d_{cg}, d_c, d_1 and e are explained in Figure D.1.

The uncertainty in the inertia was estimated using the relations derived below, from equation D.13

The parameters d_c and d_1 were measured at the four points N, S, E and W (see Figure C.6, section C.4) and are listed are in Table D.11. The estimated values of d_{RC} are presented in Table D.12 while the average values of d_{RC} for the two directions $N-S$ and $E-W$ are presented in Table D.13. The uncertainty in d_{RC}, also presented in Table D.13, was estimated using the following equation:

$$u_{d_{RC}} = \sqrt{u_{d_{cg}}^2 + u_{d_c}^2 + u_{d_1}^2 + 2u_e^2} \tag{D.15}$$

The results obtained for the period T in each measurement are listed in Table D.14. The results of the intermediate calculations of the uncertainty are presented in Tables D.15 and D.16 and the final results of the uncertainty are presented in Table D.17.

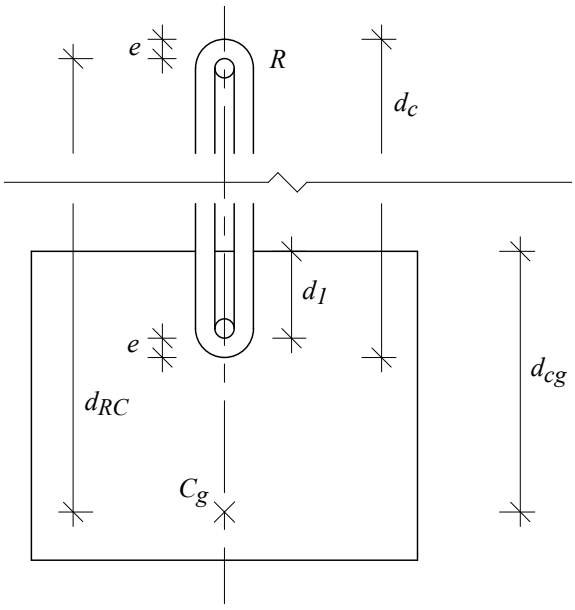

Figure D.1: Estimation of the distance d_{RC}. The cable that goes around the pivot point and around the attachment to the hull has a thickness e.

Table D.11: Measurements of d_c and d_1.

Parameter	Value (m)	b_X (m)
d_{cN}	0,1625	
d_{cS}	0,1600	±0,0005
d_{cE}	0,1605	
d_{cW}	0,1625	
d_{1N}	0,0515	
d_{1S}	0,0490	±0,0005
d_{1E}	0,0505	
d_{1W}	0,0515	
e	0,000 300	±0,000 025

Table D.12: Estimated values of d_{RC}.

Parameter	Value (m)	b_X (m)
$d_{RC/N}$	0,435 11	
$d_{RC/S}$	0,435 11	±0,002 078 294
$d_{RC/E}$	0,434 11	
$d_{RC/W}$	0,435 11	

Table D.13: Average value and uncertainty of d_{RC} for the two directions used in the determination of the moment of inertia of buoy.

Parameter	Value
$\overline{d}_{RC/NS}$ (m)	0,435 11
$\overline{d}_{RC/EO}$ (m)	0,434 61
$b_{d_{RC}}$ (m)	0,002 08
$s_{d_{RC/NS}}$ (m)	0,000 00
$s_{\overline{d}_{RC/NS}}$ (m)	0,000 00
$s_{d_{RC/EO}}$ (m)	0,000 71
$s_{\overline{d}_{RC/EO}}$ (m)	0,000 50
$u_{d_{RC/NS}}$ (m)	0,002 08
$u_{d_{RC/EO}}$ (m)	0,002 19

Table D.14: Average oscillation period of the buoy and systematic uncertainty in the tests for the determination of the moment of inertia.

Measurement	Axis	d_{RC} (m)	T (s)	b_T (m)
1	NS	0,435 11	1,404 380 000	0,000 98
2	NS	0,435 11	1,405 020 000	0,001 64
3	NS	0,435 11	1,406 460 000	0,000 98
4	NS	0,435 11	1,404 200 000	0,000 94
5	NS	0,435 11	1,406 860 000	0,001 20
6	NS	0,435 11	1,416 180 000	0,000 98
7	NS	0,435 11	1,411 260 000	0,000 98
8	NS	0,435 11	1,409 720 000	0,001 30
9	NS	0,435 11	1,402 720 000	0,001 14
10	NS	0,435 11	1,402 820 000	0,001 24
11	EW	0,434 61	1,404 620 000	0,001 22
12	EW	0,434 61	1,404 200 000	0,001 08
13	EW	0,434 61	1,403 840 000	0,001 10
14	EW	0,434 61	1,413 500 000	0,000 94
15	EW	0,434 61	1,406 720 000	0,001 20
16	EW	0,434 61	1,406 280 000	0,000 94
17	EW	0,434 61	1,404 280 000	0,001 48
18	EW	0,434 61	1,405 200 000	0,001 20
19	EW	0,434 61	1,404 760 000	0,001 06
20	EW	0,434 61	1,405 280 000	0,000 98

Table D.15: Partial derivatives of equation D.13 with respect to its variables, for each measurement presented in Table D.14.

Measurement	$\lvert\partial I_{cg}/\partial W\rvert$ (m/s^2)	$\lvert\partial I_{cg}/\partial m\rvert$ (kg/m)	$\lvert\partial I_{cg}/\partial d_{RC}\rvert$ (kg/m)	$\lvert\partial I_{cg}/\partial T\rvert$ (kg/(m s))
1	2,173 745 019	1,893 207 121	0,134 945 068	0,107 808 082
2	2,175 726 696	1,893 207 121	0,134 786 458	0,107 857 212
3	2,180 188 771	1,893 207 121	0,134 429 320	0,107 967 755
4	2,173 187 835	1,893 207 121	0,134 989 664	0,107 794 264
5	2,181 429 047	1,893 207 121	0,134 330 051	0,107 998 461
6	2,210 427 329	1,893 207 121	0,132 009 075	0,108 713 916
7	2,195 095 364	1,893 207 121	0,133 236 221	0,108 336 229
8	2,190 307 299	1,893 207 121	0,133 619 450	0,108 218 010
9	2,168 609 252	1,893 207 121	0,135 356 126	0,107 680 651
10	2,168 918 464	1,893 207 121	0,135 331 377	0,107 688 328
11	2,171 989 263	1,888 858 521	0,134 530 597	0,107 702 599
12	2,170 690 550	1,888 858 521	0,134 634 664	0,107 670 394
13	2,169 577 676	1,888 858 521	0,134 723 839	0,107 642 790
14	2,199 538 681	1,888 858 521	0,132 323 050	0,108 383 494
15	2,178 488 653	1,888 858 521	0,134 009 798	0,107 863 621
16	2,177 126 072	1,888 858 521	0,134 118 982	0,107 829 883
17	2,170 937 894	1,888 858 521	0,134 614 844	0,107 676 528
18	2,173 783 362	1,888 858 521	0,134 386 835	0,107 747 072
19	2,172 422 253	1,888 858 521	0,134 495 902	0,107 713 333
20	2,174 030 882	1,888 858 521	0,134 367 001	0,107 753 206

Table D.16: Systematic uncertainty due to the different variables of equation D.13 for each measurement presented in Table D.14.

Measurement	$b^W_{I_{cg}}$ (kg m^2)	$b^m_{I_{cg}}$ (kg m^2)	$b^{d_{RC}}_{I_{cg}}$ (kg m^2)	$b^T_{I_{cg}}$
1	2,153 662 733	1,893 207 121	2,959 240 211	1,056 519 205
2	2,155 626 103	1,893 207 121	2,955 762 013	1,768 858 278
3	2,160 046 954	1,893 207 121	2,947 930 272	1,058 083 995
4	2,153 110 697	1,893 207 121	2,960 218 169	1,013 266 084
5	2,161 275 772	1,893 207 121	2,945 753 364	1,295 981 530
6	2,190 006 152	1,893 207 121	2,894 856 178	1,065 396 379
7	2,174 815 832	1,893 207 121	2,921 766 527	1,061 695 049
8	2,170 072 001	1,893 207 121	2,930 170 440	1,406 834 136
9	2,148 574 414	1,893 207 121	2,968 254 403	1,227 559 424
10	2,148 880 769	1,893 207 121	2,967 711 681	1,335 335 264
11	2,151 923 198	1,888 858 521	2,950 151 199	1,313 971 704
12	2,150 636 483	1,888 858 521	2,952 433 296	1,162 840 257
13	2,149 533 891	1,888 858 521	2,954 388 835	1,184 070 693
14	2,179 218 098	1,888 858 521	2,901 741 401	1,018 804 843
15	2,158 362 543	1,888 858 521	2,938 730 479	1,294 363 454
16	2,157 012 550	1,888 858 521	2,941 124 805	1,013 600 901
17	2,150 881 542	1,888 858 521	2,951 998 663	1,593 612 620
18	2,153 700 722	1,888 858 521	2,946 998 610	1,292 964 859
19	2,152 352 188	1,888 858 521	2,949 390 349	1,141 761 335
20	2,153 945 955	1,888 858 521	2,946 563 668	1,055 981 416

Table D.17: Estimation of the uncertainty in moment of inertia through the centre of gravity of the buoy.

Parameter	Value
$\bar{I}_{cg}$ (kg m^2)	0,874 651 797
$b_{I_{cg}}$ (kg m^2)	0,007 138 529
$s_{I_{cg}}$ (kg m^2)	0,038 251 001
$s_{\bar{I}_{cg}}$ (kg m^2)	0,008 553 184
$u_{I_{cg}}$ (kg m^2)	0,011 140 716
$t_{95\%y_{cg}}$	2
$U_{95\%y_{cg}}$ (kg m^2)	0,022 281 432

D.7 Clumpweights

The submerged weight of the clumpweights was determined using a Jolly-type scale, with an expanded uncertainty of $U_{95\%} = 0{,}0001$ kgf or 0,000 981 N which is rounded to 0,001 N. The dry mass was determined in a scale with an expanded uncertainty of $U_{95\%} = 0{,}001$ kg. These results are summarised in Table D.18

Table D.18: Uncertainty in the mass and submerged weight of the clumpweights.

	Mass (kg)	Submerged weight (N)
W1	$1{,}115 \pm 0{,}001$	$9{,}968 \pm 0{,}001$
W2	$1{,}125 \pm 0{,}001$	$10{,}051 \pm 0{,}001$
W3	$1{,}113 \pm 0{,}001$	$9{,}959 \pm 0{,}001$

D.8 Floaters

D.8.1 Diameter

The diameter, $D_{\mathrm{F}i}$, of the floaters was determined indirectly from five measurements of the perimeter, $P_{\mathrm{F}i}$, Table D.19 assuming the floaters to be perfect spheres:

$$D_{\mathrm{F}i} = P_{\mathrm{F}i}/\pi \tag{D.16}$$

The uncertainty in the diameter of the floaters was then determined by propagating the uncertainty in the measurements of the perimeter to the diameter, Tables D.20 to D.21.

Table D.19: Measurements of the perimeter of the floaters.

Measurement	P_{F1}(m)	P_{F2}(m)	P_{F3}(m)
1	0,4230	0,4270	0,4200
2	0,4220	0,4220	0,4250
3	0,4280	0,4240	0,4270
4	0,4210	0,4245	0,4205
5	0,4190	0,4205	0,4205
b_P		$\pm$0,0005	

Table D.20: Partial derivatives of equation D.16 with respect to its variables, for each measurement presented in Table D.19.

Measurement	$\partial D_{F1}/\partial P_{F1}$	$\partial D_{F2}/\partial P_{F2}$	$\partial D_{F3}/\partial P_{F3}$
1	0,134 645 082	0,135 918 321	0,133 690 152
2	0,134 326 772	0,134 326 772	0,135 281 702
3	0,136 236 631	0,134 963 392	0,135 918 321
4	0,134 008 462	0,135 122 547	0,133 849 307
5	0,133 371 842	0,133 849 307	0,133 849 307
b_{D_F}		0,000 159 155	

Table D.21: Uncertainty in the diameter of the floaters.

Parameter	F1	F2	F3
$\overline{D}_F$(m)	0,134 517 758	0,134 836 068	0,134 517 758
b_{D_F} (m)	0,000 159 155	0,000 159 155	0,000 159 155
s_{D_F} (m)	0,001 070 014	0,000 790 986	0,001 015 354
$s_{\overline{D}_F}$ (m)	0,000 478 525	0,000 353 740	0,000 454 080
u_{D_F} (m)	0,000 504 298	0,000 387 894	0,000 481 164
$t_{95\%}$		2,776	
$U_{D_F 95\%}$ (m)	0,001 399 930	0,001 076 794	0,001 335 712

D.8.2 Mass and Buoyancy

The mass of the floaters was measured directly with a scale and is presented in Table D.22, so uncertainty is that of the scale.

Table D.22: Mass of the floaters and respective uncertainty.

	Mass (kg)
F1	$0{,}252 \pm 0{,}001$
F2	$0{,}276 \pm 0{,}001$
F3	$0{,}232 \pm 0{,}001$

The buoyancy of the floaters and its uncertainty were measured as indicated in section C.6 and are presented in Table D.23

Table D.23: Buoyancy of the floaters and respective uncertainty.

	Buoyancy (N)
F1	$9{,}97 \pm 0{,}06$
F2	$10{,}05 \pm 0{,}06$
F3	$9{,}96 \pm 0{,}06$

D.9 Chain and Cable Properties

D.9.1 Mass and Submerged Weight per Unit Length

The mass per unit length m_l and the submerged weight per unit length γ_l of the chain and of the synthetic cable were obtained my dividing the mass m_c and the submerged weight γ_c of samples by their length l:

$$m_l = m_c/l \tag{D.17}$$

$$\gamma_l = \gamma_c/l \tag{D.18}$$

The uncertainty in the mass per unit length m_l and in the submerged weight per unit length γ_l were then determined by propagating the uncertainty in the measurements.

Ten samples were used to determine the uncertainty in the of the mass per unit length of the chain, Tables D.24 to D.27, while only five were used to determine its submerged weight per unit length, Tables D.28 to D.31.

In the case of the synthetic cable, since it was extremely lightweight, it was not feasible to use several samples. Instead, a single long sample was used, heavy enough for the scales to measure its mass and submerged weight without significant error and long enough for it to be representative. The results are presented in Table D.32.

Table D.24: Measurement of the mass and length of 10 samples of chain.

Sample	l (m)	m_c (kg)	m_l (kg)
1	1,0005	0,1456	0,145 527 236
2	1,0000	0,1452	0,145 200 000
3	1,0050	0,1448	0,144 079 602
4	0,9995	0,1448	0,144 872 436
5	1,0000	0,1450	0,145 000 000
6	1,0015	0,1449	0,144 682 976
7	1,0035	0,1452	0,144 693 572
8	1,0030	0,1448	0,144 366 899
9	1,0025	0,1444	0,144 039 900
10	0,9995	0,1446	0,144 672 336
b_X	0,0005	0,0001	-

Table D.25: Partial derivatives of equation D.18 with respect to its variables, for each measurement presented in Table D.24.

Sample	$\partial m_\mathrm{l}/\partial m_\mathrm{c}$ (m^{-1})	$\partial m_\mathrm{l}/\partial l$ (kg)
1	0,999 500 250	0,145 454 509
2	1,000 000 000	0,145 200 000
3	0,995 024 876	0,143 362 788
4	1,000 500 250	0,144 944 909
5	1,000 000 000	0,145 000 000
6	0,998 502 247	0,144 466 276
7	0,996 512 207	0,144 188 911
8	0,997 008 973	0,143 935 094
9	0,997 506 234	0,143 680 699
10	1,000 500 250	0,144 744 709

Table D.26: Systematic uncertainty due to the different variables of equation D.18 for each measurement presented in Table D.24.

Sample	$b^{m_\mathrm{c}}_{m_\mathrm{l}}$ (kg)	$b^{l}_{m_\mathrm{l}}$ (m)	b_{m_l} (kg/m)
1	0,000 499 750	0,000 014 545	0,000 499 962
2	0,000 500 000	0,000 014 520	0,000 500 211
3	0,000 497 512	0,000 014 336	0,000 497 719
4	0,000 500 250	0,000 014 494	0,000 500 460
5	0,000 500 000	0,000 014 500	0,000 500 210
6	0,000 499 251	0,000 014 447	0,000 499 460
7	0,000 498 256	0,000 014 419	0,000 498 465
8	0,000 498 504	0,000 014 394	0,000 498 712
9	0,000 498 753	0,000 014 368	0,000 498 960
10	0,000 500 250	0,000 014 474	0,000 500 459

Table D.27: Estimation of the uncertainty in the mass per unit length of the chain.

Parameter	Value
$\overline{m}_\mathrm{l}$ (kg/m)	0,144 713 496
$s_{m\mathrm{l}}$ (kg/m)	0,000 469 623
$s_{\overline{m\mathrm{l}}}$ (kg/m)	0,000 148 508
$b_{m\mathrm{l}}$ (kg/m)	0,000 157 944
$u_{m\mathrm{l}}$ (kg/m)	0,000 216 797
$t_{95\%}$	2
$U_{m\mathrm{l}95\%}$ (kg/m)	0,000 433 594

Table D.28: Measurement of the submerged weight and length of 5 samples of chain.

Sample	l (m)	γ_c (N)	γ_l (N/m)
1	1,0010	1,242 927	1,241 685 315
2	1,0020	1,244 889	1,242 404 192
3	1,0005	1,248 813	1,248 188 906
4	0,9995	1,244 889	1,245 511 756
5	1,0035	1,242 927	1,238 591 928
b_X	0,0005	0,000 981	-

Table D.29: Partial derivatives of equation D.18 with respect to its variables, for each measurement presented in Table D.28.

Sample	$\partial\gamma_l/\partial\gamma_c$ (N^{-1})	$\partial\gamma_l/\partial l$ (N)
1	0,999 000 999	0,001 240 445
2	0,998 003 992	0,001 239 924
3	0,999 500 250	0,001 247 565
4	1,000 500 250	0,001 246 135
5	0,996 512 207	0,001 234 272

Table D.30: Systematic uncertainty due to the different variables of equation D.18 for each measurement presented in Table D.28.

Sample	$b_{\gamma_l}^{\gamma_c}$ (N/m)	$b_{\gamma_l}^{l}$ (N/m)	$b_{\gamma l}$ (N/m)
1	0,000 499 500	0,000 001 217	0,000 499 502
2	0,000 499 002	0,000 001 216	0,000 499 003
3	0,000 499 750	0,000 001 224	0,000 499 752
4	0,000 500 250	0,000 001 222	0,000 500 252
5	0,000 498 256	0,000 001 211	0,000 498 258

Table D.31: Estimation of the uncertainty in the submerged weight per unit length of the chain.

Parameter	Value
$\overline{\gamma}_l$ (kg/m)	1,243 276 419
$s_{\gamma l}$ (kg/m)	0,003 686 669
$s_{\overline{\gamma}_l}$(kg/m)	0,001 648 728
$b_{\gamma l}$(kg/m)	0,000 223 318
$u_{\gamma l}$(kg/m)	0,001 663 784
$t_{\gamma l 95\%}$	2,776
$U_{\gamma l 95\%}$(kg/m)	0,004 619 404

Table D.32: Estimation of the uncertainty in the mass and submerged weight per unit length of the synthetic cable.

Parameter	Value
l (m)	$5{,}980 \pm 0{,}001$
m_c (kg)	$0{,}0189 \pm 0{,}0001$
γ_c (N)	$0{,}0481 \pm 0{,}0001$
$u_{ml} = b_{ml} = U_{ml95\%}$ (kg/m)	0,000 017 0
$u_{\gamma l} = b_{\gamma l} = U_{\gamma l 95\%}$ (N/m)	0,000 166 6

D.9.2 Dimensions of the Chain

Ten chain links were used to estimate the representative dimensions of the chain. The measurements are presented in Table D.33 and the uncertainty estimates are presented in Table D.34.

Table D.33: Measurements of the dimensions of 10 samples of chain links.

Sample	Inner length (m)	Inner height (m)	Thickness (m)
1	0,0205	0,0055	0,0030
2	0,0209	0,0057	0,0030
3	0,0207	0,0059	0,0031
4	0,0204	0,0059	0,0030
5	0,0208	0,0058	0,0030
6	0,0208	0,0056	0,0030
7	0,0206	0,0057	0,0030
8	0,0206	0,0059	0,0029
9	0,0206	0,0057	0,0029
10	0,0205	0,0055	0,0030

Table D.34: Estimation of the uncertainty in the dimensions of the chain links. X represents each of the three dimensions analysed.

Parameter	Inner length	Inner height	Thickness
$\overline{X}$ (m)	0,020 64	0,005 72	0,002 99
s_X (m)	0,000 16	0,000 15	0,000 06
$s_{\overline{X}}$ (m)	0,000 05	0,000 05	0,000 02
b_X(m)		0,000 05	
u_X (m)	0,000 07	0,000 07	0,000 05
$t_{X95\%}$		2,262	
$U_{X95\%}$ (m)	0,000 11	0,000 11	0,000 04

D.9.3 Stiffness

As the laboratories of the Faculty of Engineering of the University of Porto could only execute tensile tests on rigid materials, the determination of the stiffness of the chain and of the synthetic cable was requested to an independent laboratory. Due to the lack of experience of that laboratory on testing cables, there were problems during the tests and inconsistencies in the reported results. Firstly, there is a large variability in the breaking loads of the samples. Secondly, at least two different values of the length of the samples have to be used in the determination of the stiffness: the value in the official report and the value in the unofficial notes of each test, Table D.35. The consequence is that the stiffness results are highly unreliable and must be seen as indicative.

The stiffness was calculated by determining the slope of the initial portion of the force-elongation curve of each test sample and then multiplying it by the sample's length, Table D.36. The uncertainty estimates are presented in Table D.37.

Table D.35: Length of the samples as reported officially, l_r, and as taken from the test notes, l_n.

	Synthetic cable	Chain
l_r (m)	0,0700	0,0700
l_n (m)	0,3775	0,2465

Table D.36: Axial stiffness of the samples of synthetic cable and chain.

	EA-l_n (N)		EA-l_r (N)	
Sample	Synthetic cable	Chain	Synthetic cable	Chain
1	137 874	1 641 143	25 572	466 045
2	171 298	1 153 132	31 771	327 461
3	170 109	1 227 905	31 550	348 695
4	187 855	2 606 617	34 842	740 216
5	146 502	1 585 530	27 172	450 252

Table D.37: Uncertainty estimates in the stiffness of the synthetic cable and of the chain.

Parameter	Value l_n		Value l_r	
	Synthetic cable	Chain	Synthetic cable	Chain
$\overline{EA}$ (N)	162 728	1 642 865	30 181	466 534
s_{EA} (N)	20 250	579 685	3756	164 616
$s_{\overline{EA}} = u_{EA}$ (N)	9056	259 243	1680	73 619
$t_{95\%}$		2,776		
$U_{95\%}$ (N)	25 140	719 658	4663	204 365

D.10 Oscillation Periods

The resonance periods of the different degrees of freedom of the buoy were estimated from the recorded displacement during the decay tests. For each test run it was measured the time span between the first and the last crest of the displacement, which was then divided by the number of complete cycles encompassed by that time span. This was repeated for the troughs, providing two average oscillation periods for each test run.

The uncertainty in the time span Δt_i of test i is the combination of, respectively, the uncertainty in the values of the start, t_{start}, and finishing time, t_{finish}, instants, equation D.20, while the uncertainty in each measured period T_i, is the uncertainty in the time span divided by the number of oscillations, equation D.20:

$$u_{\Delta t_i} = \sqrt{u_{t^2_{\text{start}}} + u_{t^2_{\text{finish}}}} \tag{D.19}$$

$$u_{T_i} = \sqrt{u_{t^2_{\text{start}}} + u_{t^2_{\text{finish}}}}/N \tag{D.20}$$

where N is the number of oscillations.

The uncertainty in the value of the time instants is **at most** half of the value of the acquisition period, which, for the acquisition period of 0,01 s used in the experiments, is 0,005 s. So, the systematic uncertainty for each individual time span measured is always 0,007 071 067 8 s. The minimum number of cycles recorded (which sets the maximum limit for the systematic uncertainty in the resonance period) is 3, resulting in a systematic uncertainty of 0,002 357 022 7 s.

The results of the measured resonance periods and respective uncertainties for the four configurations tested in surge, heave and pitch are presented in Tables D.38 to D.59.

Table D.38: Measured heave resonance periods for the free buoy.

Sample	$T_{i-\text{crest}}$ (s)	$T_{i-\text{trough}}$ (s)
1	1,104016	1,106519
2	1,104307	1,097590
3	1,112994	1,120842
4	1,111026	1,110426
5	1,109427	1,118753
6	1,106851	1,101286
7	1,105955	1,103952
8	1,115628	1,108022
9	1,100137	1,101315
10	1,126604	1,123821
11	1,127088	1,130564
12	1,123439	1,117825
13	1,115760	1,101003
14	1,118023	1,117921
15	1,128684	1,127483
16	1,117765	1,115148
17	1,103160	1,100653
18	1,100802	1,090412
19	1,132639	1,125212
20	1,106823	1,118865
21	1,104750	1,110843

Table D.39: Estimated heave resonance period and uncertainty for the free buoy.

Parameter	Value
$\overline{T}$ (s)	1,112484119
s_T (s)	0,010355250
$s_{\overline{T}}$ (s)	0,001597850
b_T (s)	0,002357023
u_T (s)	0,002847574
$t_{95\%}$	2
$U_{T95\%}$ (s)	0,005695149

Table D.40: Measured pitch resonance periods for the free buoy.

Sample	$T_{i-\text{crest}}$ (s)	$T_{i-\text{trough}}$ (s)
1	1,168 848	1,169 057
2	1,169 153	1,168 644
3	1,168 855	1,169 517
4	1,170 263	1,171 408
5	1,169 383	1,168 853
6	1,167 181	1,168 618
7	1,167 652	1,170 190
8	1,171 605	1,170 704
9	1,174 000	1,172 437
10	1,171 132	1,171 544
11	1,169 527	1,169 528
12	1,167 881	1,167 373
13	1,169 291	1,169 784
14	1,167 593	1,167 632
15	1,169 468	1,170 492
16	1,169 784	1,172 070
17	1,174 548	1,172 571
18	1,170 406	1,170 465
19	1,171 279	1,169 707

Table D.41: Estimated pitch resonance period and uncertainty for the free buoy.

Parameter	Value
$\overline{T}$ (s)	1,169 959 026
s_T (s)	0,001 740 804
$s_{\overline{T}}$ (s)	0,000 282 396
b_T (s)	0,002 357 023
u_T (s)	0,002 373 879
$t_{T95\%}$	2
$U_{T95\%}$ (s)	0,004 747 759

Table D.42: Measured surge resonance periods for CON1.

Sample	$T_{i-\text{crest}}$ (s)	$T_{i-\text{trough}}$ (s)
1	8,558 512	8,565 264
2	8,544 674	8,552 932
3	8,549 998	8,547 866
4	8,558 597	8,561 349
5	8,559 936	8,565 276
6	8,561 259	8,560 222
7	8,564 380	8,551 393
8	8,561 270	8,566 496
9	8,553 642	8,565 413
10	8,557 869	8,558 321
11	8,579 183	8,552 346
12	8,568 646	8,572 719
13	8,577 044	8,583 961

Table D.43: Estimated surge resonance period and uncertainty for CON1.

Parameter	Value
$\overline{T}$ (s)	8,561 483 385
s_T (s)	0,009 549 823
$s_{\overline{T}}$ (s)	0,001 872 874
b_T (s)	0,002 357 023
u_T (s)	0,003 010 517
$t_{95\%}$	2
$U_{T95\%}$ (s)	0,006 021 035

Table D.44: Measured heave resonance periods for CON1.

Sample	$T_{i-\text{crest}}$ (s)	$T_{i-\text{trough}}$ (s)
1	1,096 024	1,104 296
2	1,131 259	1,128 169
3	1,112 264	1,103 730
4	1,145 035	1,187 481
5	1,135 861	1,118 840
6	1,117 670	1,121 126
7	1,157 403	1,133 041
8	1,132 073	1,135 860
9	1,108 991	1,119 755
10	1,113 527	1,104 453
11	1,116 026	1,115 676
12	1,111 145	1,116 299
13	1,090 694	1,070 882
14	1,112 049	1,104 776
15	1,095 777	1,100 009
16	1,117 793	1,119 191
17	1,102 488	1,099 513
18	1,121 274	1,133 295

Table D.45: Estimated heave resonance period and uncertainty for CON1.

Parameter	Value
$\overline{T}$ (s)	1,117 604 028
s_T (s)	0,020 377 729
$s_{\overline{T}}$ (s)	0,003 396 288
b_T (s)	0,002 357 023
u_T (s)	0,004 134 045
$t_{T95\%}$	2
$U_{T95\%}$ (s)	0,008 268 090

Table D.46: Measured pitch resonance periods for CON1.

Sample	$T_{i-\text{crest}}$ (s)	$T_{i-\text{trough}}$ (s)
1	1,145 093	1,144 366
2	1,147 032	1,146 793
3	1,141 374	1,140 530
4	1,144 999	1,145 036
5	1,144 724	1,144 562
6	1,145 513	1,145 474
7	1,144 190	1,144 512
8	1,149 224	1,150 302
9	1,148 573	1,149 758
10	1,145 389	1,145 364
11	1,142 512	1,141 953
12	1,142 302	1,142 331
13	1,143 963	1,144 325
14	1,144 554	1,145 124
15	1,145 469	1,146 098
16	1,150 212	1,151 728
17	1,147 221	1,147 476
18	1,143 900	1,143 726
19	1,143 823	1,145 036

Table D.47: Estimated pitch resonance period and uncertainty for CON1.

Parameter	Value
$\overline{T}$ (s)	1,145 383 184
s_T (s)	0,002 543 456
$s_{\overline{T}}$ (s)	0,000 412 603
b_T (s)	0,002 357 023
u_T (s)	0,002 392 864
$t_{95\%}$	2
$U_{T95\%}$ (s)	0,004 785 728

Table D.48: Measured surge resonance periods for CON2.

Sample	$T_{i-\text{crest}}$ (s)	$T_{i-\text{trough}}$ (s)
1	8,092495	8,230233
2	9,281521	9,278130
3	8,929140	8,918393
4	9,285090	9,285564
5	9,283016	9,287502
6	9,278361	9,280473
7	9,283872	9,284310
8	9,278250	9,287015
9	9,275347	9,289242
10	9,281112	9,291882
11	9,280400	9,290851
12	9,288295	9,284344
13	9,287495	9,289908
14	9,281317	9,289972
15	9,284420	9,287095
16	9,285582	9,285336
17	9,279306	9,295332
18	9,262891	9,263071
19	9,273627	9,266235
20	9,279655	9,287763
21	9,275559	9,278288
22	9,275014	9,283079

Table D.49: Estimated surge resonance period and uncertainty for CON2.

Parameter	Value
$\overline{T}$ (s)	9,214904159
s_T (s)	0,245034969
$s_{\overline{T}}$ (s)	0,037809717
b_T (s)	0,002357023
u_T (s)	0,037883113
$t_{95\%}$	2
$U_{T95\%}$ (s)	0,075766225

Table D.50: Measured heave resonance periods for CON2.

Sample	$T_{i-\text{crest}}$ (s)	$T_{i-\text{trough}}$ (s)
1	1,131 091	1,132 490
2	1,168 234	1,168 301
3	1,145 988	1,146 196
4	1,138 877	1,133 866
5	1,114 005	1,114 734
6	1,136 298	1,131 027
7	1,147 686	1,135 998
8	1,127 448	1,125 681
9	1,141 449	1,137 199
10	1,137 681	1,133 785
11	1,123 963	1,124 826
12	1,137 103	1,136 197
13	1,126 965	1,127 907
14	1,124 734	1,128 347
15	1,126 756	1,132 711
16	1,134 966	1,132 412
17	1,133 840	1,126 524
18	1,132 592	1,133 756
19	1,145 080	1,137 646
20	1,131 713	1,134 805
21	1,117 647	1,122 951
22	1,125 938	1,127 870
23	1,121 623	1,124 388
24	1,116 095	1,120 372

Table D.51: Estimated heave resonance period and uncertainty for CON2.

Parameter	Value
$\overline{T}$ (s)	1,132 453 354
s_T (s)	0,010 948 425
$s_{\overline{T}}$ (s)	0,001 580 269
b_T (s)	0,002 357 023
u_T (s)	0,002 837 747
$t_{95\%}$ (s)	2
$U_{T95\%}$ (s)	0,005 675 493

Table D.52: Measured pitch resonance periods for CON2.

Sample	$T_{i-\text{crest}}$ (s)	$T_{i-\text{trough}}$ (s)
1	1,169787	1,168670
2	1,171517	1,171846
3	1,172021	1,172015
4	1,156619	1,157569
5	1,168642	1,167972
6	1,163188	1,163843
7	1,171503	1,172150
8	1,167627	1,167724
9	1,171052	1,170881
10	1,169115	1,170236
11	1,162492	1,161106
12	1,170392	1,170011
13	1,171019	1,168809
14	1,173042	1,173998
15	1,170888	1,171202
16	1,165168	1,164822
17	1,167877	1,166955
18	1,168271	1,167759
19	1,161730	1,162107
20	1,163626	1,162728
21	1,171278	1,170808

Table D.53: Estimated pitch resonance period and uncertainty for CON2.

Parameter	Value
$\overline{T}$ (s)	1,167858690
s_T (s)	0,004223476
$s_{\overline{T}}$ (s)	0,000651696
b_T (s)	0,002357023
u_T (s)	0,002445458
$t_{95\%}$	2
$U_{T95\%}$ (s)	0,004890916

Table D.54: Measured surge resonance periods for the catenary.

Sample	$T_{i-\text{crest}}$ (s)	$T_{i-\text{trough}}$ (s)
1	9,078 914	9,078 306
2	9,063 779	9,091 057
3	9,093 684	9,100 918
4	9,075 638	9,088 049
5	9,187 799	9,183 755
6	9,086 606	9,120 337
7	9,093 328	9,120 562
8	9,121 051	9,144 284
9	9,118 352	9,136 827
10	9,188 068	9,214 373
11	9,086 606	9,120 337
12	9,128 758	9,142 633
13	9,135 614	9,154 261
14	9,107 804	9,143 823
15	9,106 242	9,156 135
16	9,181 829	9,213 949
17	9,173 577	9,184 917
18	9,113 824	9,143 601
19	9,117 770	9,147 992
20	9,131 754	9,157 986
21	9,227 472	9,233 282

Table D.55: Estimated surge resonance period and uncertainty for the catenary.

Parameter	Value
$\overline{T}$ (s)	9,135 615 548
s_T (s)	0,043 770 031
$s_{\overline{T}}$ (s)	0,006 753 862
b_T (s)	0,002 357 023
u_T (s)	0,007 153 336
$t_{95\%}$	2
$U_{T95\%}$ (s)	0,014 306 671

Table D.56: Measured heave resonance periods for the catenary.

Sample	$T_{i-\text{crest}}$ (s)	$T_{i-\text{trough}}$ (s)
1	1,148662	1,142775
2	1,126058	1,119880
3	1,156484	1,160023
4	1,137993	1,134008
5	1,125456	1,119211
6	1,103790	1,096290
7	1,102856	1,100652
8	1,110291	1,109562
9	1,136071	1,149799
10	1,143903	1,148718
11	1,141938	1,141312
12	1,151259	1,148595
13	1,150070	1,134277
14	1,094876	1,102907

Table D.57: Estimated heave resonance period and uncertainty for the catenary.

Parameter	Value
$\overline{T}$ (s)	1,129918429
s_T (s)	0,020281486
$s_{\overline{T}}$ (s)	0,003832841
b_T (s)	0,002357023
u_T (s)	0,004499580
$t_{95\%}$	2
$U_{95\%}$ (s)	0,008999161

Table D.58: Measured pitch resonance periods for the catenary.

Sample	$T_{i-\text{crest}}$ (s)	$T_{i-\text{trough}}$ (s)
1	1,166 812	1,165 502
2	1,171 127	1,170 462
3	1,171 148	1,169 526
4	1,160 866	1,161 834
5	1,170 053	1,170 263
6	1,119 962	1,128 801
7	1,161 589	1,161 628
8	1,162 648	1,162 660
9	1,174 684	1,176 928
10	1,163 983	1,166 696
11	1,145 374	1,145 054
12	1,162 738	1,168 225
13	1,161 108	1,158 892
14	1,173 560	1,173 854
15	1,171 523	1,171 117
16	1,159 885	1,161 271
17	1,166 628	1,169 367
18	1,164 262	1,164 577
19	1,158 938	1,157 299
20	1,155 988	1,158 095
21	1,170 400	1,170 642
22	1,168 210	1,169 423
23	1,159 135	1,160 738
24	1,169 065	1,167 101
25	1,162 312	1,164 247

Table D.59: Estimated pitch resonance period and uncertainty for the catenary.

Parameter	Value
$\overline{T}$ (s)	1,163 324 000
s_T (s)	0,010 325 421
$s_{\overline{T}}$ (s)	0,001 593 247
b_T (s)	0,002 357 023
u_T (s)	0,002 844 994
$t_{95\%}$	2
$U_{T95\%}$ (s)	0,005 689 988

D.11 Load Cells

The mass of the load cells, including accessories, was measured using a scale with an uncertainty of 0,0001 kg, Table D.60.

Table D.60: Mass of the load cells.

Load cell	Mass (kg)
LC1	0,0131
LC2	0,0141

The reference value adopted for the mass of the load cells was the largest one 0,0141 kg, as this is the value that would cause the largest difference between the real and the theoretical measurements.

D.12 Load Cell Attachments

The mass of the load cell adapters was measured using a scale with an uncertainty of 0,0001 kg, Table D.61. Since there were four different adapters, the average value of the mass and associated uncertainty was estimated, Table D.62.

Table D.61: Mass of the load cell adapters.

Adapter	Mass (kg)
1	0,0561
2	0,0590
3	0,0564
4	0,0571

Table D.62: Average value and uncertainty of the mass of the load cell adapters.

Parameter	Value
$\overline{m}_{adap}$ (kg)	0,057 15
b_{m-adap} (kg)	0,000 10
s_{m-adap} (kg)	0,001 30
$s_{\overline{m}-adap}$ (kg)	0,000 65
$t_{95\%}$	3,182
u_{m-adap} (kg)	0,000 66
$U_{m-adap95\%}$ (kg)	0,002 10

D.13 Draft

The draft, d_b, was estimated indirectly by subtracting readings of the freeboard, f, on four points around the perimeter of the buoy from its height, H_b, Figure D.2 and equation D.21:

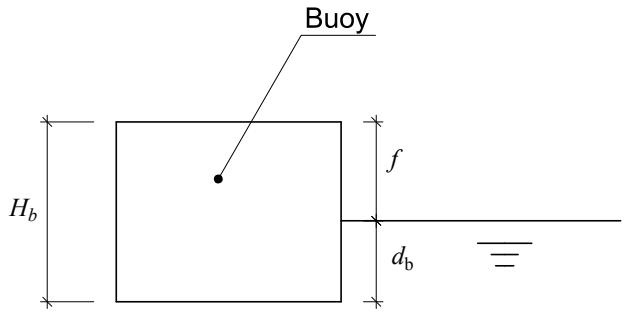

Figure D.2: Variables in the determination of the draft.

$$d_\mathrm{b} = H_\mathrm{b} - f \tag{D.21}$$

The measured values of the freeboard, the calculated values of the draft and its uncertainty for the four configurations tested are presented in Tables D.63 to D.70.

Table D.63: Freeboard and draft of the free buoy.

f (m)	d_b (m)
0,2235	0,1770
0,2255	0,1750
0,2255	0,1750
0,2225	0,1780

Table D.64: Uncertainty in the draft for the free buoy.

Parameter	Value
b_f(m)	0,00050
u_{H_b}(m)	0,00065
$\overline{d}_\mathrm{b}$(m)	0,17625
s_{d_b}(m)	0,00150
$s_{\overline{d}_\mathrm{b}}$(m)	0,00075
u_{d_b}(m)	0,00111
$t_{95\%}$	3,182
$U_{d_\mathrm{b}95\%}$(m)	0,00353

Table D.65: Freeboard and draft of the buoy in CON1.

f (m)	d_b (m)
0,2260	0,1745
0,2220	0,1785
0,2215	0,1790
0,2240	0,1765

Table D.66: Uncertainty in the draft of the buoy in CON1.

Parameter	Value
$b_f(\mathrm{m})$	0,000 50
$u_{H_\mathrm{b}}(\mathrm{m})$	0,000 65
$\overline{d}_\mathrm{b}(\mathrm{m})$	0,177 13
$s_{d_\mathrm{b}}(\mathrm{m})$	0,002 06
$s_{\overline{d}_\mathrm{b}}(\mathrm{m})$	0,001 03
$u_{d_\mathrm{b}}(\mathrm{m})$	0,001 31
$t_{95\%}$	3,182
$U_{d_\mathrm{b}95\%}(\mathrm{m})$	0,004 18

Table D.67: Freeboard and draft of the buoy in CON2.

f (m)	d_b (m)
0,2140	0,1865
0,2120	0,1885
0,2100	0,1905
0,2110	0,1895

Table D.68: Uncertainty in the draft of the buoy in CON2.

Parameter	Value
$b_f(\mathrm{m})$	0,000 50
$u_{H_\mathrm{b}}(\mathrm{m})$	0,000 65
$\overline{d}_\mathrm{b}(\mathrm{m})$	0,188 75
$s_{d_\mathrm{b}}(\mathrm{m})$	0,001 71
$s_{\overline{d}_\mathrm{b}}(\mathrm{m})$	0,000 85
$u_{d_\mathrm{b}}(\mathrm{m})$	0,001 18
$t_{95\%}$	3,182
$U_{H_\mathrm{b}95\%}(\mathrm{m})$	0,003 76

Table D.69: Freeboard and draft of the buoy moored with the catenary.

f (m)	d_b (m)
0,2240	0,1765
0,2190	0,1815
0,2180	0,1825
0,2200	0,1810

Table D.70: Uncertainty in the draft of the buoy moored with the catenary.

Parameter	Value
$b_f(\mathrm{m})$	0,000 50
$u_{d_\mathrm{b}}(\mathrm{m})$	0,000 65
$\overline{d}_\mathrm{b}(\mathrm{m})$	0,180 36
$s_{d_\mathrm{b}}(\mathrm{m})$	0,002 65
$s_{\overline{d}_\mathrm{b}}(\mathrm{m})$	0,001 33
$u_{H_\mathrm{b}}(\mathrm{m})$	0,001 56
$t_{95\%}$	3,182
$U_{d_\mathrm{b}95\%}(\mathrm{m})$	0,004 96

D.14 Calibration Errors

The quantification of the uncertainty associated with calibrations is more involved than the analyses executed in the previous sections. To simplify the analysis, it is necessary to evaluate the error sources, which are:

- the systematic uncertainty in the applied loads (load cells) or displacements (wave probes);
- the random noise in the records;
- the systematic uncertainty caused by the signal conditioning and analogue-to-digital conversion.

Taking into account the error sources, the following assumptions were made:

- in the calibration, there is no random uncertainty in the voltage readings, since each reading was the result of averaging 3000 samples, recorded for 30 s at 100 Hz;
- the systematic errors caused by the signal conditioning and by the analogue-to-digital conversion in the experiments are the same as during calibration (there was no change to the system) and so they cancel out;
- there is random uncertainty in the measurements during the experiments due to the noise in the records, which is quantified by the largest standard deviation of the voltage readings during calibration;
- all calibration points have the same systematic error magnitude, which is equal to largest systematic error determined for the loads or displacements.

The conversion of the voltage readings to force and free surface elevation was made using a straight line estimated by a least squares fit to the calibration points:

$$Y = mV + b \tag{D.22}$$

where V is the voltage reading, m and b are the slope and constant of the straight line determined in the least squares fit and Y is the force or surface elevation value. In these conditions, the evaluation of the uncertainty due to the use of a least squares fit is given by:

$$u_Y = \sqrt{u_{Y-\text{fit}}^2 + \left(\frac{\partial Y}{\partial V}\right)^2 s_V^2} \tag{D.23}$$

where s_V is the random uncertainty in the voltage and $u_{Y-\text{fit}}$ is given by

$$u_{Y-\text{fit}} = \sqrt{s_Y^2 \left(\frac{1}{N} + \frac{\left(V - \overline{V}\right)^2}{s_{VV}} \right)} \tag{D.24}$$

$$s_Y = \sqrt{\frac{\sum_{i=1}^{N} \left(Y_i - mV_i - c\right)^2}{N-2}} \tag{D.25}$$

$$s_{VV} = \sum_{i=1}^{N} X_i^2 - \frac{\left(\sum_{i=1}^{N} V_i\right)^2}{N} \tag{D.26}$$

where V_i is the voltage reading of calibration point i from a total number N of calibration points. The uncertainty due to the fit is then combined with the random and systematic uncertainties in Y and V just like what was done in the previous sections.

D.14.1 Calibration of the Wave Probes

The conversion of voltage to water surface elevation is given by equation D.27:

$$\eta = mV + b \tag{D.27}$$

where η is the water surface elevation. The systematic uncertainty in η is $b_\eta = 0{,}000\,01$ m. Since only three points were used in the calibration of the wave probes, the value of $t_{95\%}$ is 12,706. The parameters of each wave probe calibration are given in Table D.71, while the intermediate calculations of the uncertainty and the final results are given in Tables D.72 and D.73.

Table D.71: Parameters of the least squares fit for each calibration of the wave probes.

Calibration	m (m/V)	b (m)	R^2
cal-12-08-2014	0,028 873 668	−0,002 797 314	0,999 999 125
cal-13-08-2014	0,029 254 055	−0,002 193 480	0,999 994 582
cal-14-08-2014	0,028 308 565	−0,001 855 990	0,999 998 343
cal-18-08-2014	0,029 330 360	−0,002 604 095	0,999 995 200
cal-19-08-2014	0,028 218 085	−0,003 203 104	0,999 996 469
cal-20-08-2014	0,028 081 371	−0,002 063 971	0,999 972 101
cal-21-08-2014	0,028 212 225	−0,002 588 976	0,999 998 470
cal-22-08-2014	0,028 017 494	−0,003 258 077	0,999 999 422
cal-25-08-2014	0,027 997 092	−0,003 300 376	0,999 964 583
cal-26-08-2014-2	0,028 076 652	−0,002 958 296	0,999 963 086
cal-27-08-2014	0,028 365 268	−0,001 964 357	0,999 997 834
cal-28-08-2014	0,028 178 137	−0,002 949 667	0,999 999 633
cal-29-08-2014	0,027 978 028	−0,002 303 572	0,999 983 719
cal-01-09-2014	0,027 557 723	−0,003 043 433	0,999 967 239
cal-02-09-2014	0,027 864 629	−0,001 985 979	0,999 978 493
cal-03-09-2014	0,028 011 992	−0,002 320 114	0,999 992 076
cal-05-09-2014	0,027 907 459	−0,002 285 613	0,999 990 430
cal-08-09-2014	0,027 982 975	−0,002 710 427	0,999 986 506
cal-09-09-2014	0,028 537 199	−0,002 429 117	0,999 972 351
cal-10-09-2014	0,027 829 204	−0,003 015 434	0,999 971 187
cal-11-09-2014	0,028 720 279	−0,002 672 915	0,999 977 131
cal-12-09-2014	0,028 567 063	−0,002 881 163	0,999 998 640
cal-15-09-2014	0,027 118 183	−0,003 076 058	0,999 925 292
cal-16-09-2014	0,027 455 177	−0,002 368 326	0,999 978 512
cal-17-09-2014	0,027 604 804	−0,002 903 947	0,999 987 649

Table D.72: Parameters for the estimation of the uncertainty in the wave probe calibration due to the least squares fit.

Calibration	$u_{\eta-\text{fit}}$ (m)	s_V (V)	$\partial\eta/\partial V \times s_V$ (m)
cal-12-08-2014	0,000 052 926	0,016 938 302	0,000 489 071
cal-13-08-2014	0,000 131 672	0,019 179 370	0,000 561 074
cal-14-08-2014	0,000 072 818	0,016 315 949	0,000 461 881
cal-18-08-2014	0,000 123 942	0,016 055 628	0,000 470 917
cal-19-08-2014	0,000 106 292	0,016 393 480	0,000 462 593
cal-20-08-2014	0,000 298 792	0,015 511 748	0,000 435 591
cal-21-08-2014	0,000 069 977	0,016 218 185	0,000 457 551
cal-22-08-2014	0,000 043 018	0,016 231 172	0,000 454 757
cal-25-08-2014	0,000 336 651	0,017 572 773	0,000 491 987
cal-26-08-2014-2	0,000 343 694	0,016 135 106	0,000 453 020
cal-27-08-2014	0,000 083 249	0,015 453 967	0,000 438 356
cal-28-08-2014	0,000 034 290	0,015 655 376	0,000 441 139
cal-29-08-2014	0,000 228 255	0,015 878 988	0,000 444 263
cal-01-09-2014	0,000 323 785	0,015 348 027	0,000 422 957
cal-02-09-2014	0,000 262 341	0,014 659 314	0,000 408 476
cal-03-09-2014	0,000 159 239	0,014 416 403	0,000 403 832
cal-05-09-2014	0,000 174 996	0,015 005 468	0,000 418 765
cal-08-09-2014	0,000 207 801	0,015 454 355	0,000 432 459
cal-09-09-2014	0,000 297 449	0,016 249 709	0,000 463 721
cal-10-09-2014	0,000 303 649	0,015 271 369	0,000 424 990
cal-11-09-2014	0,000 270 517	0,015 601 780	0,000 448 087
cal-12-09-2014	0,000 065 980	0,016 221 301	0,000 463 395
cal-15-09-2014	0,000 488 942	0,007 887 581	0,000 213 897
cal-16-09-2014	0,000 262 227	0,008 768 118	0,000 240 730
cal-17-09-2014	0,000 198 803	0,009 346 030	0,000 257 995

Table D.73: Estimate of the uncertainty in the calibration of the wave probes.

Calibration	u_η (m)	$U_{\eta 95\%}$ (m)
cal-12-08-2014	0,000 492 028	0,006 251 708
cal-13-08-2014	0,000 576 404	0,007 323 792
cal-14-08-2014	0,000 467 693	0,005 942 506
cal-18-08-2014	0,000 487 057	0,006 188 548
cal-19-08-2014	0,000 474 752	0,006 032 204
cal-20-08-2014	0,000 528 315	0,006 712 764
cal-21-08-2014	0,000 462 979	0,005 882 614
cal-22-08-2014	0,000 456 896	0,005 805 325
cal-25-08-2014	0,000 596 225	0,007 575 638
cal-26-08-2014-2	0,000 568 729	0,007 226 269
cal-27-08-2014	0,000 446 303	0,005 670 725
cal-28-08-2014	0,000 442 583	0,005 623 459
cal-29-08-2014	0,000 499 569	0,006 347 529
cal-01-09-2014	0,000 532 756	0,006 769 198
cal-02-09-2014	0,000 485 568	0,006 169 623
cal-03-09-2014	0,000 434 209	0,005 517 062
cal-05-09-2014	0,000 453 968	0,005 768 123
cal-08-09-2014	0,000 479 898	0,006 097 583
cal-09-09-2014	0,000 551 011	0,007 001 145
cal-10-09-2014	0,000 522 417	0,006 637 828
cal-11-09-2014	0,000 523 509	0,006 651 710
cal-12-09-2014	0,000 468 175	0,005 948 637
cal-15-09-2014	0,000 533 775	0,006 782 150
cal-16-09-2014	0,000 356 110	0,004 524 728
cal-17-09-2014	0,000 325 859	0,004 140 367

D.14.2 Calibration of the Load Cells

The conversion of voltage to water surface elevation is given by equation D.28:

$$\tau = mV + b \tag{D.28}$$

where τ is the tension in the cables. The systematic uncertainty in τ is $b_\tau = 0{,}000\,990\,761\,\text{N}$. Since more than ten points were used in the calibration of the load cells, the value of $t_{95\%}$ is set to 2. The parameters of each load cell calibration are given in Table D.74, while the intermediate calculations of the uncertainty and the final results are given in Tables D.75 and D.76.

Table D.74: Parameters of the least squares fit for the calibration of the load cells.

Load cell	m (N/V)	b (N)	R^2
1	22,250 915 115	−110,796 341 390	0,999 999 077
2	22,354 139 075	−111,700 192 921	0,999 998 928

Table D.75: Parameters for the estimation of the uncertainty in the calibration of the load cells due to the least squares fit.

Load cell	$u_{\tau-\text{fit}}$ (N)	s_V (V)	$\partial\tau/\partial V \times s_V$ (N)
1	0,034 267 490	0,004 429 628	0,098 563 284
2	0,036 926 675	0,005 149 398	0,115 110 360

Table D.76: Estimate of the uncertainty in the calibration of the load cells.

Load cell	u_τ (N)	$U_{\tau 95\%}$ (N)
1	0,104 354 988	0,208 709 975
2	0,120 892 331	0,241 784 663

Bibliography

[1] J. Fitzgerald. *Position Mooring of Wave Energy Converters*. Phd thesis, Chalmers University of Technology, 2009.

[2] L. Martinelli, P. Ruol, and G. Cortellazzo. On mooring design of wave energy converters: the Seabreath application. In P. Lynett and J. McKee Smith, editors, *Proceedings of the 33rd International Conference Coastal Engineering (ICCE)*, pages 1–12, Santander, 2012.

[3] J. Fitzgerald and L. Bergdahl. Including moorings in the assessment of a generic offshore wave energy converter: A frequency domain approach. *Marine Structures*, 21(1):23–46, 2008.

[4] W. C. Webster. Mooring-induced damping. *Ocean Engineering*, 22(6):571–591, 1995.

[5] E. Angelelli, B. Zanuttigh, F. Ferri, and J.P. Kofoed. Experimental assessment of the mooring influence on the power output of floating Wave Activated Body WECs. In P. Frigaard, J. P. Kofoed, A. S. Bahaj, L. Bergdahl, A. Clément, D. Conley, A. F. O. Falcão, C. M. Johnstone, L. Margheritini, I. Masters, and D. Sarmento, A. J.and Vicinanza, editors, *Proceedings of the 10th European Wave and Tidal Energy Conference*, Aalborg, Denmark, 2013. European Wave and Tidal Energy Conference.

[6] F. Cerveira, N. Fonseca, and R. Pascoal. Mooring system influence on the efficiency of wave energy converters. *International Journal of Marine Energy*, 3–4:65 – 81, 2013.

[7] P. C. Vicente, A. F. O. Falcão, and P. A. P. Justino. Optimization of Mooring Configuration Parameters of Floating Wave Energy Converters. In *International Conference on Ocean, Offshore and Arctic Engineering, OMAE*, pages 759–765, Rotterdam, 2011. ASME.

[8] P. C. Vicente, A. F. O. Falcão, and P. A. P. Justino. Non-linear Slack-Mooring Modelling of a Floating Two-Body Wave Energy Converter. In *Proceedings of the 9th European Wave and Tidal Energy Conference*, Southampton, UK, 2011. EWTEC.

[9] L. Johanning, G. H. Smith, and J. Wolfram. Towards Design Standards for WEC Moorings. In *6th European Wave and Tidal Energy Conference*, pages 223–230, Glasgow, UK, 2005. EWTEC.

[10] N. Fonseca, R. Pascoal, T. Morais, and R. Dias. Design of a mooring system with synthetic ropes for the FLOW wave energy converter. In *Proceedings of the ASME 2009 28th International Conference on Ocean, Offshore and Arctic Engineering*, volume 4, pages 1189–1198, Honolulu, HI, United states, 2009. American Society of Mechanical Engineers.

[11] J. Fitzgerald and L. Bergdahl. Considering Mooring Cables for Offshore Wave Energy Converters. In *Proceeding of the 7th European Wave and Tidal Energy Conference*, Porto, 2007. IST/IDMEC.

[12] M. Irvine. *Cable Structures*. Dover Publication, Inc., New York, 1981.

[13] T. S. Walton and H. Polachek. Calculation of transient motion of submerged cables. *Mathematics of Computation*, (14):27–46, 1960.

[14] C. M. Larsen and I. J. Fylling. Dynamic behaviour of anchor lines. Technical Report 3, Norwegian Maritime Research, 1982.

[15] M. S. Triantafyllou, A. Bliek, and H. Shin. Dynamic Analysis as a Tool for Open-Sea Mooring System Design. *SNAME Transactions*, 93:303–324, 1985.

[16] C. M. Ablow and S. Schechter. Numerical simulation of undersea cable dynamics. *Ocean Engineering*, 10(6):443–457, 1983.

[17] K. A. Ansari and N. U. Khan. The Effect of Cable Dynamics on the Station-Keeping Response of a Moored Offshore Vessel. *Journal of Energy Resources Technology*, 108(1):52–58, 1986.

[18] J. W. Leonard and J. H. Nath. Comparison of finite element and lumped parameter methods for oceanic cables. *Engineering Structures*, 3(3):153–167, 1981.

[19] M. Nakamura, W. Koterayama, and Y. Kyozuka. Slow drift damping due to drag forces acting on mooring lines. *Ocean Engineering*, 18(4):283–296, 1991.

[20] J. J. Burgess. Equations of Motion of a Submerged Cable with Bending Stiffness. In S. K. Chakrabarti, C. Sparks, R. C. Ertekin, and S. Jagannathan, editors, *Proceedings of the 11th International Conference on Offshore Mechanics and Artic Engineering*, pages 283–289, Calgary, Alberta, Canada, 1992. ASME.

[21] M. S. Triantafyllou and C. T. Howell. Dynamic Response of Cables Under Negative Tension: An Ill-Posed Problem. *Journal of Sound and Vibrations*, 173(4):433–447, 1994.

[22] V. J. Papazoglou, S. A. Mavrakos, and M. S. Triantafyllou. Non-linear cable response and model testing in water. *Journal of Sound and Vibration*, 140(1):103–115, 1990.

[23] S. A. Mavrakos, J. Chatjigerorgiou, and V. J. Papazoglou. Use of buoys for dynamic tension reduction in deep water mooring applications. In *Proceedings of the 7th International Conference on the Behavior of Offshore Structures (BOSS'94)*, pages Vol. 2, 417–426, Boston, 1994. Pergamon.

[24] S. A. Mavrakos, V. J. Papazoglou, M. S. Triantafyllou, and J. Hatjigeorgiou. Deep water mooring dynamics. *Marine Structures*, 9(2):181–209, 1996.

[25] L. Johanning, G. H. Smith, and C. Bullen. Large scale mooring line experiments and comparison with a fully dynamic simulation program with importance to WEC installation. pages 455–462, Lisbon, Portugal, 2007. International Society of Offshore and Polar Engineers.

[26] L. Johanning, G. Smith, and J. Wolfram. Measurements of static and dynamic mooring line damping and their importance for floating WEC devices. *Ocean Engineering*, 34(14-15):1918–1934, 2007.

[27] A. Vickers and L. Johanning. Comparison of damping properties for three different mooring arrangements. In *Proceedings of the 8th European Wave and Tidal Conference*, pages 637–645, Uppsala, Sweden, 2009.

[28] O. M. Aamo and T. I. Fossen. Finite Element Modelling of Moored Vessels. *Mathematical and Computer Modelling of Dynamical Systems: Methods, Tools and Applications in Engineering and Related Sciences*, 7(1):47–75, 2001.

[29] R. Pascoal, S. Huang, N. Barltrop, and C. Guedes-Soares. Equivalent force model for the effect of mooring systems on the horizontal motions. *Applied Ocean Research*, 27(3):165–172, 2005.

[30] A. Montano, M. Restelli, and R. Sacco. Numerical simulation of tethered buoy dynamics using mixed finite elements. *Computer Methods in Applied Mechanics and Engineering*, 196(41-44):4117–4129, 2007.

[31] D. N. Arnold, F. Brezzi, B. C, and L. D. Marini. Unified Analysis of Discontinuous Galerkin Methods for Elliptic Problems. *SIAM Journal on Numerical Analysis*, 39(5):1749–1779, 2002.

[32] B. Cockburn and C.-W. Shu. The Local Discontinuous Galerkin Method for Time-Dependent Convection-Diffusion Systems. *SIAM Journal on Numerical Analysis*, 35(6):2240–2463, 1998.

[33] B. Cockburn and C. Shu. Runge–Kutta Discontinuous Galerkin Methods for Convection-Dominated Problems. *Journal of Scientific Computing*, 16(3):173–261, 2001.

[34] P. R. Thies, L. Johanning, and G. H. Smith. Towards component reliability testing for marine energy converters. *Ocean Engineering*, 38(2–3):360–370, 2011.

[35] G. E. Karniadakis and S. J. Sherwin. *Spectral/hp Element Methods for CFD*. Oxford University Press, Oxford, New York, 2nd edition, 2003.

[36] J. S. Hesthaven and T. Warburton. *Nodal Discontinuous Galerkin Methods - Algorithms, Analysis, and Applications*. Springer, New York, 2008.

[37] J. N. Newman. *Marine Hydrodynamics*. The MIT Press, Cambridge, 1977.

[38] O. M. Faltinsen. *Sea Loads on Ships and Offshore Structures*. Cambridge University Press, Cambridge, 1993.

[39] Q. W. Ma and S. Yan. QALE-FEM for numerical modelling of non-linear interaction between 3D moored floating bodies and steep waves. *International Journal for Numerical Methods in Engineering*, 78(6):713–756, 2009.

[40] Y.-H. Yu and Y. Li. Preliminary results of a RANS simulation for a floating point absorber wave energy system under extreme wave conditions. In *Proceedings of the ASME 30th International Conference on Ocean, Offshore and Arctic Engineering OMAE2011*, Rotherdam, The Netherlands, 2011. ASME.

[41] C. Eskilsson, J. Palm, J. P. Kofoed, and E. Friis-Madsen. CFD study of the overtopping discharge of the Wave Dragon wave energy converter. In *Renewable Energies Offshore*, pages 287–294. CRC Press, 2015.

[42] W. E. Cummins. The impulse response function and ship motions. Technical Report 1661, David Taylor Model Basin Washington D. C., 1962.

[43] G. van Oortmerssen. *The Motions of a Moored Ship in Waves*. Phd, Delft University of Technology, 1976.

[44] L. Bergdahl and N. Mårtensson. Certification of Wave-Energy Plants - Discussion of Existing Guidelines, especially for mooring design. In *Second European Wave Power Conference*, Lisbon, 1995.

[45] R. E. Harris, L. Johanning, and J. Wolfram. Mooring systems for wave energy converters: A review of design issues and choices. In *3rd International Conference on Marine Renewable Energy*, pages 180–189, Blyth, UK, 2004.

[46] Det Norske Veritas. Guidelines on design and operation of wave energy converters. Technical report, Carbon Trust, 2005.

[47] Det Norske Veritas. Offshore Standard DNV-OS-E301 - Position Mooring, 2004.

[48] Mooring design approach for wave energy converters. *Proceedings of the Institution of Mechanical Engineers, Part M: Journal of Engineering for the Maritime Environment*, 220(4):159–174, 2006.

[49] N.D.P. Barltrop. *Floating Structures - A Guide for Design and Analysis, Volumes 1-2*. Energy Institute, 1998.

[50] J. Falnes. *Ocean Waves and Oscillating Systems Linear Interactions Including Wave-Energy Extraction*. Cambridge University Press, 2002.

[51] N. Fonseca, R. Pascoal, J. Marinho, and T. Morais. Analysis of Wave Drift Forces on a Floating Wave Energy Converter. In *27th International Conference on Offshore Mechanics and Arctic Engineering*, number 2003, pages 831–839, Estoril, 2008. ASME.

[52] C. Retzler. Measurements of the slow drift dynamics of a model Pelamis wave energy converter. *Renewable Energy*, 31(2):257–269, 2006.

[53] W. Sheng, A. W. Lewis, and R. Alcorn. Numerical Investigation into Hydrodynamics of Moored Floating Wave Energy Converters. In *Proceedings of the 10th European Wave and Tidal Energy Conference*, Aalborg, 2013. EWTEC.

[54] Equimar. *Protocols for the Equitable Assessment of Marine Energy Converters*. The Institute for Energy Systems, School of Engineering, The University of Edinburgh, Edinburgh, 1st edition, 2011.

[55] C. T. Howell and M. S. Triantafyllou. Stable and Unstable Nonlinear Resonant Response of Hanging Chains: Theory and Experiment. *Proceedings: Mathematical and Physical Sciences*, 440(1909):345–364, 1993.

[56] W. S. Yang. *Hydrodynamic Analyis of Mooring Lines Based on Optical Tracking Experiments*. Phd, Texas A&M University, 2007.

[57] W. Tomaszewski, P. Pieranski, and J. C. Geminard. The motion of a freely falling chain tip. *American Journal of Physics*, 74(9):776–783, 2006.

[58] R. J. Montague, J. Watton, and K. J. Brown. A machine vision measurement of slab camber in hot strip rolling. *Journal of Materials Processing Technology*, 168(1):172–180, 2005.

[59] D. C. Brown. Close-range camera calibration. *Photogrammetric Engineering*, 37(8):855–866, 1971.

[60] D. C. Brown. Decentering Distortion of Lenses. *Photometric Engineering*, 32(3):444–462, 1966.

[61] J. Heikkila and O. Silven. A four-step camera calibration procedure with implicit image correction. In *Proceedings of IEEE Computer Society Conference on Computer Vision and Pattern Recognition*, pages 1106–1112, San Juan, Puerto Rico, 1997. IEEE.

[62] L. E. Mertens. Underwater Lens and Optical Ports. In P. Halley and H. Hodara, editors, *AGARD LECTURE SERIES No. 61 on Optics of the Sea (Interface and In-water Transmission and Imaging)*, pages 5.3–1 – 5.3–25. AGARD, 1973.

[63] C. Kunz and H. Singh. Hemispherical refraction and camera calibration in underwater vision. In *OCEANS 2008*, pages 1–7, Quebec City, QC, 2008.

[64] T. Treibitz, Y. Schechner, C. Kunz, and H. Singh. Flat Refractive Geometry. *IEEE transactions on pattern analysis and machine intelligence*, 34(1):51–65, 2012.

[65] C. Eskilsson and S. Sherwin. An Introduction to Spectral/hp Element Methods for Hyperbolic Problems. Technical Report Von Karman Institute Lecture Series 2006-01, Von Karman Institute, 2005.

[66] M. S. Triantafyllou. Cable Dynamics for Offshore Applications. In J. B. Herbich, editor, *Developments in Offshore Engineering - Wave Phenomena and Offshore Topics*, chapter 6, pages 283–284. Gulf Publishing Company, Houston, Texas, 1st edition, 1999.

[67] J. Palm. *Developing Computational Methods for Moored Floating Wave Energy Devices*. Report. X - Department of Shipping and Marine Technology, Chalmers University of Technology, Göteborg, Sweden, no: 14:151 ISSN:1652-9189. Department of Shipping and Marine Technology, Chalmers University of Technology,, 2014.

[68] J. Lindahl. Implicit numerisk lösning av rörelseekvationerna för en förankringskabel. Technical Report Series A:11, Chalmers University of Technology, Gothenburg, 1984.

[69] Orcina Ltd. *OrcaFlex Manual Version 9.5a*. Daltongate Ulverston Cumbria, 2012.

[70] J. Palm, G. Moura Paredes, C. Eskilsson, F. Taveira-Pinto, and L. Bergdahl. Simulation of Mooring Cable Dynamics Using a Discontinuous Galerkin Method. In B. B. Wriggers and Rinkmann P., editors, *V International Conference on Computational Methods in Marine Engineering - MARINE 2013*, 2013.

[71] A. Sjöberg and L. Bergdahl. Förankringar och förankringskrafter. Technical Report Series B:30, Chalmers University of Technology, Department of Hydraulics, 1981.

[72] W. Greiner. *Classical Mechanics: Systems of Particles and Hamiltonian Dynamics*. Springer, New York, 2003.

[73] J. Lindahl. Modellförsök med en förankringskabel. Technical Report Series A:12, Chalmers University of Technology, Department of Hydraulics, 1985.

[74] G. Moura Paredes, C. Eskilsson, J. Palm, L. Bergdahl, L. M. Leite, and F. Taveira-Pinto. Experimental and Numerical Modelling of a Moored, Generic Floating Wave Energy Converter. In *10th European Wave and Tidal Energy Conference,*, Aalborg, Denmark, 2013.

[75] S. K. Chakrabarti. *Offshore Structure Modeling*. World Scientific Publishing Co., Singapore, 1994.

[76] J. H. Ferziger and M. Peric. *Computational Methods for Fluid Dynamics*. Springer-Verlag, Berlin, 3rd, rev. edition, 2002.

[77] M. Johansson. Transient Motions of Large Floating Structures. Technical Report A:14, Chalmers University of Technology, Göteborg, 1986.

[78] G. Moura Paredes and F. Taveira-Pinto. An experimental technique to track mooring cables in small scale models using image processing. *Ocean Engineering*, 111:439–448, 2016.

[79] R. Hartley and A. Zisserman. *Multiple View Geometry in Computer Vision*. Cambridge University Press, New York, 2nd edition, 2004.

[80] R. Szeliski. *Computer Vision - Algorithms and Applications*. Springer Verlag, London, 2011.

[81] R. C. Gonzales, R. E. Woods, and S. L. Eddins. *Digital Image Processing Using Matlab*. Pearson Education, Inc., Upper Saddle River, New Jersey, 2004.

[82] S. F. Ray. *Scientific Photography and Applied Imaging*. Focal Press, Oxford, 1st edition, 1999.

[83] J. Bouguet. Camera Calibration Toolbox for Matlab, 2013.

[84] D. E. Newland. *An Introduction to Random Vibrations, Spectral and Wavelet Analysis*. Dover Publication, Inc., Mineola, New York., 3rd edition, 1993.

[85] V. Harnois, S.D. Weller, L. Johanning, P.R. Thies, M. Le Boulluec, D. Le Roux, V. Soulé, and J. Ohana. Numerical model validation for mooring systems: Method and application for wave energy converters. *Renewable Energy*, 75:869–887, 2015.

[86] V. Krivtsov and B. Linfoot. Basin Testing of Wave Energy Converters in Trondheim: Investigation of Mooring Loads and Implications for Wider Research. *Journal of Marine Science and Engineering*, 2:326–335, 2014.

[87] A. Clément. Modelling and Standardised Design Methods. In *WaveNet - Results from the European Thematic Network on Wave Energy*, chapter 6, pages 106–128. European Community, 2003.

[88] A. F. de O. Falcão. R&D Requirements for Fixed Devices. In *WaveNet - Results from the European Thematic Network on Wave Energy*, chapter C3, pages 141–174. European Community, 2003.

[89] American Petroleum Institute. Recommend Practice 2SK - Design and Analysis of Station-keeping Systems for Floating Structures, 2005.

[90] L. Bergdahl. *Wave-Induced Loads and Ship Motions*. Chalmers University of Technology, Göteborg, 2010.

[91] M. Costa, R.l Silva, and J. Vitorino. Contribuição para o Estudo do Clima de Agitação Marítima na Costa Portuguesa. In *2as Jornadas Portuguesas de Engenharia Costeira e Portuária*, Sines, 2001. AIPCN/PIANC Secção Portugal.

[92] S. A. Hughes. *Physical Models and Laboratory Techniques in Coastal Engineering*. World Scientific Publishing Co., Singapore, 1st edition, 1993.

[93] P. J. Beresford, J. M. A. Spencer, and J. Clarke. HR WaveData - Data acquisition and analysis software User Manual. Technical Report IT 493, HR Wallingford, Wallingford, 2005.

[94] H. W. Coleman and W. G. Steele. *Experimentation, Validation, and Uncertainty Analysis for Engineers*. John Wiley & Sons, Inc., New Jersey, 3rd edition, 2009.

[95] P. J. Beresford. HR WaveMaker Wave generation control program. Technical Report IT 453, HR Wallingford Limited, Wallingford, 2003.

[96] S. W. Smith. *The Scientist and Engineer's Guide to Digital Signal Processing*. California Technical Publishing, San Diego, 1997.

[97] P. Welch. The use of fast Fourier transform for the estimation of power spectra: A method based on time averaging over short, modified periodograms. *IEEE Transactions on Audio and Electroacoustics*, 15(2):70–73, 1967.

[98] IAHR Working Group on Wave Generation and Analysis. List of Sea-State Parameters. *Journal of Waterway, Port, Coastal, and Ocean Engineering*, 115(6):793–808, 1989.

[99] Measurement Computing Corporation. PCI-DAS1602/16 Analog and Digital I/O Board User's Guide, 2009.

[100] Qualisys AB. Qualisys Track Manager User Manual, 2006.